Interrogation of Fibre Optic Sensors

David Christopher Charles Norman

Doctor of Philosophy

Aston University

January 2006

Aston University

Interrogation of Fibre Optic Sensors

David Christopher Charles Norman

Doctor of Philosophy

January 2006

The aim of the research work described in this thesis was to investigate the interrogation of fibre optic sensors using "off the shelf" optical components and equipment developed mainly for the telecommunications industry. This provides a cost effective way of bringing fibre optic sensor systems to within the price range of their electro-mechanical counterparts. The research work focuses on the use of an arrayed waveguide grating, an acousto-optic tuneable filter and low-coherence interferometry to measure dynamic strain and displacement using fibre Bragg grating and interferometric sensors.

Based on the intrinsic properties of arrayed waveguide gratings and acousto-optic tuneable filters used in conjunction with interferometry, fibre Bragg gratings and interferometric sensors a number of novel fibre optic sensor interrogation systems have been realised. Special single mode fibre, namely, high-birefringence fibre has been employed to implement a dual-beam interrogating interferometer.

The first interrogation scheme is based on an optical channel monitor, which is an arrayed waveguide grating with integral photo-detectors providing a number of amplified electrical outputs. It is used to interrogate fibre Bragg grating and interferometric sensors.

Using the properties of polarisation maintainability in high-birefringent fibre an interrogating interferometer was realised by winding a length of the fibre around a piezoelectric modulator generating a low-frequency carrier signal. The system was used to interrogate both fibre Bragg grating and interferometric sensors.

Finally, the use of an acousto-optic tuneable filter is employed to interrogate fibre Bragg gratings. The device is used to generate a very high frequency carrier signal at the output of an optical interferometer.

Keywords: arrayed waveguide grating, acousto-optic tuneable filter, fibre Bragg grating, low-coherence interferometry, high-birefringence fibre.

To Dad.

Acknowledgements

The author would especially like to thank his supervisor, Dr. D. J. Webb, for all his help, advice, guidance and encouragement over the past three years. The author has the highest respect for his intellectual and scientific abilities.

I would also like to thank my wife, Stef, who has had to endure many practice presentations, been an unpaid proof reader and for all her moral support.

Thank you to my mother, Mum, whom I stayed with while writing this thesis. Although I didn't see very much of her I deeply appreciated all the support that she so gratefully gave.

My sincere thanks go to Professor I. Bennion, Dr. R. D. Pechstedt, Dr. J. A. R. Williams, Professor L. Zhang, Dr. T, Allsop, Dr. Y. Lai, Dr. K. Zhou, Mr R. Reeves and Mrs H. Yard for their assistance and advice.

I would like to also thank Mr H. E. Biggs for all his help with the day to day running of the Photonics Research Group laboratories. His willingness to give assistance was particularly essential for the completion of the work described in this thesis.

Finally, the author would like to thank firstly, the Engineering and Physical Sciences Research Council for funding the research work, and secondly, the Royal Academy of Engineering and the Institute of Physics for financial support awarded towards overseas travel.

Contents

List of Tables

Chapter 10

Appendix C

Appendix K

List of Figures

Chapter 1: Introduction

Chapter 2: Fibre Optic Sensors

Chapter 3: Arrayed Waveguide Gratings

Chapter 4: Acousto-Optic Tuneable Filters

Chapter 5: Low-Coherence Interferometry

Chapter 6: Fibre Bragg Grating Sensor Interrogation using an Arrayed Waveguide Grating

Chapter 7: Interferometric Sensor Interrogation using an Arrayed Waveguide Grating

Chapter 8: High Birefringence Fibre Interferometer for Optical Sensing Applications

Chapter 9: Fibre Bragg Grating Sensor Interrogation using an Acousto-Optic Tuneable Filter

Appendix D:

Appendix E:

Appendix F:

Appendix G:

Appendix H:

Appendix I:

Appendix J:

Appendix K:

Appendix L:

Appendix N:

List of Abbreviations

AOM	Acousto-Optic Modulator
AOTF	Acousto-Optic Tuneable Filter
AWG	Arrayed Waveguide Grating
FBG	Fibre Bragg Grating
FSR	Free Spectral Range
FWHM	Full Width Half Maximum
Hi-Bi	High Birefringence
LPG	Long Period Grating
MEMS	Micro-Electromechanical Systems
OCM	Optical Channel Monitor
OFS	Optical Fibre Sensor
PZT	Piezoelectric Transducer
RF	Radio Frequency
RMS	Root Mean Squared
SMF	Single Mode Fibre
SNR	Signal to Noise Ratio
TE	Transverse Electric
TM	Transverse Magnetic
UV	Ultra Violet
WDM	Wavelength Division Multiplexer

1 Introduction

The function of any type of sensor system, be it electrical, mechanical or optical is to accurately interpret the condition of the sensed measurand. Fibre optic sensor systems exploit changes in the intensity, phase, wavelength or polarisation of light, which is used as the information carrier. Intensity based fibre optic sensors simply detect the change in light amplitude induced by the measurand. Phase sensors require the use of interferometric techniques to detect changes in the phase of the light field. Wavelength based fibre optic sensors rely on wavelength or frequency changes of the light. Polarisation sensors detect changes in the polarisation state of the light. The advantages of using fibre optic sensors are their immunity to electromagnetic interference, small size, high sensitivity and ease of multiplexing. The concept of fibre optic sensors is far from new; its origins are traceable to the mid-to-late 1970s [1]-[8]. Since then, the mass-production of optical communications components began reducing the cost of equipment such as light-sources, couplers, optical fibre, multiplexers, filters and detectors, encouraging extensive research into optical sensors and sensor interrogation systems. However, the vision that optical sensing techniques would now be common place and replacing conventional sensing systems is yet to happen [9]. The current view is that optical fibre sensors are suited to niche applications where conventional sensors either fail to work or are inadequate [10]. These applications include environments where there is a risk of igniting flammable substances, in areas where there are electromagnetic fields such as electric-motors or alternators, point or multipoint measurements in medicine, biotechnology or monitoring of chemical compounds, applications where high sensitivity is required and in multiplexed or distributed sensing where their low-weight and reduced

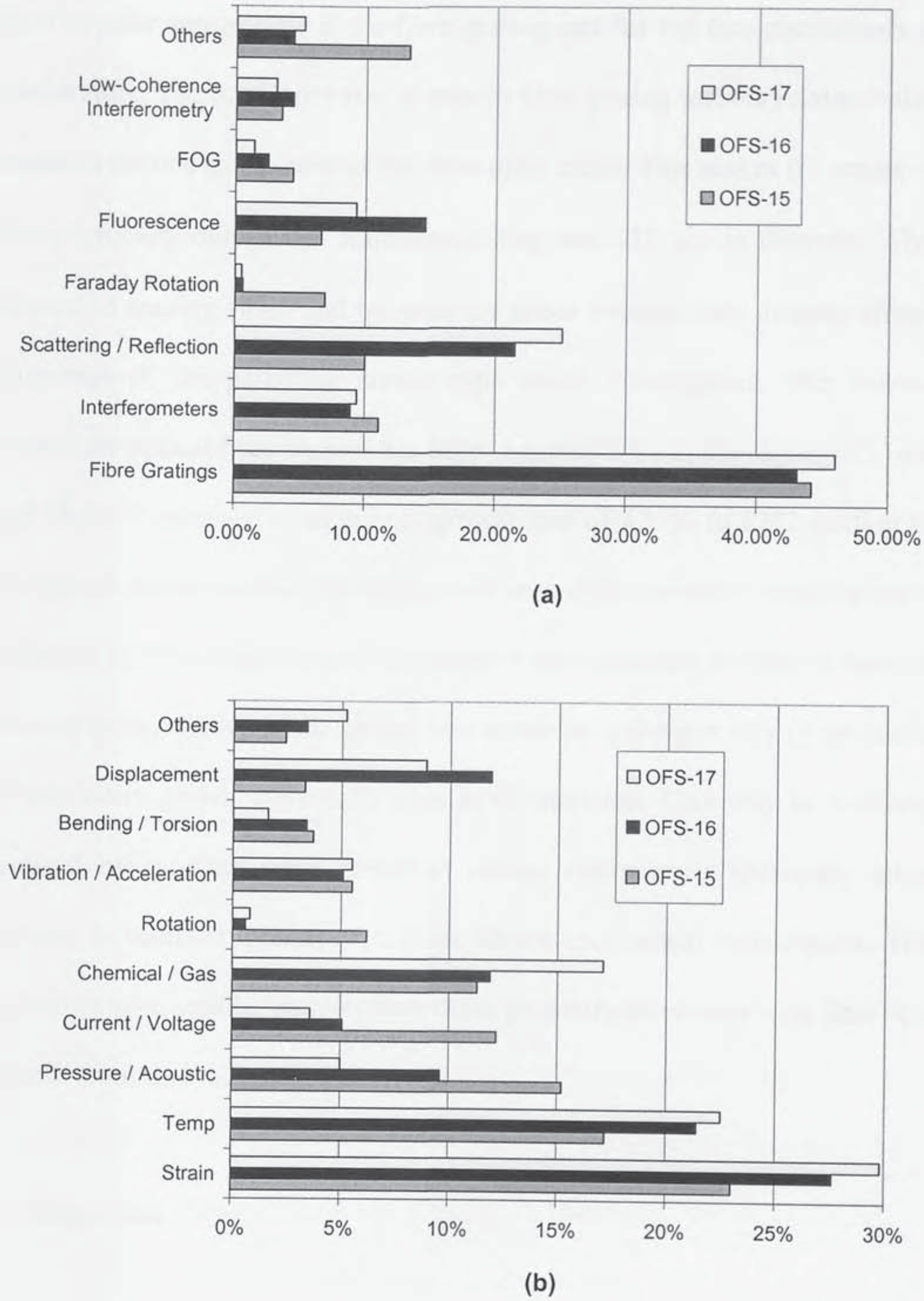

Figure 1.1 Distribution of sensor types (a) and the distribution of measurands (b) from the 15th, 16th and 17th optical fibre sensors (OFS) series of conferences.

complexity is extremely appealing. A review of the status of different sensor types and different measurands from the 15th [11], 16th and 17th optical fibre sensors (OFS) series of conferences are shown in figure 1.1(a) and 1.1(b), respectively. Demonstrating that the most popular sensor type is the fibre grating and the top two measurands are strain and temperature. The popularity that is seen in fibre grating sensors relates to the fact that the sensor is formed in the core of the fibre optic cable. This makes the sensor very compact being typically only a few millimetres long and 125 μm in diameter. The widespread interest in sensing strain and temperature arises because they directly affect the variable properties of the particular sensor type under interrogation. The current worldwide market for optical fibre sensors has been reported to be in the region of £164 million [12] and likely to increase at an annual growth rate of 4.1 % to £212 million by 2011 [12]. The global sensor market (for all types of sensor) is currently valued in the region of £30 billion [13]. Therefore, in order to improve the economic success in optical sensing and procure a bigger slice of the global sensor market a cheaper way of producing fibre optic sensor interrogation systems is seen to be required. One way to achieve this can be realised by utilising mass produced optical components ultimately allowing optical sensors to compete directly with their electro-mechanical counterparts. This will allow industries with smaller budgets than those presently associated with fibre optic sensors to benefit from their advantages.

1.1 Objectives

The objectives of the research work described in this thesis are to exploit “off the shelf”, standard, mass-produced, optical components to interrogate fibre optic sensors rather than trying to develop bespoke interrogation systems that are potentially always going to be more expensive.

The research work described in this thesis can be divided into four fields of interest:

1. To investigate the use of an arrayed waveguide grating to interrogate fibre Bragg grating sensors.
2. To investigate the use of an arrayed waveguide grating to interrogate interferometric sensors.
3. To investigate the use of a differential path interferometer constructed from high-birefringence optical fibre to interrogate fibre optic sensors.
4. To extend the use of acousto-optic tuneable filters to interrogate fibre Bragg grating sensors.

In terms of (1) and (2) the use of an arrayed waveguide grating, the aim is to study, characterise, improve and explore novel ways to interrogate fibre Bragg and interferometric sensors. (3) The motivation to demonstrate a differential path interrogating interferometer constructed from a single length of high-birefringence fibre arises from the need to relax the costs normally associated with integrated optic interferometers. The motivation behind (4) is to demonstrate the use of an acousto-optic tuneable filter to generate a high-frequency carrier at the output of a Mach-Zehnder interferometer, proposed by Boulet *et al* [14] in 2001.

Overall, the research work described in this thesis is a complex system of mechanical, optical and electronic elements. The development technique adopted to complete the work is based on a system engineering approach [15] designed to deal with the complexity of large projects by breaking them down into logical and more manageable parts.

1.2 Thesis Outline

This thesis contains 11 chapters which describe the relevant technologies used to implement the interrogation systems realised during this research project. Following this introduction, chapter 2 reviews fibre Bragg grating and interferometric sensors. Chapter 2 also highlights the important characteristics of single mode optical fibres, fibre Bragg gratings, simultaneous strain and temperature sensing, multiplexing optical fibre sensors, it also introduces the broadband light source used in the experimental work, noise and concludes with a look at the reliability and lifetime of fibre optic sensors. The next three chapters are each dedicated to a key technology that performs a very important role in the interrogation schemes that are described in subsequent chapters. Chapter 3 describes in some detail the operation of arrayed waveguide gratings. Chapter 4 introduces the operation of acousto-optic tuneable filters. Chapter 5 takes a detailed look at low-coherence interferometry. Chapter 6 is the first of the four experimental chapters and discusses the interrogation of fibre Bragg grating sensors using an arrayed waveguide grating. Chapter 7 describes the interrogation of interferometric sensors using an arrayed waveguide grating. Chapter 8 discusses the use of a fibre optic sensor interrogating interferometer formed from a length of high-birefringence fibre. Chapter 9, the concluding experimental chapter describes the use of an acousto-optic tuneable filter used to generate a high frequency carrier signal in a fibre optic sensor interrogating interferometer. The final two chapters 10 and 11 are the thesis conclusion including suggestions for future work and a list of the publications resulting from the research, respectively. There are also a number of appendices that detail aspects that are relevant to the work but not necessary to include in the chapter text. There is a clear indication throughout the content of this thesis that refers the reader to the relevant appendix.

1.3 References

[1] V. Vali and R. W. Shorthill, "Fiber ring interferometer," *Applied Optics*, vol. 17, No. 5, pp. 1099-1103, May 1976

[2] A. J. Rodgers, "Optical methods for measurement of voltage and current at high voltage," *Optical and Laser Technology*, vol. 9, pp. 273-283, December 1977

[3] J. A. Bucaro, H. D. Hardy and E. Carome, "Fiber optic hydrophone," *Journal of Acoustical Society of America*, vol. 62, No. 5, pp. 1302-1304, November 1977

[4] J. A. Cole, R. L. Johnson and P. B. Bhuta, "Fiber optic detection of sound," *Journal of Acoustical Society of America*, vol. 62, No. 5, pp. 1136-1138, November 1977

[5] C. D. Butter and G. B. Hocker, "Fibre optic strain gauge," *Applied Optics*, vol. 17, No. 18, pp. 2867-2869, September 1978

[6] G. B. Hocker, "Fibre optic sensing of temperature and pressure," *Applied Optics*, vol. 18, No. 9, pp. 1445-1448, May 1979

[7] B. Budiansky, D. C. Drucker, G. S. Kino and J. R. Rice, "The pressure sensitivity of clad optical fibre," *Applied Optics*, vol. 18, No. 24, pp. 4085-4088, December 1979

[8] J. A. Bucaro and T. R. Hickman, "Measurement of sensitivity of optical fibers from acoustic detection," *Applied Optics*, vol. 18, No. 6, pp. 938-940, March 1979

[9] D. J. Webb, "Optical-fiber sensors an overview," *Materials Research Community Bulletin*, vol. 27, No. 5, pp. 365-369, May 2002

[10] L. M. López-Higuera, "Introduction to fibre optic sensing technology," *in Handbook of Fibre Sensing Technology*, *John Wiley & Sons*, ISBN: 0471-82053-9, 2002

[11] B. Lee, "Review of the present status of optical fibre sensors," *Optical Fibre Technology*, vol. 9, pp. 57-79, 2003

[12] Electronics.ca Publications, "Fiber optic sensors research report," *Electronics Instruments and Sensors*, vol. NM5020, October 2005

[13] G. F. Fernando, D. J. Webb and P. Ferdinand, "Optical fibre sensors," *Materials Research Community Bulletin*, vol. 27, No. 5, pp. 359-361, May 2002

[14] C. Boulet, D. J. Webb, M. Douay and P. Naiy, "Simultaneous interrogation of fibre Bragg grating sensors using an acousto-optic tunable filter," *Photonics Technology Letters*, vol. 13, No. 11, pp. 1215-1217, November 2001

[15] J. C. Whitaker, "The electronics handbook," *CRC Press and IEEE Publishing*, ISBN: 0-8493-8345-5, 1996

2 Fibre Optic Sensors

Single mode fibre (SMF) has enabled the progress of many new areas in engineering and science. Since only one mode is guided its polarisation and phase can potentially be determined and utilised. The development of fibre Bragg gratings (FBGs) and its variants have evolved into useful components in optical sensing as well as in fibre lasers, filters and dispersion compensators. Dual-beam interference of light can be used to measure very small perturbations in the phase of one of the beams and has encouraged the development of a variety of interferometer based optical sensors. This chapter outlines the features of the fibre optic sensor technology relevant to the work described in this thesis. These being, single-mode fibre, fibre Bragg gratings, FBG and interferometric sensors which are both used extensively for strain and displacement measurements by the author for the work described in this thesis. Multiplexing, broadband light source, noise in fibre optic sensors, and the lifetime and reliability of fibre optic sensors conclude the chapter.

2.1 Introduction

A great deal of effort has gone into the development of fibre optic sensors attributed to the advantages over their electro-mechanical counterparts. These advantages include their immunity to electromagnetic interference [1] which means they can be used near heavy-duty switching equipment. They carry no electric current so they can be used in environments where there is a risk of explosion [2][3]. Their small size makes it easier to mount or embed them into a variety of materials [4][5]. They can be used to measure a wide range of parameters such as temperature, strain, pressure, current, voltage, vibration, bending, displacement, radiation and acoustic emissions [6]-[16]. Optical fibre sensors can be multiplexed or distributed along a single fibre unlike electrical sensors which require a pair of current carrying wires for each sensor. Fibre optic sensors can be loosely classified into two types, intrinsic and extrinsic sensors. An intrinsic sensor is when the measurand directly modulates some physical property of the fibre, such as an all fibre Mach-Zehnder interferometer or FBG. Extrinsic sensors are some form of the optical sensing element or system that is remotely deployed and illuminated via a fibre optic link and the optically encoded signal transferred by the input fibre (or other fibre) to a central processing point, for demodulation.

2.2 Single Mode Fibre

One of the many greatest engineering achievements of the last century was the work leading to the development of the laser and low-loss optical fibre, revolutionising light-wave communications and high performance fibre optic sensors. For single mode operation [17] around the 1550 nm window the core diameter is in the order of 9 μm surrounded by a lower index cladding with a standardised diameter of 125 μm [18] such that the number of propagating modes reduces to one. The key performance parameters of SMF include dispersion, attenuation and birefringence [18]-[20]. Various physical parameters that affect the fibre include the concentration and types of dopants within the core/cladding, the refractive index difference between the core and the cladding, the photosensitivity, the cross sectional index profile, bending and mechanical strength [18]-[23]. These important features characterise the fibre based devices used in this research work.

2.2.1 High Birefringence Fibre

In order to avoid unpredictable phase shifts due to the inherent birefringence and external perturbations that affects the state of polarisation in standard SMF, a special type of fibre variant known as polarisation maintaining or high birefringence (Hi-Bi) fibre has been developed. Hi-Bi fibre has two orthogonal principle axes described as the fast (lower refractive index) and slow axes (higher refractive index), referring to the phase velocity of the light travelling within them. The birefringence is a measure of the refractive index difference between the two axes. Light with its electric field aligned with either the fast or the slow axis will preserve its polarisation. Otherwise the light will distribute into two non-interfering polarised modes with different propagation velocities according to how the electric fields project onto the fast and slow axes of the fibre. An important issue with Hi-Bi fibre is how well the two axes hold a given polarisation. There are many factors that affect the polarisation maintaining properties of the fibre. These include inherent factors like structural imperfections and environmental factors such as temperature or mechanical deformations like bending and twisting. This results in random mode-coupling as the birefringence varies in strength and orientation [24]. To reduce the effects of temperature, thick nylon coatings around the fibre can be used, which have been reported to reduce the thermal sensitivity [25]. This thick nylon layer also effectively helps hold the polarisation, particularly in coiled fibres [25]. However, excess transverse pressure particularly at 45° azimuth can cause severe mode-coupling [26].

2.2.2 Photosensitivity in Optical Fibres

Photosensitivity in optical fibre manifests itself as a change in refractive index following exposure to ultra-violet (UV) radiation. This phenomenon was discovered accidentally by Hill *et al* [27][28] in 1978. Their work produced a Bragg grating as a result of a standing wave pattern formed by the back reflections from the end of a low-mode germanosilica fibre illuminated by an argon-ion laser. This discovery has led to intense research into the fabrication and applications of FBGs and their variants. However, photosensitivity and the accompanying refractive index change is yet to be fully explained by one theory [38] but is a combination of several effects and that the relative contributions from each differ according to fibre type, fibre preparation and inscription.

Point defects are important to optical fibres because their absorption bands cause detrimental transmission losses. These defects are called colour-centres produced by ionising radiation and the fibre drawing process [38]. Extensive research using electron spin resonance techniques has identified three intrinsic point defects in silica glass. These being the E' centre associated with aging effects and radiation degradation, the nonbonding oxygen-hole centre and the peroxy centre [38]. It is well established that germanium-silica (GE-Si) and germanium-germanium (Ge-Ge) wrong-bonds are responsible for the photosensitivity in germanosilica glass. Photoionisation of the wrong-bonds triggers the process responsible for the index change. Irradiation at around 240 nm ionises a wrong-bond forming a germanium E' centre [42]. The electrons released during this process are understood to form further defect centres [147].

In recent years, hydrogen-loading, flame brushing and co-doping have been used to enhance the photosensitivity of optical fibres. Hydrogen-loading is carried out by diffusing hydrogen molecules into the fibre core at high pressure (typically 150-225 bar) at temperatures of 25 °C to 80 °C. Fibres treated in such a way can experience permanent changes in the fibre core refractive index of 0.01 after UV irradiation. The mechanism that increases the photosensitivity in germanosilicate fibre stems from a reaction of the glass with hydrogen forming Si-OH groups and oxygen-deficient germanium defects. These reactions can occur at every germanium site and are not dependent on the presence of defects [34]. The UV induced refractive index change is permanent and any un-reacted hydrogen diffuses out of the fibre. The presence of dissolved un-reacted hydrogen in the area of the fabricated FBG temporarily increases the refractive index, and its subsequent, diffusion leads to a small shift in the Bragg wavelength [148].

An alternative method to hydrogen-loading optical fibre is to use a technique termed flame brushing which permanently increases the photosensitivity in the fibre core [149]. The fibre is brushed repeatedly by a flame fuelled with hydrogen and a small amount of oxygen. Flame temperatures of around 1700 °C allow hydrogen to diffuse into the fibre core. The effect is localised to the fibre core leaving the cladding properties unaffected. It has been demonstrated that after UV irradiation changes in the fibre refractive index by a value exceeding 10^{-3} are possible [149].

The addition of various co-dopants, such as boron [150], tin [151] or nitrogen [152] in germanosilicate fibre has also resulted in photosensitivity enhancement. The inclusion of boron can lead to a refractive index change around four times larger than that obtained in pure germanosilicate fibre [150]. UV photosensitivity has been measured and FBGs fabricated in non-$Ge0_2$-containing aluminophosphosilicate fibres [34] with core dopants including cerium and europium. Phosphorus-doped silica fibre presensitised by deuterium loading has been used to fabricate FBGs produced by UV exposure at 193 nm and by UV exposure at 248 nm with the fibre hydrogen-loaded and held at a temperature of 400 °C [34]. FBGs have also been successfully fabricated by UV exposure at 248 nm in flourozirconate glass fibre doped with cerium [34].

2.3 Fibre Bragg Gratings

A Bragg grating consists of periodic refractive index modulation produced within the length of the fibre core acting as a series of partially reflecting mirrors or planes illustrated in figure 2.1. When broadband light illuminates the grating the first mirror reflects only a small amount of all the light, when the illuminating beam reaches the second and subsequent mirrors, more small amounts of light are reflected. Each reflected part of the light arrives back at the preceding mirror after travelling twice through the fibre core of refractive index n over a distance or period Λ between the mirrors. This

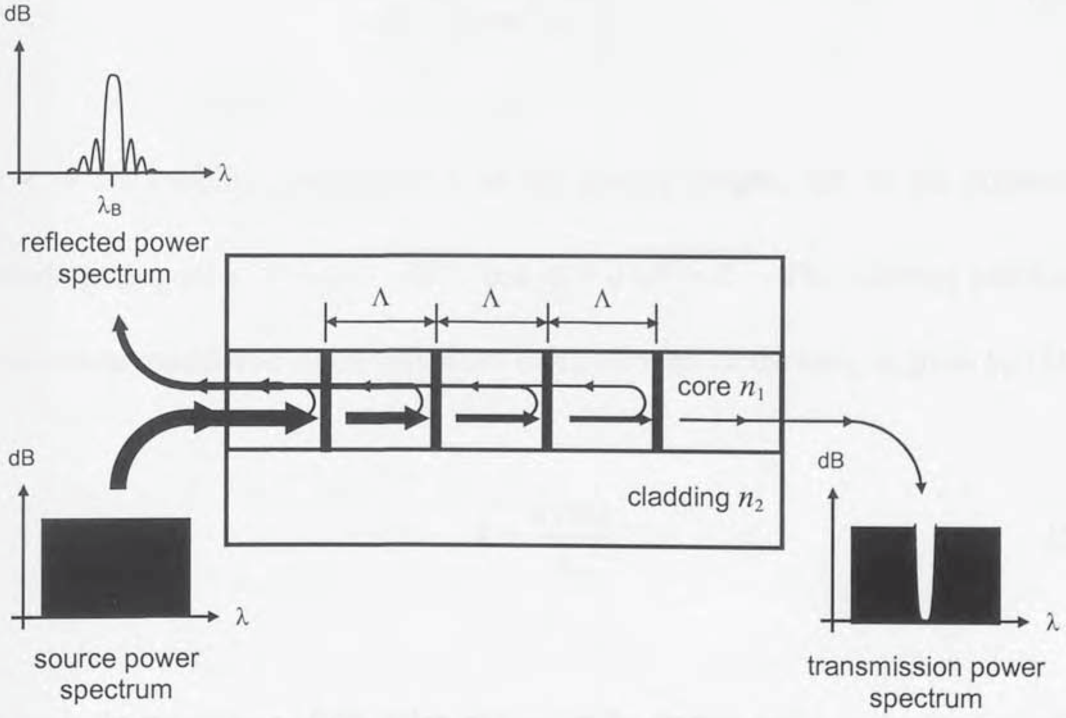

Figure 2.1 Diagram of the fibre Bragg grating concept and its optical function.

means that for a certain wavelength the reflected light constructively adds forming the grating. The wavelength of peak reflectivity or Bragg wavelength λ_B, is given by [29]

$$\lambda_B = 2n\Lambda \tag{2.1}$$

A common approach to a theoretical description of the interaction of guided waves with fibre gratings is to use couple-mode theory [30]-[32]. The reflectivity R of the grating is given by [33][34]

$$R = \frac{k^2 \sinh^2(S\,L)}{\Delta\beta^2 \sinh^2(S\,L) + S^2 \cosh^2(S\,L)} \qquad k^2 > \Delta\beta^2 \tag{2.2a}$$

$$R = \frac{k^2 \sin^2(Q\,L)}{\Delta\beta^2 - k^2 \cos^2(Q\,L)} \qquad k^2 < \Delta\beta^2 \tag{2.2b}$$

where k is the coupling coefficient, L is the grating length, $\Delta\beta$ is the differential eigenmode propagation, $S = \sqrt{k^2 - \Delta\beta^2}$ and $Q = \sqrt{\Delta\beta^2 - k^2}$. The coupling coefficient k for sinusoidal modulation of the refractive index throughout the core, is given by [34]

$$k = \frac{\pi\,\Delta n\,\eta}{\lambda_B} \tag{2.3}$$

where Δn is the magnitude of the index change in the grating and η is the fraction of the fibre mode power contained by the fibre core [34]. If the grating has been uniformly written η can be approximated by [29][35]

$$\eta \approx 1-\frac{1}{V^2}=1-\left(\frac{\lambda}{2\pi a}\right)^2\frac{1}{\left(n_1^2-n_2^2\right)} \tag{2.4}$$

where V is the fibre V-parameter (V $\leq$ 2.405 for SMF) [18], λ is the free space wavelength, a is the fibre core radius, n_1 is the fibre core refractive index and n_2 the fibre cladding refractive index. The differential eigenmode propagation $\Delta\beta$ is given by [33][34]

$$\Delta\beta=\beta-\frac{p\pi}{\Lambda} \tag{2.5}$$

$\beta=2\pi\, n/\lambda$ is the eigen propagation constant where λ is the free space wavelength and p is an integer. The maximum reflectivity R_{max} occurs when $\Delta\beta=0$

$$0=\left(\beta-\frac{p\pi}{\Lambda}\right)=\left(\frac{2\pi\, n}{\lambda}-\frac{p\pi}{\Lambda}\right)=\left(\frac{2\pi\, n}{p\lambda}-\frac{2\pi\, n}{\lambda_B}\right) \tag{2.6}$$

i.e. when

$$p\lambda=\lambda_B \tag{2.7}$$

which specifies the Bragg condition, with the Bragg wavelength λ_B of order p [34]. $\Delta\beta$ is therefore a measure of detuning from this condition. The strongest interaction occurs for the fundamental Bragg order designated by $p=1$ [34]. When $\Delta\beta=0$ equation (2.2a) becomes

$$R_{\max} = \tanh^2(k\,L) \tag{2.8}$$

Therefore the reflectivity increases as either the length L of the grating or the magnitude of the index change in the grating Δn increases. A general expression for the approximate full width half maximum bandwidth of an FBG is given by [36]

$$\Delta\lambda_{FWHM} = \lambda_B\,\alpha\,\sqrt{\left(\frac{1}{2}\frac{\Delta n}{n}\right)^2 + \left(\frac{1}{N}\right)^2} \tag{2.9}$$

where α is approximately 1 for strong gratings (near 100% reflection) and around 0.5 for weak gratings, $(\Delta n/n)$ is the refractive index perturbation which is normally determined by the exposure power and time of the ultraviolet radiation for a specified fibre [37] and N is the number of grating planes.

The complete analysis of FBGs exists in dedicated literature: there are two text books [38][39], a tutorial review paper [34] and other papers and books of a more general nature [40]-[45].

2.3.1 Fibre Bragg Grating Fabrication

Meltz *et al* [46] demonstrated that FBGs could be formed in optical fibre by exposure to a coherent two-beam UV interference pattern [29][35] through the cladding, illustrated in

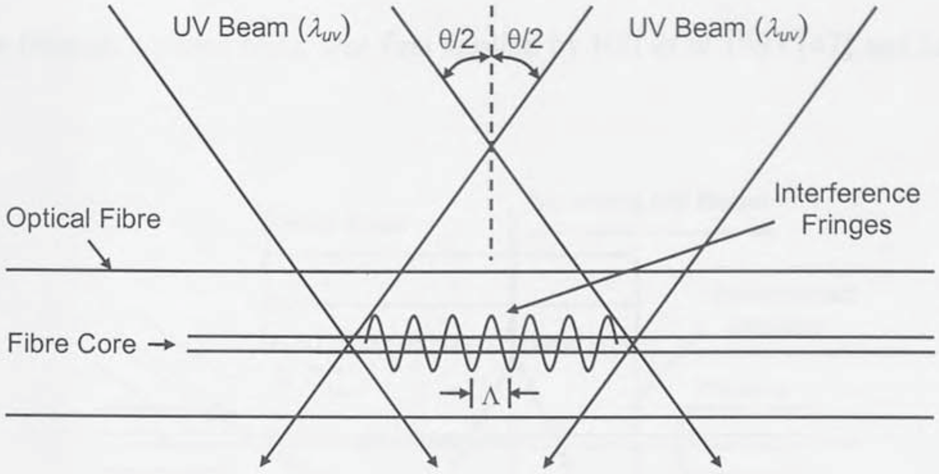

Figure 2.2 Diagram showing the inscription of a periodic fibre Bragg grating by two interfering ultra-violet beams.

figure 2.2. The FBG is photo-induced as a spatial modulation of the fibre refractive index with a grating period Λ given by [34]

$$\Lambda = \frac{\lambda_{uv}}{2\sin\frac{\theta}{2}} \tag{2.10}$$

where $\theta/2$ is the half angle between the two writing beams of wavelength λ_{uv}. From equation (2.1) and (2.10) the Bragg wavelength λ_B is therefore given as

$$\lambda_B = \frac{n\lambda_{uv}}{\sin\frac{\theta}{2}} \tag{2.11}$$

The interferometric fabrication technique allows inscription of Bragg gratings at any desired wavelength by simply changing the intersecting half angle $\theta/2$ or the UV wavelength. An alternative method of grating manufacture based on near-contact exposure through a phase mask was first applied by Hill *et al* 1993 [47] and has become the method of choice for reproducible grating fabrication, the concept of which is shown in figure 2.3. One of the advantages of near-contact exposure is the freedom to be able to angle the fibre relative to the phase mask forming tilted gratings [48]. The expression for the Bragg wavelength using a phase mask is given by [48]

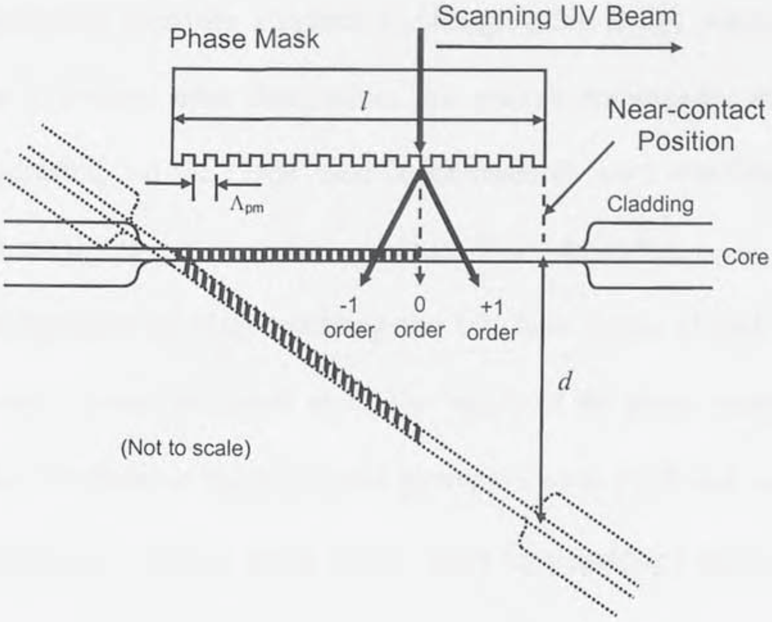

Figure 2.3 Diagram showing the grating fabrication process through ultra-violet exposure with a phase mask.

$$\lambda_B = 2n\Lambda\sqrt{1+\left(\frac{d}{l}\right)^2} \tag{2.12}$$

where l is the length of the phase mask and d is the distance from one end of the fibre core to the near-contact position when the fibre is parallel to the phase mask. When the exposed fibre core is parallel to the phase mask $d = 0$ and hence $\lambda_B = 2n\Lambda$. A disadvantage of the phase mask technique is the need to have a separate phase mask for each Bragg wavelength required. It has however been demonstrated that stretching the fibre before fabrication provides a means of changing the Bragg wavelength [49][50]. When the fibre is relaxed after fabrication, the grating compresses and the reflected wavelength is adjusted. All the FBGs used in the research work described in this thesis were fabricated using the phase mask technique. The fabrication set-up consisted of a computer controlled moving stage enabling the UV laser beam at 244 nm (around 90 mW) to be scanned at various speeds along the length of the phase mask. All the FBGs manufactured are fabricated in hydrogenated germanosilicate SMF and annealed at 70 °C for 24 hours [51][52]. Details on some of the FBGs fabricated are discussed in chapters 6, 8 and 9.

2.4 Chirped Bragg Gratings

Chirped Bragg gratings have a continuously varying grating period that creates a very broad transmission or reflection profile. Chirped Bragg grating can be realised by varying either the fibre core index and/or the grating period by position x along the grating. The Bragg condition is given by [34].

$$\lambda_B(x) = 2n(x)\Lambda(x) \tag{2.13}$$

Chirped Bragg gratings have been fabricated in optical fibres by various methods [53]-[56]. The method of choice for repeatability is based on a specially produced stepped phase mask [56] creating a series of several gratings with increasing period in the fibre to

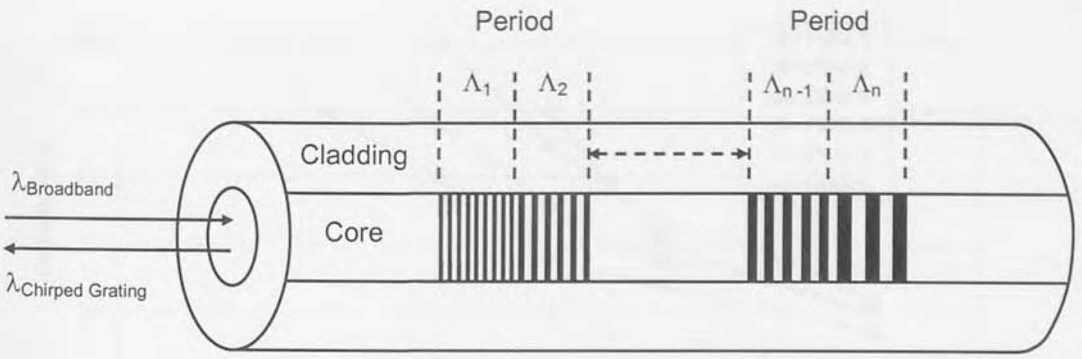

Figure 2.4 Schematic diagram of a series of several gratings with increasing period to simulate a chirped grating.

approximate a linear chirp. The principle is shown in figure 2.4 and is the fabrication method used for the research work described in this thesis. Details on one of the chirped grating fabricated is discussed in chapter 6.

2.5 Superimposed Fibre Gratings

Othonos *et al* [57] demonstrated the inscription of multiple Bragg gratings at the same location in the optical fibre using an interferometric setup. Their results are represented in figure 2.5 showing the reflectivity 2.5(a) and linewidth 2.5(b) of six Bragg gratings superimposed in the same place in the optical fibre. Superimposed gratings can also be fabricated using a phase mask and the stretch and write technique [50]. The disadvantage of superimposing gratings manifests from changes in the mode effective index of refraction and the modulation depth of refractive index perturbations each time a new grating is fabricated. This results in a small shift in the centre wavelength, a reduction in the reflectivity and a reduction in the linewidth of the overwritten gratings [57][58].

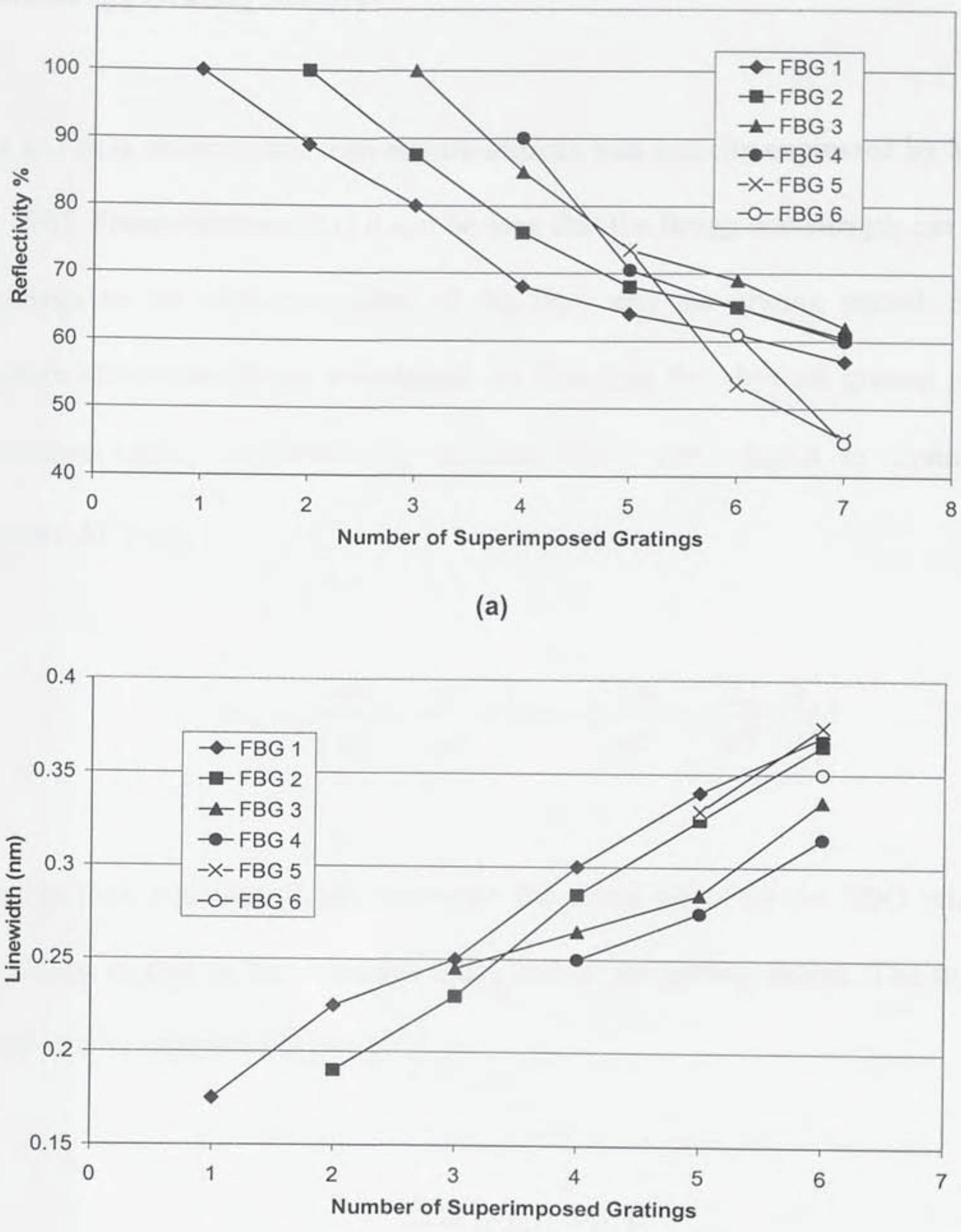

(a)

(b)

Figure 2.5 Reflectivity's for each Bragg grating as a function of the number of gratings superimposed in the same location (a) and the evolution of the full-width-half-maximum linewidths of an existing grating as a result of additional superimposed gratings (b) [57].

Details on one of the superimposed gratings fabricated using a phase mask and the stretch and write technique is discussed in chapter 6.

2.6 Fibre Bragg Grating Sensors

Interest in FBGs as strain and temperature sensors was initially expressed by Meltz *et al* [46] in 1987. From equation (2.1) it can be seen that the Bragg wavelength can be altered by a change in the refractive index of the fibre and the grating period. Strain and temperature affects the Bragg wavelength by changing the physical grating period and the refractive index. Differentiating equation (2.1) with respect to strain $\Delta\varepsilon$, and temperature ΔT gives

$$\Delta\lambda_B = 2\left(\frac{dn}{d\varepsilon}\Lambda + \frac{d\Lambda}{d\varepsilon}n\right)\Delta\varepsilon + 2\left(\frac{dn}{dT}\Lambda + \frac{d\Lambda}{dT}n\right)\Delta T \tag{2.14}$$

The first in term equation (2.14) represents the strain effect on the FBG relating to a strain induced change in the refractive index and/or the grating period. The strain effect term may also be expressed by [46]

$$\frac{\Delta\lambda_B}{\Delta\varepsilon} = \lambda_B(1-\rho_e) \tag{2.15}$$

where ρ_e is an effective photo-elastic constant given by [46]

$$\rho_e = \left(\frac{n^2}{2}\right)(\rho_{12} - \mu(\rho_{11} + \rho_{12})) \tag{2.16}$$

μ is Poisson's ratio, and ρ_{11} and ρ_{12} are components of the strain optic tensor (Pockel's coefficients) of the fibre. For silica fibre operating at room temperature (293 K) in the C-Band (the C-Band is defined as the wavelength range between 1528 nm to 1565 nm [18]) $\rho_{11} = 0.113 \pm 0.005$, $\rho_{12} = 0.252 \pm 0.005$, $\mu = 0.16 \pm 0.01$ [59] and $n = 1.45$ [60]. For a grating with a Bragg wavelength of 1550 nm the strain sensitivity $\Delta\lambda_B/\Delta\varepsilon$ is around 1.23 pm/με. The second term in equation (2.14) represents the temperature effect on the FBG and relates to the thermal expansion of the grating which affects the index of refraction and/or the grating period. The temperature effect term may also be expressed as [35]

$$\frac{\Delta\lambda_B}{\Delta T} = \lambda_B(\xi + \alpha) \tag{2.17}$$

where ξ is the thermo-optic coefficient and α is the thermal expansion coefficient of the fibre. For silica fibre operating at room temperature in the C-Band the thermo-optic coefficient is 8.03×10^{-6} [60] and the thermal expansion is 0.55×10^{-6} [60]. Therefore, the temperature sensitivity can be seen to be predominately due to the thermo-optic effect, for a grating with a Bragg wavelength of 1550 nm the thermal sensitivity $\Delta\lambda_B/\Delta T$ is approximately 13.3 pm/°C. The strain and temperature response of FBGs can be used to detect other measurands. For example inhomogeneous flow may be sensed by using an FBG as a temperature sensors mounted in a glass tube next to a heated wire. Air flow reduces the thermal equilibrium resulting in a relationship between the air speed and the temperature of the FBG [61]. FBGs can also be used to directly detect pressure [62][63] and magnetic fields [64], (see appendix A).

2.6.1 Advantages of Fibre Bragg Grating Sensors

The important advantages of FBG sensors are electrically passive operation, high sensitivity, low weight and small size. Most significantly are their wavelength-encoding multiplexing capability which allows many sensors to be fabricated into a continuous length of optical fibre and their ability to be embedded into fibre-reinforced composite materials for smart structure applications. The sensed information from FBGs is usually encoded directly into a change in the wavelength, which is an absolute measurement. Hence, the output does not depend on any fluctuations in the total light levels or system losses [37][65].

2.7 Simultaneous Strain and Temperature Sensing using Fibre Bragg Gratings

As seen in section (2.6) the Bragg wavelength changes when subjected to strain and temperature fields simultaneously. FBGs used as strain sensors will be unable to distinguish any temperature variations in the vicinity of the sensor. Various schemes have been developed to overcome the strain/temperature induced wavelength shift [66]. These include the use of a reference grating as a temperature sensor isolated from the strain sensor [62]. Another method is to use the wavelength shift based on two superimposed gratings exploiting the differential dispersion of the strain and temperature coefficients at different Bragg wavelengths [67]. A composite sensor formed from two gratings with different cladding diameters has been described [68]. When subjected to strain, the gratings produce different changes in the Bragg wavelength. However the temperature sensitivity is similar for the two gratings. Another composite sensor formed by adjoining a Type I (standard grating written in hydrogenated fibre) and a Type IA (regenerated grating after erasure of a Type I) has been described [69]. This results in the gratings being optically separated with different temperature coefficients. A method using a long period grating (LPG) and a FBG has been reported [70]. The LPG and FBG are fabricated in different types of fibre, ensuring that the LPG has a much larger thermal coefficient but a smaller strain coefficient than the FBG [71]. Chirped gratings fabricated in tapered fibre [72] can be temperature independent. Thermal effects change the grating spacing uniformly, changing the centre wavelength. Under strain, the effective spectral bandwidth increases rather than the Bragg wavelength.

2.8 Interferometric Sensors

Interference of light underlies many high precision sensor systems. The use of optical fibre allows interferometric sensors to be extremely compact and robust. There are several arrangements of interferometers such as the Sagnac, Michelson, Fabry-Pérot and Mach-Zehnder [73] which allow the measurement of extremely small phase shifts. Interferometric sensors can be used to detect a number of measurands such as acoustic fields, magnetic fields, electric fields, thermal fields, acceleration, current flow, displacement and vibrations [74]-[81]. Interferometric sensors are intrinsically quiet if mounting and packaging the sensor is done with care. However, thermal fluctuations acting on the transduction element and fluctuations in the relative state of polarisation of the interfering beams result in a fundamental phase noise. The phase noise is dealt with in detail in chapter 5.

2.8.1 Mach-Zehnder Interferometric Sensor

The Mach-Zehnder interferometer employs separate beam-splitting and recombining components allowing production of two complementary outputs. Differential path interferometers are analytically similar to the Mach-Zehnder; here the two arms of the interferometer are formed in a single fibre and subjected to stimuli at different degrees. This leads to reduced measurement sensitivity but has the advantage of reducing the effect from environmental perturbations. The two optical paths within a single fibre can be formed using various speciality fibres, high birefringence fibre [82], two mode fibre [83], twin core fibre [84] as well as standard single mode fibre [85]. A typical all fibre non-differential path Mach-Zehnder configuration [86] is shown in figure 2.6. One arm of the interferometer is normally configured as the sensing arm and the other the

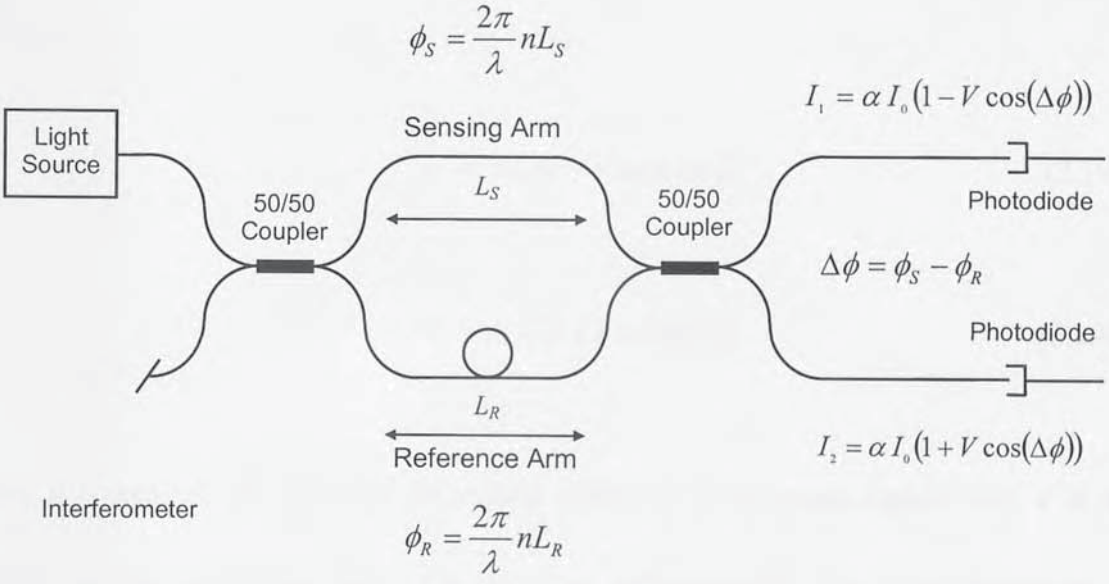

Figure 2.6 Schematic diagram of an all-fibre Mach-Zehnder interferometer.

reference arm. The optical phase delay ϕ of light passing through an optical fibre is given by [87]

$$\phi = \frac{2\pi}{\lambda} nL \tag{2.18}$$

where λ is the central wavelength of the light source, n is the refractive index of the fibre and L its physical length. The output intensity I_1 and I_2 at the detectors are given by [88]

$$I_1 = \alpha I_0 (1 - V\cos(\Delta\phi)) \tag{2.19a}$$

$$I_2 = \alpha I_0 (1 + V\cos(\Delta\phi)) \tag{2.19b}$$

where α represents the losses in the optical paths, I_0 is the mean signal level, V is the visibility of the interference and $\Delta\phi$ is the phase difference $(\phi_r - \phi_s)$ of the light between the reference and sensing beams. When the interferometer is illuminated by a low-coherent or broadband light source a complementary channelled spectrum is observed at the two outputs carrying information of the optical path imbalance between the two interferometer arms. A detailed investigation of low-coherence interferometry is found in chapter 5. The phase difference $\Delta\phi$ due to a longitudinal strain causing a change in length of a section of the sensing fibre ΔL is given by [89]

$$\frac{\Delta\phi}{\Delta L} = \frac{2\pi}{\lambda} n \left(1 - \frac{n^2}{2}\left[(1-\mu)\rho_{12} - \mu\rho_{11}\right]\right) \tag{2.20}$$

where μ is the ratio of the lateral strain to uniaxial strain (Poisson's ratio) and ρ_{11} and ρ_{12} are components of the strain optic tensor (Pockel's coefficients) of the fibre. For silica fibre operating at room temperature in the C-Band $\rho_{11} = 0.113 \pm 0.005$, $\rho_{12} = 0.252 \pm 0.005$, $\mu = 0.16 \pm 0.01$ [59] and $n = 1.45$ [60]. For a source with a central wavelength of 1545 nm the phase change per sensing fibre length change $\Delta\phi/\Delta L$ is approximately 4.75 rads/μm. The phase difference $\Delta\phi$ in response to a change in the fibre length due to thermal expansion or contraction $\Delta T\, L$ is given by [90]

$$\frac{\Delta\phi}{\Delta T\, L} = \frac{2\pi}{\lambda}\left(\frac{n}{L}\frac{dL}{dT} + \frac{dn}{dT}\right) \tag{2.21}$$

for typical silica fibre operating at room temperature in the C-Band $1/L\ dL/dT = 5\times10^{-7}$ / °C, dn/dT 1×10^{-5} / °C [90] and $n = 1.45$ [60]. The temperature sensitivity is therefore predominately due to the refractive index term. For a source with a central wavelength of 1545 nm $\Delta\phi/\Delta T\, L$ can be calculated and is approximately 43.68 rads/°Cm.

2.8.2 Fabry-Pérot Interferometric Sensor

A Fabry-Pérot interferometer consists of two parallel reflecting surfaces with reflectivity's R_1 and R_2, separated by a distance d, as shown in figure 2.7. The

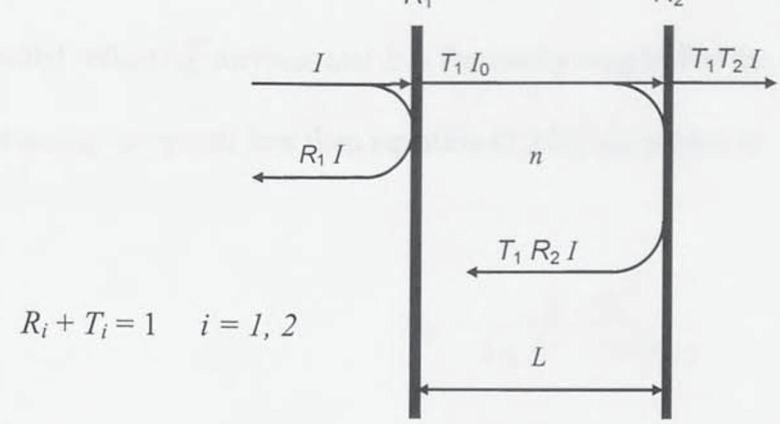

Figure 2.7 Fabry-Pérot interferometer with *I*, *R* and *T* the incident, reflected and transmitted intensity, respectively.

transmittance T_i and reflectance R_i (where $i = 1\ or\ 2$) are characterised by $R_i + T_i = 1$. Assuming normal incidence and neglecting the power lost from absorption the transfer functions for reflectance R_{FP} and transmittance T_{FP} are given by [71][91]-[93]

$$R_{FP} = \frac{R_1 + R_2 - 2\sqrt{R_1 R_2}\cos\phi}{1 + R_1 R_2 - 2\sqrt{R_1 R_2}\cos\phi} \tag{2.22a}$$

$$T_{FP} = \frac{(1 - R_1)(1 - R_2)}{1 + R_1 R_2 - 2\sqrt{R_1 R_2}\cos\phi} \tag{2.22b}$$

where ϕ is the round-trip propagation optical phase shift, given by [92]

$$\phi = \frac{4\pi}{\lambda} nL \tag{2.23}$$

λ is the central wavelength of the source, n is the refractive index of the region between the parallel reflecting surfaces and L is the cavity length. For the case where $R = R_1 = R_2$ and assuming no optical loss then equation (2.22b) simplifies to

$$T_{FP} = \frac{(1-R)^2}{1+R^2-2R\cos\phi} \tag{2.24}$$

the variation of T_{FP} with ϕ and R is shown in figure 2.8. Maximum transmission occurs when $\cos\phi = 1$ or when the phase difference between the light in the cavity is a multiple of 2π radians. This is independent of R, so high transmission occurs even when the reflecting surfaces have reflectivity's of 99%. Illuminated with a low-coherent source a channelled spectrum will be observed at the output carrying information on the state of the refractive index and/or length of the cavity. Fabry-Pérot interferometric sensors are

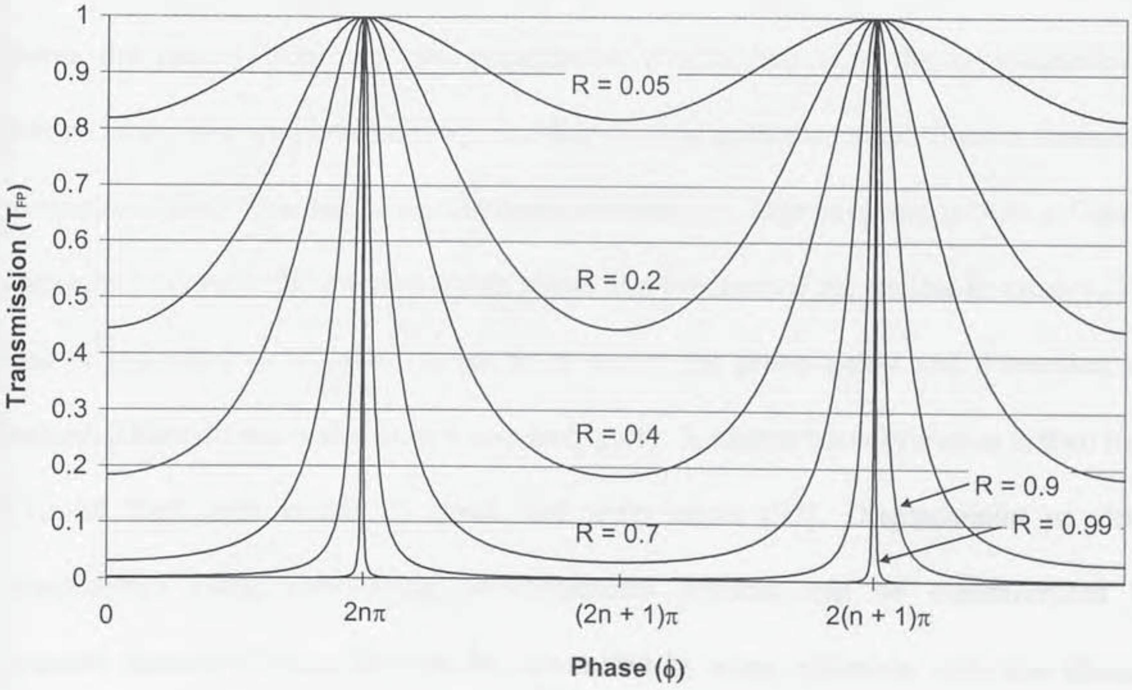

Figure 2.8 Transmission of a Fabry-Pérot interferometer.

very attractive for their simplicity and small size. This type of sensor is discussed further in chapter 7 to measure displacement.

2.9 Simultaneous Strain and Temperature Sensing using Interferometric Sensors

The inherent high sensitivity of interferometric sensors are also one of their biggest disadvantages. The majority of interferometric sensors rely on strain or temperature to produce a phase change. With such high sensitivity in the system it is difficult to distinguish the stimuli affecting the optical phase. Thus, for displacement or strain sensing any thermal effects will have a detrimental effect on the measurement [94]. Solutions to this problem include using a highly birefringent fibre interferometer to recover the phases from the two polarisation modes removing the cross-sensitivity between strain and temperature [95]. Another method uses dispersive Fourier transform spectroscopy [96]. This technique captures a broadband interferogram which is Fourier transformed to reveal the interferometer phase as a function of the optical frequency. The phase is expanded as a Taylor series from which the group delay and dispersion are obtained. These do not suffer from phase ambiguity. A matrix transformation is then used to covert them into values of strain and temperature [97]. Displacement or strain measurements using Fabry-Pérot interferometric sensors can be compromised by unwanted thermal effects. This can be minimised by using materials with low thermal expansions to construct the cavity. An attractive solution is to use an FBG or chirped Bragg grating fabricated close to the bare fibre end in the sensor cavity to simultaneously determine temperature and displacement [98][99].

2.10 Multiplexing Fibre Optic Sensors

A wide range of techniques have been developed to multiplex FBG and interferometric sensors as well as simultaneous interrogation of both types [100]. The ability to easily multiplex fibre optic sensors has a number of important advantages, reduced component costs, reduced weight and less cabling [101]-[105]. Multiplexing techniques can be classified into the following types. Time division [106][107], frequency division [108], wavelength division [109][110], space division [111], sub-carrier based [112], code division [113][114], hybrid [115]-[117] and coherence multiplexing [118][119]. The technique of interest for the work described in this thesis is wavelength division multiplexing (WDM). WDM is an optical technology that couples many light wavelengths in the same fibre simultaneously. Thus, a WDM system utilises the available fibre bandwidth very effectively. By using wavelength selective optical components, independent signal routing can be accomplished [18][120]. The use of this technique in optical sensing allows many fibre optic sensors to be supported in a single fibre line.

2.10.1 Established Wavelength Multiplexing Techniques

One of the most successfully established techniques for interrogating multiple FBG sensors employs a fibre-pigtailed Fabry-Pérot tuneable filter as a narrow bandpass filter [141]. The transmittance (see equation 2.23) of the Fabry-Pérot interferometer plotted as a function of the wavelength is useful in understanding the interrogation principle (see figure 2.9). Typically, tuneable Fabry-Pérot filters have bandwidths of around 0.2 to 0.6 nm and FSRs of 40 to 60 nm [71]. Equation (2.24) shows that the phase is proportional to

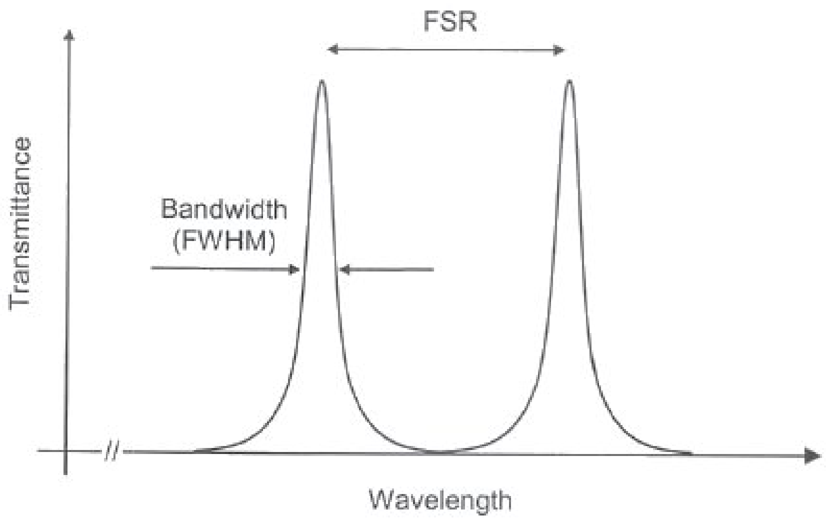

Figure 2.9 Transmittance vs. wavelength of a Fabry-Pérot filter with strong surface reflectivity's (FWHM: full width half maximum).

Figure 2.10 Schematic diagram of a tuneable fibre Fabry-Pérot filter for demodulating multiplexed FBG sensors [141].

the cavity length. Hence, if the cavity length is changed by displacing the separation of the reflecting surfaces using a piezoelectric element the transmission band can be tuned.

Multiple FBG sensors can be interrogated using a Fabry-Pérot filter by scanning the resonance wavelength using a ramp-waveform applied to a piezoelectric element. Figure 2.10 shows a schematic diagram of a tuneable Fabry-Pérot filter for demodulating multiplexed FBG sensors. If the Bragg wavelengths and operational wavelength domains of the sensors do not overlap and all fall within the spectral bandwidth of the source, and if the FSR of the Fabry-Pérot interferometer is greater than the operational wavelength domains occupied by the sensors. Then a number of FBG sensors can be interrogated [141]. Figure 2.11 shows a typical example of the ramp-waveform applied to the piezoelectric element and the signal at the photo-detector. Vohra *et al* [142] demonstrated the interrogation of 64 FBG sensors for civil structure monitoring adopting the scanning Fabry-Pérot filter approach. The system uses four light sources illuminating four lengths

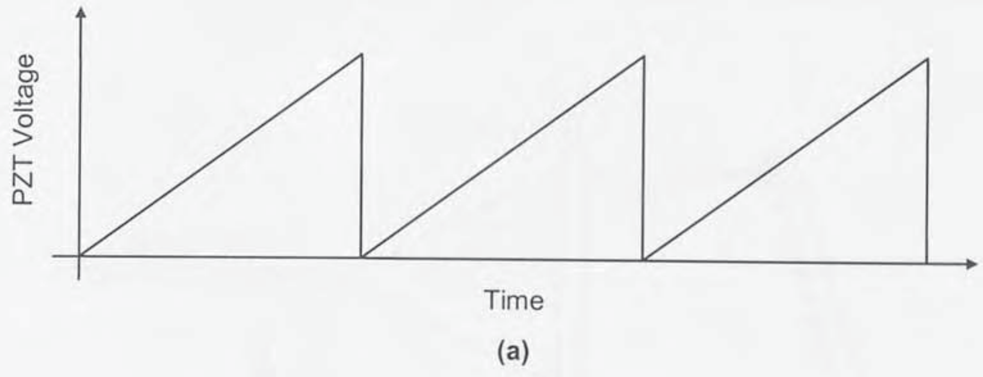

(a)

(b)

Figure 2.11 Scanning of the Fabry-Pérot for three multiplexed FBG sensors (a) PZT driving signal (b) detector signal.

of optical fibre, two Fabry-Pérot filters and two detectors. Each Fabry-Pérot filter has a FSR of 45 nm, allowing the interrogation of 16 FBG sensors spaced by approximately 2.7 nm to be interrogated per filter scan. This spacing allows strains of around ±1300 με for each FBG sensor with an effective scan rate of 45 Hz [71][142]. Henderson *et al* [143] demonstrated a system supporting the interrogation of 128 sensors using Fabry-Pérot based wavelength division demultiplexing. In this system, 16 fibres with 8 FBG sensors are spatially multiplexed. Using neighbouring fibre lines, FBG pairs are used to distinguish between strain and temperature. This results in stable strain measurements with a resolution of around 1 με and an update rate of 8 Hz [143].

Another very well established wavelength-change interrogator suitable for multiplexed FBG sensors is to use a charged coupled device (CCD). Light reflected from multiplexed FBG sensors is directed to a diffraction element and then focused to a CCD.

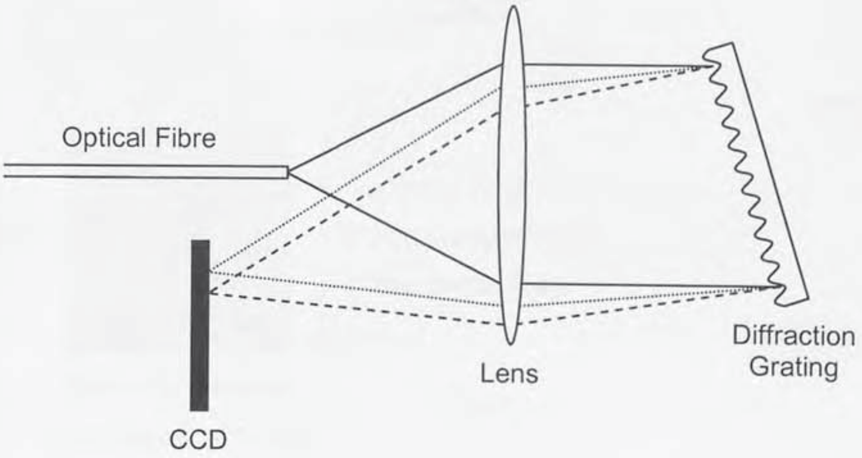

Figure 2.12 Schematic diagram of wavelength interrogation using a diffraction grating and a charged-coupled-device.

For a light incident to the diffraction grating, the diffraction angle is dependent on the wavelength of light this means lights with different wavelengths illuminate different areas of the CCD, see figure 2.12. Therefore, any change in the Bragg wavelength as a result of the measurand will be detected by the CCD [71]. Chen *et al* [144] and Hu *et al* [145] extended this method using a curved diffraction element and a two-dimensional CCD to interrogate spatial and wavelength multiplexed sensors. Figure 2.13 shows how light from different optical fibres can be spatially multiplexed and focused on different

Figure 2.13 Schematic diagram of a spatial and wavelength multiplexing scheme using a CCD [145].

columns of the CCD. Chen *et al* and Hu *et al* have demonstrated that this system is capable of interrogating large numbers of FBG sensors. Their preliminary system [144] was capable of interrogating 175 FBG sensors using a 512 by 512 pixel CCD with a sample rate of 30 Hz, a maximum measurable range of ±3500 $\mu\varepsilon$ and a strain resolution of 1.6 $\mu\varepsilon$. Their recent studies [145] have increased the multiplexing capability to more than 500 FBG sensors by optimising the image spot size.

Commercially available CCD spectrometers offer an affordable FBG sensor interrogation solution. Inexpensive silicon based photodetectors sensitive to wavelengths below 900 nm are generally used in the construction these devices. The silicon photodetectors in the CCD have sufficient sensitivity to interrogate the low-cost, low-reflectivity FBGs fabricated in-line during fibre drawing [146]. Combined with a relatively cheap short-wavelength, low-coherent source make these particular interrogation systems very attractive for optical sensor system designers.

2.11 Broadband Light Source

The properties required of a broadband source for optical sensing include a wide flat-top bandwidth, high spectral power density, stable operation, longevity and low cost. The particular light source used for the work described in this thesis is a non-polarised erbium-doped fibre amplified spontaneous emission source from EXFO Electro-Optical Engineering Incorporated (Model No. IQ-2300). This particular light source uses an erbium-doped fibre, pumped with a 980 nm laser diode providing a spectral power density of -3 dBm/nm, a total output power of 12 dBm over a spectral width at –3 dB of 33 nm centred about a wavelength of 1545 nm and a power stability of ±0.02 dB over 10 hours.

2.12 Electrical Noise in Fibre Optic Sensor Systems

The limiting noise performance of fibre optic sensors systems is associated with the optoelectronics used in the interrogating system. These being firstly the shot noise, thermal noise and beating noise [121] associated with the light source, secondly the photon noise, photocurrent shot noise, flicker noise, thermal noise and amplifier noise associated with the photodiode.

2.12.1 Source Noise

The shot noise and thermal noise associated with the light source are due to the statistical variations in the quantum nature of electric current and temperature fluctuations, respectively [122][123]. The dominant noise contribution in light sources is beating noise coming from spontaneously emitted radiation mixing coherently with the amplified signal at the detector [124]. When the source output is photodetected the signal to noise ratio (SNR) can be written as [121]

$$SNR_{source} = \frac{I_s}{\left(2eB + \frac{4kTB}{R_s} + \frac{I_s B \Delta\nu_{opt}}{\Delta\nu_{sp}^2}\right)} \qquad (2.25)$$

where e is the electron charge, B is the detector bandwidth, k is Boltzmann's constant, T is temperature, R_s is the load resistance of the source, I_s is the source photocurrent, $\Delta\nu_{opt}$ is the bandwidth of the optical filter at the output of the source (if present) and $\Delta\nu_{sp}^2$ is the source bandwidth. The first term in the denominator of equation (2.25) is the shot noise, the second term the thermal noise and the final term the beating noise.

2.12.2 Photodiode Noise

Noise contributions attributed to the photodiode are the fundamental quantum noise (or photon noise), representing the ultimate limit on the accuracy with which the light power level can be measured, the photocurrent shot noise attributed to the statistical variations in the quantum nature of electric current, flicker noise attributed to the manufacturing process of the photodiode being dominant at lower frequencies, thermal noise and amplifier noise, given by [93][125][126]

$$SNR = \sqrt{\frac{P_m}{Bh\nu}} + \frac{I_p^2}{eB\left(I_p + I_d\right)} + \frac{I_p^2 \nu}{CI_{dc}B} + \frac{I_p^2 R_d}{4kTBF_n} \qquad (2.26)$$

where P_m is the mean optical power, h is Plank's constant and ν is the light frequency, I_p is the photocurrent, I_d is the dark current, C is a constant depending on the type of material and geometry of the photodiode, I_{dc} is the photodiode direct junction current, F_n is the noise contribution from the amplifier and R_d is the load resistance in the photodetector. The first term in equation (2.26) is the photon noise, the second is the shot noise, the third term the flicker noise and the final term is the thermal and amplifier noise [93][123][127].

2.13 Lifetime and Reliability of Fibre Optic Sensors

Fibre optic sensor systems are a complex system of components between the source and the detector. With fibre optic sensors being used more and more in critical applications the serious consequences of a failure on safety and cost is very important. Assessing the reliability and lifetime of fibre optic sensors and systems is a complicated issue and very difficult to evaluate a reliable lifetime figure [128]. The subsystems in an optical sensor system are usually easily changeable and can be replaced as their lifetime expires. However, the actual sensors, especially in situations where they are embedded [129] are impossible to replace without major cost issues. FBG sensors have three important reliability issues: the degradation/decay of the refractive index pattern [130]-[133] the reduction in the fibre strength either by UV laser illumination [134] or coating removal/recoating during fabrication [135] and the adhesive join between the sensor and measurand [136][137]. An extensive study of properly annealed FBGs showed that they remained stable at 230 °C within 1 pm over a period of 5 years [138]. However, another recent study on the limits of athermally packaged FBGs from different manufacturers exhibited slow wavelength drifts of 1 pm over 3 months with more than one of the FBGs displaying an abrupt wavelength jump of 1 nm [139]. Fabry-Pérot interferometric sensor reliability is very much dependent on the particular component choice, manufacturing process, materials and adhesives used to construct the sensor [140].

2.14 Conclusion

An overview of fibre optic sensor technology has been described. Various characteristics of single mode optical fibre have been outlined. Hi-Bi fibre has been introduced which forms the basis of a fibre optic interrogation scheme in a subsequent chapter. Some important features of FBGs have been detailed. Two FBG fabrication techniques have been discussed. Chirped and multiple peaked gratings fabrication has been described using a phase mask which is the method used to fabricate all the FBGs for the work in this thesis. The effect of strain and temperature on FBGs has been described and their subsequent use as optical sensors investigated. The investigation includes a look at simultaneous strain and temperature sensing. Mach-Zehnder and Fabry-Pérot interferometric sensors have been reviewed and their issue with simultaneously sensing strain and temperature is also discussed. A brief introduction to multiplexing techniques, noise and reliability issues of optical sensors concludes the chapter.

2.15 References

[1] N. M. Theune, M. Willsch, J. Kaiser, H. Hersch, T. Bosselmann and P. Puschmann, "Temperature monitoring of overhead contact line systems. A cost cutting and power management tool for future rail lines," *in Proceedings 16th International Conference on Optical Fibre Sensors*, (OFS-16, Nara, Japan), Technical Digest, pp. 466-469, October 2003

[2] A. D. Kersey, "Optical fibre sensors for permanent downwell monitoring applications in the oil and gas industry," *Institute of Electronics, Information and Communications Engineers: Transaction on Electronics*, vol. E83-C, No. 3, pp. 400-404, March 2000

[3] T. G. Giallorenzi, J. A. Bucaro, A. Dandridge, G. H. Sigel, J. H. Cole, S. C. Rashleigh and R. G. Priest, "Optical fibre sensor technology," *Journal of Quantum Electronics*, vol. 18, No. 4, pp. 626-665, April 1982

[4] T. Liu, M. Wu, D. A. Jackson and G. F. Fernando, "A multiplexed optical fibre based extrinsic Fabry Perot sensor system for in-situ strain monitoring in composites," *Smart Materials and Structures*, vol. 7, pp. 550-556, 1998

[5] E. J. Friebele, "Distributed strain sensing with fibre Bragg grating arrays embedded in CRTM™ composites," *Electronics Letters*, vol. 30, No. 21, pp. 1783-1784, October 1994

[6] S. T. Vohra, F. Bucholtz and A. D. Kersey, "Fibre optic and low frequency electric field sensor," *Optics Letters*, vol. 16, No. 18, pp. 1445-1447, September 1991

[7] F. Farahi, J. D. C. Jones and D. A. Jackson, "High speed fibre optic temperature sensor," *Optics Letters*, vol. 16, No. 22, pp. 1800-1802, November 1991

[8] J. P. Dakin, M. J. Gunning, P. Chambers and Z. J. Lin, "Detection of gases by correlation spectroscopy," *Sensors and Actuators*, vol. B90, pp. 124-131, 2003

[9] N. E. Fisher, J. Surowiec, D. J. Webb, D. A. Jackson, L. R. Gavrilov, J. W. Hand, L. Zhang and I. Bennion, "In fibre gratings for ultrasonic medical applications," *Measurement Science and Technology*, vol.8, pp. 1050-1054, 1997

[10] R. M. Taylor, D. J. Webb, J. D. C. Jones and D. A. Jackson, "Extended range fibre polarimetric strain sensor," *Optics Letters*, vol. 12, No. 9, pp. 744-746, September 1987

[11] Y. J. Rao, D. A. Jackson, R. Jones and C. Shannon, "Development of prototype fibre optic based Fizeau pressure sensor with temperature compensation and signal recovery by coherence reading," *Journal of Lightwave Technology*, vol. 12, No. 9, pp. 1685-1695, September 1994

[12] I. Latka, W. Ecke, B. Höfer, Thomas Frangen, R. Willsch and A. Reutlinger, "Micro bending beam based optical fibre grating sensors for physical and chemical measurands," *in Proceedings 17th International Conference on Optical Fibre Sensors*, (OFS-17, Bruges, Belgium), Technical Digest, pp. 94-97, May 2005

[13] K. Krebber, H. Henschel and U. Weinand, "Fibre Bragg gratings as a high dose radiation sensors," *in Proceedings 17th International Conference on Optical Fibre Sensors*, (OFS-17, Bruges, Belgium), Technical Digest, pp. 176-179, May 2005

[14] T. Allsop, M, Dubov, A. Martinez, F. Floreani, I. Krushchev, D. J. Webb and I. Bennion, "A long period grating directional bend sensor incorporating index modification of the cladding," *in Proceedings 17th International Conference on Optical Fibre Sensors*, (OFS-17, Bruges, Belgium), Technical Digest, pp. 98-101, May 2005

[15] K. Bohnert, P. Gabus, H. Brändle and P. Guggenbach, "Fibre optic dc current sensor for the electro-winning industry," *in Proceedings 17th International Conference on Optical Fibre Sensors*, (OFS-17, Bruges, Belgium), Technical Digest, pp. 210-213, May 2005

[16] H. Yokosuka, S. Tanaka and N. Takahashi, "High sensitive fibre Bragg grating vibration sensor using intensity modulated laser source," *in Proceedings 17th International Conference on Optical Fibre Sensors*, (OFS-17, Bruges, Belgium), Technical Digest, pp. 731-734, May 2005

[17] C. Pask, A. W. Snyder and D. J. Mitchell, "Number of modes on optical waveguides," *Journal Optical Society of America*, vol. 65, No. 3, pp. 356-357, March 1975

[18] J. Gowar, "Optical communication systems," (Second Edition), *Prentice Hall International Series in Optoelectronics*, ISBN 0-13-638727-6, 1993

[19] S. Ungar, "Fibre optics theory and applications," *Wiley & Sons*, ISBN: 0-471-92758-9, 1990

[20] R. Ulrich and A. Simon, "Polarization optics of twisted single mode fibers," *Applied Optics*, vol. 18, No. 13, pp. 2241-2251, July 1979

[21] G. S. Glaesemann and S. T. Gulati, "Design methodology for the mechanical reliability of optical fiber," *Optical Engineering*, vol. 30, No. 6, pp. 709-715, June 19991

[22] R. Ulrich, S. C. Rashleigh and W. Eickhoff, "Bending induced birefringence in single mode fibers," *Optics Letters*, vol. 5, No. 6, pp. 273-275, June 1980

[23] R. J. Castilone, "Mechanical reliability: applied stress design guidelines," *Corning Incorporated White Paper*, wp5053, pp. 1-4, August 2001

[24] S. C. Rashleigh, W. K. Burns and R. P. Moeller, "Polarization holding in birefringent single mode fibres," *Optics Letters*, vol. 7, No. 1, pp. 40-42, January 1982

[25] J. Noda, K. Okamoto and Y. Sasaki, "Polarization maintaining fibers and their applications," *Journal of Lightwave Technology*, vol. Lt4, No. 8, pp. 1071-1089, August 1986

[26] A. Kumar and R. Ulrich, "Birefringence of optical fibre pressed into a V groove," *Optics Letters*, vol. 6, No. 12, pp. 644-646, December 1981

[27] K. O. Hill, Y. Fujii, D. C. Johnson and B. S. Kawasaki, "Photosensitivity in optical fiber waveguides application to reflection filter fabrication," *Applied Physics Letters*, vol. 32, No. 10, pp. 647-649, May 1978

[28] B. S. Kawasaki, K. O. Hill, D. C. Johnson and Y. Fujii, "Narrow-band Bragg reflectors in optical fibers: Application to reflection filter fabrication," *Optics Letters*, vol. 3, No. 2, pp. 66-683, August 1978

[29] G. Meltz, W. W. Morey and W. H. Glenn, "Formation of Bragg gratings in optical fibers by a transverse holographic method," *Optics Letters*, vol. 14, No. 15, pp. 823-825, August 1989

[30] H. Kogelnik, "Filter response of nonuniform almost periodic structures," *Bell Systems Technical Journal*, vol. 55, No. 1, pp. 109-126, January 1976

[31] A. Yariv, "Coupled mode theory for guided wave optics," *Journal of Quantum Electronics*, vol. QE-9, No. 9. pp. 919-933, September 1973

[32] R. Kashyap and J. M. Lópes Higuera, "Fiber grating technology theory photosensitivity fabrication and characterization," *in Handbook of Optical Fibre Sensing Technology, John Wiley & Sons*, ISBN: 0471-82053-9, 2002

[33] D. K. W. Lam and B. K. Garside, "Characterization of single mode optical fiber filters," *Applied Optics*, vol. 20, No. 3, pp. 440-445, February 1981

[34] I. Bennion, J. A. R. Williams, L. Zhang, K. Sugden and N. J. Doran, "UV-written in-fibre Bragg gratings," *Optical and Quantum Electronics*, vol. 28, pp. 93-135, 1996

[35] W. W. Morey, G. Meltz and W. H. Glenn, "Fiber optic Bragg grating sensors," *SPIE Fiber Optic and Laser Sensors VII*, vol. 1169, pp. 98-107, 1989

[36] P. St J. Russell, J. L. Archambault and L. Reekie, "Fibre gratings," *Physics World*, vol. 6, pp. 41-46, October 1993

[37] Y. J. Rao, "In-fibre Bragg grating sensors," *Measurement Science and Technology*, vol. 8, pp. 355-375, 1997

[38] A. Othonos and K. Kalli, "Fiber Bragg gratings: fundamentals and applications in telecommunications and sensing," Artech House, ISBN: 0-89006-344-3, 1999

[39] R. Kashyap, "Fibre Bragg Gratings," Academic Press, ISBN 0-12-400560-8,1999

[40] D. A. Jackson and D. J. Webb, "Optical fibre Bragg grating sensors for strain measurement," in *Handbook of Laser Technology and Applications: Volume 1: Principles*, vol. 3, CE Webb and J. Jones, Eds, 2003, pp. Part D

[41] T. Erdogan, "Fiber grating spectra," *Journal of Lightwave Technology*, vol. 15, No. 8, pp. 1277-1294, August 1997

[42] A. Othonos, "Fiber Bragg gratings," *Rev. Sci. Instrum*, vol. 68, No. 12, pp. 4309-4341, December 1997

[43] K. O. Hill and G. Meltz, "Fibre grating technology fundamentals and overview," *Journal of Lightwave Technology*, vol. 15, No. 8, pp. 1263-1276, August 1977

[44] C. R. Giles, "Lightwave applications of fiber Bragg gratings," *Journal of Lightwave Technology*, vol. 15, No. 8, pp. 1391-1404, August 1997

[45] B. Culshaw and J. Dakin, "Optical fibre sensors components and subsystems," *Artech House*, volume 3, ISBN 0-89006-932-8, 1996

[46] G. Meltz, J. R. Dunphy, W. H. Glenn, J. D. Farina and F. J. Leonberger, "Fibre optic temperature and strain sensors," *SPIE Fibre Optic Sensors II*, vol. 798, pp. 104-114, 1987

[47] K. O. Hill, B. Malo, F. Bilodeau, F. Johnson and J. albert, "Bragg gratings fabricated in monomode photosensitive optical fiber by UV exposure through a phase mask," *Applied Physics Letters*, vol. 62, No. 10, pp. 1035-1037, March 1993

[48] A. Othonos and X. Lee, "Novel and improved methods of writing Bragg gratings with a phase masks," *Photonics Technology Letters*, vol. 7, No. 10, pp. 1183-1185, October 1995

[49] R. J. Campbell and R. Kashyap, "Spectral profile and multiplexing of Bgragg gratings in photosensitive fibre," *Optics Letters*, vol. 16, No. 12, pp. 898-900, June 1991

[50] Q Zhang, D. A. Brown, L. Reinhart, T. F. Morse, J. Q. Wang and G. Xiao, "Tuning Bragg wavelength by writing gratings on prestrained fibers," *Photonics Technology Letters*, vol. 6, No. 7, pp. 839-841, July 1994

[51] R. M. Atkins, P. J. Lemaire, T. Erdogan and V. Mizrahi, "Mechanisms of enhanced UV photosensitivity via hydronen loading in germanosilicate glasses," *Electronics Letters*, vol. 29, No. 14, pp. 1234-1235, July 1993

[52] H. Patrick, S. L. Gilbert, A. Lidgard and M. D. Gallagher, "Annealing of Bragg gratings in hydrogen loaded optical fibre," *Journal of Applied Physics*, vol. 78, No. 5, pp. 2940-2945, September 1995

[53] K. C. Byron, K. Sugden, T. Bircheno and I. Bennion, "Fabrication of chirped Bragg gratings in photosensitive fibre," *Electronics Letters*, vol. 30, No. 18, pp. 1659-1660, September 1993

[54] K. Sugden, I. Bennion, A. Molony and N. J. Copner, "Chirped gratings produced in photosensitive optical fibres by fibre deformation during exposure," *Electronics Letters*, vol. 29, No. 5, pp. 440-442, March 1994

[55] K. C. Byron and N. Rourke, "Fabrication of chirped fibre gratings by novel stretch and write technique," *Electronics Letters*, vol. 31, No. 1, pp. 60-61, January 1995

[56] R. Kashyap, P. F. McKee, R. J. Campbell and D. L. Williams, "Novel method of producing all fibre photoinduced chirped gratings," *Electronics Letters*, vol. 30, No. 12, pp. 996-998, June 1994

[57] A. Othonos, X. Lee and R. M. Measures, "Superimposed multiple Bragg gratings," *Electronic Letters*, vol. 30, No. 23, pp. 1972-1974, November 1994

[58] A. Arigiris, M. Konstantaki, A. Ikiades, D. Chronis, P. Floias, K. Kallimani and G. Pagiatakis, "Fabrication of high reflectivity superimposed multiple fibre Bragg gratings with unequal wavelength spacing," *Optics Letters*, vol. 27, No. 15, pp. 1306-1308, August 2002

[59] A. Bertholds and R. Dandliker, "Determination of the individual strain optic coefficients in single mode optical fibers," *Journal of Lightwave Technology*, vol. 6, No. 1, pp. 17-20, January 1988

[60] D. N. Nikogosyan, "Properties of optical and laser related materials," *John Wiley & Sons*, ISBN: 0-471-97384, 1998

[61] M. Willsch, T. Bosselmann, P. Kraemmer and R. Gerner, "Distributed optical flow sensing using a novel fibre Bragg grating sensor," *in Proceedings 17th International Conference on Optical Fibre Sensors*, (OFS-17, Bruges, Belgium), Technical Digest, pp. 286-289, May 2005

[62] W. W. Morey, G. Meltz and W. H. Glenn, "Evaluation of a fibre Bragg grating hydrostatic pressure sensor," *in Proceedings 8th International Conference on Optical Fibre Sensors*, (OFS-8, Monterey, USA), Technical Digest, pp. 1-4, January 1992

[63] M. G. Xu, L. Reekie, Y. T. Chow and J. P. Dakin, "Optical in-fibre grating high pressure sensor," *Electronics Letters*, vol. 29, No. 4, pp. 398-399, February 1993

[64] A. D. Kersey and M. J. Marrone, "Fibre Bragg grating high magnetic field probe," *in Proceedings 10th International Conference on Optical Fibre Sensors*, (OFS-10, Glasgow, United Kingdom), Technical Digest, pp. 53-56, May 1994

[65] A. D. Kersey, M. A. Davies, H. J. Patrick, M. LeBlanc, K. P. Koo, C. G. Askins, M. A. Putnam and E. J. Friebele, "Fibre grating sensors," *Journal of Lightwave Technology*, vol. 15, No. 8, pp. 1442-1463, August 1997

[66] J. D. C. Jones, "Review Of fibre sensor techniques for temperature-strain discrimination," *in Proceedings 12th International Conference on Optical Fibre Sensors*, (OFS-12, Williamsburg, USA), Technical Digest, pp. 36-39, October 1997

[67] M. G. Xu, J. L. Archambault, L. Reekie and J. P. Dakin, "Discrimination between strain and temperature effects using dual wavelength fibre grating sensors," *Electronics Letters*, vol. 30, No. 13, pp. 1085-1087, June 1994

[68] S. W. James, M. L. Dockney and R. P. Tatam, "Simultaneous independent temperature and strain measurements using in fibre Bragg grating sensors," *Electronics Letters*, vol. 32, No. 12, pp. 1133-1134, June 1996

[69] G. Simpson, K. Kalli, K. Zhou, L. Zhang and I. Bennion, "An idealised method for the fabrication of temperature invariant Ia-I strain sensor," *in Proceedings 16th International Conference on Optical Fibre Sensors*, (OFS-16, Nara, Japan), Post-deadline paper PD-4, pp. 14-17, October 2005

[70] H. Patrick, G. M. Williams, A. D. Kersey, J. R. Pedrazzani and A. M. Vengsarkar, "Hybrid fibre Bragg grating / long period fiber grating sensor for strain / temperature discrimination," *Photonics Technology Letters*, vol. 8, No. 9, pp. 1223-1225, September 1996

[71] F. T. S. Yu and S. Yin, "Fibre optic sensors," *Marcel Dekker Inc*, ISBN: 0-8247-0732-X, 2002

[72] M. G. Xu, L. Dong, L. Reekie, J. A. Tucknott and J. L. Cruz, "Temperature independent strain sensor using a chirped Bragg grating in tapered optical fibre," *Electronics Letters*, vol. 31, No. 10, pp. 823-825, May 1995

[73] D. A. Jackson, "Recent progress in monomode fibre optic sensors," *Measurement Science and Technology*, vol. 5, pp. 621-638, 1994

[74] J. A. Bucaro, H. D. Dardy and E. Carome, "Fiber optic hydrophone," *Journal Acoustic Society of America*, vol. 62, No. 5, pp. 1302-1304, November 1977

[75] A. B. Tveten, A. Dandridge, C. M. Davies and T. G. Giallorenzi, "Fibre optic accelerometer," *Electronics Letters*, vol. 16, No. 22, pp. 854-856, October 1980

[76] T. A. Berkoff and A. D. Kersey, "Interferometric fibre displacement/strain sensor based on source coherence synthesis," *Electronics Letters*, vol. 26, No. 7, pp. 452-453, March 1990

[77] Y. J. Rao, D. A. Jackson, R. Jones and C. Shannon, "Development of prototype fibre optic based Fizeau pressure sensors with temperature compensation and signal recovery by coherence reading," *Journal of Lightwave Technology*, vol. 12, No. XX, pp. 1685-1695, September 1994

[78] D. M. Dagenais, F. Bucholtz and K. P. Koo, "Heterodyne detection of magnetic fields from 0.1Hz to 10MHz in a magnetostrictive fiber sensor," *in Proceedings 6th International Conference on Optical Fibre Sensors*, (OFS-6, Paris, France), Technical Digest, pp. 255-260, September 1989

[79] K. P. Koo and G. H. Sigel, "An electric field sensor utilising a piezoelectric PVF_2 film in single mode fiber interferometer, "*Journal of Quantum Electronics*, vol. QE-18, No. 4, pp. 670-675, April 1980

[80] G. S. Maurer, S. Dellinges and J. Finegan, "A broadband interferometric sensor system for the determination of hard disk dynamic properties," *in Proceedings 12th International Conference on Optical Fibre Sensors*, (OFS-12, Williamsburg, USA), Technical Digest, pp. 182-185, October 1997

[81] A. Dandridge, A. B. Tveten and T. G. Giallorenzi, "Interferometric current sensor using optical fibres," *Electronics Letters*, vol. 17, No. 15, pp. 523-525, July 1981

[82] W. Zhang, J. A. R. Williams and I. Bennion, "Optical delay line filter free of limitation imposed by optical coherence," *Electronics Letters*, vol. 35, No. 24, pp. 2133-2134, November 1999

[83] J. N. Blake, S. Y. Huang and B. Y. Kim, "Elliptical core two mode fiber strain gauge," *in Proceedings SPIE Fibre Optic Sensors V*, vol. 838, pp. 332-339, August 1987

[84] G. Meltz, J. R. Dunphy and F. J. Leonberger, "Multi wavelength twin core fiber optic sensors," *in Proceedings 4th International Conference on Optical Fibre Sensors*, (OFS-4, Tokyo, Japan), Technical Digest, pp. 67-70, October 1986

[85] F. C. Garcia, M. Fokine, W. Margulis and R. Kashyap, "Mach Zehnder interferometer using single standard telecommunication optical fibre," *Electronics Letters*, vol. 37, No. 24, pp. 1440-1442, November 2001

[86] A. Dandridge and A. D. Kersey, "Overview of Mach Zehnder sensor technology and applications," *in Proceedings SPIE Fibre Optic and Laser Sensors VI*, vol. 985, pp. 34-52, September 1988

[87] E. Udd, "Fiber optic sensors an introduction for engineers and scientists," *John Wiley & Sons*, ISBN: 0471-83007-0, 1990

[88] H. C. Lefevre, "White light interferometry in optical fibre sensors," *in Proceedings 7th International Conference on Optical Fibre Sensors*, (OFS-7, Sydney, Australia), Technical Digest, pp. 345-351, December 1990

[89] C. D. Butter and G. B. Hocker, "Fiber optic strain gauge," *Applied Optics*, vol. 17, No. 18, pp. 2867-2869, September 1978

[90] G. B. Hocker, "Fibre optic sensing of temperature and pressure," *Applied Optics*, vol. 18, No. 9, pp. 1445-1448, May 1979

[91] M. Born and E. wolf, "Principles of Optics," *Cambridge University Press*, ISBN: 0-521-642221, 1999

[92] J. L. Santos, A. P. Leite and D. A. Jackson, "Optical fibre sensing with a low finesse Fabry Pérot cavity," *Applied Optics*, vol. 31, No. 34, pp. 7361-7366, December 1992

[93] K. T. V. Grattan and B. T. Meggitt, "Optical fibre sensor technology," *Chappman & Hall*, ISBN: 0412-59210-X, 1995

[94] J. D. C. Jones, "Review of fibre sensor techniques for temperatute strain discrimination," *in Proceedings 12th International Conference on Optical Fibre Sensors*, (OFS-12, Williamsburg, USA), pp. 36-39, October 1997

[95] F. Farahi, D. J. Webb, J. D. C. Jones and D. A. Jackson, "Simultaneous measurement of temperature and strain cross sensitivity considerations," *Journal of Lightwave Technology*, vol. 8, No. 2, pp. 138-142, February 1990

[96] D. A. Flavin, R. McBride and J. D. C. Jones, "Simultaneous measurement of temperature and strain by dispersive Fourier transform spectroscopy," *in Proceedings 9th International Conference on Optical Fibre Sensors*, (OFS-9, Florence, Italy), pp. 333-336, October 1993

[97] D. A. Flavin, R. McBride and J. D. C. Jones, "Temperature insensitive interferometric measurement of strain using grating coupled LED sources," *in Proceedings 10th International Conference on Optical Fibre Sensors*, (OFS-10, Glasgow, United Kingdom), Technical Digest, pp. 195-198, May 1994

[98] L. A. Ferreira, A. B. Lobo Ribeiro, J. L. Santos and F. Farahi, "Simultaneous measurement of displacement and temperature using a low finesse cavity and a fibre Bragg grating," *Photonics Technology Letters*, vol. 8, No. 11, pp. 1519-1521, November 1996

[99] Y.J. Rao, X. K. Zeng, Y. Zhu, Y. P. Wang, T. Zhu, Z. L. Ran, L. Zhang and I. Benion, "Temperature strain discrimination sensor using WDM chirped in fibre Bragg grating and extrinsic Fabry-Pérot," *Chinese Physics Letters*, vol. 18, No. 5, pp. 643-645, May 2001

[100] G. Brady, K. Kalli, D. J. Webb, D. A. Jackson, L. Reekie and J. L. Archambault, "Simultaneous interrogation of interferometric and Bragg grating sensors," *Optics Letters*, vol. 20, No. 11, pp. 1340-1342, June 1995

[101] A. D. Kersey, A. Dandridge, A. B. Tveten, "Overview of multiplexing techniques for interferometric fiber sensors," *in SPIE Fiber Optic and Laser Sensors V*, vol. 838, pp. 184-193, 1987

[102] A. D. Kersey, "Interrogation and multiplexing techniques for fiber Bragg grating strain sensors," *in SPIE Distributed and Multiplexed Fiber Optic Sensors III*, vol. 2071, pp. 30-48, 1993

[103] A. D. Kersey and A. Dandridge, "Fiber Optic Multisensor Networks," *SPIE Fiber Optic and Laser Sensors VI*, vol. 985, pp. 90-104, 1988

[104] J. P. Dakin and M. Volanthen, "Distributed and multiplexed fibre grating sensors," *in Proceedings 13th International Conference on Optical Fibre Sensors*, (OFS-13, Kyongju, Korea), Technical Digest, pp. 134-140, April 1994

[105] A. D. Kersey, "Multiplexed fiber optic sensors," *in SPIE Distributed and Multiplexed Fiber Optic Sensors II*, vol. 1797, pp. 161-185, 1992

[106] A. D. Kersey, K. L. Dorsey and A. Dandridge, "Charactererization of an eight element time division multiplexed interferometric fiber sensor array," *SPIE Fiber Optic and Laser Sensors VI*, vol. 985, pp. 105-112, 1988

[107] A. D. Kersey, A. Dandridge and A. B. Tveten, "Time division multiplexing of interferometric fiber sensors using passive phase generated carrier interrogation," *Optics Letters*, vol. 12, No. 10, pp. 775-777, October 1987

[108] D. T. Jong and K. Hotate, "Frequency division multiplexing of optical fibre sensors using an optical delay line with a frequency shifter," *in Proceedings 5th International Conference on Optical Fibre Sensors*, (OFS-5, New Orleans, USA), Technical Digest, pp. 76-79, January 1988

[109] G. P. Brady, S. Hope, A. B. L. Ribeiro, D. J. Webb, L. Reekie, J. L. Archambault and D. A. Jackson, "Bragg grating temperature and strain sensors," *in Proceedings 10th International Conference on Optical Fibre Sensors*, (OFS-10, Glasgow, United Kingdom), Technical Digest, pp. 510-513, May 1994

[110] M. A. Davies and A. D. Kersey, "All fibre Bragg grating strain sensor demonstration technique using a wavelength division coupler," *Electronics Letters*, vol. 30, No. 1, pp. 75-77, January 1994

[111] P. J. Henderson, D. J. Webb, D. A. Jackson, L. Zhang and I. Bennion, "Highly multiplexed grating sensor for temperature referenced quasi static measurements of strain in concrete bridges," *in Proceedings 13th International Conference on Optical Fibre Sensors*, (OFS-13, Kyongju, Korea), Technical Digest, pp. 134-140, April 1994

[112] M. J. Marrone, A. D. Kersey, A. Dandridge and C. A. Wade, "Quasi-distributed fiber optic sensor system with subcarrier filtering," *in Proceedings 6th International Conference on Optical Fibre Sensors*, (OFS-6, Paris, France), Technical Digest, pp. 519-525, September 1989

[113] H. Ryu, H. Lee and K. Kim, "An economical and multiple fibre grating sensor system with rapid response using code division multiple access," *Measurement Science and Technology*, vol. 12, pp. 906-908, 2001

[114] H. Lee, "Multiple fiber Bragg grating sensor system using code division multiple access," *Applied Optics*, vol. 41, No. 25, pp. 5245-5248, September 2002

[115] K. Kalli, G. P. Brady, D. J. Webb, D. A. Jackson, L. Zhang and I. Bennion, "Wavelength division and spatial multiplexing using tandem interferometers for Bragg grating sensor networks," *Optics Letters*, vol. 20, No. 24, pp. 2544-2546, December 1995

[116] Y. Rao, D. A. Jackson, L. Zhang and I. Bennion, "Strain sensing of modern composite materials with a spatial / wavelength division multiplexed fiber grating network," *Optics Letters*, vol. 21, No. 9, pp. 683-685, May 1996

[117] M. A. Davis, D. G. Bellemore, M. A. Putnam and A. D. Kersey, "Interrogation of 60 fibre Bragg grating sensors with microstrain resolution capability," *Electronics Letters*, vol. 32, No. 15, pp. 1393-1394, July 1996

[118] J. L. Brooks, R. H. Wentworth, R. C. Youngquist, M. Tur, B. Y. Kim and H. Shaw, "Coherence multiplexing of fiber optic interferometric sensors," *Journal of Lightwave Technology*, vol. LT-3, No. 5, pp. 1062-1072, October 1985

[119] F. Farahi, T. P. Newson, J. D. C. Jones and D. A. Jackson, "Coherence multiplexing of remote fibre optic Fabry Pérot sensing system," *Optics Communications*, vol. 65, No. 5, pp. 319-321, March 1988

[120] S. V. Kartapoloulos, "Introduction to DWDM technology," *SPIE Optical Engineering Press*, ISBN: 0-7803-1005-5, 1994

[121] J. M. López-Higuera, "Superfluorescent fiber optic sources," *in Handbook of Fibre Sensing Technology*, *John Wiley & Sons*, ISBN: 0471-82053-9, 2002

[122] G. P. Agrawal, "Fiber optic communications systems," *Wiley & Sons*, (Second Edition), ISBN: 0-471-21571-6, 2001

[123] P. Horowitz and W. Hill, "The art of electronics," (second edition), *Cambridge University Press*, ISBN: 0-521-37095-7, 1989

[124] G. P. Agrawal, "Applications of nonlinear fiber optics," *Academic Press*, ISBN: 0-12-045144-1, 2001

[125] J. Dakin and B. Culshaw, "Optical fiber sensors principles and components," *Artech House*, ISBN: 0-89006-317-6, 1988

[126] B. Nguyen and A. Dao, "Some noise features and noise equivalent circuit of photodiode using measurement and optical instruments," *Communications in Physics*, vol. 9, No. 1, pp. 51-60, 1999

[127] B. Culshaw, "Optical fibre sensing and signal processing," *Peter Peregrinus Ltd*, ISBN: 0-906048-99-0, 1984

[128] F. Berghmans, "Reliability of optical fibers and components," *in Proceedings 17th International Conference on Optical Fibre Sensors*, (OFS-17, Bruges, Belgium), Technical Digest, pp. 20-23, May 2005

[129] S. N. Kukureka, A. Pedicini and D. R. Cairns, "Embedded fiber optic sensor performance and the singe fiber fragmentation test," *in Poceedings SPIE Optical fiber and fiber component mechanical reliability and testing*, vol. 4215, pp. 218-224, April 2001

[130] T. Erdogen, V. Mizrahi, P. J. Lemaire and D. Monroe, "Decay of ultraviolet induced fiber Bragg gratings," *Journal of Applied Physics*, vol. 76, No. 1, pp. 73-80, July 1994

[131] S. Pal, J. Mandal, T. Sun, and K. T. V. Grattan, "Analysis of thermal decay and prediction of operational lifetime for a type I boron germanium codoped fiber Bragg grating," *Applied Optics*, vol. 42, No. 12, pp. 2188-2197, April 2003

[132] F. Berghmans, B. Brichard, A. F. Fernandez and M. V. Uffelen, "Reliability issues for fibre technology in nuclear applications," *in Proceedings of 8th Working Group 2 meeting of COST270*, (Berlin Germany), C270-176, December 2003

[133] S. R. Baker, H. N. Rourke, V. Baker and D. Goodchild, "Thermal decay of fiber Bragg gratings written in Boron and Germanium codoped silica fiber," *Journal of Lightwave Technology*, vol. 15, No. 8, pp. 1470-1477, August 1997

[134] S. W. James, C. Y. Wei, C. C. Ye, R P. Tatam and P. E. Irving, "An investigation of the tensile strength of fibre Bragg gratings," *in Proceedings 13th International Conference on Optical Fibre Sensors*, (OFS-13, Kyongju, Korea), Technical Digest, pp. 38-41, April 1994

[135] A. J. Tarpey, S. N. Kukureka and K. Jerkschat, "The mechanical reliability of stripped and recoated fibre Bragg gratings for optical fibre sensors," *in Proceedings of SPIE Optical Fiber and Fiber Component Mechanical Reliability and Testing II*, vol. 4639, pp. 22-34, 2002

[136] A. Frank, P. M. Nellen and U. Sennhauser, "Fiber adhesive joint analysis with intra Bragg grating sensing," *in Proceedings 14th International Conference on Optical Fibre Sensors*, (OFS-14, Venice, Italy), Technical Digest, pp. 784-787, October 2000

[137] B. Glisic and D. Inaudi, "Sensing tape for easy integration of optical fiber sensors in composite structures," *in Proceedings 16th International Conference on Optical Fibre Sensors*, (OFS-16, Nara, Japan), Technical Digest, pp. 482-486, October 2003

[138] P. M. Nellen, P. Mauron, A. Frank, U. Sennhauser, K. Bohnert, P. Pequignot, P. Bodor and H. Brändle, "Reliability of fiber Bragg grating based sensors for downhole applications," *Sensors and Actuators*, vol. 3618, pp. 1-13, November 2002

[139] S. D. Dyer, P. A. Williams, R. J. Espejo, J. D. Kofler and S. M. Etzel, "Fundamental limits in fiber Bragg grating peak wavelength measurements," *in Proceedings 17th International Conference on Optical Fibre Sensors*, (OFS-17, Bruges, Belgium), Technical Digest, pp. 88-93, May 2005

[140] V. Bhatia, K. A. Murphy, R. O'Claus, T. A. Tran and J. A. Greene, "Recent developments in optical fibre based extrinsic Fabry Pérot interferometric strain sensing technology," *Smart Materials and Structures*, vol. 4, pp. 246-251, 1995

[141] A. D. Kersey, T. A. Berkhoff and W. W. Morey, "Multiplexed fiber Bragg grating strain sensor system with fibre Fabry-Pérot wavelength filter," *Optics Letters*, No. 16, Vol. 18, pp. 1370-1372, August 1993

[142] S. T. Vohra, M. D. Todd, G. A. Johnson, C. C. Chang and B. A. Danver, "Fiber Bragg garting sensor system for civil structure monitoring applications and field test," *in Proceedings 13th International Conference on Optical Fibre Sensors*, (OFS-13, Kyongju, Korea), Technical Digest, pp. 32-37, April 1994

[143] P. J. Henderson, D. J. Webb, D. A. Jackson, L. Zhang and I. Bennion, "Highly multiplexed grating sensors for temperature referenced quasi static measurements of strain in concrete bridges," *in Proceedings 13th International Conference on Optical Fibre Sensors*, (OFS-13, Kyongju, Korea), Technical Digest, pp. 320-323, April 1994

[144] Y. Hu, S. Chen, L. Zhang and I. Bennion, "Multiplexing Bragg gratings using combined wavelength and spatial division techniques with digital resolution enhancement," *Electronics Letters*, vol. 33, No. 23, pp. 1973-1975, November 1997

[145] Y. Hu, B. Bridge, L. Zhang, I. Bennion and S. Chen, "Improvements on the multiplexing system using a 2D spectrograph for FBG based sensor arrays," *in Proceedings of the European Workshop Optical Fibre Sensors*, (Santander, Spain), Technical Digest, pp. 288-291, June 2004

[146] E. J. Friebele, C. G. Askins, A. B. Bosse, A. D. Kersey, H. J. Patrick, W. R. Pogue, M. A. Putnam, W. R. Simon, F. A. Tasker, W. S. Vincent and S. T. Vohra, "Optical fiber sensors for spacecraft applications," *Smart Materials and Structures*, vol. 8, pp. 813-838, August 1999

[147] R. M. Atkins, V. Mizrahi and T. Erdogan, "248 nm induced vacuum UV spectral changes in optical fiber perform cores - support for a color center model of photosensitivity," *Electronics Letters*, vol. 29, No. 4, pp. 385-387, February 1997

[148] B. Malo, J. Albert, K. O. Hill, F. Bilodeau and D. C. Johnson, "Effective index drift from molecular hydrogen diffusion in hydrogen-loaded optical fibres and its effect on Bragg grating fabrication," *Electronics Letters*, vol. 30, No. X, pp. 442-443, March1994

[149] F. Bilodeau, B. Malo, J. Albert, D. C. Johnson, K. O. Hill, Y. Hibino, Y. Abe and M. Kawachi, "Photosensitization of optical fibre and silica-on0silica/silica waveguides," *Optics Letters*, vol. 18, No. X, pp. 953-955, June 1993

[150] D. L. Williams, B. J. ainsile, J. R. Armitage, R. Kashyap and R. Campbell, "Enhanced UV photosensitivity in boron co-doped germanosilicate fibres," *Electronics Letters*, vol. 29, No. 1, pp. 45-47, January 1993

[151] L. Dong, J. L. Cruz, L. Reekie, M. G. Xu and D. Payne, "Enhanced photosensitivity in tin co-doped germanosilicate fibers," *Photonics Technology Letters*, vol. 7, No. 3, pp. 1048-1050, September 1995

[152] E. M. Dianov, K. M. Golant, V. M. Mashinsky, O. I. Medvedkov, I. V. Nikolin, O. D. Sazhin and S. A. Vasiliev, "Highly photosensitive nitrogen-doped germanosilicate fibre for index grating writing," *Electronics Letters*, vol. 33, No. X, pp. 1334-1336, July 1997

3 Arrayed Waveguide Gratings

Arrayed waveguide gratings (AWGs) image input light to a set of output waveguides in a dispersive and wavelength dependent way. AWGs offer a practical and simple solution for simultaneously interrogating fibre optic sensors. This chapter describes the operation, key performance features and applications of AWGs in fibre optic sensing.

3.1 Introduction

Research and commercial interest in optical components based on wavelength division multiplexing have already been developed and deployed in the communications network. One such key component is the wavelength demultiplexer, of which there are several types, including the diffraction grating, Mach-Zehnder filter, acousto-optic filters, holographic filters and thin film filters [1]-[5]. Since the late 1980s research interest started to focus on AWGs [6]-[8] as wavelength demultiplexers. Planar lightwave circuits [9][10], the technology that enables AWGs, is achieved by fabricating the designed

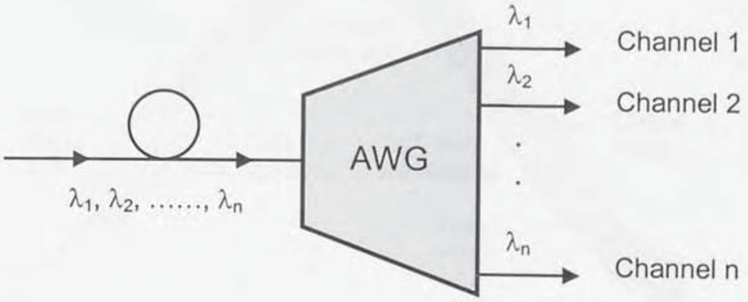

Figure 3.1 Arrayed waveguide grating.

circuits on the surface of a silicon wafer or other substrates. Hence, they are suitable for integration with other devices [11] such as photodiodes and better suited for mass production [9]. AWGs can precisely multiplex a high number of wavelength channels at relatively low loss, have high stability and high reliability. The channel wavelengths are normally matched to the channels specified by the International Telecommunications Union recommendation G.694.1 and display typical channel separations of 25, 50 or 100 GHz roughly 0.2, 0.4 or 0.8 nm in the C-Band.

3.2 Arrayed Waveguide Grating Operation

A schematic of an AWG demultiplexer is shown in figure 3.2. When the light propagating through the input waveguide enters the first slab waveguide it is no longer laterally confined and diverges. On arriving at the input plane the light is coupled into the waveguide array and propagates to the output plane through the individual arrayed

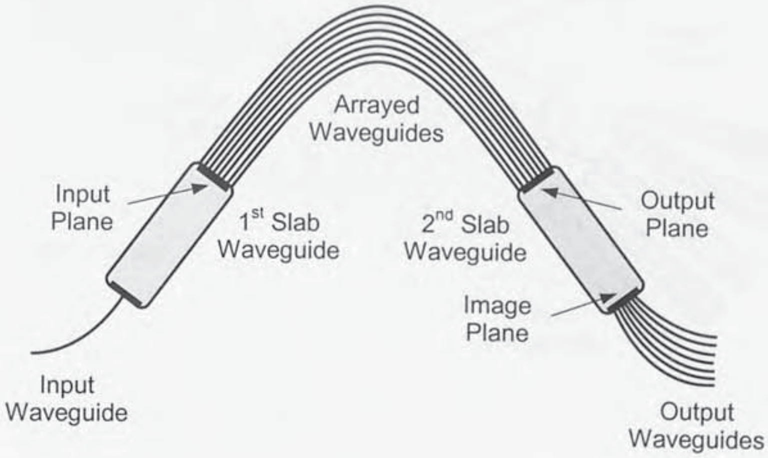

Figure 3.2 Schematic of an arrayed waveguide grating demultiplexer.

waveguides. Each arrayed waveguide differs in length ΔL from an adjacent waveguide, given by [12]

$$\Delta L = \frac{m\lambda}{n_w} \tag{3.1}$$

where m is the order of the array, λ is the central operational wavelength of the AWG and n_w is the refractive index of the arrayed waveguides. Figure 3.3 shows the geometry

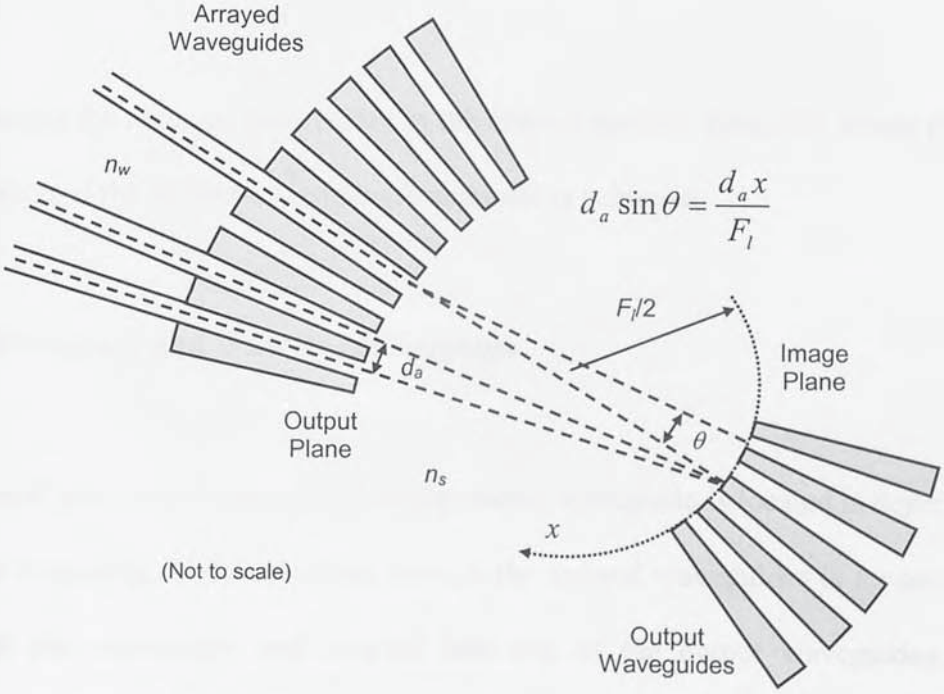

Figure 3.3 Geometry inside the second slab waveguide.

inside the second slab waveguide. The light emitted from the arrayed waveguides is diffracted at an angle θ satisfying the following expression [7][12]

$$n_w \Delta L + n_s d_a \sin\theta = m\lambda \tag{3.2}$$

where n_s is the refractive index of the slab waveguide and d_a is the spacing of the waveguides on the output plane. The dispersion of the array is described as a lateral displacement of x (the focal point) along the image plane per unit wavelength change $\Delta x/\Delta\lambda$ [7][12][13]. By making the substitution ($\sin\theta = x/F_l$) [6] where, F_l is the focal length, rearranging equation (3.2) for x (the focal point) and differentiating with respect to the wavelength, the dispersion is given by

$$D = \frac{\Delta x}{\Delta\lambda} = \frac{F_l m}{n_s d_a} \tag{3.3}$$

By placing the receiver waveguides in the correct position along the image plane, spatial separation of the different wavelength channels is achieved.

3.2.1 Frequency and Wavelength Response

The focal point where the corresponding output waveguide is located is dependent on the optical frequency. Light travelling through the arrayed waveguides is focused across the second slab waveguide and coupled into one of the output waveguides. The focal position across the image plane is dependent on the optical frequency [13]. For single-mode devices operating with a V-parameter around 2 the modal fields will be approximately Gaussian [14] and the frequency response $T(f)$, given by [13]

$$T_i(f) = \exp\left(-\left(\frac{\Delta x}{\Delta f}\frac{(f - f_i)}{a_0}\right)^2\right) \tag{3.4}$$

where a_0 is the power density distribution or spot size of the fields [14]. Hence, the frequency response is the same as a Gaussian bandpass filter with a full width half maximum (FWHM) given by [13]

$$FWHM = \frac{2\sqrt{\ln 2}\, a_0\, \Delta f}{\Delta x} \tag{3.5}$$

Therefore, the frequency response of an AWG channel $T(f)$ can be written as

$$T_i(f) = \exp\left(-\left(\frac{2\sqrt{\ln 2}}{FWHM_i}(f - f_i)\right)^2\right) \tag{3.6}$$

The wavelength response $T(\lambda)$ is analogous to the frequency response, given by

$$T_i(\lambda) = \exp\left(-\left(\frac{\Delta x}{\Delta \lambda}\frac{(\lambda - \lambda_i)}{a_0}\right)^2\right) \tag{3.7}$$

where the ratio $\Delta x/\Delta\lambda$ is the wavelength dispersion D given by equation (3.3) and λ_i is the central wavelength of the ith AWG channel. The full width half maximum (FWHM) is given by

$$FWHM = \frac{2\sqrt{\ln 2}\, a_0\, \Delta \lambda}{\Delta x} \tag{3.8}$$

Therefore, the wavelength response of an AWG channel $T(\lambda)$ can be written as

$$T_i(\lambda) = \exp\left(-\left(\frac{2\sqrt{\ln 2}}{FWHM_i}(\lambda - \lambda_i)\right)^2\right) \tag{3.9}$$

In some applications, a flattop frequency response could be important in order to relax wavelength control requirements [12]. There are several ways to achieve this including the use of multimode output waveguides [15], a multimode interference filter at the end of the input waveguide [16] and shaping the phase transfer to a sinc distribution [17].

3.2.2 Channel Crosstalk

AWG crosstalk is attributed to a number of mechanisms. It is normally common practice to express the crosstalk performance by specifying the maximum single channel crosstalk power level. Typically, crosstalk values are in the order of -25 dB for indium phosphide based AWGs to better than -30 dB for silica AWGs [12]. Several mechanisms contribute to the overall channel crosstalk level. These include coupling between receiver waveguides through the exponential tails of the field distributions, mode conversion at the junctions between straight and curved waveguides and phase errors attributed to optical path length fluctuations caused by small deviations in the effective refractive index of the waveguides or the waveguide width. The crosstalk can be kept to a minimum by correct AWG design and fabrication [12][18][19].

3.2.3 Insertion Loss

Typical commercially available AWGs display insertion losses of between 3 and 7 dB [12]. The primary cause of insertion loss is due to imperfect capture of light between the arrayed and slab waveguides. Other minor sources of insertion loss include the fibre to waveguide connection, the curved waveguide bending loss and the materials intrinsic loss [20]-[22].

3.2.4 Temperature Drift

The refractive index and length of the waveguides varies with changes in temperature causing the centre wavelengths of the AWG channels to drift. This relationship is determined by rearranging equation (3.1) for the wavelength λ and differentiating with respect to ΔT, to give

$$\frac{\Delta\lambda}{\Delta T} = \frac{1}{m}\left(\frac{d\Delta L}{dT}n_w + \frac{dn_w}{dT}\Delta L\right) \tag{3.10}$$

for silica waveguides operating at room temperature in the C-Band, the thermal expansion coefficient $1/\Delta L \;\; d\Delta L/dT = 5 \times 10^{-7}$ / °C [23], the temperature derivative of refractive index $dn_w/dT = 1 \times 10^{-5}$ / °C [23] and the waveguide refractive index n_w = 1.45 [23]. Therefore, silica based AWGs display a thermal drift $\Delta\lambda/\Delta T$ of approximately 11.5 pm/°C (see appendix B). For comparison, indium phosphide devices display much worse thermal drifts, around 107 pm/°C (see appendix B), making silica based AWGs a far more attractive material in regards to thermal stabilisation. The effects of temperature drifts can be considerably reduced by using temperature stabilisation. The temperature is controlled at an elevated level by an internal heater which also acts to tune the AWG channels to their operating wavelength. Feedback is provided by an internal thermal sensor stabilising the AWG channels. In recent years athermal AWGs have attracted much interest because they are independent of temperature control. There are several reports that compensate for temperature drift in AWGs without active thermal stabilisation [24]-[29]. Because these devices have no heater, heater controller or monitoring electronics they incur no operating costs making them very attractive in both optical sensing and telecommunications networks. There are already commercially availably devices [30]-[31] offering stable wavelength demultiplexing over a wide ambient operating temperature range.

3.2.5 Polarisation Dependent Frequency and Loss

Polarisation dependence of AWGs is caused by the inherent waveguide birefringence. The refractive index of the arrayed waveguide can be different for the orthogonal polarisation modes due to stress induced birefringence [33]. Therefore, the focal field position along the image plane is different for the transverse electric (TE) and transverse magnetic (TM) modes. The central wavelength shift $\Delta\lambda$ due to the waveguide birefringence is given by [34]

$$\Delta\lambda = \frac{(n_{TM} - n_{TE})\Delta L}{m} \tag{3.11}$$

where $(n_{TM} - n_{TE})$ is the refractive index difference between the two polarisation modes. There are several methods to significantly reduce the polarisation dependence. The simplest and most practical is the use of a halfwave plate in the middle of the array to swap the polarisation states so they experience the same phase transfer [9][34][35]. Other techniques include matching the free spectral range to the polarisation dispersion [36], matching the thermal expansion of the waveguides to the substrate [37][38] and the use of non-birefringent waveguides [12][39][40]. Typical polarisation dependent frequency values for low polarisation dependent silica devices are in the order of 1 to 5 GHz (or 10 to 40 pm in the C-Band) relating to polarisation dependent losses of less than 0.5 dB [34][35][40].

3.3 The Bookham Optical Channel Monitor

The Bookham optical channel monitor (Model No. BKM-54005-01-UN) is a solid-state, thermally stabilised 40 channel outputs. The optical channel monitor is used by the author in the majority of the fibre optic sensor interrogation schemes described in this thesis. The optical channel monitor is fabricated using Bookham's patented active silicon

Figure 3.4 The Bookham arrayed waveguide grating passband diagram [41].

optical circuit technology, has a channel spacing of 100 GHz (roughly 0.8 nm in the C-Band) and a 3 dB passband for each channel of a little over 0.2 nm [41]. The passband diagram for the AWG is shown in figure 3.4. Each photodetector anode pin is connected to a variable gain transimpedance amplifier circuit to amplify the photo current. The channel wavelength allocations for the Bookham device can be found in appendix C.

3.4 Arrayed Waveguide Gratings as Fibre Optic Sensor Interrogation Devices

AWGs with photodetection [42] function in a similar fashion to a charged coupled device based spectrometer with a diffraction grating as the dispersive element. The advantages using an AWG system leads to a far more compact and sturdy interrogation unit. The outputs of the AWG photodetectors are available simultaneously, allowing the interrogation of multiple fibre optic sensors concurrently. Reports of wavelength division multiplexers used in optical interrogation schemes go back to the 1980s [43][44]. Fibre Bragg grating sensor interrogation was first demonstrated using a wavelength division multiplexer in 1996 [45]. The first report using an AWG to interrogate fibre Bragg grating sensors was published by Sano *et al* [46] in 2000. Webb *et al* [47] in 2002 extended the work and demonstrated the use of AWGs to interrogate interferometric sensors and dynamic strain in fibre Bragg grating sensors. Since then the author has extended the interferometric and fibre Bragg grating sensor interrogation using AWGs. As yet there seems to be no reports to the author's knowledge of any AWG based optical fibre sensor interrogation systems used in industrial applications. One reason for this is the financial decline of the telecommunications industry from 2001 [48] to 2003 [49] which drastically changed the economic environment of the optical component business. However, with the recovery slowly regaining momentum there seems to be a revival in research and development of planar lightwave circuit technology enabling rugged, flexible, multi-functioning optical components including AWGs capable of being manufactured in high volumes at low cost [50][51].

3.5 Conclusion

An overview of AWG technology has been outlined. The operation of AWGs has been discussed showing how the input light is channelled to the appropriate output waveguide. Insertion loss, crosstalk, polarisation dependence and temperature drift have been discussed along with some solutions to overcome their operational effects. The AWG device used for the work described in this thesis has been introduced for reference in chapters 6, 7 and 8.

3.6 References

[1] C. S. Murthy and G. Mohan, "WDM optical networks, concepts, design and algorithms," *Prentice Hall*, ISBN: 0-13060637-5, 2001

[2] A. K. Dutta, N. K. Dutta and M. Fujiwara, "WDM technologies optical networks," ISBN: 0-12225263-2, 2004

[3] Y. Lia, W. Zhang and J. A. R. Williams, "All fibre multichannel flattop filter based on coherent fibre delay line filter," *Electronic Letters*, vol. 38, No. 10, pp. 473-475, May 2002

[4] S. Breer and K. Buse, "Wavelength demultiplexing with volume phase holograms in photorefractive lithium niobate," *Applied Physics B Lasers and Optics*, vol. 66, pp. 339-345, March 1998

[5] H. Hsich, G. Panotopoulos, M. Liger, Y. Tai and D. Psaltis, "Athermal holographic filters," *Photonics Technology Letters*, vol. 16, No. 1, pp. 177-179, January 2004

[6] M. K. Smit, "New focusing and dispersive planar component based on an optical phased array," *Electronic Letters*, vol. 24, No. 7, pp. 385-386, March 1998

[7] H. Takahashi, S. Suzuki, K. Kato and I. Nishi, "Arrayed waveguide grating for wavelength division multi/demultiplexer with nanometer resolution," *Electronic Letters*, vol. 26, No. 2, pp. 87-89, January 1990

[8] H. Takahashi, I. Nishi and Y. Hibino, "10Ghz spacing optical frequency division multiplexer based on arrayed waveguide grating," *Electronic Letters*, vol. 28, No. 4, pp. 380-382, February 1992

[9] A. Himeno, K. Kato and T. Miya, "Silica based planar lightwave circuits," *Journal of Selected Topics in Quantum Electronics*, vol. 4, No. 6, pp. 913-924, November 1998

[10] K. Okamoto, "Planar lightwave circuits for optical communications and sensing," *in Proceedings 13th International Conference on Optical Fibre Sensors*, (OFS-13, Kyongju, Korea), Technical Digest, pp. 17-22, April 1994

[11] J. Lam, A. Liu and M. Yan, "Multi function integrated AWG devices," *in Proccedings of Optical Fibre Communications Conference*, (OFC 2005), Anaheim, pp. OTuD1, March 2005

[12] M. K. Smit and C. van Dam, "PHASAR based WDM devices: Principles, design and applications," *IEEE Journal of Selected Topics in Quantum Electronics*, vol. 2, No. 2, pp. 236-250, June 1996

[13] H. Takahashi, K. Oda, H. Toba and Y. Inoue, "Transmission characteristics of arrayed waveguide N x N wavelength multiplexer," *Journal of Lightwave Technology*, vol. 13, No. 3, pp. 447-455, March 1995

[14] J. Gowar, "Optical communication systems," (Second Edition), *Prentice Hall International Series in Optoelectronics*, ISBN 0-13-638727-6, 1993

[15] M. R. Amersfoort, C. R. de Boer, F. P. G. M. van Ham, M. K. Smit, P. Demeester, J.J. G. M. van der Tol and A. Kuntze, "Phased array wavelength demultiplexer with flattened wavelength response," *Electronic Letters*, vol. 30, No. 4, pp. 300-302, February 1994

[16] M. R. Amersfoort, J. D. B. Soole, H. P. Leblanc, N. C. Andreadakis, A. Rajhel and C. Caneau, "Passband broadening of integrated arrayed waveguide filters using multimode interference couplers," *Electronic Letters*, vol. 32, No. 5, pp. 449-451, February 1996

[17] K. Okamoto and H. Yamada, "Arrayed waveguide grating multiplexer with flat spectral response," *Optics Letters*, vol. 20, No. 1, pp. 43-45, January 1995

[18] Chu. Y, Zheng. X, Zhang. H, Lui. X and Guo. Y, "The impact of phase errors on arrayed waveguide gratings," *IEEE Journal of Selected Topics in Quantum Electronics*, vol. 8, No. 6, pp. 11221129, December 2002

[19] H. Yamada, K. Takada, Y. Inoue, Y. Ohmori and S. Mitachi, "Statically phase compensated 10GHz spaced arrayed waveguide grating," *Electronics Letters*, vol. 32, No. 17, pp. 1580-1582, August 1996

[20] J. C. Chen and C. Dragone, "A study of fiber-to-fiber losses in waveguide grating routers," *IEEE Journal of Lightwave Technology*, vol. 15, No. 10, pp. 1895-1899, October 1997

[21] D. Marcuse, "Bending loss of the asymmetric slab waveguide," *Bell System Technology*, vol. 50, pp. 2551-2561, October 1971

[22] K. Takada, H. Yamada, Y. Hida, Y. Ohmori and S. Mitachi, "Rayleigh backscattering measurements of 10m long silica-based waveguides," *Electronics Letters*, vol. 32, No. 18, pp. 1665-1667, August 1996

[23] D. N. Nikogosyan, "Properties of optical and laser related materials," *John Wiley & Sons*, ISBN: 0-471-97384, 1998

[24] J. B. D. Soole, M. Schlax, C. Narayanan and R. Pafchek, "Athermalisation of silica arrayed waveguide grating multiplexers," *Electronics Letters*, vol. 39, No. 16, pp. 1182-1184, August 2003

[25] A. Kaneko, S. Kamei, Y, Inoue, H. Takahashi and A. Sugita, "Athermal silica based arrayed waveguide grating (AWG) multi/demultiplexers with new low loss grove design," *Electronics Letters*, vol. 36, No. 4, pp. 318-319, February 2000

[26] N. Ooba, Y. Hibino, Y. Inoue and A. Sugita, "Athermal silica based arrayed waveguide grating multiplexer using bimetal plate temperature compensator," *Electronics Letters*, vol. 36, No. 21, pp. 1800-1801, October 2000

[27] Y. Inoue, A. Kaneko, F. Hanawa, H. Takahashi, K. Hattori and S. Sumida, "Athermal silica-based arrayed waveguide grating multiplexer," *Electronics Letters*, vol. 33, No. 23, pp. 1945-1946, November 1997

[28] A. J. Ticknor, B. P. McGinnis, T. Tarter and M. Yan, "Efficient passive and active wavelength stabilization techniques for AWGs and intergrated optical filters," *in Proccedings of Optical Fibre Communications Conference*, (OFC 2005), Anaheim, pp. NThL3, March 2005

[29] J. Lee, J. Ahn, S. Park an M. Lee, "Athermalized polymeric arrayed waveguide grating by partial detachment from a si substrate," *in Journal of the Electronics and Communications Research Institute*, vol. 26, No. 3, pp. 281-284, June 2004

[30] T. Saito, K. Nara, K. Tanaka, Y. Nekado, J. Hasegawa and K. Kashihara, "Temperature insensitive athermal AWG modules," *in Furukawa Review of Furukawa Electric (Japan)*, No. 24, pp. 29-33, October 2003

[31] J. Hasegawa and K. Nara, "Ultra low loss athermal AWG module with a large number of channels," *in Furukawa Review of Furukawa Electric (Japan)*, No. 26, pp. 1-5, September 2004

[32] A. J. Ticknor, B. P. McGuiness, T. Tarter and M. Yan, "Efficient passive and active wavelength stabilization techniques for AWGs and integrated optical filters," *in Proccedings of Optical Fibre Communications Conference*, (OFC 2005, Anaheim, USA), pp. NThL3, March 2005

[33] F. Zhong, F. Parhami and J. G. Bornstein, "A comprehensive method to reduce PDW in arrayed waveguide grating," *in Proceedings of Optical Fibre Communications Conference*, (OFC2003, Atlanta, USA), pp. Tuk5, April 2003

[34] Y. Inoue, H. Takahashi, S. Ando, T. Sawada, A. Himeno and M. Kawachi, "Elimination of polarization sensitivity in silica based wavelength division multiplexer using a polyimide half waveplate," *Journal of Lightwave Technology*, vol. 15, No. 10, pp. 1947-1949, October1997

[35] H. Takahashi, Y. Hibino and I. Nishi, "Polarization insensitive arrayed waveguide grating wavelength multiplexer on silicon," *Optics Letters*, vol. 17, No. 7, pp. 400-501, April 1992

[36] L. H. Spiekman, M. R. Amersfoort, A. H. de Vreede, F. P. G. M. van Ham, a. Kuntze, J. W. Pedersen, P. Demeester and M. K. Smit, "Design and realization of polarization independent phased array wavelenghth demultiplexers using different array orders for TE and TM," *Journal of Lightwave Technology*, vol. 14, No. 6, pp. 991-995, June 1996

[37] S. Suzuki, S. Sumida, Y. Inoue, M. Ishii and Y. Ohmori, "Polarisation insensitive arrayed waveguide gratings using dopant rich silica based glass with thermal expansion adjusted to Si substrate," *Electronics Letters*, vol. 33, No. 13, pp. 1174-1176, June 1997

[38] S. M. Ojha, C. Cureton, T. Bricheno, S. Day, D. Moule, A. J. Bell and J. Taylor, "Simple method of fabricating polarisation insensitive and very low crosstalk AWG grating devices," *Electronics Letters*, vol. 34, No. 1, pp. 78-79, January 1998

[39] J. H. den Besten, M. P. Dessens, C. G. P. Herben, X. J. M. Leijitens, F. H. Groen, M. R. Leys and M. K. Smit, "Low loss, compact polarization independent PHASAR demultiplexer fabricated by using a double etched process," *Photonics Technology Letters*, vol. 14, No, 1, pp. 62-64, January 2002

[40] J. B. D. Soole, M. R. Amersfoort, H. P. Leblanc, N. C. Andreadakis, A. Rajhel, C. Caneau, M. A. Koza, R. Bhat, C. Youtsey and I. Adesida, "Polarisation independent InP arrayed waveguide filter using square cross-section waveguides," *Electronics Letters*, vol. 32, No. 4, pp. 323-324, February 1996

[41] Bookham Technology, "Operation outline of an optical channel monitor for DWDM systems," *Technical Note TN018-1.0*, pp. 4-5, October 2000

[42] M. R. Amersfoot, C. R. de Boer, B. H. Verbeek, P. Demster, A. Looyen and J. J. G. M. van der Tol, "Low loss phased array based 4 channel wavelength demultiplexers integrated with photodetectors," *Photonics Technology Letters*, vol. 6, No. 1, pp. 62-64, January 1994

[43] D. Varshneya and W. L. Glomb, "Applications of time and wavelength division multiplexing to digital optical code plates," *in Proceedings SPIE Fibre Optic Sensors V*, vol. 838, pp. 210-213, August 1987

[44] J. T. Newmaster, M. R. Brininstool, T. Hofer and S. L. Garrett, "Remote fiber optic sensors for angular orientation," *in Proceedings SPIE Fibre Optic Sensors V*, vol. 838, pp. 28-38, August 1987

[45] T. A. Berkoff and A. D. Kersey, "Fiber Bragg grating array sensor system using a bandpass wavelength division multiplexer and interferometric detection," *Photonics Technology Letters*, vol. 8, No. 11, pp. 1522-1524, November 1996

[46] Y. Sano, N. Hirayama and T. Yoshino, "Wavelength interrogator employing arrayed waveguide grating for distributed fibre Bragg gratings," *in Proceedings 14th International Conference on Optical Fibre Sensors*, (OFS-14, Venice, Italy), Technical Digest, pp. 788-791, October 2000

[47] D. J. Webb and R. D. Pechstedt, "Sensing applications of arrayed waveguide grating devices," *in Proceedings 15th International Conference on Optical Fibre Sensors*, (OFS-15, Portland, USA), Technical Digest, pp. 569-572, May 2002

[48] "The great telecoms crash," *The Economist*, vol. 364, No. 8282, 20th July 2002

[49] "Beyond the Bubble," *The Economist*, vol. 369, No. 8345, 11th October 2003

[50] A. Kaneko, Y. Hashizume, S. Kamei, Y. Doi, R. Kasahara, Y. Tamura, I. Ogawa, M. Ishii, T. Kominato and S. Suzuki, "Ultra small and low power consumption 8ch variable optical attenuator multiplexer (V-AWG) using multi-chip PLC integration technology," *in Proccedings of Optical Fibre Communications Conference*, (OFC 2005, Anaheim, USA), pp. OTuD3, March 2005

[51] D. J. Dougherty, "Advances in planar lightwave circuits," *in Proccedings of Optical Fibre Communications Conference*, (OFC 2005, Anaheim, USA), pp. OThN5, March 2005

4 Acousto-Optic Tuneable Filters

Acousto-optic tuneable filters (AOTFs) are electro-optical, solid-state devices that operate on the principle of acousto-optic interaction in an anisotropic medium. The spectral bandpass of the filter can be tuned fairly rapidly by changing an applied radio frequency (RF). This chapter describes the operation and performance of AOTFs relevant to the work described in this thesis.

4.1 Introduction

Brillouin predicted light diffraction by an acoustic wave propagating in a medium of interaction in 1922 [1]. Sound waves cause periodic compression and rarefaction of an optically transparent medium in which they are propagating, resulting in periodic variations of the medium's refractive index, which acts as a phase grating that diffracts part or the entire incident light. A parameter called the quality-factor Q determines the interaction regime, given by [1]

$$Q = \frac{2\pi\,\lambda\,L}{n\,\Lambda^2} \tag{4.1}$$

where λ is the wavelength of light, L is the interaction length, n is the refractive index of the medium and Λ is the wavelength of the acoustic wave. The condition for obtaining multiple diffractions is when $Q << 1$ and is termed the Raman-Nath regime. The condition for obtaining a single diffracting beam is when $Q >> 1$, this

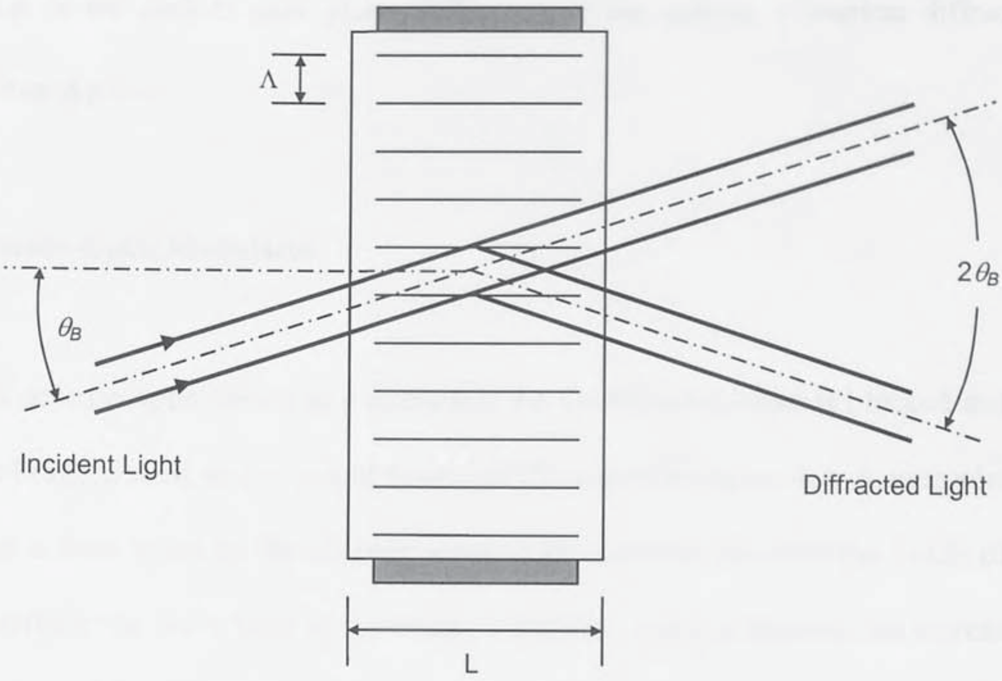

Figure 4.1 An acousto-optic device operating in the Bragg regime.

is called Bragg diffraction is illustrated in figure 4.1. At incident angles of $\pm\theta_B$ the diffracted beam exists at $2\theta_B$. The Bragg angle θ_B is given by [1]

$$\sin\theta_B = \frac{\lambda}{n2\Lambda} \tag{4.2}$$

The phase grating can be interpreted as a stack of reflectors spaced by the wavelength of the acoustic wave. The fraction of the incident light intensity I_0 to the diffracted light intensity I is related to the amplitude of the phase grating given by [1]

$$\frac{I}{I_0} = \sin^2\left(\frac{\Delta\phi}{2}\right) \tag{4.3}$$

where $\Delta\phi$ is the peak-to-peak phase difference of the grating. Complete diffraction occurs when $\Delta\phi = \pi$.

4.1.1 Acosuto-Optic Modulator

To use an acousto-optic device as a modulator the un-deflected beam is blocked and the deflected beam is used as the output beam, as illustrated in figure 4.2. A piezoelectric transducer is used to set up the acoustic wave in the material. Because the inside of the material reflects the wave back at the source a standing wave is formed. An increase in the frequency of the acoustic wave increases the refractive index of the material. When the acoustic drive frequency is off, the light in the direction of the deflected beam is zero.

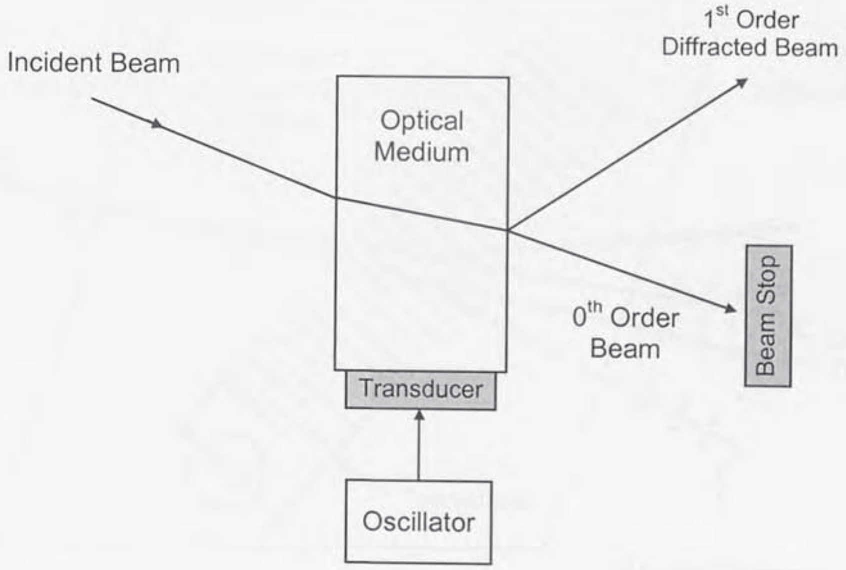

Figure 4.2 Illustration of an acousto-optic modulator.

Conversely, when the acoustic drive frequency is on, light is diffracted into the direction of the deflected beam. Thus, the device controls the light in the direction of the deflected beam by simply turning the acoustic drive frequency on and off. The device is operated as a modulator by keeping the acoustic drive frequency fixed and varying the drive power to control the amount of light in the deflected beam.

4.1.2 Acousto-Optic Tuneable Filter

An AOTF is a device that is based on the acoustic diffraction of light by varying the applied RF signal. AOTFs with wide tuning range in the ultraviolet and infrared have been developed, using both collinear and non-collinear configurations. Figure 4.3 shows an illustration of a non-collinear AOTF. It consists of a birefringent crystal to which a piezoelectric transducer is bonded. When an RF signal is applied, acoustic waves are launched into the crystal. The propagating acoustic waves produce a periodic modulation of index of refraction. This generates a travelling phase grating which will diffract portions of an incident light beam. For a fixed acoustic frequency and a long enough

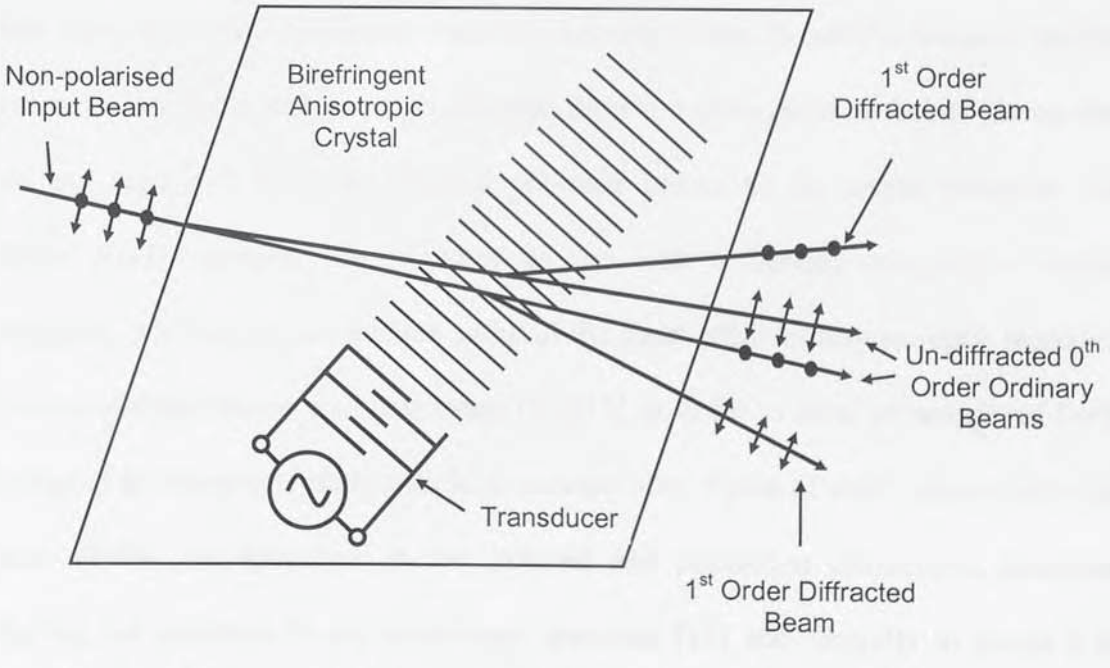

Figure 4.3 Non-collinear acousto-optic tuneable filter diffraction process.

interaction length only a limited band of optical frequencies can approximately satisfy the phase-matching condition and be diffracted. As the RF frequency is altered, the centre of the optical passband is changed accordingly. Alternatively, AOTFs can be driven simultaneously with multiple RF signals. AOTFs were first proposed in 1969 [2][3] operating in the visible spectra, but it wasn't until the late 1970s [4] when the first devices working in the infrared were demonstrated. The operation and performance of AOTFs have been incorporated into a number of different types of optical systems such as optical sensing [5]-[9], laser wavelength tuning [10][11], spectral imaging [12] and multiplexing of optical communication channels [13][14]. As mentioned earlier, AOTFs are configured to operate through either collinear or a non-collinear mechanism. In collinear AOTFs the acoustic wave is launched along the optic axis of the crystal. The incident optical beam is passed through a polariser and follows the same path along the crystal axis interacting collinearly with the acoustic wave. A narrow band of spectral wavelengths are diffracted into a polarisation direction orthogonal to that of the incident beam and separated from the coupled collinear beams by an output polariser. The collinear AOTF geometry is restricted to use with a limited category of optical waveguides, which does not include some of the most efficient acousto-optic materials. The non-collinear device was developed [15][16] in order to take advantage of firstly birefringent anisotropic crystals with high acousto-optic figure of merit such as tellurium dioxide (TeO_2) for operation in the infrared and potassium dihydrogen phosphate (KH_2PO_4) for operation in the ultra-violet spectrum [17] and secondly to utilise a far simpler geometry (no input or output polariser). In the non-collinear design the diffracted light and incident light is physically separated and because they exit the crystal through different pathways, polarisers are not required for operation. When non-polarised incident light is employed the diffracted portion of the beam comprises of two spatially separated 1st order beams, which are orthogonally polarised (see figure 4.3). Usually only one of the diffracted beams is used for the output, the other 1st order and the 0th order beams are effectively blocked by a beam stop.

4.2 Non-Collinear Acousto-Optic Tuneable Filter Operation

The basic operating concept is illustrated in figure 4.4 showing the wave-vector diagram for acousto-optic diffraction in a birefringent crystal [18]. In a birefringent crystal there are two distinct refractive index surfaces, the extraordinary n_e and ordinary n_o, the birefringence Δn of the crystal is hence given by $(n_e - n_o)$. An extraordinary input wave incident at an angle θ_i relative to the optic axis is diffracted into an ordinary output

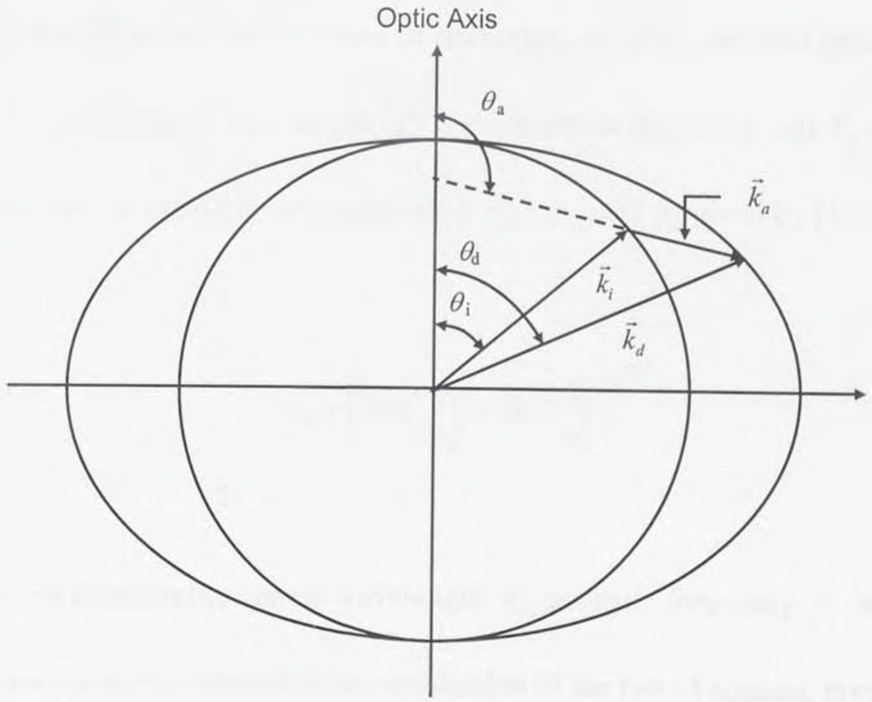

Figure 4.4 Wave-vector diagram for a birefringent anisotropic crystal.

wave. Diffraction occurs only for the wavelength that satisfies the specific phase-matching condition, given by [19][20]

$$\vec{k}_d = \vec{k}_i \pm \vec{k}_a \tag{4.4}$$

where $\vec{k}_d$ is the diffracted wave vector, $\vec{k}_i$ the incident wave vector and $\vec{k}_a$ the acoustic wave vector, given by [19]

$$\vec{k}_a = \frac{2\pi f_a}{V_a} \qquad \vec{k}_i = \frac{2\pi n_i}{\lambda_o} \qquad \vec{k}_d = \frac{2\pi n_d}{\lambda_o} \tag{4.5}$$

where n_d is the diffracted optical index of refraction, n_i is the incident optical index of refraction, λ_o is the optical wavelength, f_a is the acoustic frequency and V_a the acoustic wave velocity. For an extraordinary input wave $n_d = n_o$ and n_i given by [19]

$$n_i = \left(\cos^2 \frac{\phi_i}{n_o^2} + \sin^2 \frac{\phi_i}{n_e^2} \right)^{-1/2} \tag{4.6}$$

The relationship between the optical wavelength λ_o, acoustic frequency f_a and the wave velocity V_a can be easily determined by application of the law of cosines, given by [21]

$$\vec{k}_a^2 = \vec{k}_d^2 + \vec{k}_i^2 + 2\vec{k}_d\,\vec{k}_i \cos(\theta_i - \theta_d) \tag{4.7}$$

substituting the wave vector magnitudes, simplifying and rearranging, gives

$$\frac{f_a^2 \lambda_o^2}{V_a^2} = n_o^2 + n_i^2 + 2 n_o n_i \cos(\theta_i - \theta_d) \tag{4.8}$$

Therefore, the diffracted wavelength varies as a function of the RF signal applied to the crystal.

4.2.1 Bandpass Characteristics

The central wavelength λ_{centre} of the passband is determined from the peak amplitude of the acoustic wave driving the AOTF i.e. when $(\theta_d - \theta_i) = \pi/2$. Therefore, from equation (4.8)

$$\lambda_{centre} = \frac{V_a}{f_a} \Delta n \tag{4.9}$$

where $\Delta n = n_d + n_i$. Consequently varying the frequency and power of the RF signal provides a mechanism for selecting the wavelength and intensity of the light filtered by the AOTF. The peak transmission T_o of an AOTF is given by the ratio of the intensity of the diffracted light to that of the incident light, given by [20]

$$T_o = \sin^2\left(P_d L^2 \frac{\pi^2}{2} \frac{M}{\lambda_o^2} \right)^{1/2} \tag{4.10}$$

where P_d is the acoustic power density [20], L is the acoustic interaction length in the crystal [14] and M is the acousto-optic figure of merit [20]. Peak transmission occurs when $P_d = \lambda_o^2 / 2 M L^2$ i.e. when $T_o = \sin^2(\pi/2)$. The wavelength response $T(\lambda)$ of an AOTF is given by [20]

$$T(\lambda) = T_o \operatorname{sinc}^2\left(0.886 \frac{(\lambda - \lambda_o)}{FWHM}\right) \tag{4.11}$$

where $(\lambda - \lambda_o)$ is the deviation from the phase-matching wavelength and $FWHM$ is the full width half maximum or spectral resolution, given by [15]

$$FWHM = \frac{0.8 \pi \lambda_o^2}{L\, b \sin^2 \theta_i} \tag{4.12}$$

where b is a wavelength dependent constant [20]. For an infinitely long interaction length, only the optical wave with the frequency that exactly satisfies the phase-matching condition will be transmitted through the AOTF [20].

4.3 The Gooch & Housego Acousto-Optic Tuneable Filter

The Gooch & Housego (Model No. TF1450-500-3-F2S) acousto-optic tuneable filter used for the work in this thesis is a solid-state, anisotropic, non-collinear, tellurium dioxide device with high speed tuning. The AOTF has a response time of less than 10 μs,

Figure 4.5 Relationship between the drive frequency and the filtered wavelength [22].

a spectral resolution in the C-Band of 4.5 nm and an operating wavelength range from 1.2 μm to 1.7 μm. The tuning relationship between the drive frequency and diffracted wavelength is shown in figure 4.5. The device has good side-lobe suppression, less than 5 % of the main transmission peak. The insertion loss is < 6 dB for unpolarised input light and < 3 dB if the input light is polarised.

4.4 Conclusion

An overview of the operation of AOTFs has been outlined. The function of an AOTF has been described. Strong acousto-optic interactions occur when the phase-matching condition between a light wave and a sound wave is satisfied. Therefore, the wavelength of the diffracted light can be selected or tuned by varying the applied acoustic frequency. AOTFs can also be driven with multiple RF signals making them ideal for use in multiplexed sensor systems. The Gooch & Housego AOTF used for the experimental work described in this thesis has been introduced for reference in chapter 9.

4.5 References

[1] E. E. Basch, "Optical fiber transmission," *Howard W. Sam & Co*, pp. 303-333, 1986, ISBN: 0-672-22301-5

[2] S. E. Harris and R. W. Wallace, "Acousto-optical tunable filter," *Journal of the Optical Society of America*, vol. 59, No. 6, pp. 744-747, June 1969

[3] S. E. Harris, S. T. K. Nieh and D. K. Winslow, "Electronically tunable acousto-optic filter," *Applied Physics Letters*, vol. 15, No. 10, pp. 325-326, November 1969

[4] J. D. Feichtner, N. Gottlieb and J. J. Conroy, "Tl_3AsSe_3 non-collinear acousto-optic filter operation at 10 μm," *Applied Physics Letters*, vol. 34, No. 1, pp. 1-3, January 1979

[5] M. G. Xu, H. Geiger and J. P. Dakin, "Modelling and performance analysis of a fibre Bragg grating interrogation system using an acousto-optic tunable filter," *Journal of Lightwave Technology*, vol. 14, No. 3, pp. 391-396, March 1996

[6] M. G. Xu, H. Geiger, J. L. Archambault and J. P. Dakin, "Novel interrogating system for fibre Bragg grating sensors using an acousto-optic tunable filter," *Electronics Letters*, vol. 29, No. 17, pp. 1510-1511, August 1993

[7] M. G. Xu, H. Geiger and J. P. Dakin, "Interrogating of fibre-optic interferometric sensors using an acousto-optic tunable filter," *Electronics Letters*, vol. 31, No. 17, pp. 1487-1488, August 1995

[8] M. Volanthen, H. Geiger, M. G. Xu and J. P. Dakin, "Simultaneous monitoring of multiple fibre gratings with a single acousto-optic tunable filter," *Electronics Letters*, vol. 32, No. 13, pp. 1228-1229, June 1996

[9] C. Boulet, D. J. Webb, M. Douay and P. Naiy, "Simultaneous interrogation of fibre Bragg grating sensors using an acousto-optic tunable filter," *Photonics Technology Letters*, vol. 13, No. 11, pp. 1215-1217, November 2001

[10] D. J. Taylor, S. E. Harris, S. T. K. Nieh and T. W. Hansch, "Electronic tuning of a dye laser using the acousto-optic filter," *Applied Physics Letters*, vol. 19, No. 8, pp. 269-271, October 1971

[11] G. A. Coquin and K. W. Cheung, "Electronically tunable external cavity semiconductor laser," *Electronics Letters*, vol. 24, No. 10, pp. 599-600, May 1988

[12] D. R. Suhre and J. G. Theodore, "White light imaging by use of a multiple passband acousto-optic tunable filter," *Applied Optics*, vol. 35, No. 22, pp. 4494-4501, August 1996

[13] K. W. Cheung, D. A Smith, J. E. Baran and B. L. Heffner, "Multiple channel operation of integrated acousto-optic tunable filter," *Electronics Letters*, vol. 25, No. 6, pp. 375-376, March 1989

[14] K. W. Cheung, S. C. Liew and C. N. Lo, "Simultaneous five-wavelength filtering at 2.2 nm wavelength separation using integrated-optic acousto-optic tunable filter with subcarrier detection," *Electronics Letters*, vol. 25, No. 10, pp. 636-637, May 1989

[15] I. C. Chang, "Noncollinear acousto-optic filter," *Electronics Letters*, vol. 11, No. 25, pp. 617-618, December 1975

[16] I. C. Chang, "Noncollinear acousto-optic filter with large angular aperture," *Applied Physics Letters*, vol. 25, No. 7, pp. 370-372, October 1974

[17] V. Voloshinov and N. Gupta, "Ultraviolet-Visible Imaging Acousto-Optic Tunable Filters in KDP," *Applied Optics*, vol. 43, No. 19, pp. 3901-3909, July 2004

[18] M. Born and E. wolf, "Principles of Optics," *Cambridge University Press*, ISBN: 0-521-642221, 1999

[19] D. R. Suhre and N. Gupta, "Acousto-optic tunable filter sidelobe analysis and reduction with telecentric confocal optics," *Applied Optics*, vol. 44, No. 27, pp. 5797-5801, September 2005

[20] I. C. Chang, "Acousto-optic tunable filters," *Optical Engineering*, vol. 20, No. 6, pp. 824-829, December 1981

[21] P. A. Gass and J. R. Sambles, "Accurate design of a noncollinear acousto-optic tunable filter," *Optics Letters*, vol. 16, No. 6, pp. 429-431, March 1991

[22] Gooch & Housego, "AO Tunable Filter TF1450-500-3-F2x," *Technical Note TF1450-500-3-F2x*, pp. 1-2, September 2003

5 Low-Coherence Interferometry

This chapter discusses the principles and techniques of low-coherence interferometry in the domain of optical fibre sensors, with an emphasis on the applications to the work described in this thesis. The mathematical description of temporal coherence and the characteristics of a low-coherent light source are used to determine the theoretical output of a Mach-Zehnder interferometer. This leads into an investigation of two processing schemes, spectral and matched path.

5.1 Introduction

Low-coherence interferometry is a well recognized phenomenon in optics [1]-[3]. Low-coherence optical fibre interferometric sensors allow very high resolution measurements, such as displacement, strain, vibration, temperature, pressure and refractive index [4]-[8]. Low-coherence interferometry provides a channelled output spectrum that carries accurate and unambiguous information of the optical path imbalance, which can be observed through interferometric fringe pattern analysis using either spectral or phase domain processing. Because the information on the path imbalance is coded in the frequency and phase of the light, it is undisturbed by varying power losses.

5.2 Non-Monochromatic Light

The analytical representation of a non-monochromatic or broad-band light signal is given by [2][3]

$$u(t)=2\int_{0}^{\infty}U(\nu)e^{-j2\pi\nu t}d\nu \tag{5.1}$$

where ν is the frequency of the light, $U(\nu)$ is the analytical representation of a monochromatic signal and t is time. Equation (5.1) is derived from the real time varying field associated with the light by suppressing the negative frequencies and doubling the amplitudes of the positive frequencies [2][3].

5.3 Coherence

The concept of coherence, the interference phenomena is described in great detail by Born & Wolf [2] and Goodman [3]. Light waves which have a constant phase relationship between them are said to be coherent. The interference phenomenon is the superposition of coherent waves. Temporal coherence is the ability of a light beam to interfere with a delayed version of itself [3].

5.3.1 Interferometry

The temporal coherence concept can be described using an all fibre Mach Zehnder interferometer. Light from a low-coherent or broad-band source is launched into a length of optical fibre. The light is then split into two beams of equal intensity by a 50/50 coupler [9][10]. One arm of the interferometer has a longer optical path than the other. The light is then recombined by a second 50/50 coupler creating a complementary interference signal (see figure 5.1). The theoretical description of the interferometer output begins with determining the time delay of the light travelling through the longer

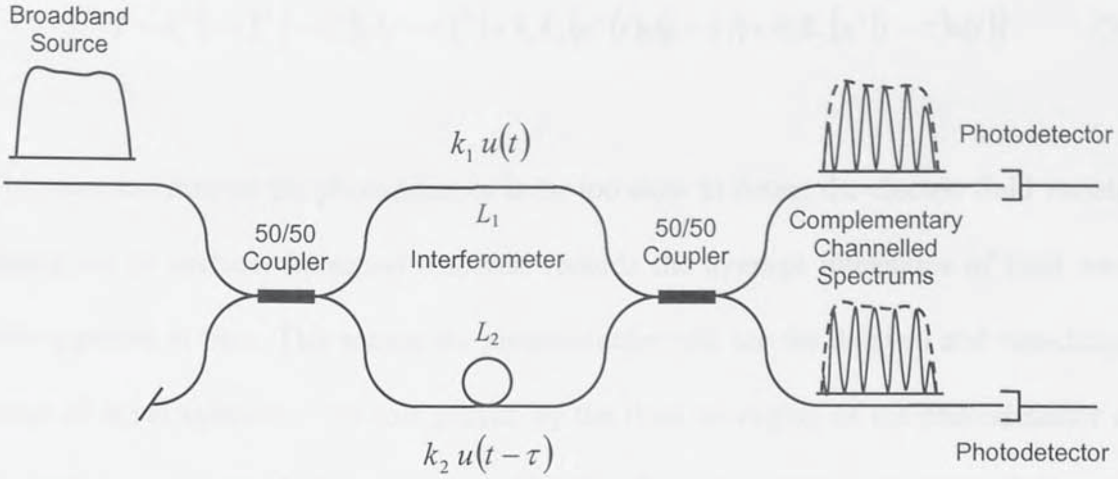

Figure 5.1 Complementary channelled spectrums in an unbalance Mach-Zehnder interferometer.

optical path. For an interferometer with an optical path difference $\delta = n(L_1 - L_2)$, where n is the refractive index of the fibre, L_1 and L_2 are the physical lengths of the two interferometer arms. One of the waves is delayed in time τ given by [2]

$$\tau = \frac{\delta}{c} \tag{5.2}$$

where c is the speed of light in a vacuum. The light intensity incident on the photodetector at the interferometer output is given by [3]

$$I = \left\langle \left| k_1 u(t) + k_2 u(t-\tau) \right|^2 \right\rangle \tag{5.3}$$

where k_1 and k_2 are losses in the two optical paths and $u(t)$ is the analytical signal representation of the non-monochromatic light source. Expanding equation (5.3), gives [3]

$$I = k_1^2\left(|u(t)|^2\right) + k_2^2\left(|u(t-\tau)|^2\right) + k_1k_2\left(u^*(t)u(t-\tau)\right) + k_1k_2\left(u^*(t-\tau)u(t)\right) \qquad (5.4)$$

The response time of the photodetector is far too slow to detect the electric field variation falling on its surface. Its actual response records the average intensities of light waves over a period of time. This means the photodetector will see the delayed and non-delayed beam of equal intensity. The role played by the time averaging of the photodetector can be used to create some special symbols [3]. The first two terms in equation (5.4) can be replaced by the notation [3]

$$I_0 = \left(|u(t)|^2\right) = \left(|u(t-\tau)|^2\right) \qquad (5.5)$$

and the last two terms replaced by the notation [3]

$$\Gamma(\tau) = \left(u^*(t)u(t-\tau)\right) \qquad (5.6)$$

where I_0 is the mean signal level and $\Gamma(\tau)$ is the autocorrelation function [3] of the analytical signal $u(t)$ known as the self coherence function. If there is no time delay between the two waves, then the self coherence function $\Gamma(0)$ is equal to I_0. Using the abbreviated notation of equations (5.5) and (5.6) the intensity at the detector can be rewritten as [3]

$$I = \left(k_1^2 + k_2^2\right)I_0 + 2k_1k_2\,\mathrm{Re}\left(\Gamma(\tau)\right) \qquad (5.7)$$

where $\mathrm{Re}(\Gamma(\tau))$ is the real part of the self coherence function. It is convenient to work with a normalised version of the self coherence function. Normalising to the quantity $\Gamma(0) = I_0$ [3], gives

$$g(\tau) = \frac{\Gamma(\tau)}{\Gamma(0)} \tag{5.8}$$

where $g(\tau)$ is known as the complex degree of coherence of the light [3]. The complex degree of coherence can also be expressed in the following general form [3], which mathematically describes the shape of the interferogram

$$g(\tau) = \gamma(\tau)\exp(-j\,\Delta\phi) \tag{5.9}$$

where $\gamma(\tau)$ is a function related to the power spectral density of the source and $\Delta\phi$ is the phase difference $(\phi_1 - \phi_2)$ between the light in the two interferometer arms, given by

$$\Delta\phi = \frac{2\pi}{\lambda}\delta \tag{5.10}$$

where δ is the optical path difference and λ the source wavelength. The intensity at the detector can be now be rewritten as

$$I = \left(k_1^2 + k_2^2\right)I_0 + 2k_1k_2\,\mathrm{Re}(g(\tau)I_0) \tag{5.11}$$

Solving equation (5.11) for the real part of the complex degree of coherence the intensity at the detector and rearranging, gives [3]

$$I = \left(k_1^2 + k_2^2\right)I_0\left(1 + \frac{2k_1k_2}{k_1^2 + k_2^2}\gamma(\tau)\cos\Delta\phi\right) \tag{5.12}$$

The depth of the cosine fringe pattern or the fringe visibility V for a given optical path difference is defined by [2][3]

$$V = \frac{I_{\max} - I_{\min}}{I_{\max} + I_{\min}} \tag{5.13}$$

where $I_{\max}$ and $I_{\min}$ are the maximum and minimum intensities of the cosine fringes respectively. The fringe visibility from equation (5.12) for equal optical path losses i.e. when $\left(k_1 = k_2 = k\right)$ is given by [3]

$$V = \gamma(\tau) \tag{5.14}$$

And for unequal losses the visibility where $\left(k_1 \neq k_2\right)$ is given by [2][3]

$$V = \frac{2k_1k_2}{k_1^2 + k_2^2}\gamma(\tau) \tag{5.15}$$

showing that the output intensity and visibility of the interferometer arising from the superposition of two beams of light originating from the same source is determined by the intensity of each beam, the visibility of the fringes and the real part of the complex degree of coherence. However, significant losses in the fringe visibility can also occur from fluctuations in the state of polarisation of the interfering beams. These losses are discussed in the next section.

5.3.2 Polarisation-Induced Phase Noise

The birefringence in single mode fibre and fibre components used to construct interferometers causes fluctuations in the state of polarisation of the interfering beams caused by variations in temperature or the position of the fibre. This can dramatically affect the visibility of the fringes and is commonly known as polarised induced signal fading [11][12]. In general, polarised induced fading occurs from polarisation wandering in the two interferometer arms and that in the input fibre to the interferometer [13]-[16]. There have been several schemes designed to overcome this effect, including manual or

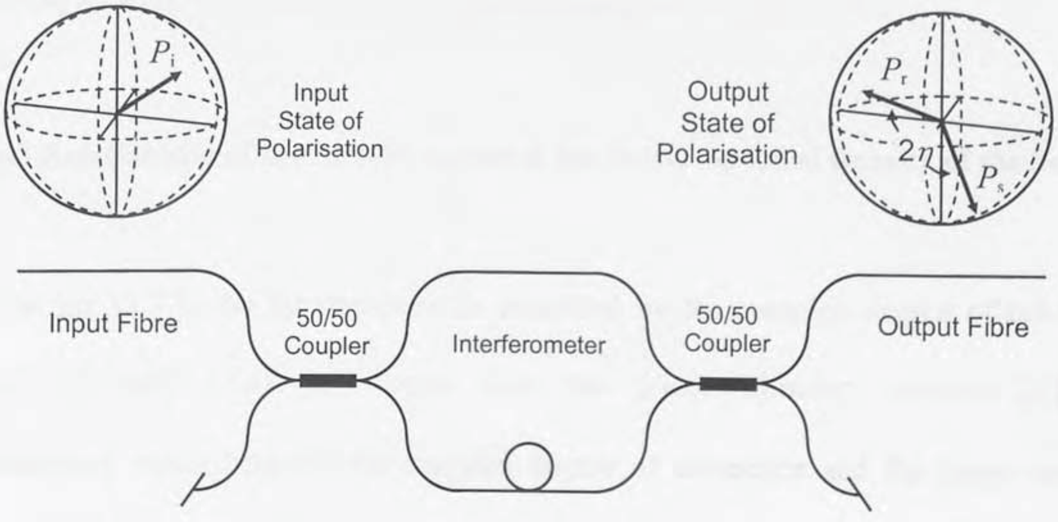

Figure 5.2 Poincaré sphere representation of the state of polarisation through a Mach-Zehnder interferometer.

automatic polarisation controllers in the arms of the interferometer [17][18], input polarisation control [19][20] and output polarisation control [21][22]. Figure 5.2 shows the schematic of a Mach-Zehnder interferometer and the Poincaré sphere representation [23] of the state of polarisations of the light in the input fibre P_i, in the sensing arm P_s and the reference arm P_r. The angle 2η defines the polarisation matching of the sensing and reference beams which is dependent on the net polarisation evolution in the interferometer arms and the input polarisation state. The output fringe visibility can therefore now be more accurately defined by [16]

$$V = V_0 \cos \eta \tag{5.16}$$

where V_0 is either $V_0 = \gamma(\tau)$ for equal optical path losses or $V_0 = 2k_1k_2/k_1^2 + k_2^2 \ \gamma(\tau)$ for unequal optical path losses, as defined by equations (5.14) and (5.15). Detailed analysis of the polarisation effects in two beam interferometers can be found in the work of Born & Wolf [2], Kersey *et al* [14] and Dandridge *et al* [16].

5.3.3 Relationship of the Interferogram to the Power Spectral Density of the Source

In section (5.3.1) the interferogram is described by the complex degree of coherence $g(\tau) = \gamma(\tau)\exp(-j\Delta\phi)$. As known from the Wiener-Khinchin theorem [2][3], a relationship exists between the complex degree of coherence and the power spectral density of the source. Spectral analysis of radiation emitted by spontaneous emission from level $2 \rightarrow 1$ transitions shows that it occupies a finite spectral width. The distribution of emitted intensity verses frequency is referred to as the lineshape function of the transition $2 \rightarrow 1$. The same lineshape function also applies to stimulated emission and absorption.

Homogeneous broadening: All atoms in the emission process are assumed to be identical and have the same lineshape and frequency response. Lifetime and collision broadening are two examples of homogeneous broadening which results in a Lorentzian power spectral density. Lifetime broadening is caused by a natural spread in the energy of transitions between energy levels in individual atoms causing a natural linewidth. Collision broadening is caused by atoms colliding in gases or atoms in a solid lattice interacting with phonons.

Inhomogeneous broadening: Different atoms or groups of atoms exhibit slightly different resonance frequencies for the same transition. Examples of inhomogeneous broadening are Doppler and imperfection broadening which results in a Gaussian power spectral density. Doppler broadening is due to the distribution of atomic velocities which have been Doppler shifted, individual atoms travel at different velocities and thus interact with different frequencies. Crystal lattice imperfections and strain fields also produce inhomogeneous broadening.

The interferogram envelope $\gamma(\tau)$ for a light source with a Lorentzian power spectral density is given by [3]

$$\gamma(\tau) = \exp(-\pi\Delta\nu|\tau|) \tag{5.17}$$

The interferogram envelope $\gamma(\tau)$ for a light source with a Gaussian power spectral density is given by [3]

$$\gamma(\tau) = \exp\left(-\left(\frac{\pi\Delta\nu\tau}{2\sqrt{\ln 2}}\right)^2\right) \tag{5.18}$$

and for a source with a rectangular power spectral density the interferogram envelope is given by the equation [3]

$$\gamma(\tau) = \left|\mathrm{sinc}\Delta\nu\tau\right| \tag{5.19}$$

The relationship between the interferogram envelope $\gamma(\tau)$ and the function $\Delta\nu\tau$ is depicted in figure 5.3.

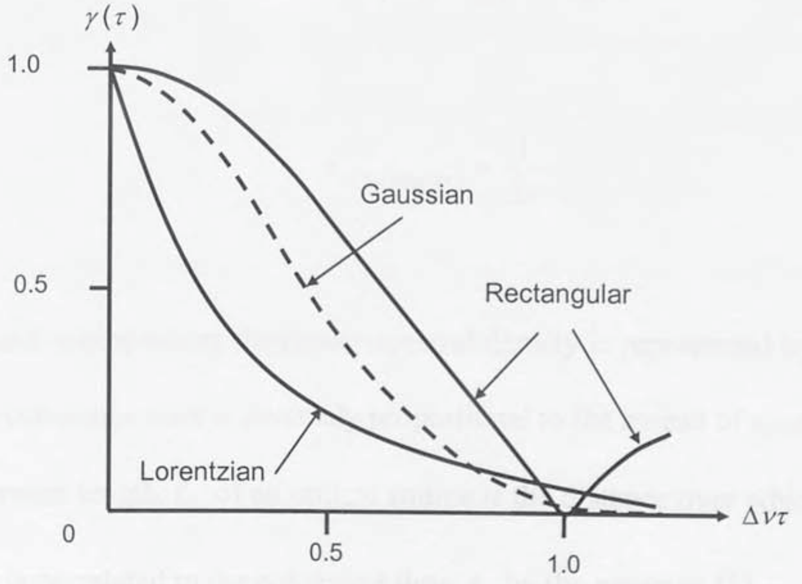

Figure 5.3 Normalised interferogram envelope $\gamma(\tau)$ verses $\Delta\nu\tau$ for the Lorentzian, Guassian and rectangular power spectral densities.

5.3.4 Coherence Time and Coherence Length

The coherence time of the source τ_c in relation to the complex degree of coherence is given by [3]

$$\tau_c = \int_{-\infty}^{\infty} |g(\tau)|^2 \, d\tau \tag{5.20}$$

solving for the Lorentzian, Gaussian and rectangular envelopes gives [3]

$$\tau_{c(\mathrm{Lorentzian})} = \frac{1}{\pi \Delta \nu} = \frac{0.318}{\Delta \nu} \tag{5.21}$$

$$\tau_{c(Gaussian)} = \sqrt{\frac{2 \ln 2}{\pi}} \frac{1}{\Delta \nu} = \frac{0.664}{\Delta \nu} \tag{5.22}$$

$$\tau_{c(Rectangular)} = \frac{1}{\Delta \nu} \tag{5.23}$$

For a broadband source where the power spectral density is represented by a rectangular envelope, the coherence time is inversely proportional to the spread of source frequencies $\Delta \nu$. The coherence length L_c of an optical source is the distance over which the phase of a light source is correlated to the coherence time τ_c by the equation [1]

$$L_c = c\tau_c \tag{5.24}$$

The source coherence length with respect to the wavelength is found by differentiating the magnitude of the source frequency $\nu = |c/\lambda|$, which gives $\Delta\nu/\Delta\lambda = c/\lambda^2$. Since, $\tau_c = 1/\Delta\nu$ and $L_c = c\tau_c$, the coherence length of a broadband light source is given by [1]

$$L_c = \frac{\lambda^2}{\Delta\lambda} \tag{5.25}$$

The broadband light source used for the experimental work described in this thesis having a central wavelength of 1545 nm and a linewidth of 33 nm, has a coherence length of approximately 72 um.

5.4 Spectral Domain Processing

An optical spectrum analyser can be used to inspect the interferometer output. For a fixed optical path difference δ the output spectral pattern seen on an optical spectrum analyser is the convolution of the optical source power spectrum and the periodic interference fringes (see figure 5.4). The total number and periodicity of the cosine fringes will depend upon the interferometer optical path difference δ, the source coherence length L and the central wavelength of the source λ. The number of fringes N is given by [24]

$$N = \frac{\delta}{L_c} \tag{5.26}$$

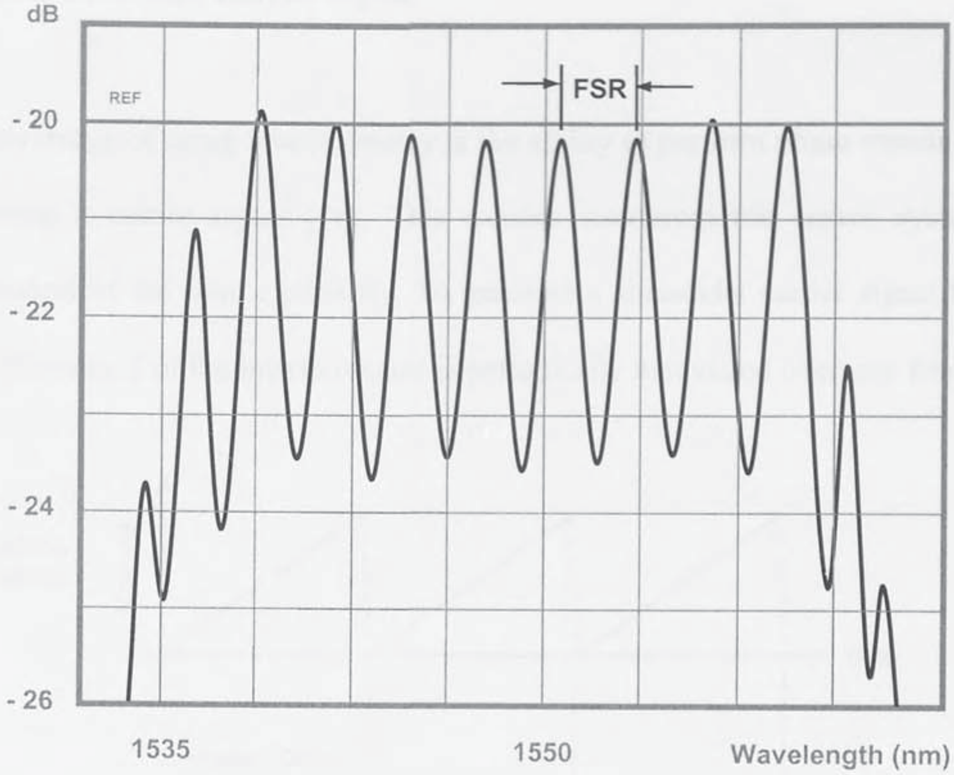

Figure 5.4 Channelled spectrum as seen on an optical spectrum analyser.

Fringe peaks occur when the phase difference $\Delta\phi$ is equal to an integer multiple of 2π. The wavelength difference between adjacent fringes is called the free spectral range (FSR) of the interferometer, given by [24]

$$FSR = \frac{\lambda^2}{\delta} \tag{5.27}$$

Therefore any change in the optical path difference caused by a measurand alters the free spectral range of the channelled spectrum. This has been successfully used by a number of fibre optic sensor interrogation schemes [25]-[27].

5.5 Phase Generated Carrier Signal

One advantage of using interferometry is the ability to perform phase measurements by generating a carrier signal [16]. This enables interferometric sensor systems to be independent of the source intensity. To generate a sinusoidal carrier signal the optical path difference δ of the interferometer is periodically modulated over one fringe using a sawtooth or serrodyne waveform. The physical path difference due to this modulation is denoted by $\delta = \delta + \delta_1 t$ as a function of time t during one period. Hence, the output intensity of the interferometer from equations (5.10) and (5.12), is given by

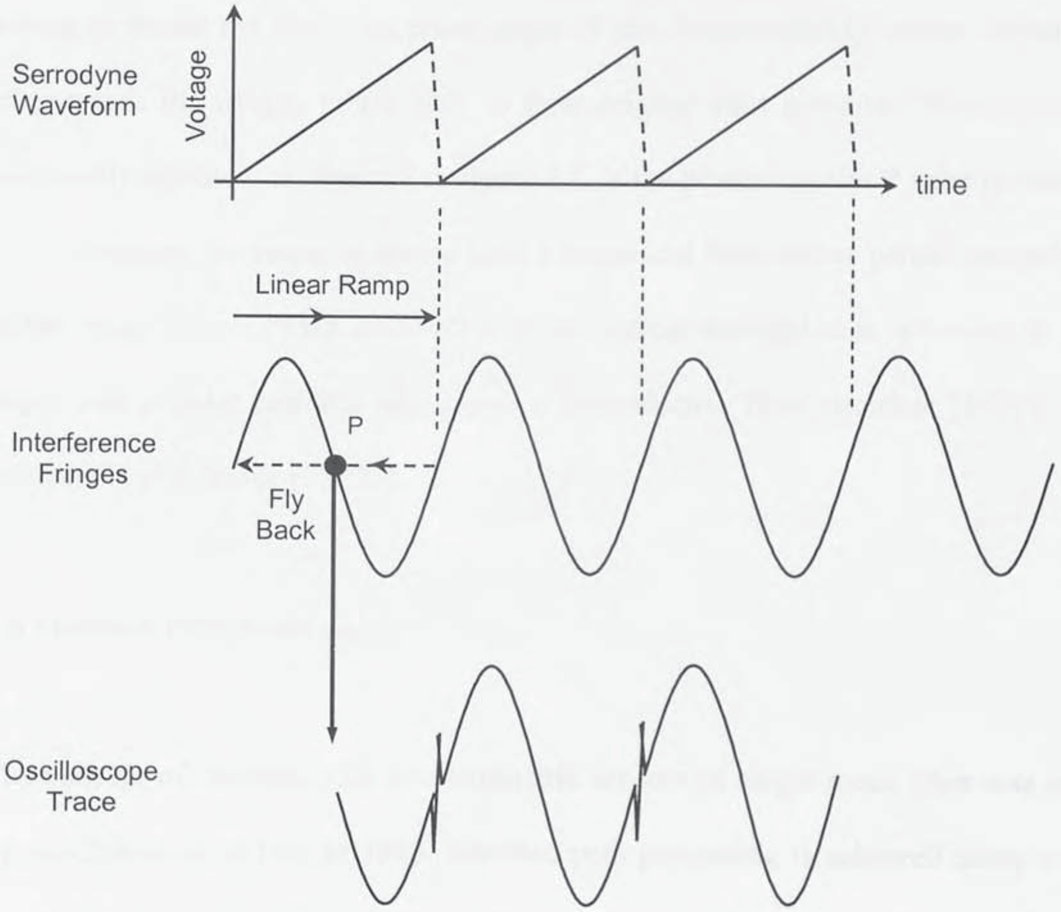

Figure 5.5 Periodically modulating the fringes using a serrodyne waveform.

$$I = \left(k_1^2 + k_2^2\right) I_0 \left[1 + V \cos \frac{2\pi n}{\lambda}\left(\delta + \delta_1 t\right)\right] \tag{5.28}$$

As the linear ramp of the sawtooth waveform is increased the optical path difference of the interferometer increases and the phase angle of the interference fringes change. If the linear ramp is extended to match a phase angle equal to 2π then the positions of the fringes traverse and effectively occupy neighbouring fringe locations. As the linear ramp returns to repeat the cycle the phase angle of the fringes quickly returns to zero or in other words the fringes return back to their original start position. This cycle is then continually repeated, as depicted in figure 5.5. If the power at point P were monitored on an oscilloscope, the response would have a sinusoidal form whose period is equal to that of the ramp signal. Phase modulation of an optical waveguide is achieved in various ways: two popular methods are to use a piezoelectric fibre stretcher [28]-[31] or an integrated optic device [32][33].

5.6 Matched Path Processing

The concept of matched path interferometric sensors in single mode fibre was reported by Al-Chalabi *et al* [34] in 1983. Matched path processing is achieved using a second processing interferometer, creating four optical paths through the system [35][36], see figure 5.6. By configuring paths (1) and (2) so that they are closely matched within a fraction of the source coherence length L_c, interference occurs at the output. The phase and fringe visibility will be a function of the difference between the two optical paths. To overcome unwanted coherent mixing from the other optical paths through the system, the optical path differences (δ_1 and δ_2) of the two interferometers are made much larger

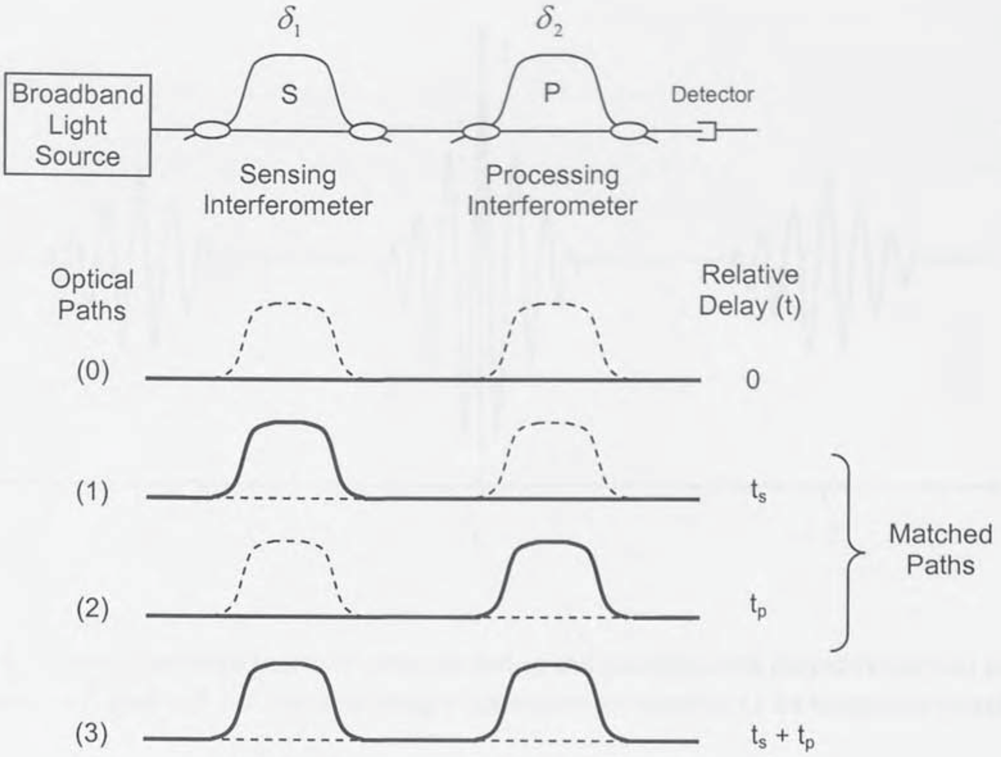

Figure 5.6 Matched path differential interferometry.

than the coherence length of the source such that no interference is observed at the output. The transfer function of tandem interferometers is given by [24][37]

$$I = \left(k_1^2 + k_2^2\right)I_0\left[1 + V\cos\left(\frac{2\pi}{\lambda}\left(\delta_1 - \delta_2\right)\right)\right] \tag{5.29}$$

For the case where a Mach-Zehnder interferometer with a scanning air gap in one arm is used as the processing interferometer, the optical path difference can be made both positive and negative ($+\delta$ and $-\delta$) relative to its balanced position. Therefore, two positions of the scanning air gap exist at which the path imbalance matches that of the sensing interferometer as depicted in figure 5.7. Also shown in figure 5.7 are the fringes as the scanning interferometer passes through its balanced region. However, only the two

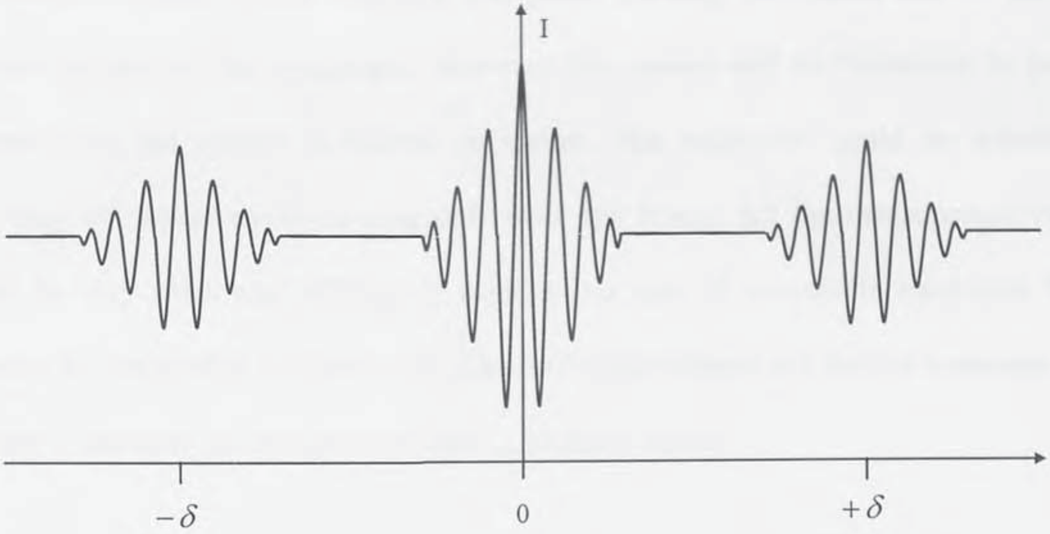

Figure 5.7 Low-coherence interferogram showing the positive and negative optical path difference ($-\delta$ and $+\delta$) of the scanning interferometer relative to its balanced position.

side fringe profiles at $\pm\delta$ contain phase information of the sensing interferometer cavity. The optical path difference of the sensing interferometer can therefore be tracked by scanning the central fringe position by monitoring the displacement of the processing interferometer. However, the very small intensity differences between the central and its adjacent fringes can make identification of the peak fringe very difficult and time consuming. This has largely been resolved using source-synthesising techniques [38]-[40] however the speed of identification still remains relatively slow because of the scanning speed of the processing interferometer due to mechanical constrictions inherent in the equipment.

5.6.1 Fringe Order Ambiguity

Fringe order ambiguity results when the operational range of the measurand induced phase change exceeds 2π. An ambiguity will exist when measurements are to be made over several fringes. Fringe counting and phase tracking techniques can be used to monitor the state of the measurand. However, the system will be vulnerable to power failures since the system is historic in nature. The ambiguity could be solved by restricting the sensor cavity to scan only over one fringe, but the measurement range would be very small and difficult to achieve any sort of reasonable resolution from scanning the processing interferometer. The method developed and used to overcome this problem is the dual-wavelength technique as outlined below.

5.6.2 Dual-Wavelength Technique

The dual-wavelength technique allows differential phase measurements between two closely matched wavelengths λ_1 and λ_2. The sensing range is considerably increased because the optical path difference can be adjusted over number of fringes before they eventually differ by 2π, the principle of which is shown in figure 5.8. The distance over which they differ by 2π is called the unambiguous range δ_u (see appendix M) given by [24]

$$\delta_u = \frac{\lambda_1 \lambda_2}{\lambda_2 - \lambda_1} \tag{5.30}$$

As an example two sources with central wavelengths of $\lambda_1 = 1540$ nm and $\lambda_2 = 1550$ nm give a unambiguous range of approximately 0.25 mm. However, the problem of the

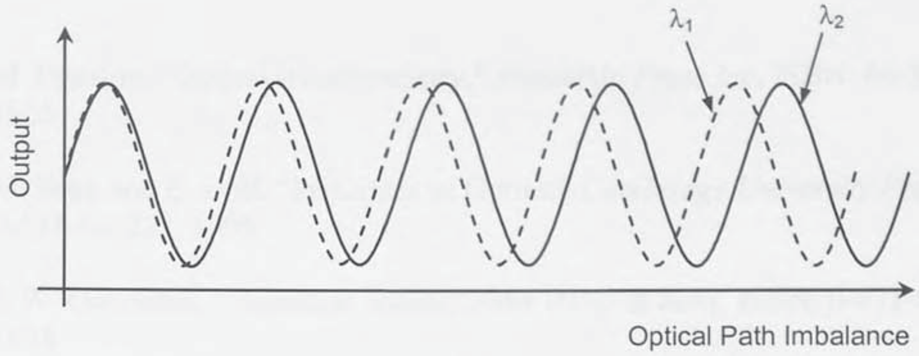

Figure 5.8 Interferometric output response with the dual wavelength technique.

scanning speed is still restricted to the mechanical limitations of the processing interferometer. The method used to resolve this problem is by generating a phase carrier [41][42] in the processing interferometer and monitoring the phase difference between the two wavelengths.

5.7 Conclusion

This chapter has introduced the concepts of low-coherent interferometry using a mathematical description of a Mach-Zehnder interferometer including the importance of controlling the polarisation, the relationship of the interferogram to the power spectral density of the source, the coherence time and coherence length. Two processing schemes have been described (spectral and matched path) which serve as a reference for the experimental work described in succeeding chapters.

5.8 References

[1] M. Françon, "Optical interferometry," *Academic Press Inc*, ISBN: 66-28312, 1966

[2] M. Born and E. wolf, "Principles of Optics," *Cambridge University Press*, ISBN: 0-521-642221, 1999

[3] J. W. Goodman, "Statistical optics," *John Wiley & Sons*, ISBN: 0-471-015024, 1985

[4] G. Brady, K. Kalli, D. J. Webb, D. A. Jackson, L. Reekie and J. L. Archambault, "Simultaneous interrogation of interferometric and Bragg grating sensors," *Optics Letters*, vol. 20, No. 11, pp. 1340-1342, June 1995

[5] H. S. Choi, H. F. Taylor and C. E. Lee, "High performance fibre optic temperature sensor using low coherence interferometry," *Optics Letters*, vol. 22, No. 23, pp. 1814-1816, December 1997

[6] P. M. Nellen, H. Pierhofer, R. Bronnimann and U. Sennhauser, "Absolute strain measurements with multiplexed low coherence demodulated fibre Fabry Pérot sensor structures," *in Proceedings 10th International Conference on Optical Fibre Sensors*, (OFS-10, Glasgow, United Kingdom), Technical Digest, pp. 518-521, October 1994

[7] Y. J. Rao and D. A. Jackson, "A prototype fibre optic based Fizeau medical pressure and temperature sensor system using coherence reading," *Measurement Science and Technology*, vol. 5, pp. 741-746, 1994

[8] D. Trouchet, F. X. Desforges, O. Graindorge and H. C. Lefevre, "Remote fibre optic measurement of air index with white light interferometry," *in Proceedings 8th International Conference on Optical Fibre Sensors*, (OFS-8, Monterey, USA), Technical Digest, pp. 57-60, January 1992

[9] D. C. Johnson, K. O. Hill, F. Bilodeau and S. Faucher, "New design concept for a narrowband wavelength selective optical tap and combiner," *Electronics Letters*, vol. 23, No. 13, pp. 668-669, June 1987

[10] J. Noda and I. Yokohama, "Fiber devices for fiber sensors," *in Proceedings 5st International Conference on Optical Fibre Sensors*, (OFS-5, New Orleans, USA), Technical Digest, pp. 468-471, January 1988

[11] S. K. Sheen and T. G. Giallorenzi, "Polarization effects on single mode optical fibre sensors," *Applied Physics Letters*, vol. 35, No. 12, pp. 914-917, December 1979

[12] D. W. Stowe, D. R. Moore and R. G. Priest, "Polarisation fading in fibre interferometric sensors," *Journal of Quantum Electronics*, vol. QE-18, No. 10, pp. 1644-1646, October 1982

[13] R. Ulrich and A. Simon, "Polarization optics of twisted single mode fibers," *Applied Optics*, vol. 18, No. 13, pp. 2241-2251, July 1979

[14] A. D. Kersey, A. Dandridge and A. B. Tveten, "Dependence of visibility on input polarisation in interferometric fibre optic sensors," *Optics Letters*, vol. 13, No. 4, pp. 288-290, April 1988

[15] A. D. Kersey, M. J. Marrone and A. Dandridge, "Observations of input polarisation induced phase noise in interferometric fiber optic sensors," *Optics Letters*, vol. 13, No. 10, pp. 847-849, October 1988

[16] A. Dandridge and A. D. Kersey, "Overview of Mach Zehnder sensor technology and applications," *in Proceedings SPIE Fibre Optic and Laser Sensors VI*, vol. 985, pp. 34-52, September 1988

[17] R. Ulrich, "Polarization stabilization on single mode fiber," *Applied Physics Letters*, vol. 35, No. 11, pp. 840-842, December 1979

[18] T. Okoshi, "Polarization state control schemes for heterodyne or homodyne optical fiber communications," *Journal of Lightwave Technology*, vol. LT-3, No. 6, pp. 1232-1237, December 1985

[19] K. H. Wanser and N. H. Safar, "Remote polarization control for fiber optic interferometers," *Optics Letters*, vol. 12, No. 3, pp. 217-219, March 1987

[20] A. D. Kersey, A. Dandridge and A. B. Tveten, "Elimination of polarization induced signal fading in interferometric fiber sensors using input polarization control," *in Proceedings 5st International Conference on Optical Fibre Sensors*, (OFS-5, New Orleans, USA), Technical Digest, pp. 44-47, January 1988

[21] N. J. Frigo, A. Dandridge and A. B. Tveten, "Technique for the elimination of polarisation fading in fiber interferometers," *Electronics Letters*, vol. 20, No. 8, pp. 319-320, April 1984

[22] C. K. Kirkendall and A. Dandridge, "Polarization induced phase noise in fiber optic interferometers with polarizer based polarization diversity receivers," *in Proceedings 15st International Conference on Optical Fibre Sensors*, (OFS-15, Portland, USA), Technical Digest, pp. 375-378, May 2002

[23] M. Johnson, "Poincare sphere representation of birefringent networks," *Applied Optics*, vol. 20, No. 12, pp. 2075-2080, June 1981

[24] K. V. T. Grattan and B. T. Meggitt, "Optical fibre sensor technology," *Chapman & Hall*, ISBN: 0-412-59210-X, 1995

[25] S. R. Taplin, A. G. Podoleanu, D. J. Webb an D. A. Jackson, "Displacement sensor using channelled spectrum dispersed on a linear CCD array," *Electronics Letters*, vol. 29, No. 10, pp. 896-897, May 1993

[26] M. T. Velluet, Ph. Graingorge, H. J. Arditty, "Fibre optic pressure sensor using white light interferometry," *in Proceedings SPIE Fibre Optic Sensors V*, vol. 838, pp. 78-83, August 1987

[27] J. C. Harl, E. W. Saaski, G. L. Mitchell, "Fibre optic temperature sensor using spectral modulation," *in Proceedings SPIE Fibre Optic Sensors V*, vol. 838, pp. 257-261, August 1987

[28] D. E. N. Davis and S. A. Kinsley, "Method of phase modulating signals in optical fibres: applications to optical telemetry systems," *Electronics Letters*, vol. 10, No. 2, pp. 21-22, January 1974

[29] S. A. Kinsley, "Optical fibre phase modulator," *Electronics Letters*, vol. 11, No. 19, pp. 453-454, September 1975

[30] D. A. Jackson, R. G. Priest, A. D. Dandridge and A. B. Tveten, "Elimination of drift in single mode optical fibre interferometer using a piezoelectrically stretched coiled fiber," *Applied Optics*, vol. 19, No. 17, pp. 2926-2929, September 1980

[31] J. Dakin and B. Culshaw, "Optical fiber sensors: principles and components," *Artech House*, ISBN: 0-89006-317-6, 1988

[32] C. Laskoskie, H. Hung and C. L. Chang, "Theory and experiment on opticl phase modulator for serrodyne modulation," *in Proceedings SPIE Fibre Optic Sensors V*, vol. 838, pp. 152-159, August 1987

[33] E. L. Wooten, K. M. Kissa, A. Yi-Yan, E. J. Murphy, D. A. Lafaw, P. F. Hallemeier, D. Maack, D. V. Attanasio, D. J. Fritz, G. J. McBrien and D. E. Bossi, "A review of lithium niobate modulators for fiber optic communications systems," *Journal of Selected Topics in Quantum Electronics*, vol. 6, No. 1, pp. 69-82, February 2000

[34] S. A. Al-Chalabi, B. Culshaw and D. E. N. Davies, "Partially coherent sources in interferometry," *in Proceedings 1st International Conference on Optical Fibre Sensors*, (OFS-1, London, United Kingdom), Technical Digest, pp. 132-136, April 1983

[35] J. L. Brooks, R. H. Wentworth, R. C. Youngquist, M. Tur, B. Y. Kim and H. Shaw, "Coherence multiplexing of fiber optic interferometric sensors," *Journal of Lightwave Technology*, vol. LT-3, No. 5, pp. 1062-1072, October 1985

[36] H. C. Lefevre, "White light interferometry in optical fibre sensors," *in Proceedings 7th International Conference on Optical Fibre Sensors*, (OFS-7, Sydney, Australia), Technical Digest, pp. 345-351, December 1990

[37] Y. J. Rao and D. A. Jackson, "Recent progress in fibre optic low coherence interferometry," *Measurement Science and Technology*, vol. 7, pp. 981-999, 1996

[38] Y. J. Rao, Y. N. Ning and D. A. Jackson, "Synthesised source for white light sensing systems," *Optic Letters*, vol. 18, No. 6, pp. 462-464, March 1993

[39] S. Chen, K. T. V. Grattan, B. T. Meggitt and A. W. Palmer, "Instantaneous fringe order identification using dual broadband sources with widely spaced wavelengths," *Electronics Letters*, vol. 29, No. 4, pp. 334-335, February 1993

[40] Y. J. Rao and D. A. Jackson, "Improved synthesised source for white light interferometry," *Electronics Letters*, vol. 30, No. 17, pp. 1440-1441, August 1994

[41] D. A. Jackson, A. D. Kersey, A. D. Corke and J. D. C. Jones, "Pseudo heterodyne detection scheme for optical interferometers," *Electronics Letters*, vol. 18, No. 25, pp. 1081-1082, December 1982

[42] A. D. Kersey and A. Dandridge, "Dual wavelength approach to interferometric sensing," *in Proceedings SPIE; Fiber Optic Sensors II*, vol. 798, pp. 178-181, 1987

6 Fibre Bragg Grating Sensor Interrogation using an Arrayed Waveguide Grating

This is the first of the four experimental chapters and describes the use of an arrayed waveguide grating (AWG) to interrogate static and dynamic strains using fibre Bragg grating (FBG) sensors. Three methods are discussed: the first technique makes use of the wavelength dependent transmission profile of an AWG channel passband, the second approach uses a wide bandwidth or a chirped grating larger than the channel spacing of the AWG, monitoring the intensity present in several neighbouring AWG channels and the third and final method utilises a heterodyne approach based on interferometric wavelength shift detection.

6.1 Introduction

AWGs offer an excellent solution for simultaneously interrogating static and dynamic strains in FBG sensors, as will be demonstrated in this chapter. Since AWGs were first proposed as FBG sensor interrogating units by Sano *et al* [1][2] and Webb *et al* [3] in the early 2000s there has surprisingly been very little published work [4]-[6] on their use. FBGs are considered excellent sensor elements [7] offering strain sensitivities of 1.2 pm/με (see section 2.6). By using "off the shelf" components such as AWGs competitively priced optical sensor interrogation systems could be realised. For all the interrogation schemes described in this chapter the Bookham optical channel monitor (OCM) (described in section 3.3) is used to de-multiplex spectral information recovered from FBG sensors.

6.2 Fibre Bragg Grating Function

The spectral reflectance function for the unapodised fibre Bragg gratings [8] that are used for the work described in this chapter, is given by (see section 2.3)

$$B(\lambda)=\frac{k^2\sinh^2(S\,L)}{\Delta\beta^2\sinh^2(S\,L)+S^2\cosh^2(S\,L)} \tag{6.1}$$

where k is the coupling coefficient, L is the grating length, $\Delta\beta$ is the differential eigenmode propagation, $S=\sqrt{k^2-\Delta\beta^2}$ and $Q=\sqrt{\Delta\beta^2-k^2}$.

6.3 Arrayed Waveguide Grating Function

The spectral transmission function [9] of a AWG channel, as described in section (3.2.1), is given by

$$T_i(\lambda)=\exp\left(-\left(\frac{2\sqrt{\ln 2}}{FWHM_i}(\lambda-\lambda_i)\right)^2\right) \tag{6.2}$$

where $FWHM_i$ is the full width half maximum (FWHM) and λ_i is the central wavelength of the i^{th} AWG channel.

6.4 Wavelength Interrogation

The value of the optical power appearing in each AWG channel from the spectral reflectance of the Bragg grating sensors is obtained by integrating the product of the reflectance function of the gratings $B(\lambda)$, the transmission function of the AWG $T(\lambda)$ and the emission spectrum of the light source $S(\lambda)$. Considering the interrogation of *m* Bragg gratings the output power $P_i(\lambda)$ from the *i*th channel of the AWG is given by

$$P_i(\lambda) = \int_0^{\infty} S(\lambda) \cdot \left(\sum_{k=1}^{m} B_k(\lambda)\; L_k^2(\lambda) \right) \cdot T_i(\lambda) \cdot d\lambda + H_i \qquad (6.3)$$

where L is the wavelength-dependent loss in the fibre and optical components and H is a bias signal independent of the Bragg gratings due to Rayleigh backscattering R in long fibre lengths [2], given by

$$H_i = \int_0^{\infty} S(\lambda) \cdot R \cdot T_i(\lambda) \cdot d\lambda \qquad (6.4)$$

6.5 Simple Fibre Bragg Grating Sensor Interrogation

The simplest technique to interrogate FBG sensors using an AWG makes use of the wavelength response of the AWG channels. If the nominal wavelength of an FBG lies within an AWG passband, any variation in the FBG wavelength produces a related variation in the detected output intensity of the OCM. To show this principle experimentally, broadband light was directed via a coupler to illuminate an FBG sensor

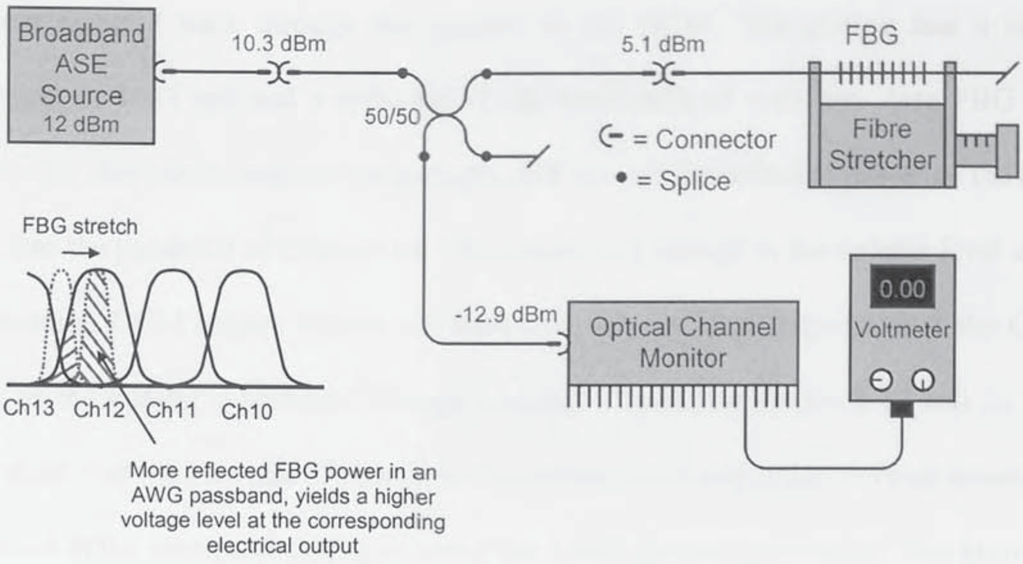

Figure 6.1 Experimental set-up for simple fibre Bragg grating interrogation.

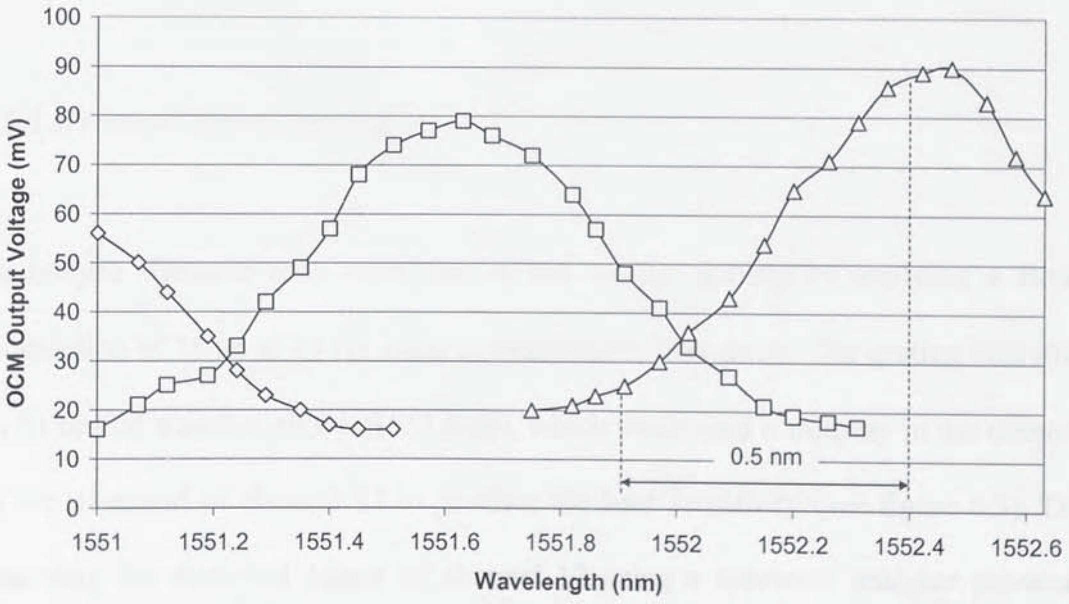

Figure 6.2 Change in the OCM output voltage as an FBG is stretched through channel 13 (diamonds), channel 12 (squares) and channel 11 (triangles).

mounted onto a fibre stretcher, as shown in figure 6.1. The reflected spectrum from the FBG was directed back through the coupler to the OCM. The grating had a centre wavelength of 1551 nm and a reflected -3 dB bandwidth of 0.43 nm (see FBG 1 in appendix E). Any strain-induced wavelength shift moved the reflected power of the FBG further into the passband of channel 13. This results in a change in the voltage level at the corresponding OCM output. Figure 6.2 shows the change in voltage level at the OCM outputs as the grating is stretched through channel 13 and into channels 12 and 11. The results show that the best rate of change in the voltage level and hence the best sensitivity is achieved in the rising and falling edges of the AWG channel passbands. This limits the useable range to less than 0.5 nm, equivalent to around 500 $\mu\varepsilon$. The gradual overall increase in the signal-level with wavelength is due to the non-uniform source spectrum. Figure 6.2 clearly depicts the effect of crosstalk as the FBG passes between adjacent channels. Channel crosstalk is discussed later in section 6.8.

6.5.1 Dynamic Strain Sensing

Homodyne dynamic tests were carried out on the grating by applying a sinusoidal modulation of 15 $\mu\varepsilon$ at 13 Hz using a piezoelectric transducer. The grating was stretched so its central wavelength was 1551.4 nm, which positioned it midway in the steepest part of the passband of channel 12 to produce the best sensitivity (see figure 6.3). Directly analysing the electrical output of channel 12 using a spectrum analyser produced the spectrum of figure 6.4. The peaks in order of increasing frequency are the signal at 13 Hz its first and third harmonics and the 50 Hz mains voltage noise. The noise limited strain

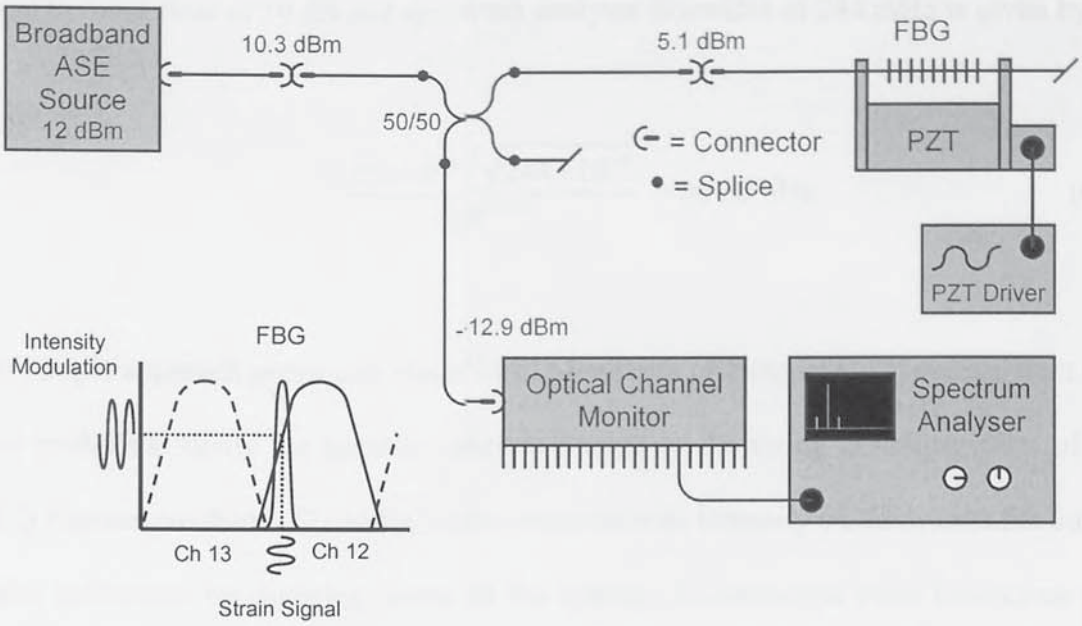

Figure 6.3 Experimental set-up for simple dynamic strain sensing.

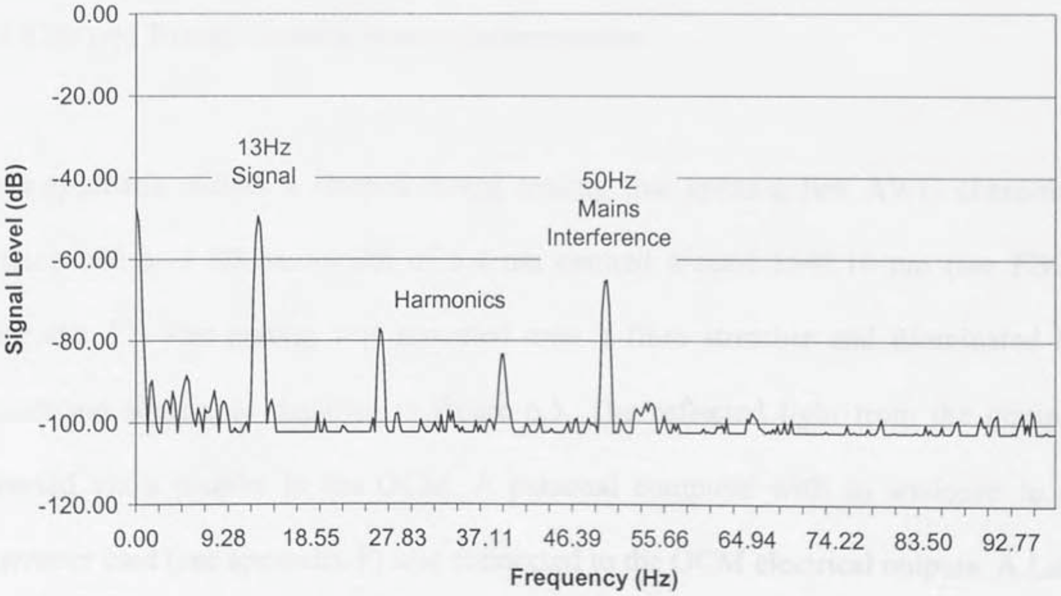

Figure 6.4 Homodyne test results due to a FBG with an applied sinusoidal modulation of 15 $\mu\varepsilon$ at 13 Hz (244 mHz Bandwidth).

amplitude resolution is 96 nε/√Hz. Calculated from the strain modulation of 15 με, the signal to noise ratio of 50 dB and spectrum analyser linewidth of 244 mHz is given by

$$\frac{15\times10^{-6}/\sqrt{244\times10^{-3}}}{10^{50/20}} = 96\ \text{n}\varepsilon/\sqrt{\text{Hz}} \qquad (6.6)$$

This simple approach previously described in the work of Sano *et al* [2] suffers from two main problems: firstly the useable range is limited to the rising or falling parts of the AWG channel passband. Secondly, being essentially an intensity based system the output is also influenced by changing losses in the system. To overcome these limitations two approaches have been investigated: firstly a chirped Bragg grating scanned over several AWG channels and secondly a heterodyne scheme using interferometric wavelength shift detection.

6.6 Chirped Bragg Grating Sensor Interrogation

This approach utilises a chirped Bragg grating that spans a few AWG channels. The grating had a -3 dB bandwidth of 5.4 nm centred around 1548.16 nm (see FBG 2 in appendix E). The grating was mounted onto a fibre stretcher and illuminated by the broadband source, as depicted in figure 6.5. The reflected light from the grating was directed via a coupler to the OCM. A personal computer with an analogue to digital converter card (see appendix F) was connected to the OCM electrical outputs. A Labview program was developed which selectively displayed the voltage level output of the OCM channels numerically and graphically (see appendix G). Figure 6.6 depicts the response

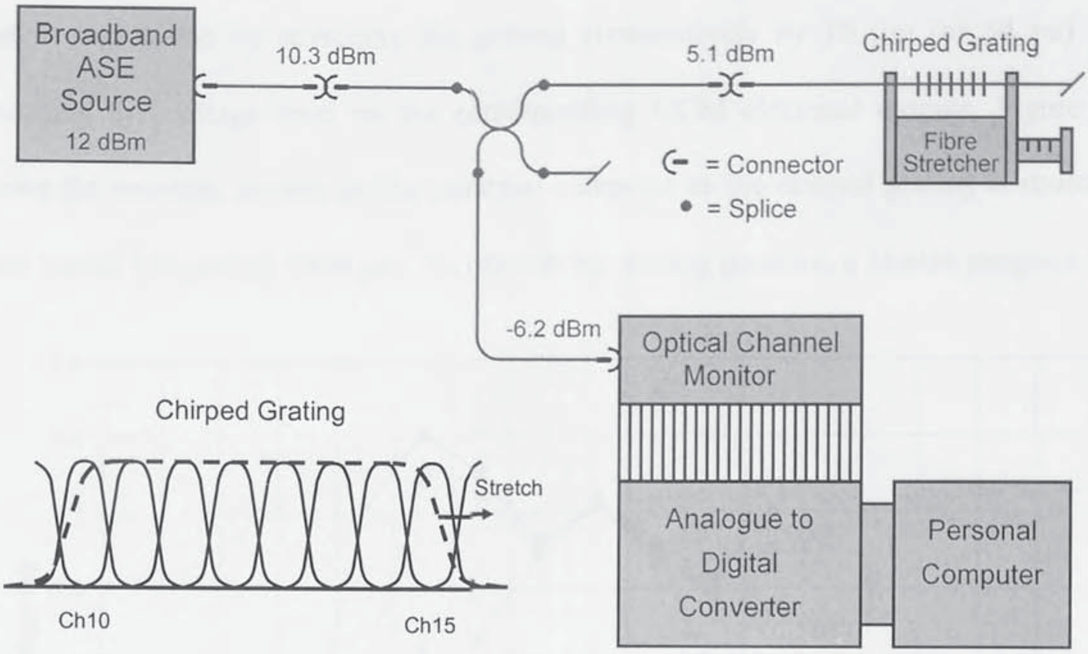

Figure 6.5 Experimental set-up for chirped grating sensor interrogation.

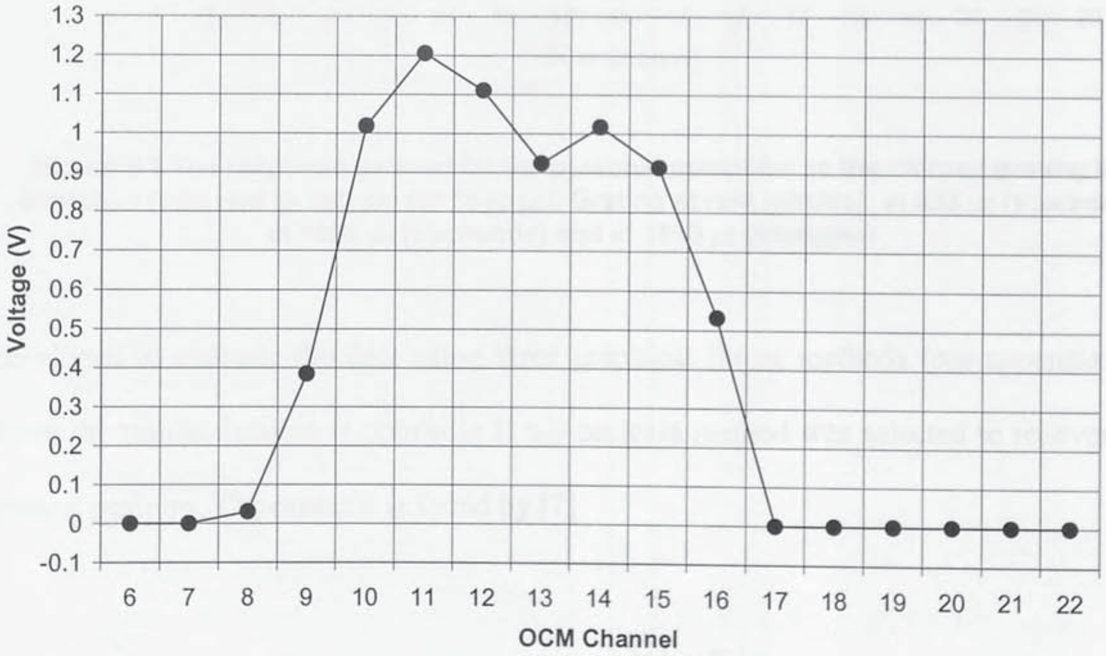

Figure 6.6 Reflected chirped grating response as seen on a personal computer.

of the chirped grating as seen on the personal computer in the absence of any strain. The system was tested by stretching the grating consecutively by 10 μm (or 54 με) and recording the voltage level on the corresponding OCM electrical outputs. Figure 6.7 shows the response as seen on the personal computer as the chirped grating is stretched from rest to 350 μm (or 1890 με). To recover the grating position, a Matlab program was developed to evaluate the data using three graphical fitting methods (see appendix H). From the results detailed in appendix H the centroid method was selected to recover the grating position. The centroid is found by [7]

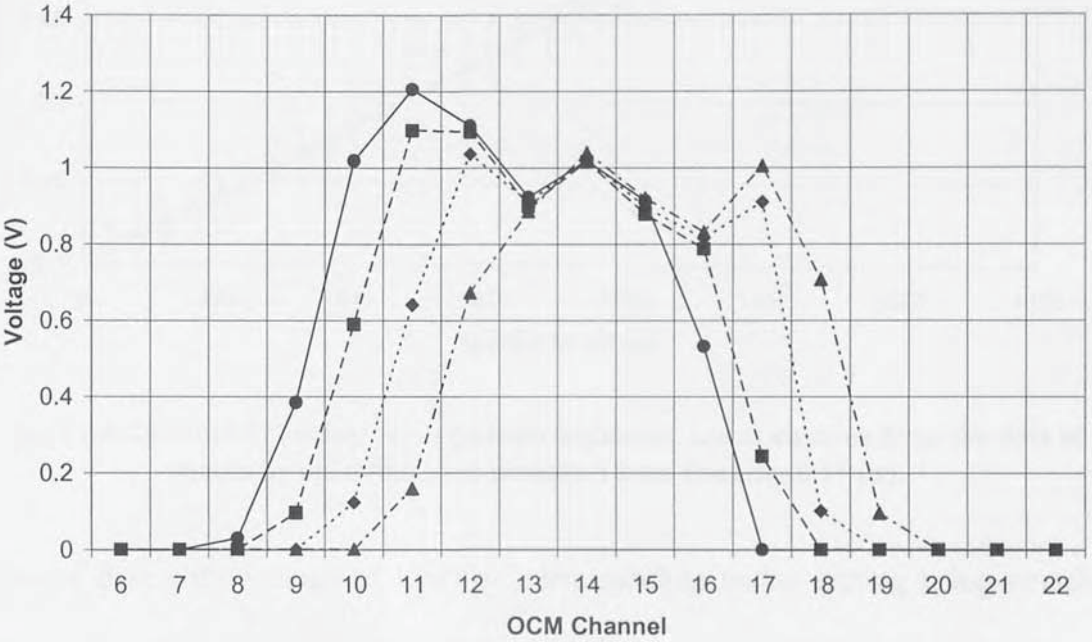

Figure 6.7 The response as seen on the personal computer as the chirped grating is stretched from rest to 350 μm (or 1890 με). Grating at rest (circles), at 630 με (squares), at 1260 με (diamonds) and at 1890 με (triangles).

$$Centroid = \frac{\sum (i \times V_i)}{\sum V_i} \tag{6.7}$$

where i is the sampled OCM channel and V_i is the ith OCM channel voltage level output. The centroid results are shown in figure 6.8 displaying a near linear response of the recovered data with a range of 1890 με corresponding to the grating being stretched through the equivalent of only two AWG channels or 1.6 nm. The range is a considerable improvement over the simple FBG interrogation technique discussed in section (6.5). The resolution for these quasi-static measurements, defined as the root mean squared deviation from linearity [10] is 5.17 με.

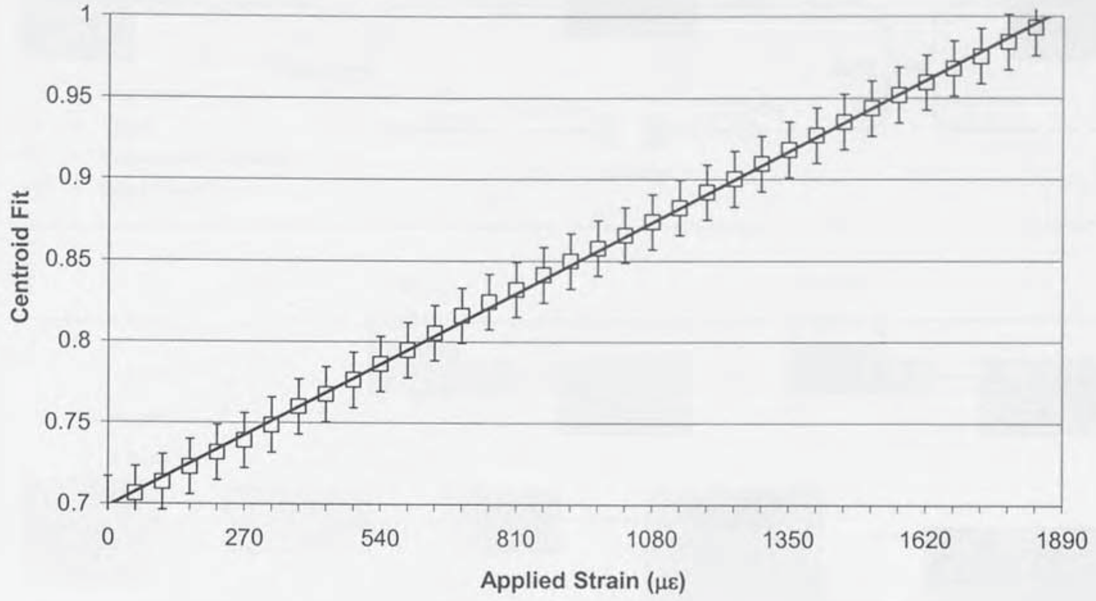

Figure 6.8 Centroid fit verses applied strain (squares). Least squares fit to the data is shown by solid line (rms deviation from linearity 5.17 με).

6.7 Heterodyne Approach

With this approach, the source illuminates an all fibre Mach-Zehnder interferometer (see appendix D) with one arm containing an integrated-optic phase modulator (see appendix F) to which a serrodyne waveform was applied, using a high frequency function

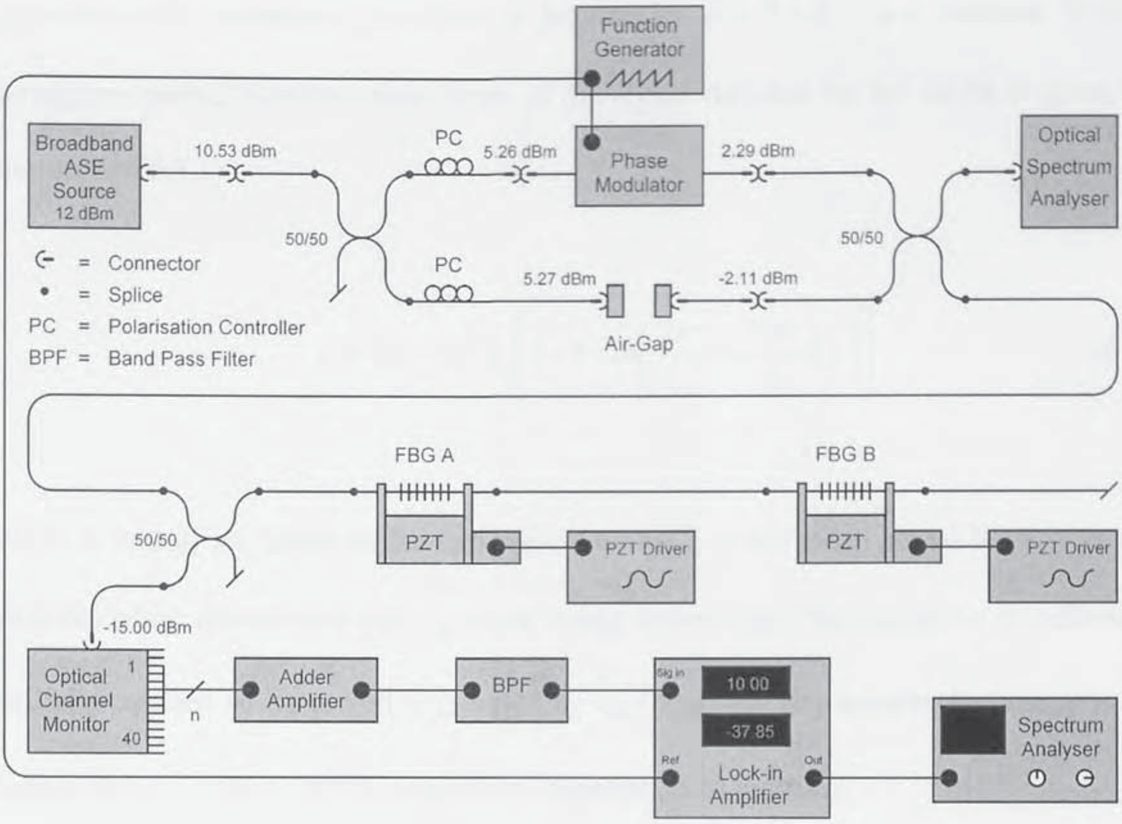

Figure 6.9 Experimental set-up for heterodyne processing.

generator (see appendix F). The optical path difference in the other arm could be adjusted using the air gap, as depicted in figure 6.9. The two polarisation controllers were used to optimise the fringe visibility (see section 5.3.2). Light from the interferometer output was passed through a twin coupler arrangement directing the light to an optical spectrum analyser monitoring the interferometer output and to the FBG sensors. FBG A was mounted onto a piezoelectric fibre stretcher so that dynamic strain signals could be applied. The second FBG (FBG B) had a wavelength several nanometres from the first, so that light reflected from it appeared in an AWG channel some distance away from the reflected spectrum of FBG A. The OCM electrical outputs were connected through an adder circuit, amplifier, bandpass filter, lock-in-amplifier to a spectrum analyser (see appendix F for details of this equipment). If the optical path difference δ due to the application of a serrodyne waveform is denoted by $\delta = \delta + \delta_1 t$ as a function of time during one period, then the phase term of the signal detected by the OCM is given by (see section 5.3.1)

$$I = \left(k_1^2 + k_2^2\right) I_0 \left[1 + V \cos\left(\frac{2\pi}{\lambda_B}\delta + \frac{2\pi}{\lambda_B}\delta_1 \, t\right)\right] \tag{6.8}$$

where k_1 and k_2 are losses in the two optical paths, I_0 is the mean signal level, V is the visibility of the interference and λ_B is the Bragg wavelength. The serrodyne waveform is carefully applied so its period T is equal to λ_B / δ_1 [11]. The angular frequency ω_c is defined by $\omega_c = 2\pi/T$ [12][13] therefore, equation (6.8) becomes

$$I = \left(k_1^2 + k_2^2\right) I_0 \left[1 + V \cos\left(\frac{2\pi}{\lambda_B}\delta + \omega_c \, t\right)\right] \tag{6.9}$$

where $2\pi\,\delta/\lambda_B = \phi_c$ and ω_c are the carrier phase and angular frequency, respectively. If a strain changes the Bragg wavelength of the sensor, then λ_B is given by $\lambda_B = \lambda_B + \Delta\lambda_B$ and the carrier phase term of equation (6.9) becomes

$$\phi_c = \frac{2\pi\,\delta}{\lambda_B + \Delta\lambda_B} \tag{6.10}$$

expanding this equation, gives

$$\phi_c = \left(\frac{2\pi\,\delta}{\lambda_B + \Delta\lambda_B} \frac{\lambda_B - \Delta\lambda_B}{\lambda_B - \Delta\lambda_B} \right) \tag{6.11}$$

and simplifying, gives

$$\phi_c = \frac{2\pi\,\delta\,\lambda_B - 2\pi\,\delta\,\Delta\lambda_B}{\lambda_B^2 - \Delta\lambda_B^2} \tag{6.12}$$

assuming that the value of $\Delta\lambda_B^2$ is much smaller than compared to λ_B^2 so it can be ignored, then the signal detected at the corresponding OCM channel is given by

$$I = \left(k_1^2 + k_2^2\right) I_0 \left[1 + V \cos\left(\omega_c\, t + \left(\frac{2\pi}{\lambda_B}\delta - \frac{2\pi}{\lambda_B^2}\delta\,\Delta\lambda_B \right) \right) \right] \tag{6.13}$$

If the FBG is modulated by a strain-induced tone signal of angular frequency ω_t then the signal detected at the corresponding OCM channel is given by [13]

$$I = \left(k_1^2 + k_2^2\right) I_0 \left[1 + V \cos\left(\omega_c\, t + \left(\frac{2\pi}{\lambda_B}\delta - \frac{2\pi}{\lambda_B^2}\delta\,\Delta\lambda_B \right) \cos(\omega_t\, t) \right) \right] \tag{6.14}$$

The dynamic strain-induced phase change can now be detected by monitoring (with a lock in amplifier) the sensor carrier phase shift relative to the fixed phase of the serrodyne modulation. This can be done either directly from the function generator driving the phase modulator [14][15] or from the reflected light from FBG B, used as an isolated reference grating fundamentally cancelling the effects of random phase bias drift

[16]. For a dynamic strain induced modulation in the FBG sensor the phase sensitivity $d\phi/d\varepsilon$ is given by [16][17]

$$\frac{d\phi}{d\varepsilon} = -\frac{2\pi}{\lambda_B^2}\frac{\Delta\lambda_B}{\Delta\varepsilon}\delta \tag{6.15}$$

where δ is the optical path difference in the Mach-Zehnder and $\Delta\lambda/\Delta\varepsilon$ is the strain sensitivity of the FBG sensor ($\Delta\lambda_B/\Delta\varepsilon$ = 1.2 pm/με, see section 2.6). Therefore, to maximise the phase sensitivity the optical path difference in the Mach-Zehnder interferometer needs to be made as large as possible. Similarly, to maximise the optical power reflected by the FBG sensors their reflection bandwidths should be made as large as possible since the power spectral density of the broadband source is fixed [18]. However, by increasing the optical path difference in the Mach-Zehnder interferometer the free spectral range is reduced (see section 5.4) and will eventually be in the order of the bandwidth of the FBG causing carrier amplitude reduction. This is because the coherence length L_c of the reflected light from the FBG is inversely proportional to its bandwidth, given by $L_c = \lambda_B^2/\Delta\lambda_B$ (see section 5.3.4). When the coherence length is in the order of the optical path difference the free spectral range $\left(FSR = \lambda^2/\delta\right)$ is the same order as the bandwidth of the FBG and destructive interference reduces or completely destroys the carrier amplitude. Thus, a trade off exists between the sensitivity and the bandwidth of the FBG sensors.

6.7.1 Extending the Dynamic Sensing Range

To extend the range of the demodulation scheme using an AWG, several adjacent electrical outputs of the OCM are electrically summed. The issue then becomes how the signal-to-noise ratio varies with the strain amplitude, particularly when the FBG is situated between two AWG channel passbands. To investigate this dependence, low frequency strain amplitudes of 1.5 με at 30 Hz were applied to four different FBGs mounted successively on the fibre stretcher. Three of the gratings were fabricated with increasing -3 dB bandwidths of 0.125, 0.46 and 0.63 nm and a fourth grating produced with a double peaked structure [19][20] having a -3 dB bandwidth in each peak of 0.22 nm.

6.7.1.1 First Fibre Bragg Grating

The first FBG tested had a centre wavelength of 1558.29 nm and a reflected -3 dB bandwidth of 0.125 nm (see FBG 3 appendix E). A serrodyne modulation was applied at a frequency of 10 kHz via the phase modulator creating a carrier. The free spectral range of the interferometer was set to 0.8 nm at the central wavelength of the source, corresponding to an optical path difference in the interferometer of approximately 3 mm, ensuring the FBGs reflect only a portion of the time varying oscillating interferometer output (see section 5.5). A typical recovered signal as seen on the spectrum analyser is shown in figure 6.10, demonstrating a noise limited strain amplitude resolution of 19.2 nε/√Hz. Calculated from the strain modulation of 1.5 με, a signal to noise ratio of 44 dB and a spectrum analyser linewidth of 244 mHz (see equation 6.6) which is a significantly better result than that obtained using the homodyne approach (96 nε/√Hz) described in

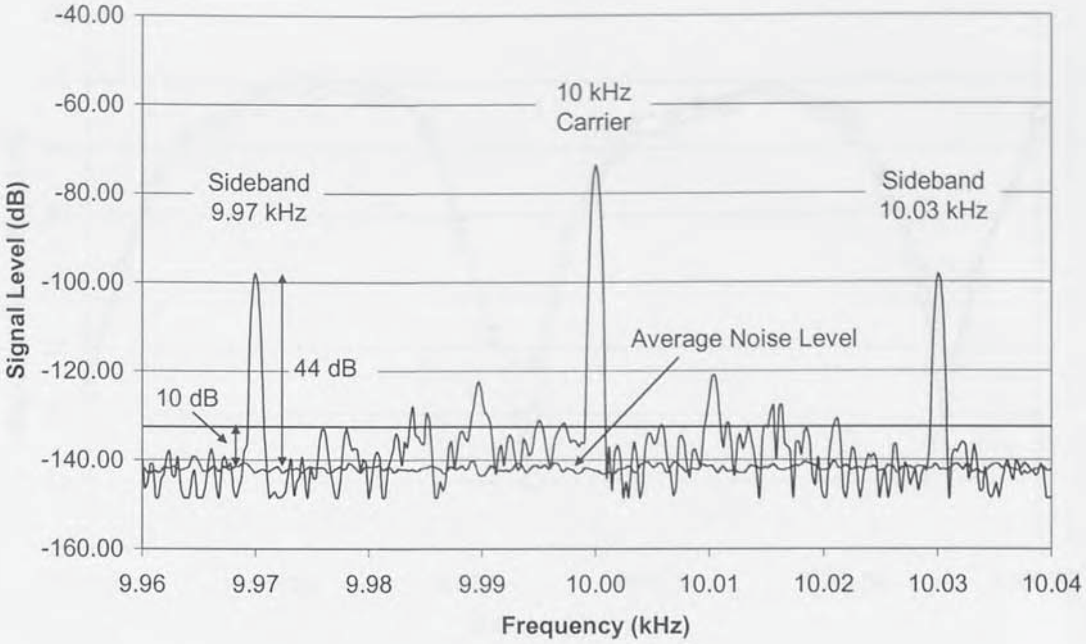

Figure 6.10 Typical spectrum due to a FBG with applied sinusoidal modulation of 1.5 με at 30 Hz on a 10 kHz carrier (244 mHz bandwidth). Average noise level indicated by the dotted line.

section (6.5.1). The resolution of the system is however fundamentally limited by shot noise I_s in the photodetector, given by

$$I_s = (2eIB)^{1/2} \tag{6.16}$$

where e is the electron charge, I the mean photodetector current and B the detector bandwidth. Hence, for the particular photodetector used (see appendix F) in this and subsequent systems the shot noise is 1.3 μA/√Hz, indicating that a signal smaller than that will never be observed. Thus, providing a comprehensive indication of how much improvement might be squeezed out of the system. The grating was then stretched repeatedly by 10 μm (or 54 με) through a few channels of the AWG and the signal-to-noise ratio of a sideband recorded. The base noise level was determined by removing the

Figure 6.11 Signal to noise ratio vs. wavelength for the first FBG stretched through channel 3 to channel 1. Channel 3 (squares), channel 2 (circles), channel 1 (crosses) and 3+2+1 (triangles).

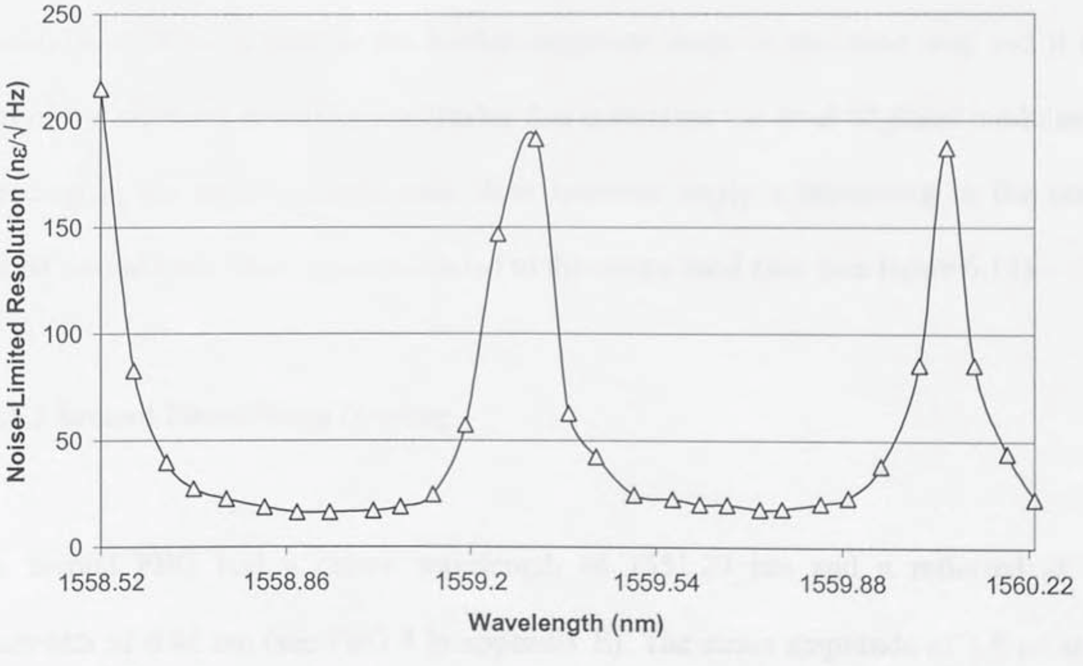

Figure 6.12 Noise-limited resolution vs. wavelength for the first FBG stretched through channel 3 to channel 1 (OCM channels 3+2+1).

strain modulation and carrier to view the noise only. The averaging facility on the spectrum analyser was used to determine the average noise level (see figure 6.10). Any signal-to-noise ratios below 10 – 15 dB were not recorded as they could not be clearly differentiated from the varying noise level caused by low frequency fluctuations in the Mach-Zehnder interferometer due to draughts or temperature changes in the laboratory. This is not, however, a fundamental problem as the effects would be much reduced if an integrated optic interferometer [21][22] was used instead. Figure 6.11 shows the results of the individual channel outputs and the summation of channels 3, 2 and 1 as the grating was stretched through them. As expected, the best signal-to-noise ratio lies at the centre of an AWG channel i.e. when the peak power is reflected from the FBG. The added channel response (triangles) shows a slight 5 dB increase in the centre-of-passband signal-to-noise level compared to the individual channels. The fall in the signal-to-noise ratio does not imply a drop in the sensitivity (phase change per unit strain) of the demodulation. This is because the carrier amplitude drops in the same way and it is a ratio of the sideband to carrier amplitudes that determine the level of phase modulation. The drop in the signal-to-noise ratio does however imply a worsening in the noise-limited resolution in this region compared to the centre band case (see figure 6.12).

6.7.1.2 Second Fibre Bragg Grating

The second FBG had a centre wavelength of 1551.29 nm and a reflected -3 dB bandwidth of 0.46 nm (see FBG 4 in appendix E). The strain amplitude of 1.5 $\mu\varepsilon$ at 30 Hz was applied and the grating stretched through the corresponding AWG channels, this time channel 12 to channel 10. Figure 6.13 shows the separate channel signal-to-noise ratios from this grating along with the summed output. Because the bandwidth of this

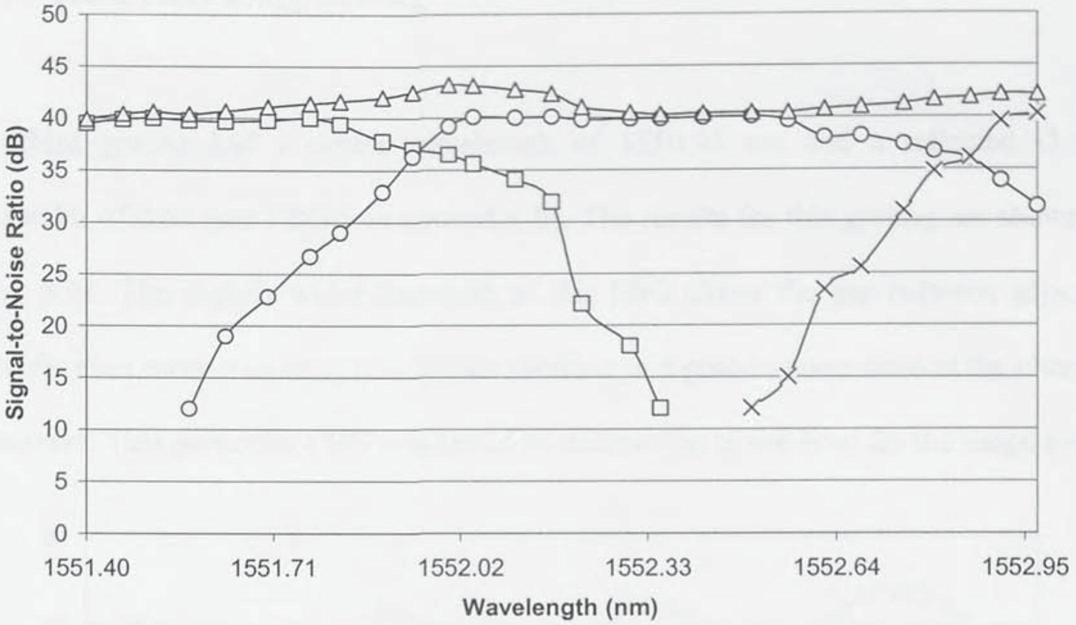

Figure 6.13 Signal-to-noise ratio vs. wavelength for the second FBG stretched through channel 12 to channel 10. Channel 12 (squares), channel 11 (circles), channel 10 (crosses) and channels 12+11+10 (triangles).

FBG is wider than the first grating the channel crossover regions have a higher signal level, due to the fact that more of the reflected light is present in adjacent channels. When the channels are added together the resultant signal level (triangles) is relatively constant with a slight increase in the signal level at the crossovers.

6.7.1.3 Third Fibre Bragg Grating

The third grating had a centre wavelength of 1550.95 nm and a reflected -3 dB bandwidth of 0.63 (see FBG 5 in appendix E). The results for this grating are shown in figure 6.14. The slightly wider linewidth of this FBG closes the gap between adjacent channels even more, resulting in a further increase in signal-to-noise ratio at the channel crossovers. This particular FBG was tested to destruction to see how far the range could be extended. The response continued over a range of about 4.7 nm (nearly 5 mε) before the fibre broke.

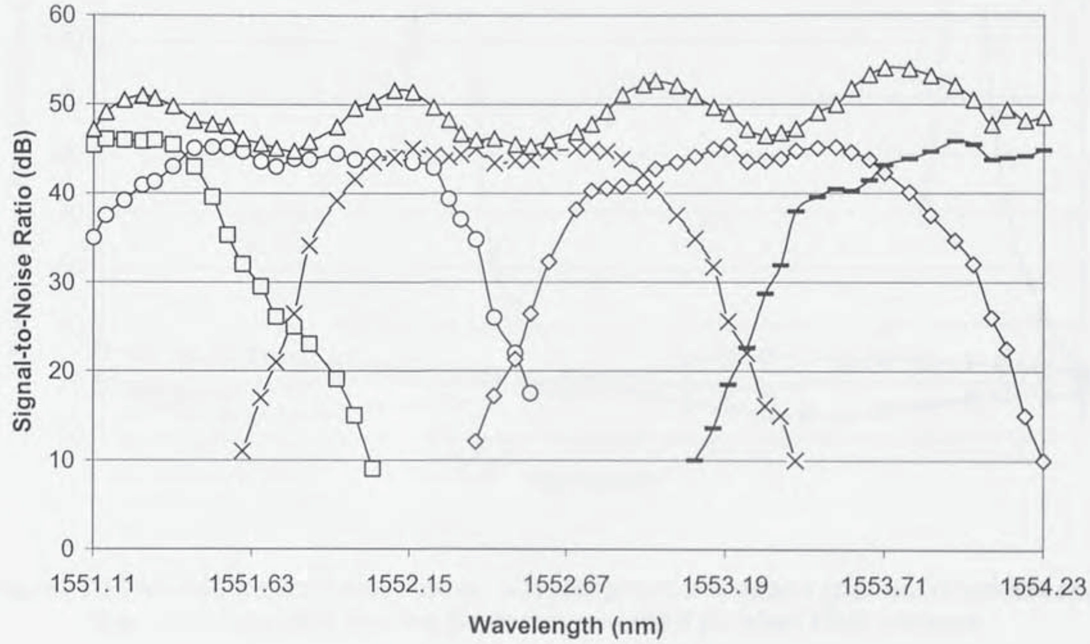

Figure 6.14 Signal-to-noise ratio vs. wavelength for the third FBG stretched through channel 13 to channel 9. Channel 13 (squares), channel 12 (circles), channel 11 (crosses), channel 10 (diamonds), channel 9 (lines) and 13+12+11+10+9 (triangles).

6.7.1.4 Summary of the First Three Fibre Bragg Gratings Under Test

From the above results, it is clear that the use of wider gratings allows the recovery of an approximately constant signal level and noise-limited resolution as the FBG sweeps through the corresponding added AWG channels (see figure 6.15). However, the width of the FBG ultimately places a limit on the sensitivity available as previously discussed (see section 6.7) which may be problematic if wide bandwidth FBGs are used.

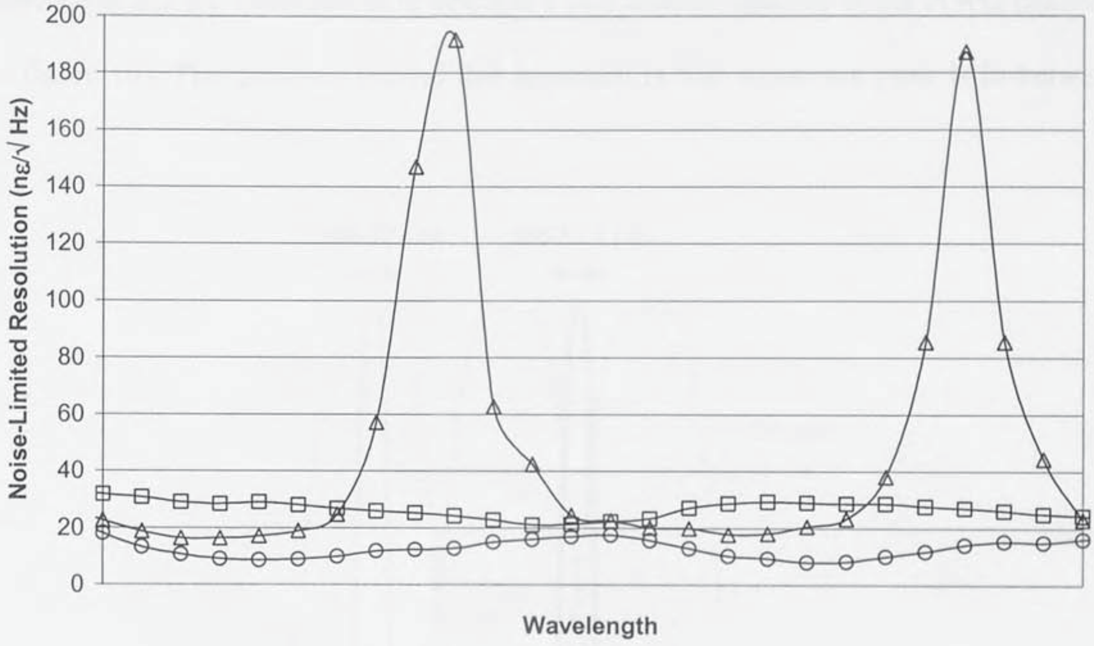

Figure 6.15 Noise-limited resolution vs. wavelength of the added channel response for the first (triangles), second (squares) and third (circles) FBG sensors.

6.7.1.5 Fourth Fibre Bragg Grating

To overcome these problems, the final grating was fabricated with double peaks: one at 1549.72 nm and a reflected -3 dB bandwidth of 0.22 nm and the other at 1550.91 nm and a reflected -3 dB bandwidth of 0.22 nm (see FBG 6 in appendix E). The peak-to-peak difference of 1.2 nm corresponds to one and a half channel spacing of the AWG channels (see figure 16). The rationale behind this approach is that when one peak is in-between two channels and hence returning a weak signal-to-noise ratio, the other peak is centred on another channel and returning a strong signal. The optical path difference of the Mach-Zehnder interferometer was adjusted so that the free spectral range was equal to 0.6 nm, corresponding to an integral sub-multiple of the FBG peak spacing, which ensures that the signals from the two peaks are in-phase and add constructively. The recovered response as the double peaked FBG is stretched through channels 14 to 12 is

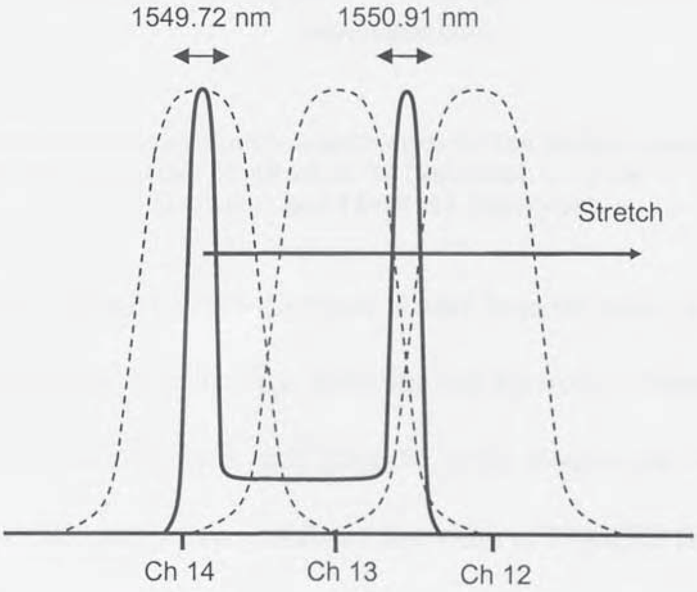

Figure 6.16 Principle of the double peaked grating being stretched through channels 14, 13 and 12.

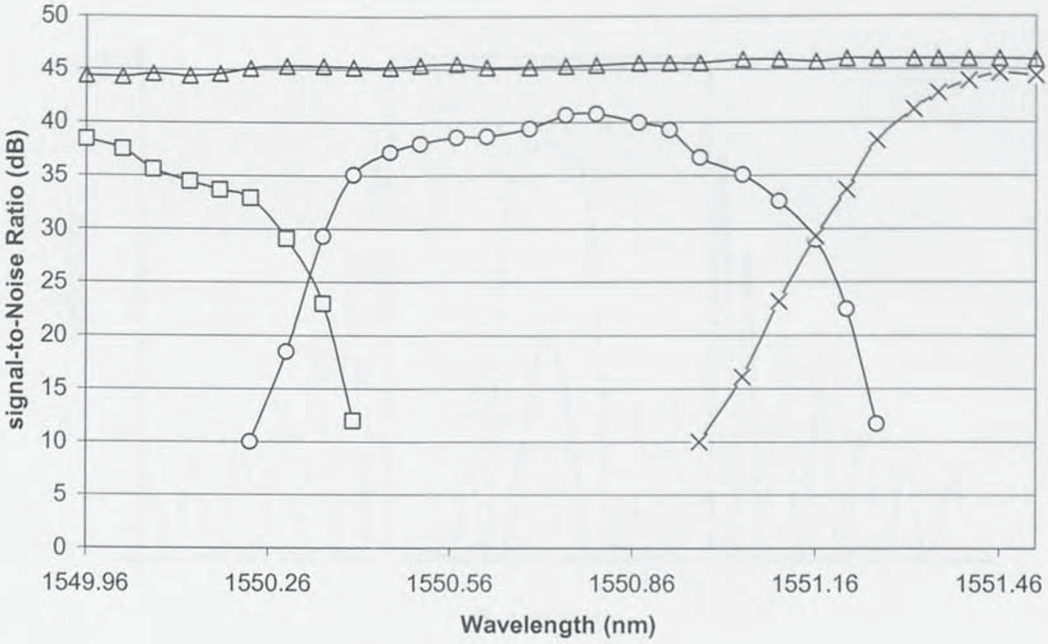

Figure 6.17 Signal-to-noise ratio vs. wavelength for the double peaked FBG stretched through channel 14 to channel 12. Channel 14 (squares), channel 13 (circles), channel 12 (crosses) and 14+13+12 (triangles).

shown in figure 6.17. It can be seen that there is very little variation in the signal-to-noise ratio across the channels. The average noise limited resolution obtained for the double peaked FBG was 17 nε/√Hz, calculated from the strain modulation of 1.5 με, the signal to noise ratio of 45 dB and spectrum analyser linewidth of 244 mHz (see equation 6.6).

6.8 Channel Crosstalk

Figure 6.2 at the beginning of this chapter clearly demonstrated the effect of crosstalk between neighbouring AWG channels. The level of crosstalk is determined from the shape of the reflected grating spectrum. For strong unapodised FBGs the side lobes are increased over a wider spectral width. Figure 6.18 represents the reflectivity of three

Figure 6.18 Normalised reflectivity vs. wavelength for unapodised Bragg gratings, strong grating (dots), weak grating (solid line) [22].

unapodised gratings with their strength increasing towards unity [23]. It is clear that strong unapodised gratings will incur considerably more channel crosstalk than weaker unapodised gratings. The solution to reduce this effect is to apodise the gratings [2]. Crosstalk in AWG systems interrogating FBG sensors is going to be application specific. For example the simple strain system discussed in section (6.5) would require one channel separation to implement a multiplexed system using other similar strength gratings. To demonstrate the worst achievable crosstalk a strong unapodised FBG was fabricated. The FBG had a centre wavelength of 1551.05 nm and a reflected -3dB bandwidth of 0.81 nm (see FBG 7 appendix E). A strain amplitude of 6 με at 30 Hz was applied to the grating. The FBG was then stretched every 10 μm (or 54 με) from channel 13 through to channel 9 (see figure 6.19) and the signal level recorded from channel 11. The results shown in figure 6.20 display the signal level in channel 11 verses the position of the FBG as it is stretched through channels 13 to 9. The results

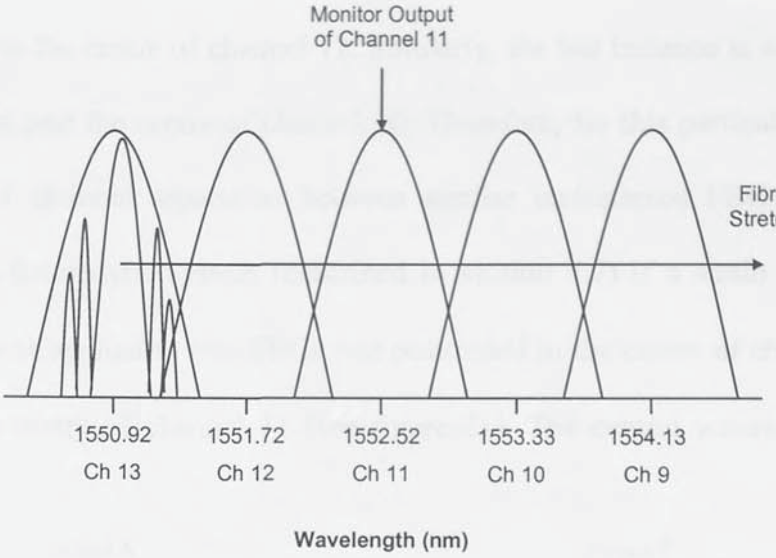

Figure 6.19 Diagram showing how the channel crosstalk was determined using a strong unapodised grating.

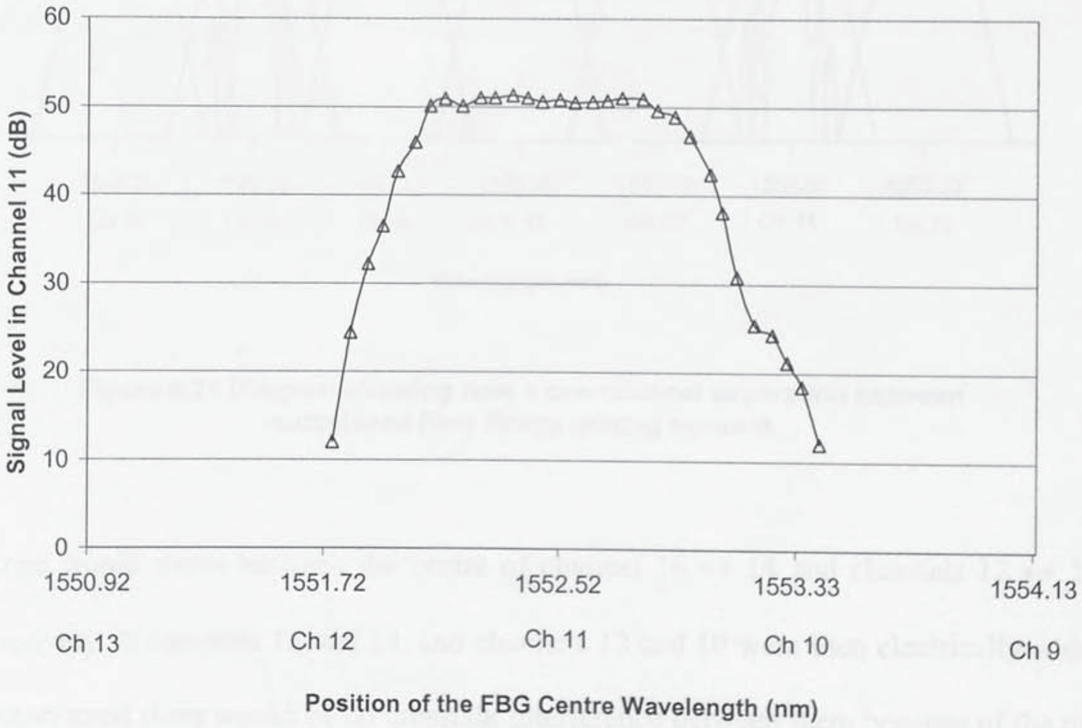

Figure 6.20 Signal-to-noise ratio in channel 11 vs. position of the FBG centre wavelength as it is stretched through channels 13 to 9.

show the first instance of channel 11 recording the signal from the FBG is when it is positioned near to the centre of channel 12. Similarly, the last instance is when the FBG is positioned just past the centre of channel 10. Therefore, for this particular FBG there needs to be a 1 channel separation between similar multiplexed FBG sensors. For example, in the heterodyne system (described in section 6.7) if a strain amplitude of around 800 με was applied to two FBGs one positioned in the centre of channel 15 and the other in the centre of channel 11 (see figure 21). The central wavelengths of the

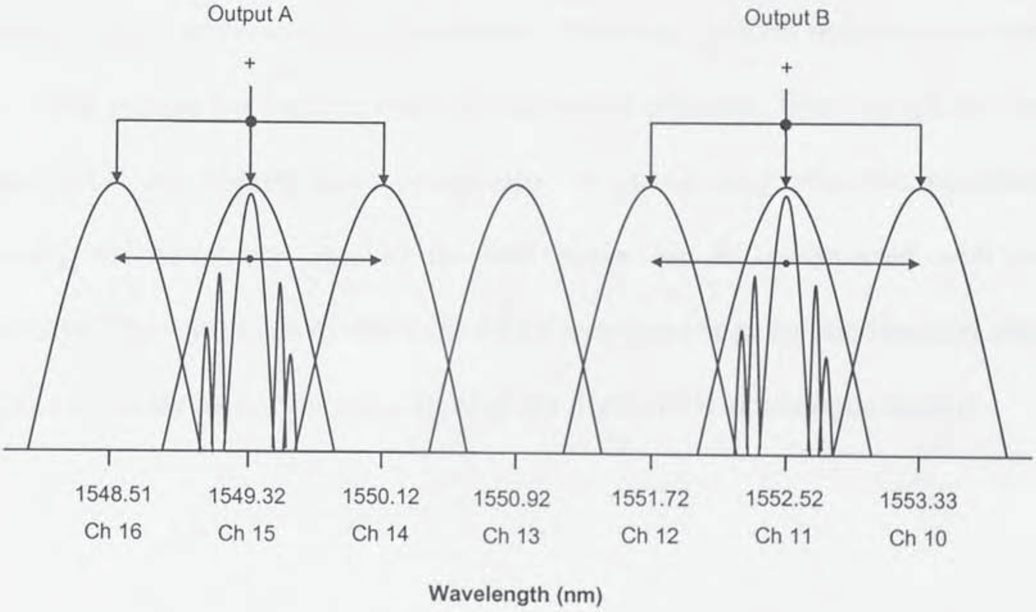

Figure 6.21 Diagram showing how a one channel separation between multiplexed fibre Bragg grating sensors.

gratings would move between the centre of channel 16 ↔ 14 and channels 12 ↔ 10, respectively. If channels 16 and 14, and channels 12 and 10 were then electrically added and monitored there would be no crosstalk interference between them because of the one channel separation. Channel 13 however will experience crosstalk from both FBGs.

6.9 Conclusion

The experimental work reported in this chapter has demonstrated that AWGs can successfully be used to interrogate FBG sensors. The static range was improved by using a chirped grating spanning several channels of the AWG and detecting the grating position using the centroid fit of the recovered data. The dynamic range was improved by implementing a heterodyne approach based on interferometric wavelength shift detection. By electrically adding channels of the OCM, the range of the strain-induced wavelength shift can be extended indefinitely. The most uniform response was obtained with a wide grating bandwidth or the double-peaked structure. Even though the double-peaked FBGs are slightly more complicated to record they offer the possibility of increasing the sensitivity because the two peaks can be constructed with narrow bandwidths. The advantage of using the OCM arrangement as an interrogation unit is in the ease of processing the voltage outputs in the digital [24] or analogue domain.

6.10 References

[1] Y. Sano, N. Hirayama and T. Yoshino, "Wavelength interrogator employing arrayed waveguide grating for distributed fibre Bragg grating sensing," *in Proceedings 14th International Conference on Optical Fibre Sensors*, (OFS-14, Venice, Italy), Technical Digest, pp. 788-791, October 2000

[2] Y. Sano and T. Yoshino, "Fast optical wavelength interrogator employing arrayed waveguide grating for distributed fiber Bragg grating sensors," *Journal of Lightwave Technology*, vol. 21, No. 1, pp 132-139, January 2003

[3] D. J. Webb and R. D. Pechstedt, "Sensing applications of arrayed waveguide grating devices," *in Proceedings 15th International Conference on Optical Fibre Sensors*, (OFS-15, Portland, USA), Technical Digest, pp. 569-572, May 2002

[4] A. A. Chtcherbakov and P. L Swart, "Multiplexed Bragg grating sensor with chirped fiber optic grating interrogator," *in Proceedings 16th International Conference on Optical Fibre Sensors*, (OFS-16, Nara, Japan), Technical Digest, pp.552-555, October 2003

[5] P. Niewczas, A. J. Wiltshire, L. Dziuda and J. R. McDonald, "Performance analysis of the fiber Bragg grating interrogation system based on an arrayed waveguide grating," *Instrumentation and Measurement*, vol. 53, No. 4, August 2004

[6] G. Z. Xiao, P. Zhao, F. G. Sun, Z. G. Lu and Z. Zhang, "Arrayed waveguide grating based interrogator for wavelength modulated multi fibre optic sensor applications," *Photonics Technology Letters*, vol. 17, No. 8, pp. 1710-1712, August 2005

[7] A. Othonos and K. Kalli, "Fiber Bragg gratings: fundamentals and applications in telecommunications and sensing," Artech House, ISBN: 0-89006-344-3, 1999

[8] D. K. W. Lam and B. K. Garside, "Characterization of single mode optical fiber filters," *Applied Optics*, vol. 20, No. 3, pp. 440-445, February 1981

[9] H. Takahashi, K. Oda, H. Toba and Y. Inoue, "Transmission characteristics of arrayed waveguide N x N wavelength multiplexer," *Journal of Lightwave Technology*, vol. 13, No. 3, pp. 447-455, March 1995

[10] J. R. Taylor, "An introduction to error analysis the study of uncertainties in physical measurements," *University Science Books*, (Second Edition), ISBN: 0-935702-75-X, 1997

[11] F. T. S. Yu and S. Yin, "Fibre optic sensors," *Marcel Dekker Inc*, ISBN: 0-8247-0732-X, pp. 322-324, 2002

[12] A. Croft, R. Davison and M. Hargreaves, "Engineering Mathematics," *Addison Wesley*, 2nd Edition, ISBN: 0201-87744-9, 1996

[13] D. Petersen, "Audio video and data telecommunications," *McGraw and Hill*, ISBN: 0077-07427-0, 1992

[14] D. A. Jackson, A. Dandridge and S. K. Sheem, "Measurement of small phase shifts using a single mode optical fibre interferometer," *Optics Letters*, vol. 5, No. 4, pp. 139-141, April 1980

[15] K. Kalli, G. P. Brady, D. J. Webb and D. A. Jackson, "wavelength division and special multiplexing using tandem interferometers for Bragg grating sensor networks," *Optics Letters*, vol. 20, No. 24, pp. 2544-2546, December 1995

[16] A. D. Kersey, T. A. Berkoff and W. W. Morey, "Fiber optic Bragg grating strain sensor with drift compensated high resolution interferometric wavelength shift detection," *Optics Letters*, vol. 18, No. 1, pp. 72-74, January 1993

[17] A. D. Kersey, T. A. Berkoff and W. W. Morey, "High resolution fibre grating based strain sensor with interferometric wavelength shift detection," *Electronics Letters*, vol. 28, No. 3, pp. 236-238, January 1992

[18] R. S. Weiss, A. D. Kersey and T. A. Berkoff, "A four element fiber grating sensor array with phase sensitive detection," *Photonics Technology Letters*, vol. 6, No. 12, pp. 1469-1472, December 1994

[19] A. Othonos, X. Lee and R. M. Measures, "Superimposed multiple Bragg gratings," *Electronic Letters*, vol. 30, No. 23, pp. 1972-1974, November 1994

[20] A. Arigiris, M. Konstantaki, A. Ikiades, D. Chronis, P. Floias, K. Kallimani and G. Pagiatakis, "Fabrication of high reflectivity superimposed multiple fibre Bragg gratings with unequal wavelength spacing," *Optics Letters*, vol. 27, No. 15, pp. 1306-1308, August 2002

[21] B. J. Luff, J. S. Wilkinson, J. Piehler, U. Ho;;enbach, J. Ingenhoff and N. Ramaswamy, "Integrated optical Mach-Zehnder bio-sensor," *Journal of Lightwave Technology*, vol. 16, No. 4, pp. 583-592, April 1998

[22] P. Hua, B. J. Luff, G. R. Quigley, J. S. Wilkinson and K. Kawaguchi, "Integrated optical dual Mach-Zehnder interferometer sensor," *Sensors and Actuators B*, vol. 87, pp. 250-257, June 2002

[23] T. Erdogan, "Fiber grating spectra," *Journal of Lightwave Technology*, vol. 15, No. 8, pp. 1277-1294, August 1997

[24] B. Griffin and M. J. Connelly, "Digital signal processing of interferometric fiber optic sensors," *in Proceedings of Lightwave Technologies in Instrumentation & Measurement Conference*," (IEEE LTIMC 2004, New York, USA), Technical Digest, pp.153-156, October 2004

7 Interferometric Sensor Interrogation using an Arrayed Waveguide Grating

The phenomenon of the interference of light underlies many high-precision measurement systems. One of the earliest extrinsic interferometric sensor configurations is that of short cavity Fabry-Pérot interferometers which make use of a reflecting surface positioned near to the cleaved or polished end of an optical fibre. This chapter describes the use of an arrayed waveguide grating (AWG) to measure the cavity length in such a sensor using the dual wavelength technique introduced in chapter 5.

7.1 Introduction

Low coherence signal recovery (combining heterodyne processing using the dual-wavelength technique) is a well known method of interrogating interferometric sensors [1]. Single source interrogation using the dual-wavelength technique was reported by Webb *et al* [2] in 1988. In this scheme an interference filter was used at the output to effectively synthesise the two wavelengths. Jáuregui *et al* [3] in 2000 used a wavelength division multiplexer for the same purpose. The first report using an AWG to interrogate interferometric sensors was proposed by Webb *et al* [4] in 2002. For numerous fibre optic based sensor applications, short cavity extrinsic Fabry-Pérot interferometric sensors are particularly attractive in structural heath monitoring and medical applications because of their high sensitivity, simplicity, low-cost and small size [5]-[9].

7.2 Extrinsic Fizeau Interferometer

The extrinsic Fizeau interferometric sensor is formed by the surface of a high-reflective mirror acting as the sensing element and the cleaved end of a single mode fibre such that only the 1st order reflected beams from the fibre end and the mirror contribute significantly to the interferometric signal [9] (see figure 7.1). Since the light in the cavity is not confined optical loss due to diffraction limits the practical length of the optical cavity to a few hundred micrometers to around 2 mm depending on the power of the light emitted from the fibre end, the reflection coefficient of the mirror and the coupling efficiency back into the fibre. The normalised reflected output signal I of the two interfering beams is given by [10]

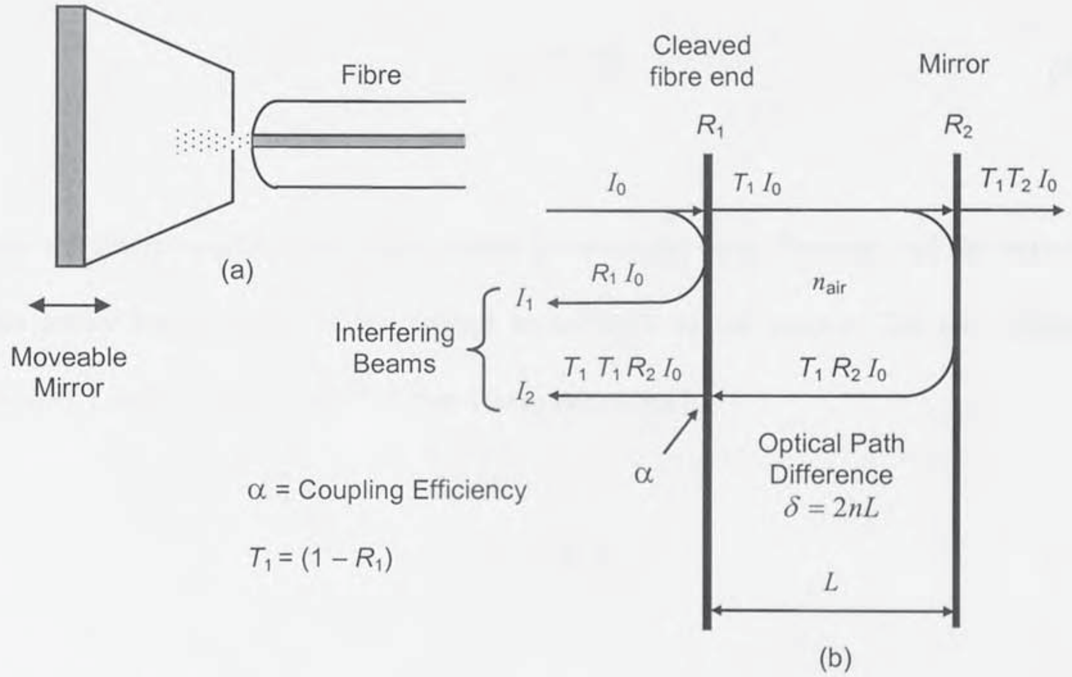

Figure 7.1 Extrinsic Fizeau interferometer formed from a cleaved fibre end and a mirror (a) and a schematic of the incident, reflected and transmitted optical power.

$$I = I_1 + I_2 + 2\gamma(\tau)\sqrt{I_1 I_2}\cos\phi \tag{7.1}$$

Where I_1 is the intensity of the reflected beam from the bare fibre end, I_2 is the intensity of the reflected beam from the mirror, $\gamma(\tau)$ is a function related to the power spectral density of the source (see section 5.3.1) and ϕ is the round-trip propagation phase shift in the interferometer, given by

$$\phi = \frac{4\pi\, n\, L}{\lambda} \tag{7.2}$$

where n is the refractive index of the region between the bare fibre end and the mirror, L is the cavity length and λ is the central wavelength of the source. The two reflected intensities I_1 and I_2 as depicted in figure 7.1(b) are given by

$$I_1 = R_1\, I_0 \tag{7.3}$$

and

$$I_2 = \alpha\, T_1\, T_1\, R_2\, I_0 = \alpha\left(1 - R_1\right)^2 R_2\, I_0 \tag{7.4}$$

where α is the coupling efficiency of the light back into the fibre, R_1 is the intensity reflection coefficient of the bare fibre end related to the transmission T_1 by $T_1 = 1 - R_1$, R_2 is the intensity reflection coefficient of the mirror and I_0 is the mean signal level.

Therefore, the normalised reflected output signal I from the two interfering beams can be written as

$$I = R_1 I_0 + \alpha (1 - R_1)^2 R_2 I_0 + 2\,\gamma(\tau)\sqrt{R_1 I_0\, \alpha (1 - R_1)^2 R_2 I_0}\,\cos\phi \tag{7.5}$$

and rearranged into a familiar interferometer output intensity formula, given by

$$I = \frac{1}{2} I_0 \left(R_1 + \alpha (1 - R_1)^2 R_2\right)\left[1 + \frac{(1 - R_1)\sqrt{\alpha R_1 R_2}}{R_1 + \alpha (1 - R_1)^2 R_2}\gamma(\tau)\cos\phi\right] \tag{7.6}$$

where the visibility V of the interferometer is given by

$$V = \frac{(1 - R_1)\sqrt{\alpha R_1 R_2}}{R_1 + \alpha (1 - R_1)^2 R_2}\gamma(\tau) \tag{7.7}$$

The reflection coefficient R_1 of the bare fibre end is obtained from the phenomenon of Fresnel reflection. For the light incident normal to the boundary between the two media, the reflection coefficient is given by [11]

$$R_1 = \left(\frac{n_1 - n_2}{n_1 + n_2}\right)^2 \tag{7.8}$$

where $n_1 = 1.45$ [12] is the refractive index of the fibre and $n_2 = 1.0003$ [13] is the refractive index of air at normal atmospheric pressure, hence, $R_1 = 0.034$. Assuming the reflectivity of the mirror R_2 is around 90% efficient, then $R_2 = 0.9$.

7.3 Interferometric Sensing

When the OCM is used to interrogate an interferometer illuminated by a broadband source, it provides information equivalent to illuminating the interferometer with 40 discrete light sources, each with the bandwidth of an AWG passband. This provides a considerable amount of spectral information, which can be utilised in various ways [4]. The dual-wavelength technique [14] extends the unambiguous range of an interferometric sensor by monitoring the interferometric phase difference between two wavelengths (see section 5.6.2). In the dual-wavelength technique, the two phases are normally obtained by illuminating the interferometer with two separate light sources, the selection of which determines the unambiguous range of the system.

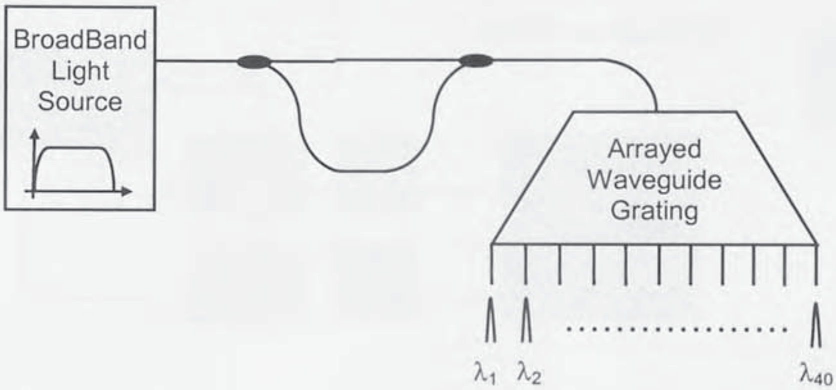

Figure 7.2 Schematic representation of the effect of interrogating an interferometer illuminated with a broadband source using an arrayed waveguide grating.

7.3.1 Active Sensor Interrogation

To implement the dual-wavelength technique in its simplest form using an AWG, broadband light was directed via a coupler to the piezoelectric transducer mounted mirror (see figure 7.3). Selecting two OCM channels effectively synthesises the two separate light sources illuminating the system. A 20 Hz serrodyne waveform sufficient to drive the interferometer over one fringe to generate a carrier was applied to the piezoelectric transducer mounted mirror. If the optical path difference $\delta = 2nL$ due to the application of a serrodyne waveform is denoted by $2nL = 2nL + 2nL_1 t$ as a function of time during one period, then the phase term of the signal detected by the OCM from equation (7.6) becomes

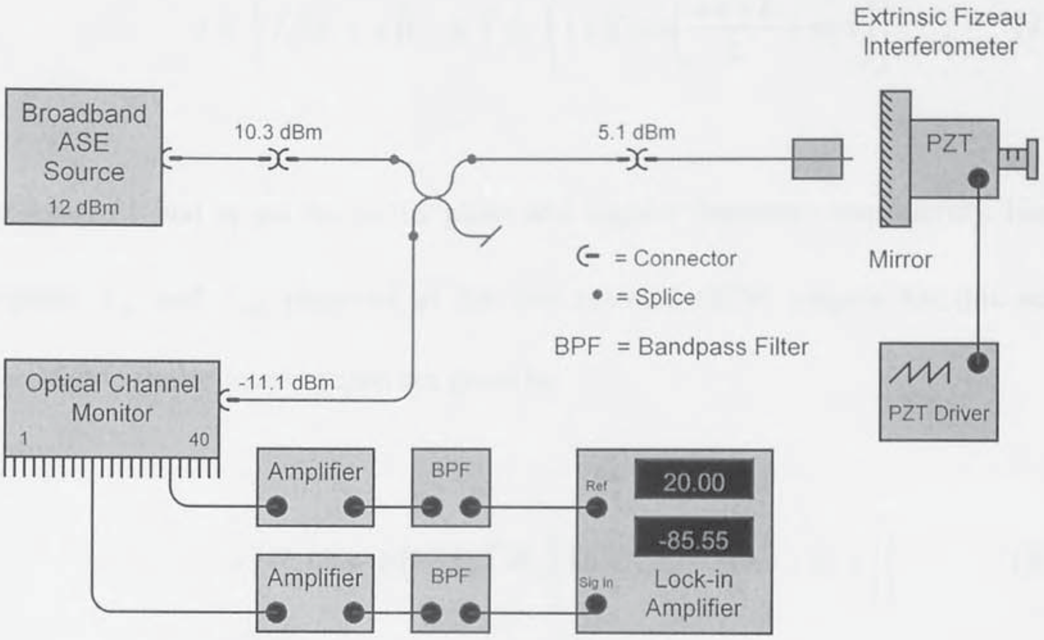

Figure 7.3 Experimental set-up for active sensor interrogation.

$$I = \frac{1}{2} I_0 \left(R_1 + \alpha (1 - R_1)^2 R_2 \right) \left[1 + V \cos\left(\frac{4\pi nL}{\lambda} + \frac{4\pi nL_1}{\lambda} t \right) \right] \tag{7.9}$$

the serrodyne waveform is applied so its period T is equal to $\lambda/2\pi n L_1$ [15] and the angular frequency ω_c defined by $\omega_c = 2\pi/T$ [16] therefore, equation (7.9) becomes

$$I = \frac{1}{2} I_0 \left(R_1 + \alpha(1 - R_1)^2 R_2\right)\left[1 + V \cos\left(\frac{4\pi n L}{\lambda} + \omega_c t\right)\right] \tag{7.10}$$

where $4\pi n L/\lambda$ and ω_c are the carrier phase and angular frequency respectively. Hence, the signals I_{A1} and I_{A2} observed at the two selected OCM outputs for this active interferometric sensor interrogation are given by

$$I_{A1} = \frac{1}{2} I_0 \left(R_1 + \alpha(1 - R_1)^2 R_2\right)\left[1 + V \cos\left(\frac{4\pi n L}{\lambda_1} + \omega_c t\right)\right] \tag{7.11}$$

and

$$I_{A2} = \frac{1}{2} I_0 \left(R_1 + \alpha(1 - R_1)^2 R_2\right)\left[1 + V \cos\left(\frac{4\pi n L}{\lambda_2} + \omega_c t\right)\right] \tag{7.12}$$

where λ_1 and λ_2 are the central wavelengths of the two selected OCM channels. From equations (7.11) and (7.12) it is clear that the carrier phase at the two selected OCM channels are defined by

$$\phi_1(\lambda_1) = \frac{4\pi n L}{\lambda_1} \tag{7.13}$$

and

$$\phi_2(\lambda_2)=\frac{4\pi\, n\, L}{\lambda_2} \tag{7.14}$$

hence the phase difference $\Delta\phi=\phi_1-\phi_2$ is given by

$$\Delta\phi=\frac{4\pi\, n\, L}{\lambda_1}-\frac{4\pi\, n\, L}{\lambda_2} \tag{7.15}$$

The difference in the phase is a function of the optical path difference and displays an unambiguous range δ_u dependent on the wavelength separation of the two selected OCM channels given by (see appendix M)

$$\delta_u=\frac{1}{2}\left(\frac{\lambda_1\lambda_2}{\lambda_2-\lambda_1}\right) \tag{7.16}$$

To test the system, the electrical output from OCM channel 13 (λ_{13} = 1550.92 nm) was amplified, bandpass-filtered (see appendix F) at the carrier frequency and used as the reference to a lock-in-amplifier (see appendix F). Channels 12 (λ_{12} = 1551.72 nm), 19 (λ_{19} = 1546.12 nm) and 40 (λ_{40} = 1529.55 nm) were in turn connected to the lock-in-amplifier to determine the relative phase difference as the mirror position was adjusted manually at 10 μm intervals. The results are shown in figure 7.4. Also shown are the least squares fit of the data [17]. The unambiguous range in terms of the mirror displacement are approximately 1500 μm (full range not shown), 250 μm and 55 μm for channels $(13 \leftrightarrow 12)$, $(13 \leftrightarrow 19)$ and $(13 \leftrightarrow 40)$, respectively. The experimental data agrees very well with the theoretical values (not shown, see appendix I) calculated from equation (7.16) displaying a mean error of $\pm 0.15^0$ (corresponding to a mirror displacement of 0.63 μm) for channels $(13 \leftrightarrow 12)$, $\pm 0.75^0$ (corresponding to a mirror displacement of 0.53 μm) for channels $(13 \leftrightarrow 19)$ and $\pm 1.95^0$ (corresponding to a mirror displacement of 0.3 μm) for channels $(13 \leftrightarrow 40)$. The increasing error is due to the increasing sensitivity in the system. The phase difference per unit mirror displacement increases as the optical separation between the two selected OCM channels widens. This makes the system much more susceptible to phase-noise from draughts and temperature fluctuation in the laboratory. However, these effects could be significantly reduced if a fully enclosed, industrial-standard, interferometric sensor was used.

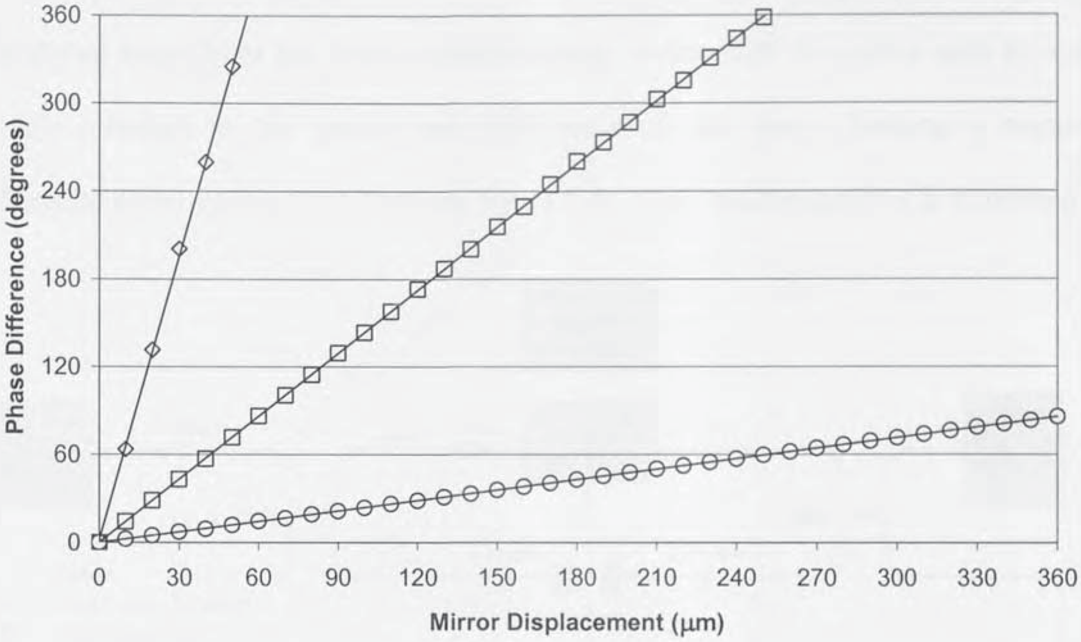

Figure 7.4 Phase difference vs. mirror displacement for channels 13 ↔ 12 (circles), 13 ↔ 19 (squares) and 13 ↔ 40 (diamonds). Least squares fit to the data indicated by solid lines.

7.4 Composite Coherence Tuned System

In the majority of applications, the requirement for active components at the sensor is undesirable. To overcome this problem a second processing interferometer was introduced away from the Fizeau interferometric sensor with its optical path difference closely matched to the optical path difference of the sensor forming a composite coherence-tuned system [18]-[20] (see figure 7.5). With this approach, it is important that the optical path differences of the two interferometers are much greater than the coherence length of the effective source; otherwise interference within the sensor alone introduces unwanted coherent mixing (see section 5.6). Selecting a single channel of the AWG where the optical bandwidth is around 0.2 nm and calculating its effective

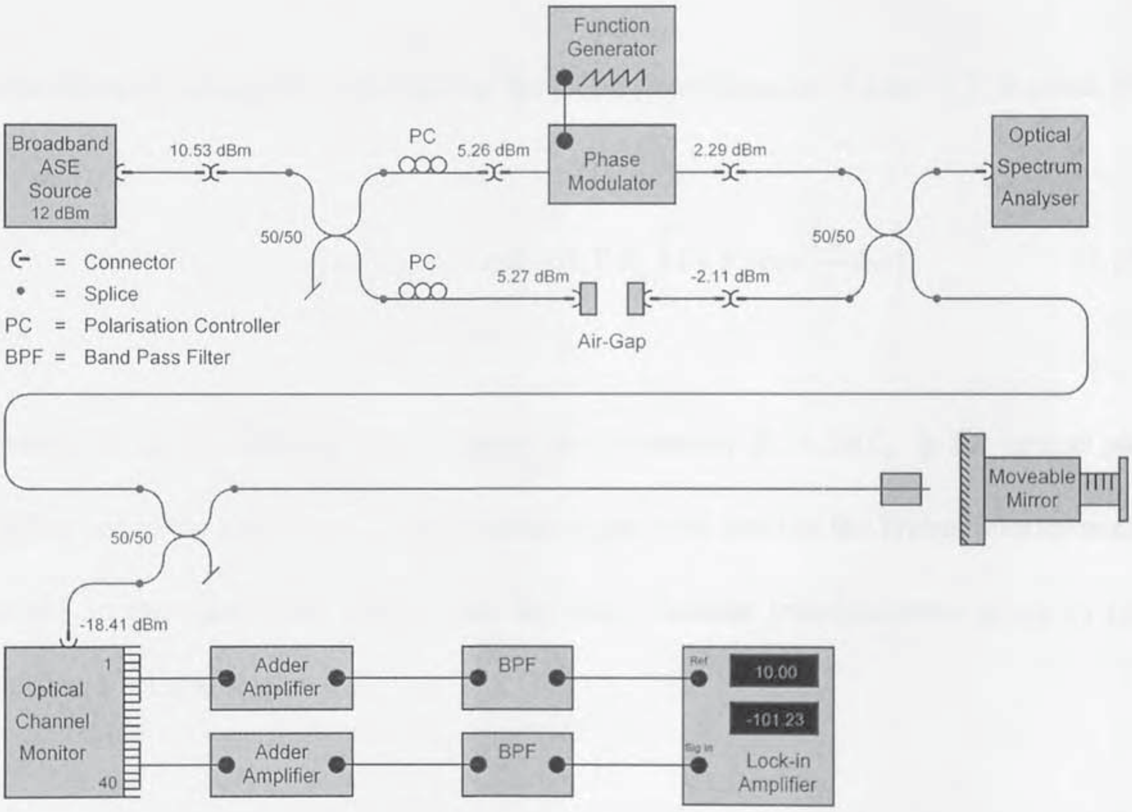

Figure 7.5 Experimental set-up for composite coherence tuned system.

coherence length $L_c = \lambda^2/\Delta\lambda$ (see section 5.3.4) means an optical path difference in the interferometric sensor greater than 1.2 cm or a cavity length of 6 mm, which is unacceptably large for the short cavity Fizeau interferometer used in this work. The solution is to electrically add together a number of outputs from the OCM to synthesise a source with a larger bandwidth and a lower coherence length.

7.4.1 Passive Sensor Interrogation

The intensity I observed at the input to the OCM (from equation 7.2 and 7.7) is given by

$$I = \frac{1}{2} I_0 \left(R_1 + \alpha (1 - R_1)^2 R_2 \right) \left[1 + V_F \cos \frac{2\pi}{\lambda} \delta_F \right] \tag{7.17}$$

where V_F is the visibility of the Fizeau interferometer, $\delta_F = 2nL_F$ is the optical path difference in the cavity and I_0 is the mean signal level input to the Fizeau interferometer which in this case is the output from the Mach-Zehnder interferometer, given by (see section 5.3.1 and section 6.7)

$$I_0 = \left(k_1^2 + k_2^2 \right) I_M \left[1 + V_M \cos(\phi_c + \omega_c t) \right] \tag{7.18}$$

where V_M is the visibility of the Mach-Zehnder interferometer, ϕ_c is the carrier phase and ω_c the angular frequency due to the application of a serrodyne waveform. The two intensities I_{P1} and I_{P2} at the two selected sets of OCM are given by

$$I_{P1} = \frac{1}{2} I_0 \left(R_1 + \alpha \left(1 - R_1\right)^2 R_2 \right) \left[1 + V_F \cos\left(\frac{4\pi\, n\, L_F}{\lambda_1} \right) \right] \tag{7.19}$$

and

$$I_{P2} = \frac{1}{2} I_0 \left(R_1 + \alpha \left(1 - R_1\right)^2 R_2 \right) \left[1 + V_F \cos\left(\frac{4\pi\, n\, L_F}{\lambda_2} \right) \right] \tag{7.20}$$

where λ_1 and λ_2 are the central wavelengths of the selected OCM channels. Therefore, the phase difference $\Delta\phi$ (between equation 7.19 and 7.20) is given by

$$\Delta\phi = \frac{4\pi\, n\, L_F}{\lambda_1} - \frac{4\pi\, n\, L_F}{\lambda_2} \tag{7.21}$$

To test the system, a 10 kHz serrodyne waveform was applied to the phase modulator in the Mach-Zehnder interferometer to generate a carrier. The Fizeau interferometric sensor cavity L was set to 0.465 mm and its optical path difference $\delta = 2nL = 0.93$ mm matched with that of the Mach-Zehnder interferometer. Ten neighbouring OCM outputs 21 ↔ 30 ($\lambda_{21} = 1544.53$ nm ↔ $\lambda_{30} = 1537.40$ nm) were electrically added, amplified, bandpass filtered (at the carrier frequency) and used as the reference to the lock-in-amplifier. This results in an effective optical bandwidth $\Delta\lambda$ of 7.2 nm and a corresponding effective coherence length of 329.8 μm, obtained from (equation 5.23). The mirror was then adjusted so that the optical path difference δ was equal to the coherence length of the source i.e. the cavity length L was adjusted to 165 μm. The following OCM channels were then in turn added, amplified, bandpass filtered (at the carrier frequency) and connected to the lock-in-amplifier.

1. 20 ↔ 29 (λ_{20} = 1545.32 nm ↔ λ_{29} = 1538.19 nm), effective coherence length 330.1 μm and optical bandwidth 7.2 nm.
2. 17 ↔ 26 (λ_{17} = 1546.92 nm ↔ λ_{26} = 1539.77 nm), effective coherence length 330.82 μm and optical bandwidth 7.2 nm.
3. 11 ↔ 20 (λ_{11} = 1552.52 nm ↔ λ_{20} = 1545.32 nm), effective coherence length 333.2 μm and optical bandwidth 7.2 nm.
4. 6 ↔ 15 (λ_{6} = 1556.55 nm ↔ λ_{15} = 1549.32 nm), effective coherence length 334.92 μm and optical bandwidth 7.2 nm.

The mirror was displaced manually away from the bare fibre at 10 μm intervals and the phase difference recorded. The results are shown in figure 7.6. Also shown are the theoretical values calculated from equation (7.21). The maximum achievable unambiguous range in terms of mirror displacement for this set-up is around 370 μm for channels 21 ↔ 30 and 17 ↔ 26 which have an optical separation of 4 channels (3.2 nm). The theoretical values agree quite well with the experimental values (see appendix J) displaying mean errors of:

1. $\pm 0.29^0$ for channels 21 ↔ 30 and 20 ↔ 29, corresponding to a mirror displacement of 1.21 μm.
2. $\pm 0.67^0$ for channels 21 ↔ 30 and 17 ↔ 26, corresponding to a mirror displacement of 0.71 μm.

3. $\pm 0.98^0$ for channels 21 ↔ 30 and 11 ↔ 20, corresponding to a mirror displacement of 0.45 μm.

4. $\pm 1.99^0$ for channels 21 ↔ 30 and 6 ↔ 15, corresponding to a mirror displacement of 0.61 μm.

As in the active sensor interrogation discussed in section (7.3.1) the increasing error is due to the increasing sensitivity as the phase difference per unit mirror displacement increases as the optical separation between the two selected OCM channels widens. This makes the system much more susceptible to phase-noise from draughts and temperature fluctuation in the laboratory.

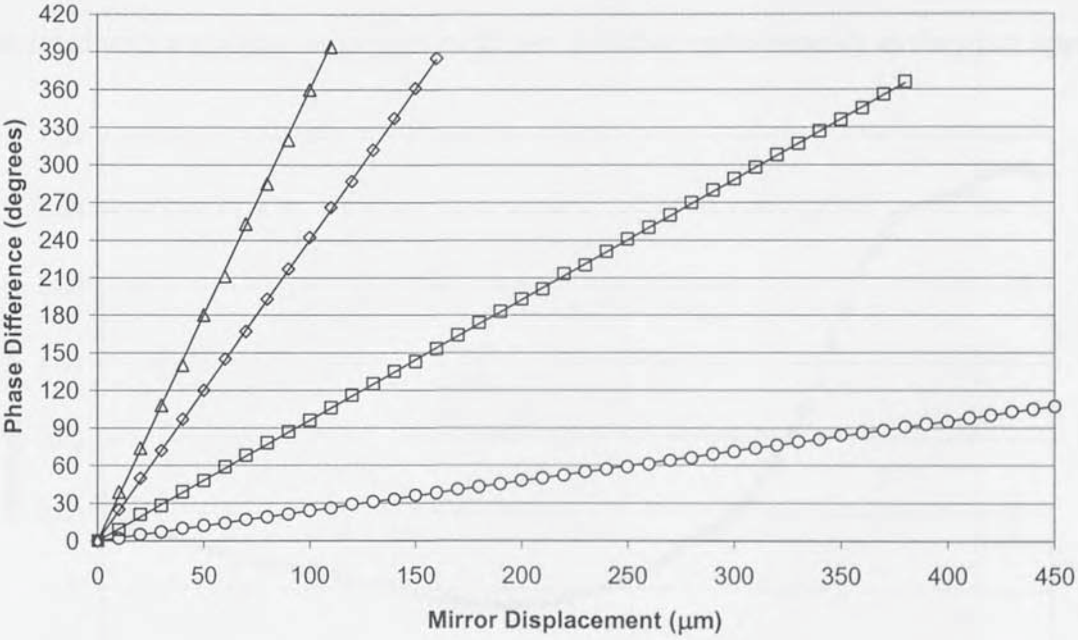

Figure 7.6 Phase difference vs. mirror displacement for channels 21 ↔ 30 and 20 ↔ 29 (circles), 21 ↔ 30 and 17 ↔ 26 (squares) and 21 ↔ 30 and 11 ↔ 20 (diamonds), 21 ↔ 30 and 6 ↔ 15 (triangles). Theoretical relationship indicated by solid lines.

7.4.4.1 Noise and Resolution

To measure the interferometric resolution of the system at a specific mirror displacement, the ten added and bandpass filtered OCM channels 21 ↔ 30 (λ_{21} = 1544.53 nm ↔ λ_{30} = 1537.40 nm) were connected directly to a spectrum analyser. The observed output on the spectrum analyser showed the 10 kHz carrier rising above the system noise floor. The noise floor indicates the minimum detectable signal sideband level and hence the minimum amplitude of the mirror movement that can be detected. If the mirror is modulated with a sinusoid at frequency f_n then the observed sidebands as they just appear over the noise will indicate the system resolution. An alternative and easier method to measure the sideband signal level can be achieved mathematically using the first two terms of the Bessel functions (see appendix K). The results are shown in figure 7.7 displaying the noise limited resolution as a function of the mirror position. As expected

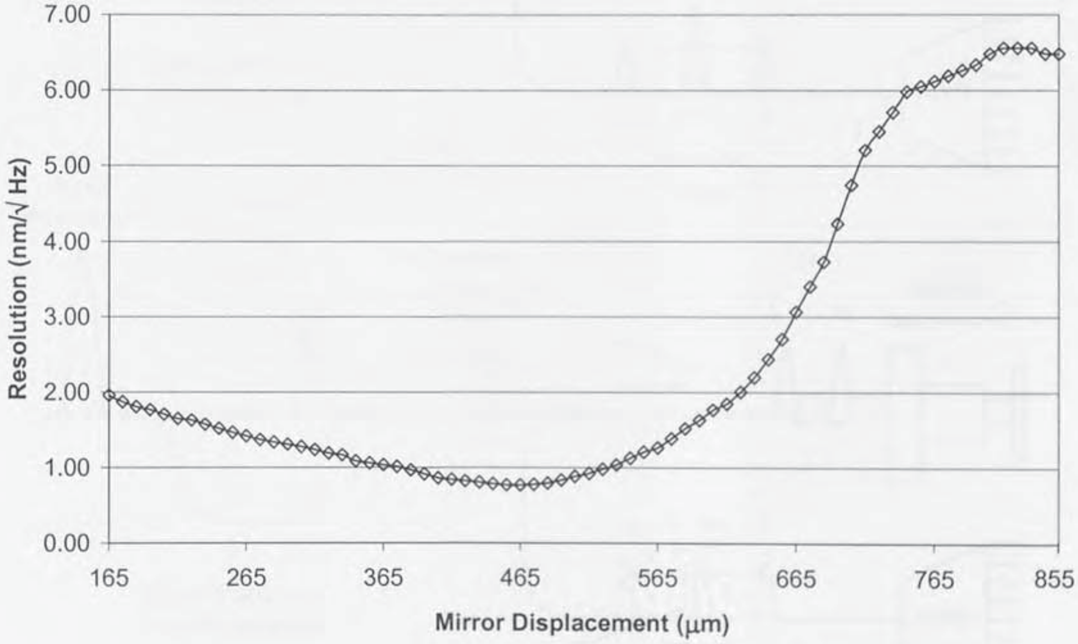

Figure 7.7 Resolution (nm/√Hz) vs. mirror displacement (μm).

the best resolution occurs when the optical path differences of the two interferometers are matched. Only for this situation does the fringe visibility reach its maximum. Either side of this point there is a lack of symmetry which is best explained in the time domain [20]. Figure 7.8 depicts two situations, firstly (a) where the optical path differences in two

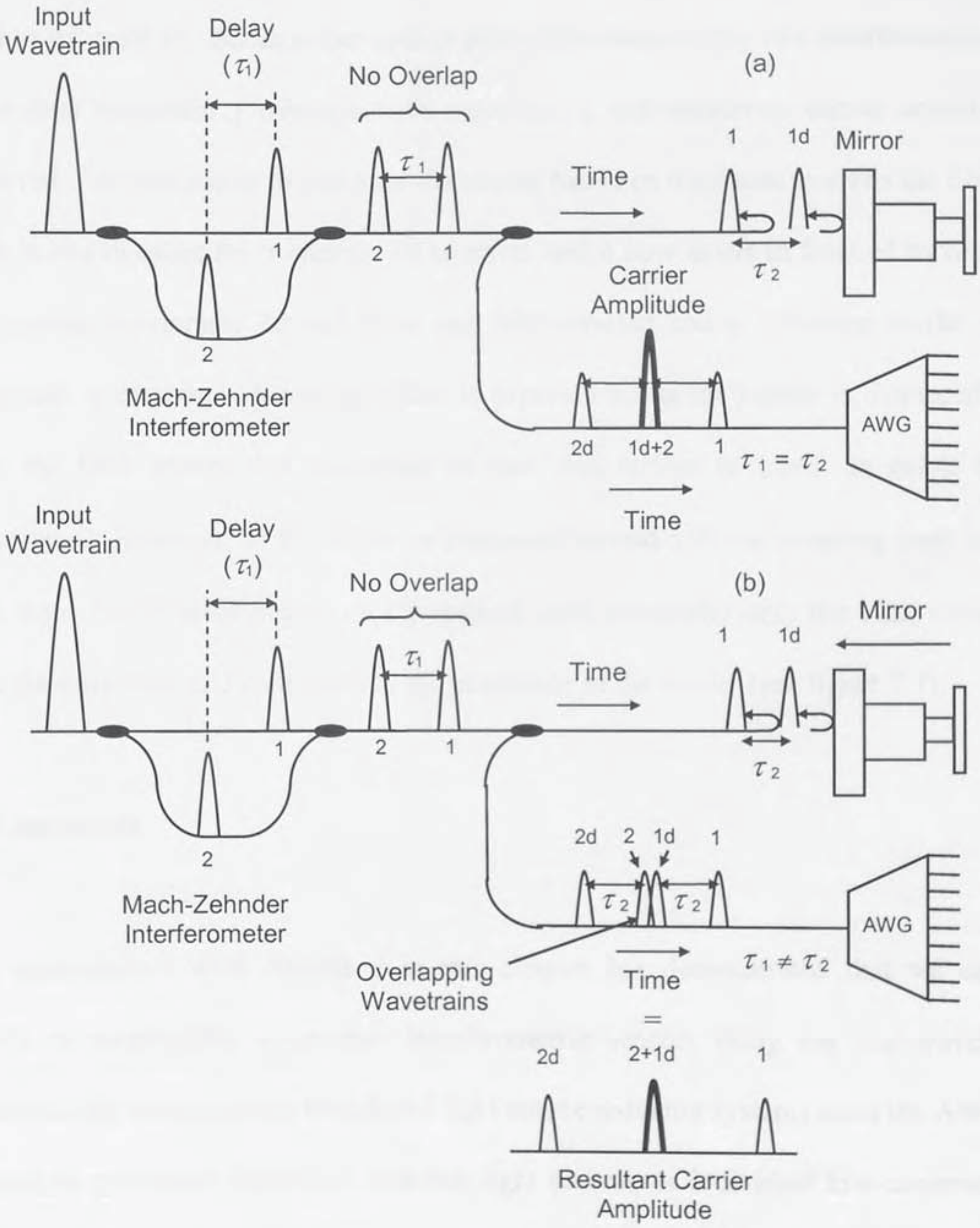

Figure 7.8 Propagation of a wavetrain through the coherence tuned system. Optical paths of both interferometers matched (a) and with a path imbalance in the sensor interferometer (b).

interferometers are the same and secondly (b) where the mirror has been displaced away from the balance position. Starting with situation (a), if the light source is considered to be emitting uncorrelated wavetrains then the Mach-Zehnder generates two output wavetrains one delayed in time. At the Fizeau interferometer wavetrain 1 generates a delayed version of itself 1d. Wavetrain 2 following behind also generates a delayed version of itself 2d. Because the optical path differences of the two interferometers are equal then wavetrain 1 overlaps with wavetrain 2 and maximum carrier amplitude is observed. For the case in (b) because the mirror has been displaced towards the fibre end there is less distance for wavetrain 1d to travel and it now exists in front of wavetrain 2. This means wavetrains 1d and 2 do not fully overlap and a reduction in the carrier amplitude is observed. A similar effect is experienced as the mirror is displaced away from the fibre except that wavetrain 1d now has further to travel an exists behind wavetrain 2. However, as the mirror is displaced beyond 550 μm coupling back into the fibre from the 1st order beam quickly reduces until eventually only the back reflections from the bare fibre end contribute to the amplitude of the carrier (see figure 7.7).

7.5 Conclusion

The experimental work described in this chapter has demonstrated that we can use AWGs to successfully interrogate interferometric sensors using the dual-wavelength technique. By using a single broadband light source reducing systems costs the AWG can be used to synthesise individual coherent light sources or individual low-coherent light sources by adding a number of neighbouring AWG channels at the output. The AWG, therefore represents a highly flexible component for use in sensor interrogation systems, being reconfigurable in real time if necessary.

7.6 References

[1] A. D. Kersey and A. Dandridge, "Dual-wavelength approach to interferometric sensing," *in Proceedings SPIE Fiber Optic Sensors II*, vol. 798, pp. 178-181, 1987

[2] D. J. Webb, J. D. C. Jones and D. A. Jackson, "Extended range interferometry using a coherence tuned, synthesized dual-wavelength technique with multimode fibre links," *Electronics Letters*, vol. 24, No. 24, pp. 1173-1175, September 1988

[3] C. Jáuregui, F. M. Araújo, L. A. Ferreira, J. L. Santos and J. M. López-Higuera, "Interrogation of low-finesse Fabry-Pérot cavities based on coupling length modulation of a wavelength division multiplexer," *in Proceedings 14th International Conference on Optical Fibre Sensors*, (OFS-14, Venice, Italy), Technical Digest, pp. 716-719, October 2000

[4] D. J. Webb and R. D. Pechstedt, "Sensing applications of arrayed waveguide grating devices," *in Proceedings 15th International Conference on Optical Fibre Sensors*, (OFS-15, Portland, USA), Technical Digest, pp. 569-572, May 2002

[5] Y. J. Rao and D. A. Jackson, "Recent progress in fibre optic low coherence interferometry," *Measurement Science and Technology*, vol. 7, pp. 981-999, 1996

[6] E. Udd, "Fiber optic sensors an introduction for engineers and scientists," *John Wiley & Sons*, ISBN: 0471-83007-0, 1990

[7] Y. J. Rao, D. A. Jackson, R. Jones and C. Shannon, "Development of prototype fibre optic based Fizeau pressure sensor with temperature compensation and signal recovery by coherence reading," *Journal of Lightwave Technology*, vol. 12, No. 9, pp. 1685-1695, September 1994

[8] R. A. Wolthuis, G. L. Mitchell, E. Saaski, J. C. Hartl and M. A. Afromowitz, "Development of medical pressure and temperature sensors employing optical spectrum modulation," *IEEE Transactions Biomedical Engineering*, vol. 38, No. 10, pp. 974-981, October 1991

[9] K. A. Murphy, M. F. Gunther, A. M. Vengsarkar and R. O. Claus, "Quadrature phase-shifted extrinsic Fabry-Pérot optical fibre sensors," *Optics Letters*, vol. 16, No. 4, pp. 273-275, February 1991

[10] M. Francon, "Optical interferometry," *Academic Press INC*, ISBN: 66-28312, 1966

[11] K. Booth and S. Hill, "The essence of optoelectronics," *Prentice Hall*, ISBN: 0-13533654-6, pp. 98-99, 1998

[12] D. N. Nikogosyan, "Properties of optical and laser related materials," *John Wiley & Sons*, ISBN: 0-471-97384, 1998

[13] R. Muncaster, "A-level physics," *Stanley Thornes Ltd*, (Fourth Edition), ISBN: 0-7487-1584-3, 1993

[14] A. D. Kersey and A. Dandridge, "Dual wavelength approach to interferometric sensing," *in Proceedings SPIE Fiber Optic Sensors II*, vol. 798, pp. 178-181, 1987

[15] F. T. S. Yu and S. Yin, "Fibre optic sensors," *Marcel Dekker Inc*, ISBN: 0-8247-0732-X, 2002

[16] A. Croft, R. Davison and M. Hargreaves, "Engineering Mathematics," *Addison Wesley*, 2nd Edition, ISBN: 0201-87744-9, 1996

[17] J. R. Taylor, "An introduction to error analysis the study of uncertainties in physical measurements," *University Science Books*, (Second Edition), ISBN: 0-935702-75-X, 1997

[18] S. A. Al-Chalabi, B. Culshaw and D. E. N. Davies, "Partially coherent sources in interferometry," *in Proceedings 1st International Conference on Optical Fibre Sensors*, (OFS-1, London, United Kingdom), Technical Digest, pp. 132-136, April 1983

[19] R. A. Patten, "Michelson interferometer as a remote gauge," *Applied Optics*, vol. 10, No. 12, pp. 2717-2721, December 1971

[20] H. C. Lefevre, "White light interferometry in optical fiber sensors," *in Proceedings 7th International Conference on Optical Fibre Sensors*, (OFS-7, Sydney, Australia), Technical Digest, pp. 345-351, December 1990

8 High Birefringence Fibre Interferometer for Optical Sensing Applications

This chapter describes the use of high birefringence (Hi-Bi) fibre forming a differential path interferometer for heterodyne fibre optic sensing applications. Two optical sensing schemes are demonstrated: firstly, fibre Bragg grating sensing used to recover low frequency strain and secondly interferometric sensing using the dual wavelength technique used to measure the change in optical path length of a Mach-Zehnder interferometric sensor.

8.1 Introduction

From a technical and industrial application point of view, the best way of implementing an interrogating interferometer with the ability to apply optical path length modulation is to use an integrated optic based Mach-Zehnder interferometer. This option however would currently require a bespoke and expensive device, which does not facilitate, at this time, the provision of a low cost sensing solution. The normal laboratory method is to use a fibre or combined fibre and free-space Mach-Zehnder interferometer with one of the arms optically modulated using a piezoelectric fibre stretcher. This type of interferometer does employ low cost components, however, precise adjustment of the optical path difference is time consuming and the system is susceptible to environmental perturbations that affect the arms of the interferometer unequally. The solution described in this chapter permits a relatively easy method to adjust the optical path difference and is of potentially low cost. The idea is to exploit the ability to obtain interference between the fast and slow modes of polarisation maintaining fibre forming a differential path interferometer [1][2]. This has been used directly as a sensing mechanism [3]-[8], but to the author's knowledge never used to interrogate other optical sensors.

8.2 High Birefringence Fibre Interferometer

Consider an input light at an azimuth 45° with respect to the birefringence axes of a length of Hi-Bi fibre, the input light will spread into two non-interfering orthogonal axes.

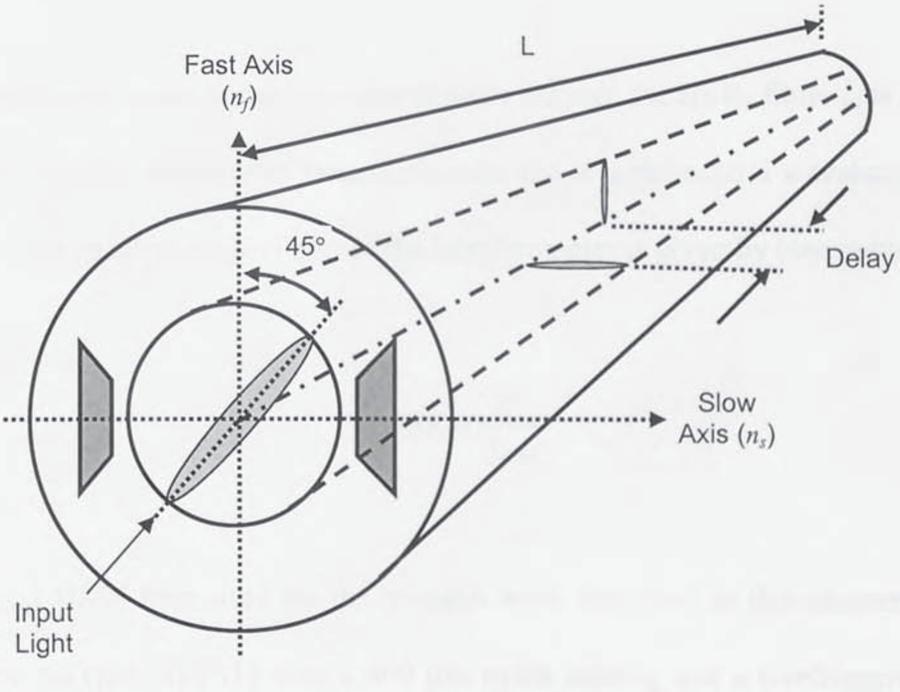

Figure 8.1 Diagram of polarised input light at 45^0 to the birefringence axes of a length of bow-tie high-birefringence fibre.

The optical path difference δ between the two eigenaxes is determined by the length L, of the fibre and the fibre birefringence $\Delta n = \left(n_s - n_f\right)$, given by

$$\delta = \Delta n\, L \tag{8.1}$$

The output intensity using an analyser to cause interference between the two modes is analogous to the Mach-Zehnder interferometer [9], given by (see section 5.3.1)

$$I = \left(k_1^2 + k_2^2\right) I_0 \left(1 + V \cos \frac{2\pi \Delta n\, L}{\lambda}\right) \tag{8.2}$$

where k_1 and k_2 are losses in the two optical paths through the Hi-Bi fibre, I_0 is the mean signal level, V is the visibility of the interference and λ is the central wavelength of the source. The free spectral range (FSR) of the interferometer is given by (see section 5.4)

$$FSR = \frac{\lambda^2}{\Delta n L} \tag{8.3}$$

The particular Hi-Bi fibre used for the research work described in this chapter is stress induced bow-tie type [10][11] with a 400 μm nylon coating and a birefringence Δn of 3.69×10^{-4}.

8.3 High Birefringence Fibre Interferometer Set-Up

A 21.56 metre length of Hi-Bi fibre was selected to form the processing interferometer, producing a FSR of 0.3 nm. 20 metres of fibre were wound onto a piezoelectric fibre stretcher and connected to a function generator able to produce a serrodyne waveform via a piezoelectric driver. Figure 8.2 shows a diagram of the Hi-Bi fibre interferometer set-up process. Using a polarimeter connected to the output (see STEP 1) the polarised broadband light was oriented using the first rotating connector (see appendix L) to equally populate both eigenmodes. The interferometer output was reconfigured (see STEP 2) allowing the light to pass through a second rotating connector into another length of polarisation maintaining fibre, through an analyser which recombined the two eigenmodes and finally to an optical spectrum analyser. The second rotating connector was adjusted to produce the best fringe visibility (relating to the eigenaxis of

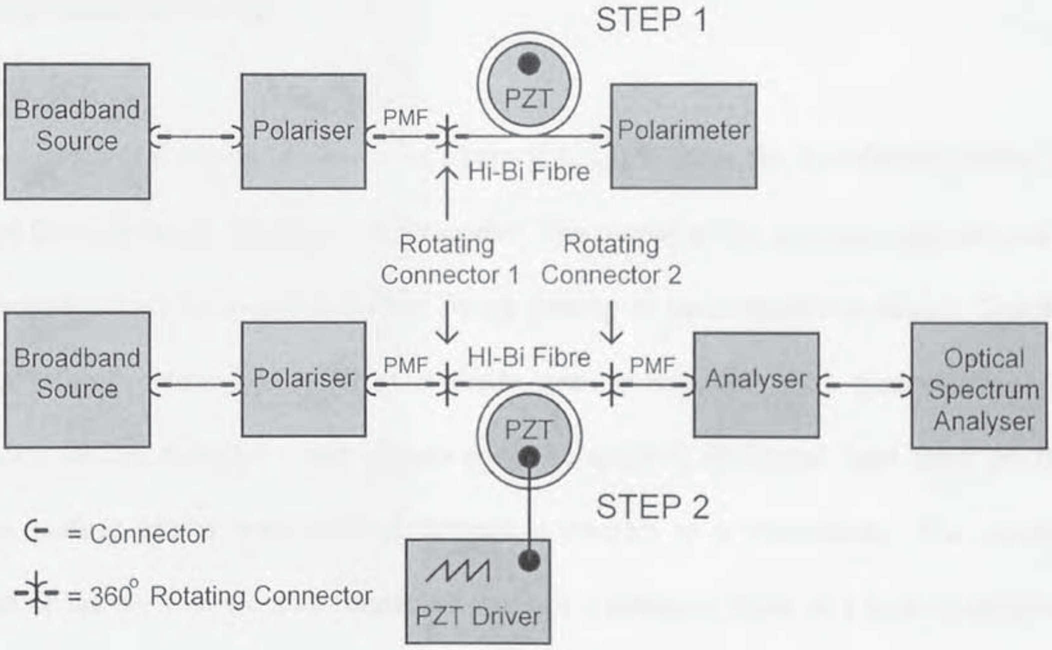

Figure 8.2 High birefringence fibre interferometer set-up process.

the second length of polarisation maintaining fibre oriented at approximately 45° to those of the Hi-Bi fibre interferometer). To drive the interferometer over one fringe in order to implement heterodyne processing differential optical path length modulation using a serrodyne waveform is required. This was realised by stretching the Hi-Bi fibre until the interferometer phase difference between the eigenmodes equalled 2π over the $1+V\cos\phi$ fringe pattern. The strain applied to the Hi-Bi fibre to achieve this result was approximately 5.5 $\mu\varepsilon$. The bend radius of the piezoelectric stretcher (25 mm) and axial stretching of the fibre had no significant effects on the output. This is due to the thickness of the coating around the fibre helping to maintain the polarisation states [12].

8.4 Experimental Set-up

The experimental set-up is shown in figure 8.3. Light from the broadband source was passed through the Hi-Bi fibre interferometer. The output of the analyser was directed via a selective connector to either a fibre Bragg grating or interferometric sensor. The fibre Bragg grating sensor consisted of a single grating mounted on a piezoelectric fibre stretcher so that dynamic strain signals could be applied. Reflected light from the fibre Bragg grating sensor was directed through a coupler to a photodiode. The electrical output of the photodiode was connected through a bandpass filter to a lock-in-amplifier. The reference to the lock-in-amplifier was provided from the serrodyne waveform driving the fibre stretcher. The output of the lock-in-amplifier was monitored with either a spectrum analyser or oscilloscope. The interferometric sensor consisted of a Mach-Zehnder interferometer with an air-gap in one arm to permit adjustment of the optical path difference. The air-gap could be adjusted manually at a resolution of 2 μm. The light output from the Mach-Zehnder interferometer was directed to an optical channel monitor

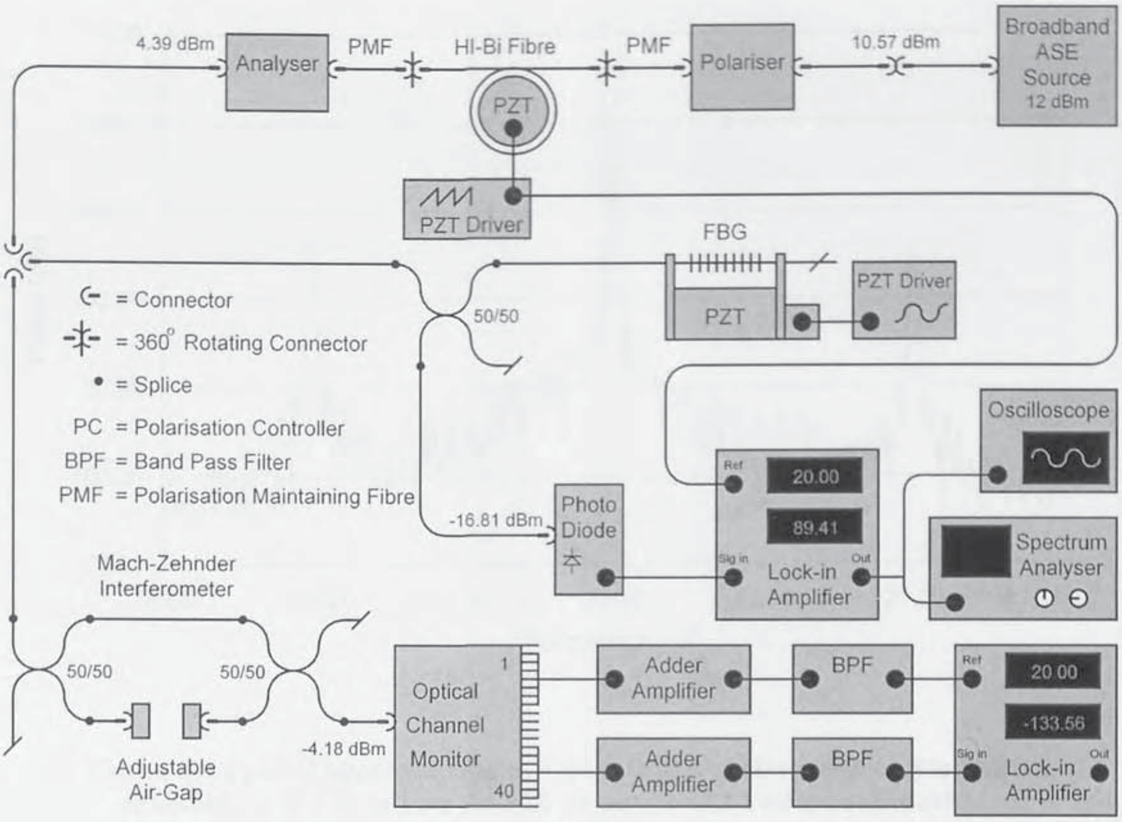

Figure 8.3 Experimental set-up.

and the electrical outputs connected via a pair of adders and bandpass filters to a lock-in-amplifier (see section 7.4).

8.5 Fibre Bragg Grating Sensing

The first demonstration using the Hi-Bi fibre interferometer adopts interferometric wavelength shift detection [13] as described in section 6.7. The phase of the Hi-Bi fibre interferometer was modulated at 20 Hz and a low frequency strain amplitude of 1 $\mu\varepsilon$ at 1 Hz applied to the fibre Bragg grating sensor. The fibre Bragg grating had a centre wavelength of 1558.29 nm and a -3 dB bandwidth of 0.125 nm (see FBG 3

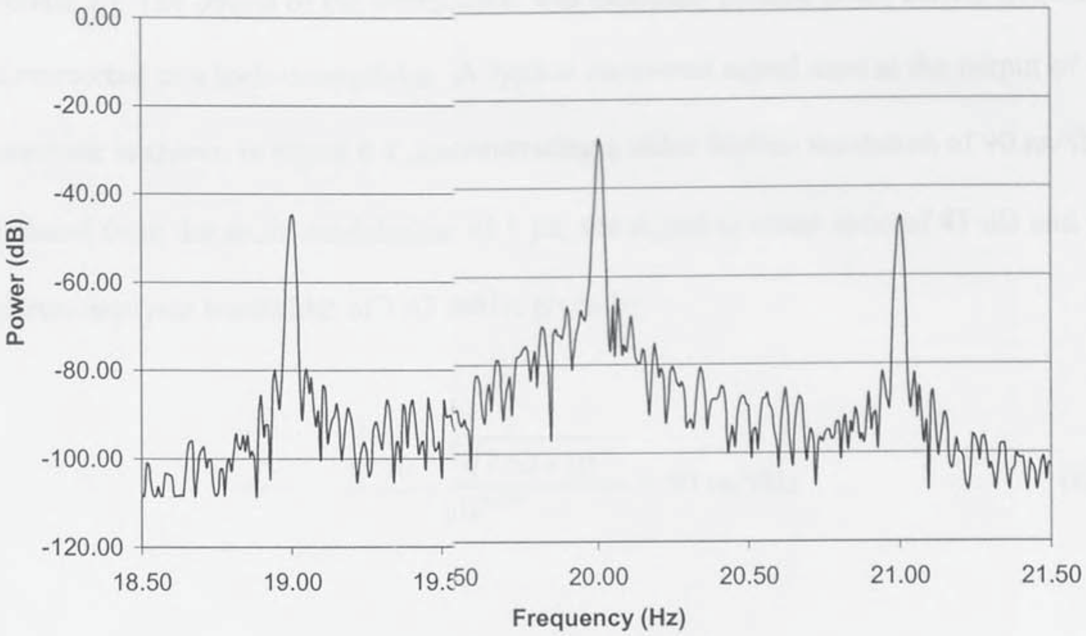

Figure 8.4 Typical spectrum due to a fibre Bragg grating with applied strain modulation of 1 με at 1 Hz on a 20 Hz carrier (7.63 mHz bandwidth).

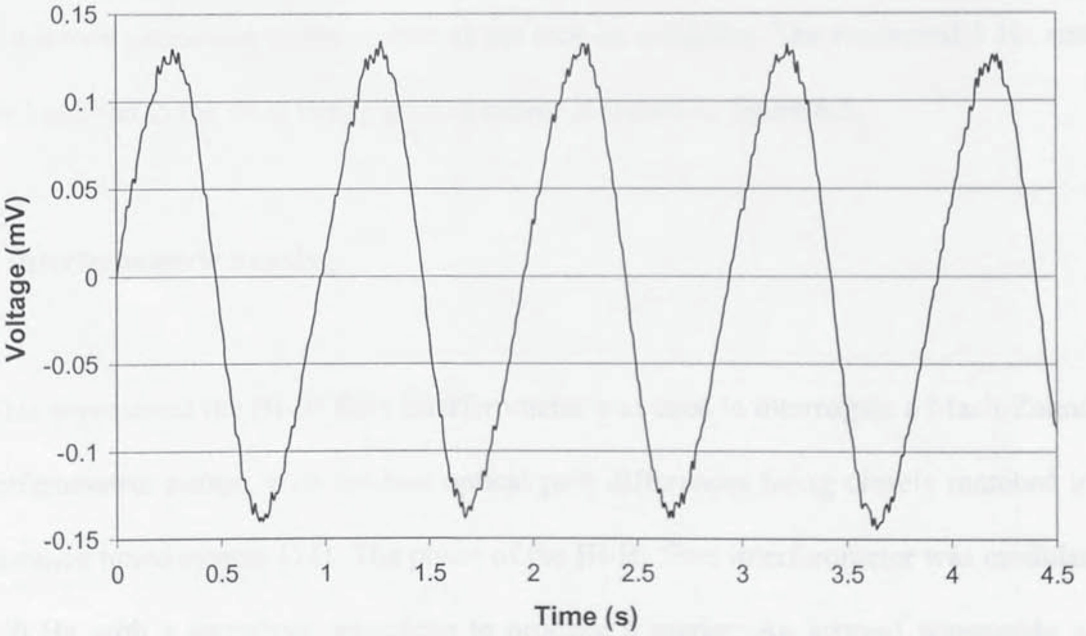

Figure 8.5 Recovered 1 με signal at 1 Hz

appendix E). The output of the photodiode was bandpass filtered at the carrier frequency and connected to a lock-in amplifier. A typical recovered signal seen at the output of the photodiode is shown in figure 8.4 demonstrating a noise limited resolution of 90 nε/√Hz, calculated from the strain modulation of 1 με, the signal-to-noise ratio of 41 dB and the spectrum analyser bandwidth of 7.63 mHz, given by

$$\frac{1\times10^{-6}/\sqrt{7.63\times10^{-3}}}{10^{41/20}} = 90\ \text{n}\varepsilon/\sqrt{\text{Hz}} \tag{8.4}$$

The resolution of the system is however fundamentally limited by shot noise in the photodetector $(2eIB)^{1/2}$ as described in section 6.7.1.1, indicating that a signal smaller than 1.3 μA/√Hz will never be observed. The serrodyne modulation frequency was used as the reference to the lock-in amplifier and the phase shift monitored using an oscilloscope connected to the output of the lock-in amplifier. The recovered 1 Hz strain signal applied to the fibre Bragg grating sensor is shown in figure 8.5.

8.6 Interferometric Sensing

In this experiment the Hi-Bi fibre interferometer was used to interrogate a Mach-Zehnder interferometric sensor, with the two optical path differences being closely matched in a coherence tuned system [14]. The phase of the Hi-Bi fibre interferometer was modulated at 20 Hz with a serrodyne waveform to produce a carrier. An arrayed waveguide was used to implement a dual wavelength interrogation scheme as described in section 7.4. The two selected sets of neighbouring OCM channels are 21 ↔ 30 (λ_{21} = 1544.53 nm ↔ λ_{30} = 1537.40 nm) and 6 ↔ 15 (λ_6 = 1556.55 nm ↔ λ_{15} = 1549.32 nm). The optical path

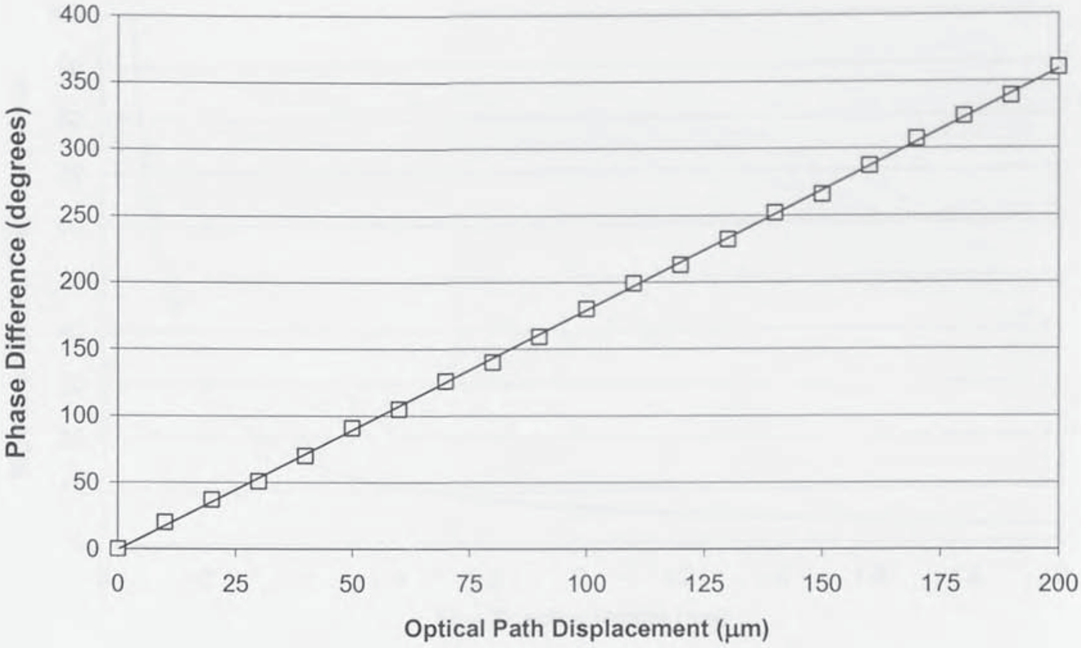

Figure 8.6 Phase difference vs. optical path displacement. Experimental results (squares). Least squares fit to the data is shown by solid line (rms deviation from linearity 1.1 μm).

difference in the Mach-Zehnder interferometer was manually adjusted at 10 μm intervals and the phase difference recorded from the lock-in-amplifier. The results are shown in figure 8.6 displaying a root mean squared deviation from linearity [15] of 1.1 μm and an unambiguous range in terms of a change in the Mach-Zehnder optical path difference of 200 μm. The theoretical values agree quite well with the experimental values (see appendix N) displaying a mean error of $\pm 1.76^0$ corresponding to a mirror displacement of 0.97 μm.

8.7 System Limitations

The three main limitations of the system are firstly the long fibre lengths needed to achieve a small free spectral range (see figure 8.7) making the interferometer more

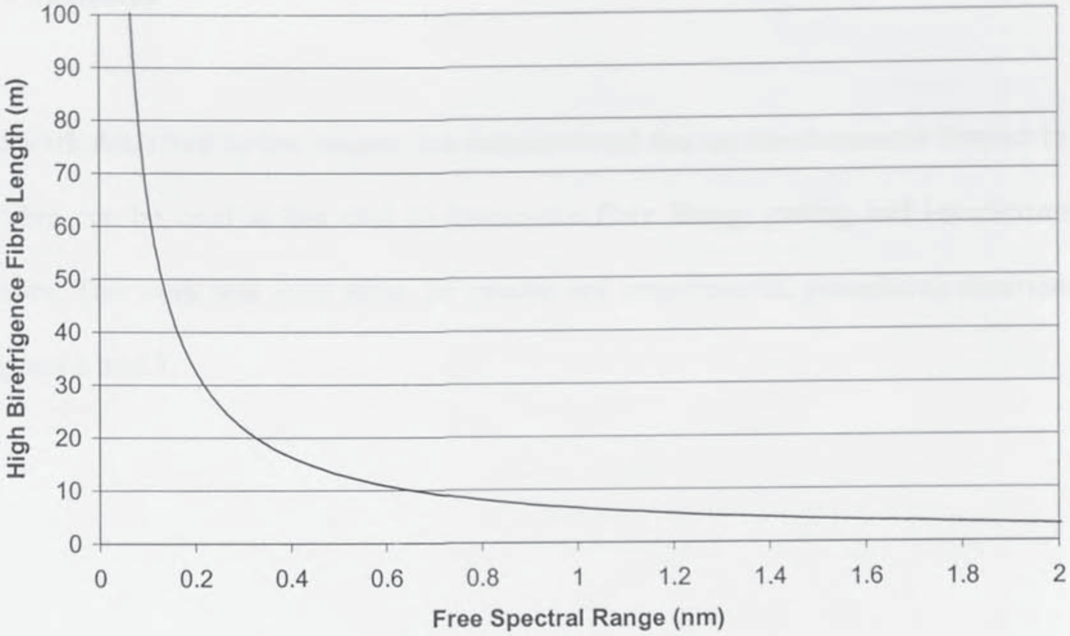

Figure 8.7 High birefringence fibre length vs. free spectral range.

susceptible to environmental changes. Secondly, if a larger free spectral range is required shorter lengths of fibre are needed. However, the increase in the amount of strain required to drive the interferometer over a fringe could cause the fibre to reach its breaking point, placing an upper limit (not tested) on the free spectral range. Finally, the low carrier frequency of 20 Hz could be improved using a power amplifier driving a multi-element piezo electric stack pushing the bandwidth up into the kilohertz range whilst enabling higher strains to be used with concomitant reduction if the fibre length and sensitivity to environmental perturbations.

8.8 Conclusion

The work described in this chapter has demonstrated that an interferometer formed in Hi-Bi fibre can be used at low cost to interrogate fibre Bragg grating and interferometric sensors. The work was built upon the results and experimental procedures described in chapters 6 and 7.

8.9 References

[1] W. Eickhoff, "Temperature sensing by mode mode interference in birefringent optical fibers," *Optics Letters*, vol. 6, No. 4, pp. 204-206, April 1981

[2] K. T. V. Grattan and B. T. Meggitt, "Optical fibre sensor technology," Chappman & Hall, pp. 198-199, 1995

[3] G. Meltz and J. R. Dunphy, "Optical fiber stress wave sensor," *in Proceedings SPIE Fibre Optic Sensors V*, vol. 838, pp. 69-77, August 1987

[4] S. C. Rashleigh, "Polarimetric sensors: exploiting the axial stress in Hi-Bi fibre," *in Proceedings 1st International Conference on Optical Fibre Sensors*, (OFS-1, London, United Kingdom), Technical Digest, pp. 210-213, April 1983

[5] A. D. Kersey, M. Corke and D. A. Jackson, "Linearised polarimetric optical fibre sensor using a heterodyne type signal recovery," *Electronics Letters*, vol. 20, No. 5, pp. 209-211, March 1984

[6] F. Picherit, "Double polarimetric interferometer with coherence multiplexing. A pressure and temperature sensor using optical fibres," *in Proceedings 7th International Conference on Optical Fibre Sensors*, (OFS-7, Sydney, Australia), Technical Digest, pp. 369-372, December 1990

[7] Y. Mitsuhashi and S. Ishihara, "Fibre optic polarization interferometer for temperature sensing using a polarization rotating coupler," *in Proceedings 2nd International Conference on Optical Fibre Sensors*, (OFS-2, Stuttgart, Germany), Technical Digest, pp. 195-198, September 1984

[8] W. J. Bock and W. Urbanczyk, "Coherence multiplexing of fiber optic pressure and temperature sensors based on highly birefringent fibers," *Transactions on Instrumentation and Measurement*, vol. 49, No. 2, pp. 392-397, April 2000

[9] K. T. V. Grattan and B. T. Meggitt, "Optical fibre sensor technology," *Chapman & Hall*, ISBN 0-412-59210-X, 1995

[10] N. Shibata, Y, Sasaki, K. Okamoto and T. Hosaka, "Fabrication of polarization maintaining and absorbtion reducing fibers," *Journal of Lightwave Technology*, vol. LT-1, No. 1, pp. 38-43, March 1983

[11] W. Eickhoff, "Stress induced single polarization single mode fiber," *Optics Letters*, vol. 7, No. 12, pp. 629-631, December 1982

[12] J. Noda, K. Okamoto and Y. Sasaki, "Polarization maintaining fibers and their applications," *Journal of Lightwave Technology*, vol. Lt4, No. 8, pp. 1071-1089, August 1986

[13] A. D. Kersey, T. A. Berkoff and W. W. Morey, "Fibre optic Bragg grating strain sensor with drift compensated high resolution wavelength shift detection," *Optics Letters*, vol. 18, No. 1, pp. 72-73, January 1993

[14] R. A. Patten, "Michelson interferometer as a remote gauge," *Applied Optics*, vol. 10, No. 12, pp. 2717-2721, December 1971

[15] J. R. Taylor, "An introduction to error analysis the study of uncertainties in physical measurements," *University Science Books*, (Second Edition), ISBN: 0-935702-75-X, 1997

9 Fibre Bragg Grating Sensor Interrogation using an Acousto-Optic Tuneable Filter

Acousto-optic scattering of light is a very well reported phenomena. Many optical sensing systems have subsequently been developed using various acousto-optic devices. The work described in this chapter uses an acousto-optic tuneable filter (AOTF) to provide wavelength demultiplexing whilst at the same time generating a high-frequency carrier signal at the output of an all fibre Mach-Zehnder interferometer. The system is then demonstrated by interrogating dynamic strains in fibre Bragg grating sensors using interferometric wavelength shift detection.

9.1 Introduction

The first reports using an AOTF to interrogate fibre Bragg grating sensors goes back to the mid 1990s [1]-[3]. Since then, there seems to have only been very little other published reports on this subject. Firstly, Christmas *et al* [4] in 2001 demonstrated the use of an AOTF to sequentially interrogate dynamic strains in serial arrays of fibre Bragg grating sensors using interferometric wavelength shift detection and secondly, Boulet *et al* [5] also in 2001 demonstrated the use of an AOTF to simultaneously interrogate dynamic strains in multiplexed fibre Bragg grating sensors using interferometric wavelength shift detection. Boulet *et al* in their work also proposed the use of an AOTF to generate a high-frequency carrier signal at the output of a Mach-Zehnder interferometer pushing the bandwidth of the recovered strain up into the megahertz region and helping to reduce the component count of the system. The work described in this chapter successfully implements this proposal as discussed below.

9.2 Generating the High-Frequency Carrier Signal

The advantage of using heterodyne interferometry in optical sensing is the ability to perform phase measurements by generating a carrier signal. In chapters 6 and 7 this was achieved by increasing the optical path in one arm of a Mach-Zehnder interferometer using an integrated optic phase modulator. To generate a carrier signal using an AOTF the device is first incorporated into one arm of a Mach-Zehnder interferometer (see appendix D). The application of a single radio frequency (RF) signal f_{rf} causes the AOTF to transmit a narrow band of light varying as a function of the RF drive frequency f_{rf} (see section 4.2). When the light is recombined interference fringes are formed over the bandwidth of the filtered light modulated at frequency f_{rf} generating a carrier.

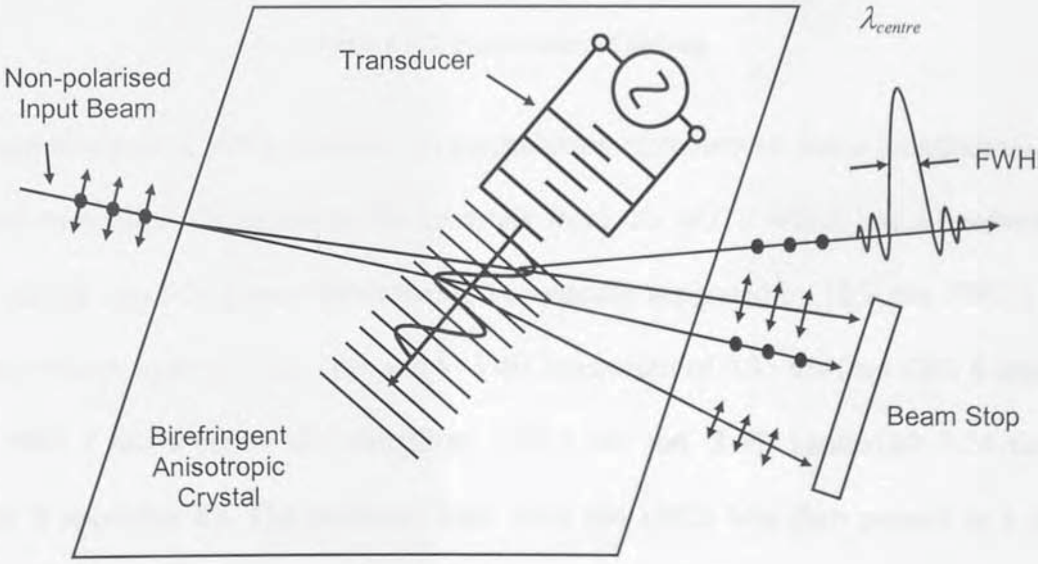

Figure 9.1 Non-collinear acousto-optic tuneable transmission characteristics.

9.3 Experimental Set-Up

The experimental set up is shown in figure 9.2. Light from the broadband source passed through an unbalanced Mach-Zehnder interferometer. One arm contained an AOTF (see section 4.3) and the other arm an air-gap to adjust the optical path difference. Polarisation controllers were used in each arm to optimise the fringe visibility [6]. The light was then irected to a pair of FBGs mounted on piezoelectric stretchers so that a longitudinal strain could be applied. To minimise the crosstalk from the AOTF which has a bandwidth of 4.5 nm the two FBGs were fabricated to be optically separated by 15.2 nm. FBG 1 had a centre wavelength of 1558.6 nm and a -3 dB bandwidth of 0.31 nm (see FBG 8 appendix E). FBG 2 had a centre wavelength of 1543.4 nm and -3 dB bandwidth 0.34 nm (see FBG 9 appendix E). The reflected light from the FBGs was then passed to a photo-detector. The output of the photo-detector was connected to a frequency mixer together with the output of the voltage control oscillator (VCO). The VCO output was also

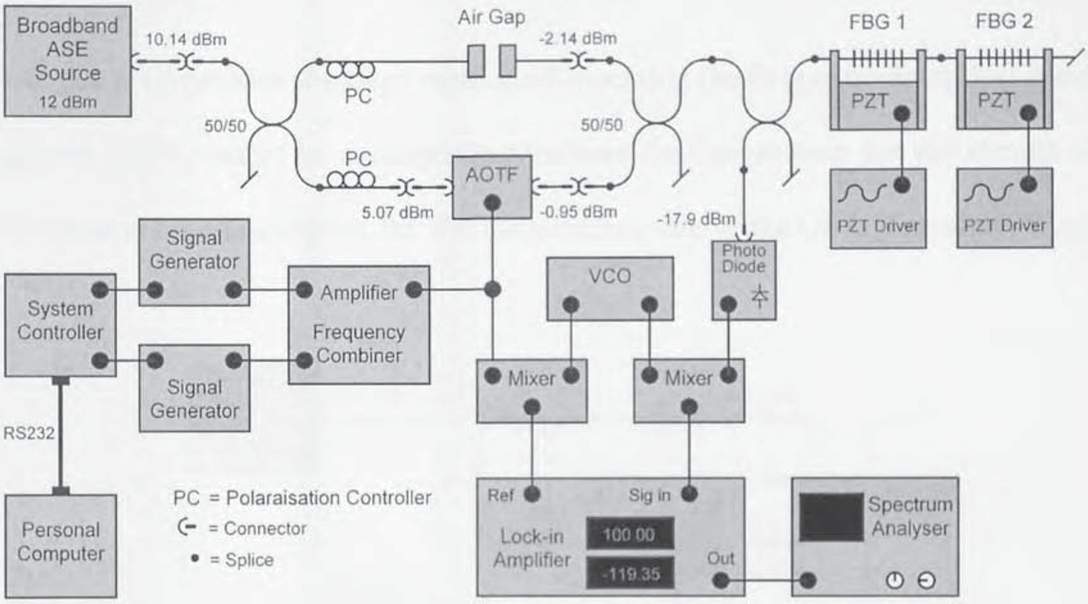

Figure 9.2 Experimental set-up.

connected to a second frequency mixer along with the RF output from the AOTF driver. The outputs from the two frequency mixers were connected to a low-frequency (1 Hz - 1 MHz) lock-in-amplifier (see appendix F). The output of the lock-in-amplifier was monitored using a spectrum analyser.

9.4 Setting the Free Spectral Range of the Interferometer

With this configuration the usual method of observing the fringes on an optical spectrum analyser (OSA) cannot be accomplished because the fringes over the wavelength range of interest are modulating too fast for the sampling rate of the OSA. Therefore, to set the free spectral range the interferometer output was connected to a RF spectrum analyser via a photodetector. The interferometer could then be balanced by optimising the power of the detected RF signal driving the AOTF by adjusting the air-gap. The free spectral range

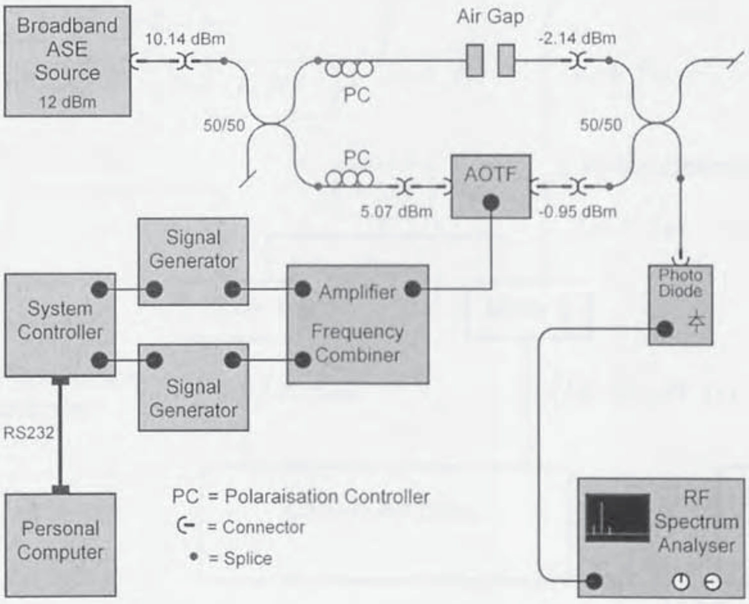

Figure 9.3 Setting the free spectral range of the interferometer output.

could then easily be set by readjusting the air-gap to the corresponding optical path difference.

9.5 Fibre Bragg Grating Sensing

To demonstrate the system the two FBG sensors were sequentially interrogated. The optical path difference in the interferometer was set to 6 mm corresponding to a free spectral range of 0.4 nm at the central wavelength of the source. FBG 1 was selected

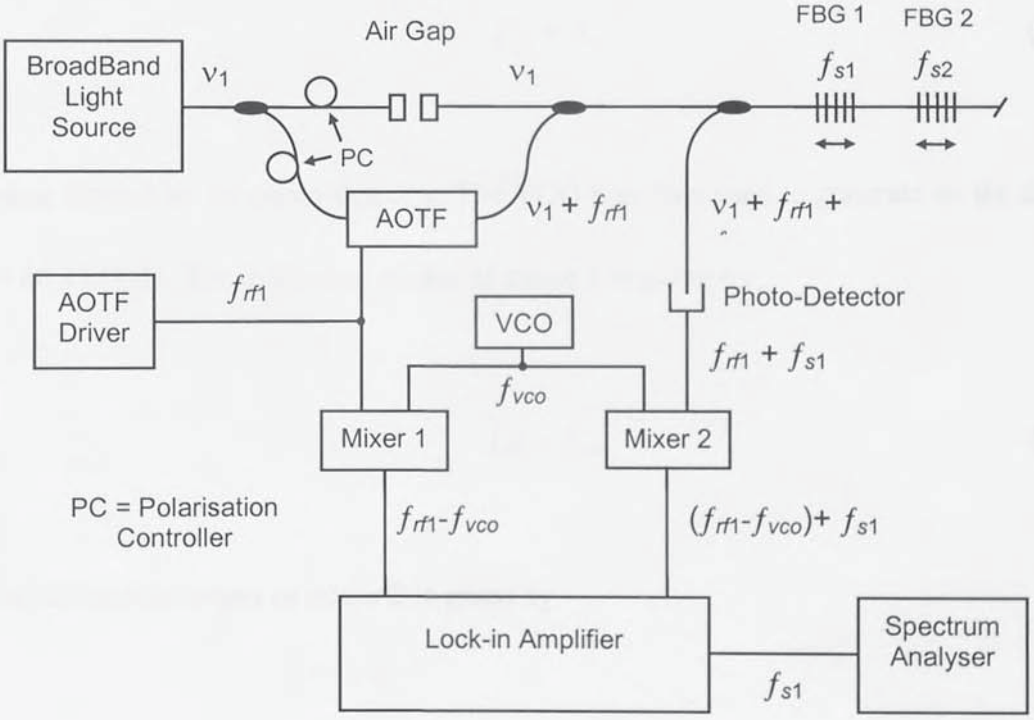

Figure 9.4 Diagram depicting the frequency response while interrogating FBG 1.

first. The AOTF was driven at f_{rf1} = 66.27 MHz corresponding to the Bragg wavelength of FBG 1. FBG 1 and FBG 2 were driven at the same time with low frequency strain amplitudes of 5.5 με at f_{s1} = 7 Hz and 5.5 με at f_{s2} = 15 Hz, respectively. The frequency response of the spectrum reflected by FBG 1 is given by

$$\nu_1 + f_{rf1} + f_{s1} \tag{9.1}$$

where ν_1 is the frequency of the light source corresponding to the Bragg wavelength of the sensor (see figure 9.4). The response at the output of the photo-detector is given by

$$f_{rf1} + f_{s1} \tag{9.2}$$

ν_1 being filtered by the photo-detector. The VCO was then used to generate an RF signal f_{vco}= 66.17 MHz. The difference output of mixer 1 is given by

$$f_{rf1} - f_{vco} \tag{9.3}$$

and the difference output of mixer 2 is given by

$$f_{rf1} - f_{vco} + f_{s1} \tag{9.4}$$

The output of mixer 1 at 100 kHz was used as the reference to the lock-in-amplifier. Mixer 2 was connected to the signal input of the lock-in-amplifier to recover the strain

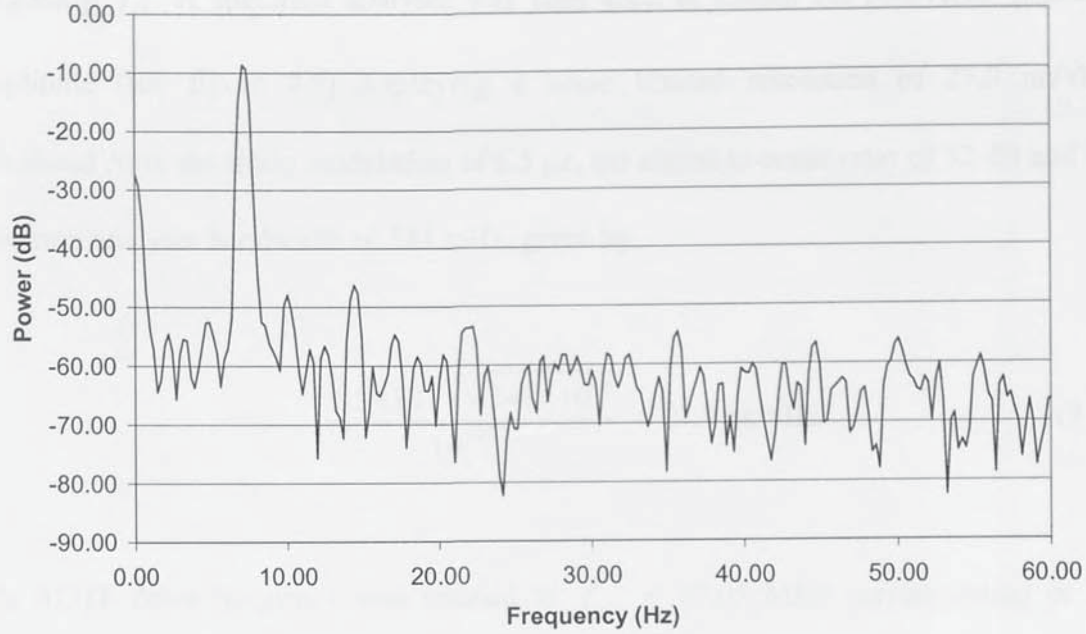

Figure 9.5 Recovered strain amplitude of 5.5 $\mu\varepsilon$ at 7 Hz applied to FBG1.

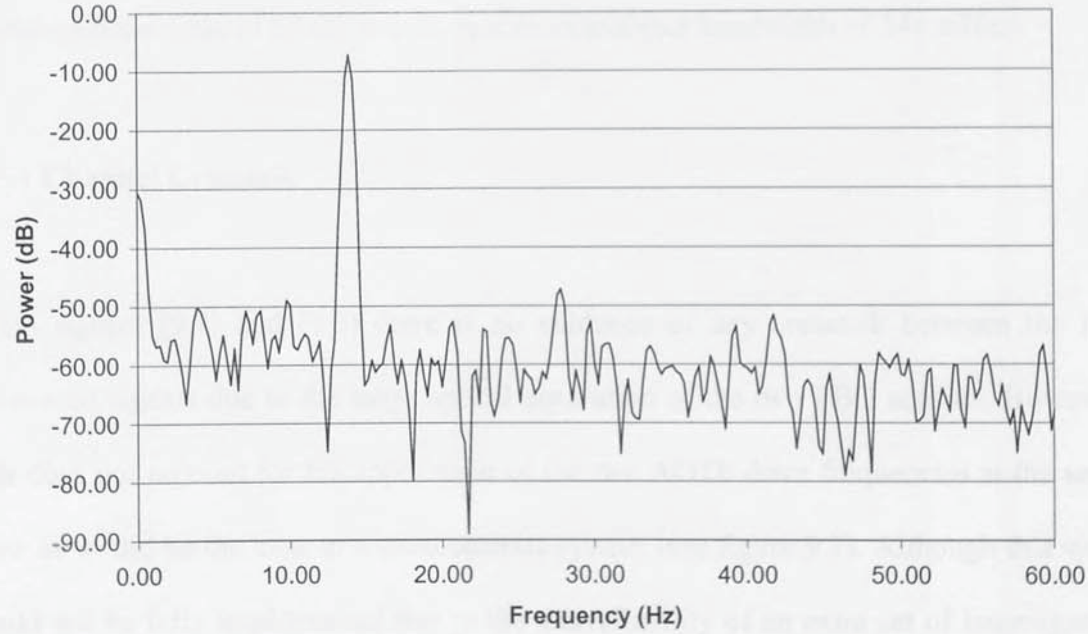

Figure 9.6 Recovered strain amplitude of 5.5 $\mu\varepsilon$ at 15 Hz applied to FBG2.

frequency f_{s1}. A spectrum analyser was then used to record the recovered sideband amplitude (see figure 9.5) displaying a noise limited resolution of 27.9 nε/√Hz, calculated from the strain modulation of 5.5 με, the signal-to-noise ratio of 52 dB and the spectrum analyser bandwidth of 244 mHz, given by

$$\frac{5.5\times10^{-6}/\sqrt{244\times10^{-3}}}{10^{52/20}} = 27.9\ \text{n}\varepsilon/\sqrt{\text{Hz}} \qquad (9.5)$$

The AOTF drive frequency was retuned to f_{rf2} = 67.05 MHz corresponding to the wavelength of FBG 2 and the VCO set to f_{vco} = 66.95 MHz. The same analogy as above was then employed to interrogate FBG 2 (see figure 9.6). FBG 2 displays a noise limited strain resolution of 24.9 nε/√Hz, calculated from the strain modulation of 5.5 με, the signal-to-noise ratio of 53 dB and the spectrum analyser bandwidth of 244 mHz.

9.5.1 Channel Crosstalk

From figures (9.4) and (9.5) there is no evidence of any crosstalk between the two recovered signals due to the large optical separation of the two FBG sensors. However, this does not account for the application of the two AOTF drive frequencies at the same time as would be the case in a simultaneous system (see figure 9.7). Although this work could not be fully implemented due to the unavailability of an extra set of interrogating electronics the crosstalk between the two FBG sensors could still be tested. This was achieved by driving the AOTF with f_{rf1} = 66.27 MHz corresponding to the Bragg wavelength of FBG 1 and f_{rf2} = 67.39 MHz corresponding to the Bragg wavelength of a

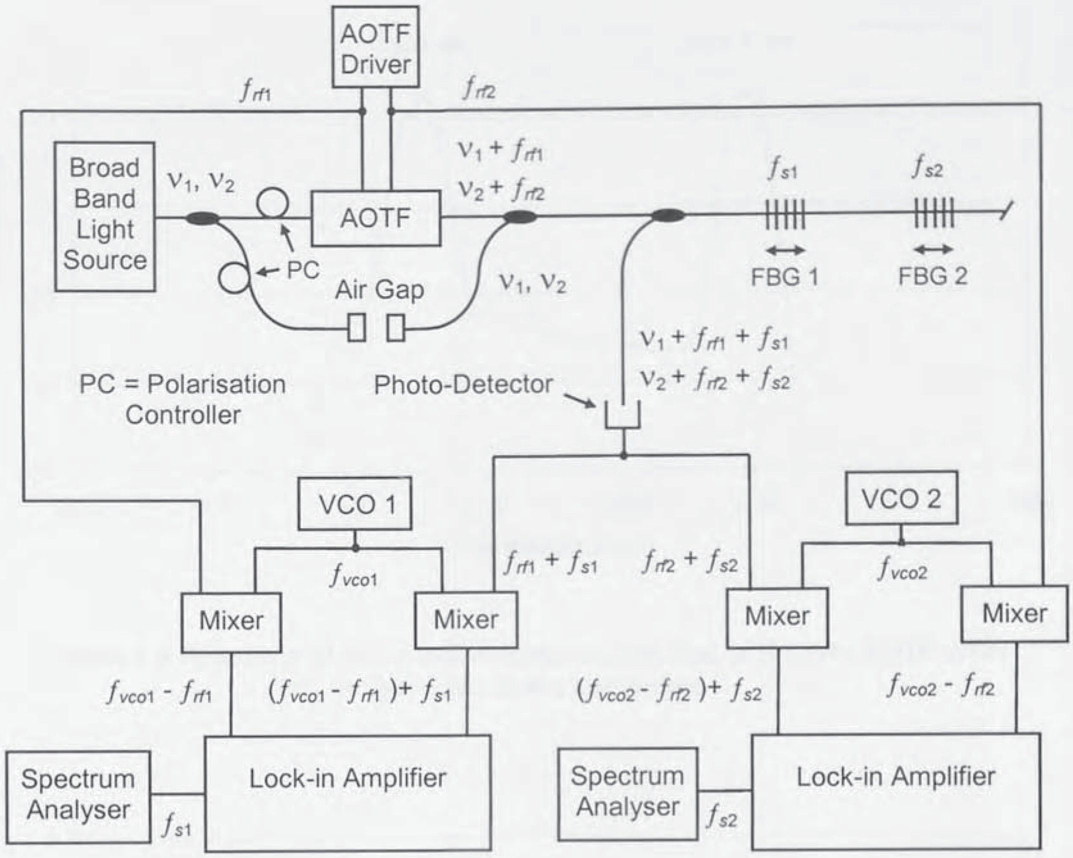

Figure 9.7 Proposed experimental set-up for simultaneous interrogation.

new FBG 2 which had a central wavelength of 1535.4 nm and a -3 dB bandwidth of 0.33 nm (see FBG 10 appendix E). The spectrum of the interferometer output as seen on an optical spectrum analyser due to the application of the two AOTF drive frequencies is shown in figure 9.8. FBG 1 and FBG 2 were driven at the same time with low frequency strain amplitudes of 5.5 με at $f_{s1} = 10$ Hz and 5.5 με at $f_{s2} = 15$ Hz, respectively. The response observed by the spectrum analyser is shown in figure 9.9 displaying a noise limited resolution of 41.3 nε/√Hz, calculated from the strain modulation of 5.5 με, the signal-to-noise ratio of 49 dB and the spectrum analyser bandwidth of 244 mHz. More

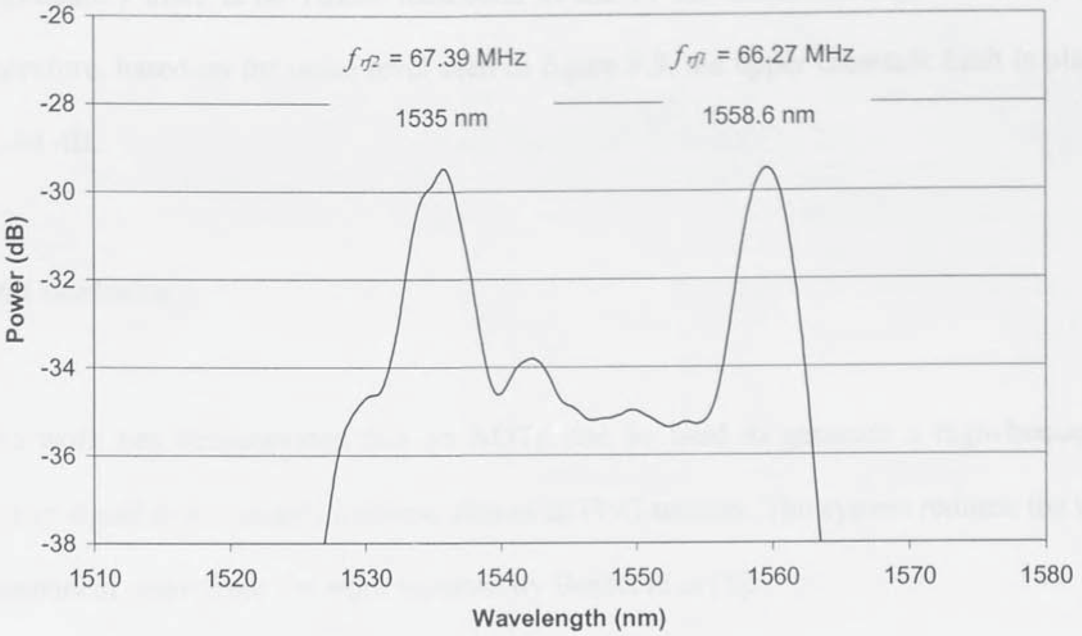

Figure 9.8 Spectrum of the interferometer output due to the two AOTF drive frequencies at the same time.

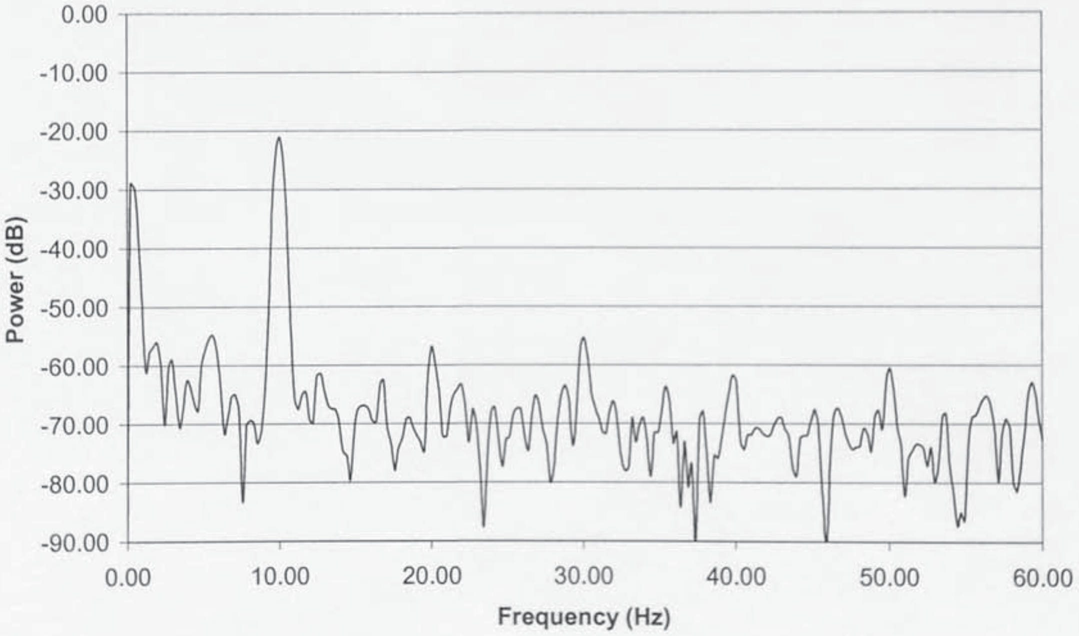

Figure 9.9 Recovered strain amplitude of 5.5 με at 10 Hz applied to FBG 1.

significantly there is no visible indication of the 15 Hz modulation applied to FBG 2. Therefore, based on the noise level seen in figure 9.9, the upper crosstalk limit is placed at -64 dB.

9.6 Conclusion

The work has demonstrated that an AOTF can be used to generate a high-frequency carrier signal to interrogate dynamic strains in FBG sensors. The system reduces the total component count from the work reported by Boulet *et al* [5].

9.7 References

[1] M. G. Xu, H. Geiger, J. L. Archambault and J. P. Dakin, "Novel interrogating system for fibre Bragg grating sensors using an acousto-optic tunable filter," *Electronics Letters*, vol. 29, No. 17, pp. 1510-1511, August 1993

[2] H. Geiger, M. G. Xu, N. C. Eaton and J. P. Dakin, "Electronic tracking system for multiplexed fibre grating sensors," *Electronics Letters*, vol. 31, No. 12, pp. 1006-1007, June 1995

[3] M. Volanthen, H. Geiger, M. G. Xu and J. P. Dakin, "Simultaneous monitoring of multiple fibre gratings with a single acousto-optic tunable filter," *Electronics Letters*, vol. 32, No. 13, pp. 1228-1229, June 1996

[4] S. P. Christmas and D. A. Jackson, "A new method for interrogation of serial arrays of dynamic FBG strain sensors," *Measurement Science and Technology*, vol. 12, pp. 897-900, May 2001

[5] C. Boulet, D. J. Webb, M. Douay and P. Naiy, "Simultaneous interrogation of fibre Bragg grating sensors using an acousto-optic tunable filter," *Photonics Technology Letters*, vol. 13, No. 11, pp. 1215-1217, November 2001

[6] A. Dandridge and A. D. Kersey, "Overview of Mach Zehnder sensor technology and applications," *in Proceedings SPIE Fibre Optic and Laser Sensors VI*, vol. 985, pp. 34-52, September 1988

10. Thesis Conclusion

This thesis has described the implementation of several novel fibre optic sensor interrogation solutions constructed using "of the shelf" optical components. The purpose of this is to enable lower-cost implementation of fibre optic sensor systems not only to the normal niche applications but also into applications where they can directly compete with their electro-mechanical counterparts. The research work focused on four fields of interest. Firstly, the use of an arrayed waveguide grating to interrogate fibre Bragg grating sensors and secondly to interrogate interferometric sensors. The use of an arrayed waveguide grating does not at the present time provide a truly low-cost interrogation system but potentially could be. However, it does have the advantage of being highly flexible. Thirdly, the investigation of a differential path interferometer constructed from high-birefringence optical fibre to interrogate interferometric and fibre Bragg grating sensors. This could be a truly low-cost interrogating interferometer in comparison with an integrated optic device. Fourth and finally, the extended use of acousto-optic tuneable filters to interrogate fibre Bragg grating sensors. This scheme is an improvement over previously reported work which may be the cheapest solution where megahertz bandwidths might be needed.

10.1 Retrospect

This thesis began by introducing the reader to the past, present and future of fibre optic sensors. Chapter 2, 3, 4 and 5 detailed the fibre optic sensing technologies relevant for the experimental work described in chapters 6, 7, 8 and 9. The four experimental chapters 6, 7, 8 and 9 are summarised in table 10.1 and each approach reviewed separately below.

Scheme	Performance	Positive Features	Negative Features	Comparison
Fibre Bragg Grating Sensor Interrogation using an Arrayed Waveguide Grating	Chirped grating. Tested useable range: 1890 με Heterodyne approach. Dynamic strain resolution: 17 nε/√Hz at 30 Hz	Highly Flexible Ease of processing the OCM outputs	Not truly low-cost	Useable range: 500 με [1] Dynamic strain resolution: 1.5 – 96 nε/√Hz [1] – [6]
Interferometric Sensor Interrogation using an Arrayed Waveguide Grating	Active interrogation. Tested Unambiguous range: 1500 μm Passive interrogation. Unambiguous range: 370 μm	Highly Flexible Ease of processing the OCM outputs	Not truly low-cost	Active interrogation. Unambiguous range: 755 μm [6] Passive interrogation. Unambiguous range: 40 - 70 μm [7] - [9]
High-Birefringence Fibre Interferometer for Optical Sensing Applications	Fibre Bragg grating sensing. Dynamic strain resolution: 90 nε/√Hz at 1 Hz Interferometric sensing. Tested unambiguous range: 200 μm	Potentially low-cost.	Long fibre lengths Low Bandwidth	Dynamic strain resolution: 96 nε/√Hz [1] Unambiguous range: 370 μm [10]
Fibre Bragg Grating Sensor Interrogation using an Acousto-Optic Tuneable Filter	Dynamic strain resolution: 24.9 nε/√Hz at 15 Hz	Cheap solution for high bandwidth sensing application (e.g. ultrasound)	Experimental work needs to be completed	Dynamic strain resolution: 150 nε/√Hz at 10 Hz [11]

Table 10.1 Summary of each experimental approach.

Fibre Bragg Grating Sensor Interrogation using an Arrayed Waveguide Grating

Arrayed waveguide gratings provide an excellent solution to interrogate fibre Bragg grating sensors as described in chapter 6. The static range of interrogation was improved using a chirped grating spanning several arrayed waveguide grating channels and detecting the grating position using a centroid fit of the recovered data. The range of the system can be selected by simply sampling the appropriate optical channel monitor outputs. The dynamic range of the system was improved by implementing a heterodyne approach based on interferometric wavelength shift detection. By electrically adding outputs of the optical channel monitor the range of the strain induced wavelength shift can be extended indefinitely. The most uniform responses were obtained with a wide-bandwidth grating or a grating with a double peak structure. Even though double peak gratings are more complicated to record, they offer the possibility of increasing the sensitivity because the two peaks can be made with narrow bandwidths.

Interferometric Sensor Interrogation using an Arrayed Waveguide Grating

This work described in chapter 7 demonstrated that arrayed waveguide gratings can also be used to successfully interrogate interferometric sensors using the dual wavelength technique. When the Bookham optical channel monitor is used to interrogate an interferometer illuminated by a broadband source, it provides information equivalent to illuminating the interferometer with 40 discrete light sources, each with the bandwidth of an arrayed waveguide grating passband. This provides a considerable amount of spectral information. By using an active interferometric sensor the cavity displacement could be measured with the desired sensitivity by selecting two optical channel monitor outputs.

However, the requirement for active components at the sensor is undesirable. Therefore, to overcome this problem a second processing interferometer was introduced away from the interferometric sensor with its optical path difference closely matched with that of the sensor forming a composite coherence-tuned system. The passive sensor interrogation provides a much more practical solution but at the cost of increased system complexity. The two low-coherence light sources required for this type of interrogation were effectively simulated by electrically adding a number of optical channel monitor outputs. Adding appropriate weighting to the optical channel monitor outputs could, for example, provide apodisation. Therefore, the arrayed waveguide grating represents a highly flexible component for use in interferometric sensor interrogation system.

High-Birefringence Fibre Interferometer for Optical Sensing Applications

In chapter 8 a differential path interrogating interferometer formed from a length of high-birefringence fibre was demonstrated at potentially lower cost to interrogate interferometric and fibre Bragg grating sensors. This type of interferometric configuration is analytically similar to the Mach-Zehnder type except in this case both interferometer arms are subjected to the serrodyne modulation. This places an upper limit on the free spectral range because of the shorter fibre lengths required to achieve the smaller optical path difference with concomitant increase in the strain modulation needed to drive the interferometer over one fringe. The two sensors types were successfully interrogated using the methods discussed in chapters 6 and 7.

Fibre Bragg Grating Sensor Interrogation using an Acousto-Optic Tuneable Filter

Chapter 9 demonstrated the use of an acousto-optic tuneable filter to generate a high-frequency carrier at the output of an interrogating Mach-Zehnder interferometer. This work was built on the proposal of Boulet *et al* [11]. In their work they suggested one way to increase their interrogating system bandwidth (to orders of megahertz's) an acousto-optic modulator could be used to generate a high-frequency carrier signal at the output of a Mach-Zehnder interferometer. This proposal was successfully demonstrated by sequentially interrogating two fibre Bragg grating sensors.

10.2 Original Contributions from this Thesis

The important original contributions described in this thesis are:

- The use of an arrayed waveguide grating to increase the sensing range of dc strains in fibre Bragg grating sensors
- The use of an arrayed waveguide grating to interrogate dynamic strains in fibre Bragg grating sensors
- The use of an arrayed waveguide grating to interrogate interferometric sensors
- The use of a differential interrogating interferometer formed from a length of high-birefringence fibre
- The use of an acousto-optic tuneable filter to generate a high-frequency carrier at the output of a Mach-Zehnder interferometer

10.3 Suggested Future Work

In terms of all the interrogation schemes described the natural progression would unquestionably be to demonstrate working prototype systems for real world sensing applications. To achieve this, a number of issues and recommendations of further research work needs to be addressed.

- Demonstrate a fibre Bragg grating and interferometric sensor interrogation scheme using an athermal arrayed waveguide grating.
- Produce a detailed comparison between the Bookham optical channel monitor (or similar device) and an athermal device regarding the system resolution, price and operating costs.
- Investigate the recovery of high frequency strain signals from fibre Bragg grating sensors using the arrayed waveguide grating. This could be achieved for instance by gluing fibre Bragg grating sensors to the diaphragm of an audio speaker and driving it with a function generator.
- Demonstrate a fully multiplexed fibre Bragg grating sensor interrogation scheme using an arrayed waveguide grating. Fully characterise the scheme using temperature/strain discriminating fibre Bragg grating sensors. Investigate and develop a prototype user interface.
- Investigate the use of an integrated optic Mach-Zehnder interferometer.
- Demonstrate the high-birefringence interrogating interferometer using a power amplifier driving a multi-element piezoelectric stack in an attempt to push the bandwidth up into the kilohertz range. Quantify the upper limit of the free spectral range before the fibre breaks.

- Study the effects of packaging the interrogation systems for non-laboratory installation.
- Demonstrate the acousto-optic tuneable filter scheme to simultaneously interrogate fibre Bragg grating sensors. Initially completing the work using two fibre Bragg grating sensors as suggested in chapter 9. Then testing the system with more than two sensors fully quantifying the crosstalk between them.
- Study and characterise the interrogation of high-frequency dynamic strains using the acousto-optic scheme and make a detailed comparison with a system utilising an integrated optic phase modulator in an all fibre Mach-Zehnder interferometer and/or an integrated optic Mach-Zehnder device.

10.4 References

[1] D. C. C. Norman, D. J. Webb and R. D. Pechstedt, "Interrogation of fibre Bragg grating sensors using an arrayed waveguide grating," *Measurement Science and Technology*, vol. 15, pp. 691-698, November 2004

[2] Y. Sano and T. Yoshino, "Fast optical wavelength interrogator employing arrayed waveguide grating for distributed fiber Bragg grating sensors," *Journal of Lightwave Technology*, vol. 21, No. 1, pp 132-139, January 2003

[3] A. D. Kersey and T. A. Berkoff, "Fiber Bragg grating array sensor system using a bandpass wavelength division multiplexer and interferometric detection," *Photonics Technology Letters*, vol. 8, No. 11, pp.1522-1524, November 1996

[4] A. D. Kersey, T. A. Berkoff and W. W. Morey, "Fiber optic Bragg grating strain sensor with drift compensated high resolution interferometric wavelength shift detection," *Optics Letters*, vol. 18, No. 1, pp. 72-74, January 1993

[5] T. A. Berkoff and A. D. Kersey, "Matched filter interrogation technique for fibre Bragg grating arrays," *Electronics Letters*, vol. 31, No. 10, pp. 822-823, May 1995

[6] D. J. Webb and R. D. Pechstedt, "Sensing applications of arrayed waveguide grating devices," *in Proceedings 15th International Conference on Optical Fibre Sensors*, (OFS-15, Portland, USA), Technical Digest, pp. 569-572, May 2002.

[7] A. D. Kersey and A. Dandridge, "Dual-wavelength approach to interferometric sensing," *in Proceedings SPIE Fiber Optic Sensors II*, vol. 798, pp. 178-181, 1987

[8] D. J. Webb, J. D. C. Jones and D. A. Jackson, "Extended range interferometry using a coherence tuned, synthesized dual-wavelength technique with multimode fibre links," *Electronics Letters*, vol. 24, No. 24, pp. 1173-1175, September 1988

[9] Y. J. Rao and D. A. Jackson, "A prototype fibre optic based Fizeau medical pressure and temperature sensor system using coherence reading," *Measurement Science and Technology*, vol. 5, pp. 741-746, 1994

[10] D. C. C. Norman, D. J. Webb and R. D. Pechstedt, "Interferometric Sensor interrogation using an arrayed waveguide grating," *Photonics Technology Letters*, Vol. 17, No. 1, pp. 172-174, January 2005

[11] C. Boulet, D. J. Webb, M. Douay and P. Naiy, "Simultaneous interrogation of fibre Bragg grating sensors using an acousto-optic tunable filter," *Photonics Technology Letters*, vol. 13, No. 11, pp. 1215-1217, November 2001

11. Publications Resulting from this Work

[1] D. C. C. Norman, D. J. Webb and R. D. Pechstedt, "Measurement of wavelength shift in fibre Bragg grating sensors using an arrayed waveguide grating," *in Proceedings PREP 2003 Conference*, (PREP2003, Exeter, United Kingdom), Technical Digest, pp. 51-52, April 2003 **(Oral Presentation)**

[2] D. C. C. Norman, D. J. Webb and R. D. Pechstedt, "Interrogation of fibre Bragg grating sensors using an arrayed waveguide grating," *in Proceedings CLEO EUROPE EQEC 2003 Conference*, (Munich, Germany), Technical Digest, pp. CI3W, June 2003 **(Poster Presentation)**

[3] D. C. C. Norman, D. J. Webb and R. D. Pechstedt, "Extended range multiplexing of fibre Bragg grating sensors using an arrayed waveguide grating," *Institute of Physics In-Fibre Gratings and Special Fibres*, (Stoneleigh Park, Warwickshire, United Kingdom), October 2003 **(Oral Presentation)**

[4] D. C. C. Norman, D. J. Webb and R. D. Pechstedt, "Wide-range multiplexed FBG interrogation using an arrayed waveguide grating," *in Proceedings 16th International Conference on Optical Fibre Sensors*, (OFS-16, Nara, Japan), Technical Digest, pp. 564-567, October 2003 **(Oral Presentation)**

[5] D. C. C. Norman, D. J. Webb and R. D. Pechstedt, "Extended range interrogation of wavelength division multiplexed fibre Bragg grating sensors using an arrayed waveguide grating," *Electronics Letters*, vol. 39, No. 24, pp. 1714-1716, November 2003

[6] D. C. C. Norman, D. J. Webb and R. D. Pechstedt, "Interferometric and fibre Bragg grating sensor interrogation using an arrayed waveguide grating," *in Proceedings SPIE Photonics Europe 2004 Conference*, (Strasbourg, France), Technical Digest, pp. 182-183, April 2004 **(Oral Presentation)**

[7] D. C. C. Norman, D. J. Webb and R. D. Pechstedt, "Interrogation of fibre Bragg grating sensors using an arrayed waveguide grating," *Measurement Science and Technology*, vol. 15, pp. 691-698, November 2004

[8] D. C. C. Norman, D. J. Webb and R. D. Pechstedt, "Interferometric Sensor interrogation using an arrayed waveguide grating," *Photonics Technology Letters*, Vol. 17, No. 1, pp. 172-174, January 2005

[9] D. C. C. Norman, Y. Lai and D. J. Webb, "High birefringence fibre interrogating interferometer for optical sensing applications," *Electronics Letters*, Vol. 41, No. 5, pp. 235-236, March 2005

[10] D. C. C. Norman, Y. Lai and D. J. Webb, "High birefringence fibre interrogating interferometer for optical sensing applications," ," *in Proceedings 17th International Conference on Optical Fibre Sensors*, (OFS-17, Bruges, Belgium), Technical Digest, pp. 615-618., May 2005 **(Poster Presentation)**

[11] D. C. C. Norman and D. J. Webb, "Fibre Bragg sensor interrogation using an acousto-optic tuneable filter and low-coherence interferometry," (In preparation for publication)

Appendix

Appendix A

Appendix B

Appendix C

Appendix D

Appendix E

Appendix F

Appendix A

Pressure Sensitivity of Fibre Bragg Gratings

For a pressure change the Bragg wavelength shift $\Delta\lambda_B$ can be found by differentiating $\lambda_B = 2n\Lambda$ with respect to a change in pressure ΔP, given by [1]

$$\Delta\lambda_B = \lambda_B\left(\frac{1}{\Lambda}\frac{\partial\Lambda}{\partial P} + \frac{1}{n}\frac{\partial n}{\partial P}\right)\Delta P \qquad \text{(A.1)}$$

The contribution to the change in the fibre diameter due to the applied pressure is negligible when compared with the change in the refractive index and physical length of the grating [2]. The change in length ΔL of the grating is given by [2]

$$\frac{\Delta L}{L} = -\frac{(1-2\mu)P}{E} \qquad \text{(A.2)}$$

where E is Young's modulus of the fibre and μ is Poisson's ratio. As a result of $\Delta L/L = \Delta\Lambda/\Lambda$ the normalised pitch-pressure is given by [3]

$$\frac{1}{\Lambda}\frac{d\Lambda}{dP} = -\frac{(1-2\mu)}{E} \qquad \text{(A.3)}$$

where Λ is the period of the grating. The change in refractive index Δn of the grating is given by [2].

$$\frac{\Delta n}{n} = \frac{n^2 P}{2E}(1-2\mu)(2\rho_{12}+\rho_{11}) \tag{A.4}$$

where ρ_{12} and ρ_{11} are components of the strain optic tensor (Pockel's coefficients) of the fibre. The normalised index-pressure is given by [3]

$$\frac{1}{n}\frac{dn}{dP} = \frac{n^2}{2E}(1-2\mu)(2\rho_{12}+\rho_{11}) \tag{A.5}$$

By substituting equations (A.3) and (A.5) into equation (A.1), the Bragg wavelength change $\Delta\lambda_B$ per change in pressure ΔP, is given by

$$\frac{\Delta\lambda_B}{\Delta P} = \lambda_B\left(-\frac{(1-2\mu)}{E} + \frac{n^2}{2E}(1-2\mu)(2\rho_{12}+\rho_{11})\right) \tag{A.6}$$

Consequently, the resulting wavelength shift is very small, for example a germainium doped fibre Bragg grating at 1.55 µm $\Delta\lambda_B/\Delta P$ was measured as -3×10^{-3} nm/MPa over a pressure range of 70 MPa [4].

Magnetic Field Sensitivity of Fibre Bragg Gratings

By using the Faraday-effect to induce very small changes in the refractive index of the fibre experienced by left and right circularly polarised light at the grating location, fibre Bragg gratings can be used to detect magnetic fields [5]. The index is altered for the two circular polarisations and as a consequence two Bragg conditions are observed, given by [5]

$$\lambda_{Br} = 2n_r\Lambda \qquad \text{(A.7a)}$$

and

$$\lambda_{Bl} = 2n_l\Lambda \qquad \text{(A.7b)}$$

where the subscripts r and l represent the Bragg wavelength and the index for the right and left circularly polarised. The sensitivity of this effect is very weak relying on the strength of the Faraday-effect in the fibre. The change in index is given by [5]

$$n_r - n_l = \frac{V H \lambda}{2\pi} \qquad \text{(A.8)}$$

where V is the Verdet constant which is a measure of the Faraday-effect in the fibre at the operating wavelength λ and H is the applied magnetic field. The small wavelength shift can be detected using an interferometric interrogation scheme [5]

References

[1] M. G. Xu, L. Reekie, Y. T. Chow and J. P. Dakin, "Optical in-fibre grating high pressure sensor," *Electronics Letters*, vol. 29, No. 4, pp. 398-399, February 1993

[2] G. B. Hocker, "Fibre optic sensing of temperature and pressure," *Applied Optics*, vol. 18, No. 9, pp. 1445-1448, May 1979

[3] Y. J. Rao, "In-fibre Bragg grating sensors," *Measurement Science and Technology*, vol. 8, pp. 355-375, 1997

[4] M. G. Xu, H. Geiger and J. P. Dakin, "Optical in-fibre grating high pressure sensor," *Electronics Letters*, vol. 29, No. 4, pp. 398-399, February 1993

[5] A. D. Kersey and M. J. Marrone, "Fibre Bragg grating high magnetic field probe," *in Proceedings 10th International Conference on Optical Fibre Sensors*, (OFS-10, Glasgow, United Kingdom), Technical Digest, pp. 53-56, May 1994

Appendix B

Thermal Drift Calculations for Silica and Indium Phosphide Arrayed Waveguide Gratings

Thermal drift in silica and indium phosphide arrayed waveguide gratings is found by rearranging equation (3.1) for the wavelength $\lambda = n_w \Delta L/m$ and differentiating with respect to T using the product rule, gives

$$\frac{\Delta\lambda}{\Delta T} = \frac{1}{m}\left(\frac{d\Delta L}{dT} n_w + \frac{dn_w}{dT}\Delta L\right) \tag{B.1}$$

and dividing through by ΔL, gives

$$\frac{\Delta\lambda}{\Delta T\,\Delta L} = \frac{1}{m}\left(\frac{1}{\Delta L}\frac{d\Delta L}{dT} n_w + \frac{dn_w}{dT}\right) \tag{B.2}$$

For silica (S_iO_2) at room temperature in the C-Band, the thermal expansion coefficient $1/\Delta L \; d\Delta L/dT = 5 \times 10^{-7}$ / °C [1] and the temperature derivative of refractive index $dn_w/dT = 1 \times 10^{-5}$ / °C [1], substituting these values into equation (B.2), gives

$$\frac{\Delta\lambda}{\Delta T\,\Delta L} = \frac{1}{m}\left(5\times10^{-7} n_w + 1\times10^{-5}\right) \tag{B.3}$$

Rearranging for $\Delta\lambda/\Delta T$, gives

$$\frac{\Delta\lambda}{\Delta T} = 5\times10^{-7}\,\frac{n_w \Delta L}{m} + 1\times10^{-5}\,\frac{\Delta L}{m} \tag{B.4}$$

From $n_w \Delta L/m = \lambda$ thus $\Delta L/m = \lambda/n_w$, therefore

$$\frac{\Delta\lambda}{\Delta T} = \left(5\times10^{-7}\lambda\right) + \left(1\times10^{-5}\,\frac{\lambda}{n_w}\right) \tag{B.5}$$

where $n_w = 1.45$ is the refractive index of the silica waveguide [1]. For a silica arrayed waveguide grating with a central operating wavelength of 1545 nm the thermal drift is

$$\frac{\Delta\lambda}{\Delta T}(Silica) = 1.147\times10^{-11} = 11.5 \text{ pm/ °C} \tag{B.6}$$

The same analogy applies for indium phosphide (InP) arrayed waveguide gratings, where at room temperature in the C-Band the thermal expansion coefficient $1/\Delta L \;\, d\Delta L/dT$ = 4.3×10^{-6} / °C [1], the temperature derivative of refractive index $dn_w/dT = 2.02 \times 10^{-4}$ / °C [1] and the refractive index of the waveguides $n_w = 3.1$ [1]. Hence, the thermal drift is given by

$$\frac{\Delta\lambda}{\Delta T}(InP) = 1.073\times10^{-10} = 107 \text{ pm/ °C} \tag{B.7}$$

References

[1] D. N. Nikogosyan, "Properties of optical and laser related materials," *John Wiley & Sons*, ISBN: 0-471-97384, 1998

Appendix C

Bookham Optical Channel Monitor Wavelength Allocation

Table C.1 shows the allocation of channel numbers to wavelengths and frequencies.

Channel	Frequency (THz)	Wavelength (nm)
C1	192.1	1560.61
C2	192.2	1559.79
C3	192.3	1558.98
C4	192.4	1558.17
C5	192.5	1557.36
C6	192.6	1556.55
C7	192.7	1555.75
C8	192.8	1554.94
C9	192.9	1554.13
C10	193.0	1553.33
C11	193.1	1552.52
C12	193.2	1551.72
C13	193.3	1550.92
C14	193.4	1550.12
C15	193.5	1549.32
C16	193.6	1548.51
C17	193.7	1547.72
C18	193.8	1546.92
C19	193.9	1546.12
C20	194.0	1545.32
C21	194.1	1544.53
C22	194.2	1543.73
C23	194.3	1542.94
C24	194.4	1542.14
C25	194.5	1541.35
C26	194.6	1540.56
C27	194.7	1539.77
C28	194.8	1538.98
C29	194.9	1538.19
C30	195.0	1537.40
C31	195.1	1536.61
C32	195.2	1535.82
C33	195.3	1535.04
C34	195.4	1534.25
C35	195.5	1533.47
C36	195.6	1532.68
C37	195.7	1531.90
C38	195.8	1531.12
C39	195.9	1530.33
C40	196.0	1529.55

Table C.1 Channel wavelength allocations for the Bookham optical channel monitor.

Appendix D

Construction of the Laboratory Mach-Zehnder Interferometer

A diagram of the all-fibre Mach-Zehnder interferometer used for the experimental work described in this thesis is shown in figure D.1. To build the interferometer the two fibre arms were laid out side by side on a bench with one arm a continuous length of fibre (including the integrated optic phase modulator) the other arm was left in two halves. An air-gap was designed into the interferometer to allow easy adjustment of the optical path

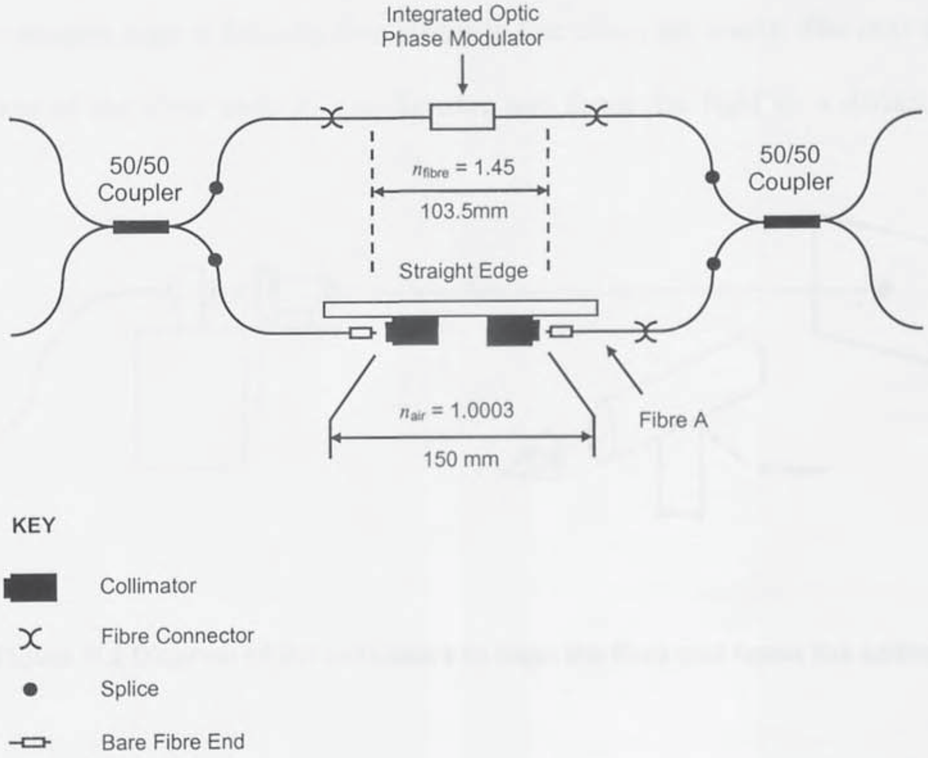

Figure D.1 Diagram of the all-fibre Mach-Zehnder interferometer.

difference during the experimental work. If the physical distance between the two fibre ends is say around 62 mm then the free-space air-gap needed to balance the interferometer is around 90 mm (i.e. $n_{fibre} = 1.45$, $n_{air} = 1.0003$, $90 \times 1.0003 = 90$ and $62 \times 1.45 = 90$). Because the air-gap uses two collimators which are 70 mm long the distance between the fibre ends was designed with a free-space air-gap of 150 mm this would provide a 20 mm gap between the faces of the two collimators. The interferometer was then transferred and set-up on an optical table. The next stage was to align the two collimators. The two collimators were each mounted onto translation stages which ran along a straight edge to keep the two stages in line along the z-axis. The next step was to align one of the fibre ends to a collimator and focus the light to a distant target, as shown in figure D.2. Once this procedure was completed the corresponding translation stage was secured to the optical table. The next step was to line the focused beam into the other bare fibre end via the second collimator. This was achieved by using fibre A (see figure D.1) connected directly to a photodiode and oscilloscope, as depicted in figure D.3. The translation stage x, y, and z axes were adjusted to achieve the best voltage output. Fibre A could then be reconnected into the interferometer and the output

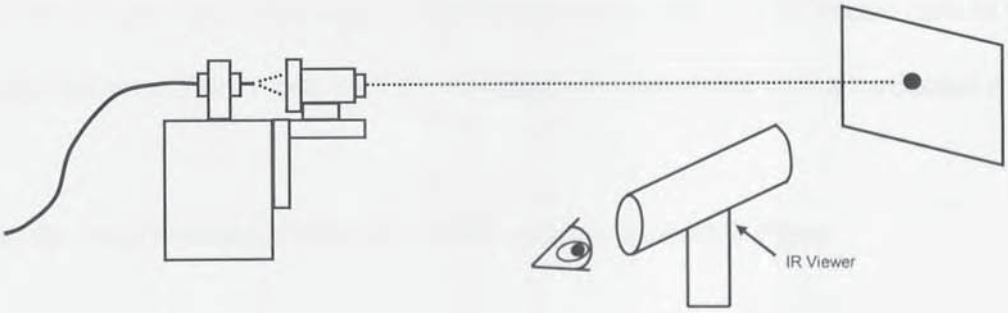

Figure D.2 Diagram of the procedure to align the fibre and focus the collimator.

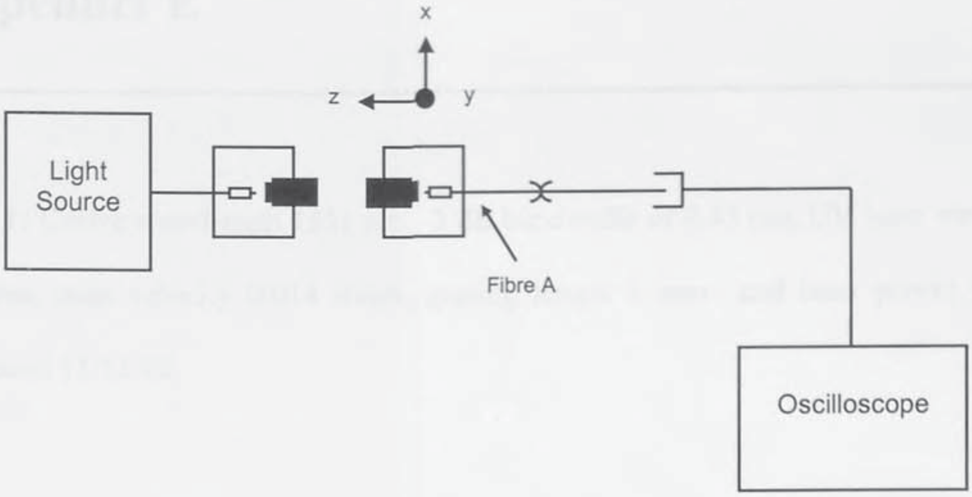

Figure D.3 Diagram depicting lining up the two collimators.

observed on an optical spectrum analyser with the optical path difference easily adjusted using the air-gap. The whole set-up was then enclosed into a large plastic case to protect the interferometer from drafts with the air-gap further insulated with a cardboard cover.

Using the Interferometer with the Acousto-Optic Tuneable Filter

The design of the laboratory interferometer allows easy insertion of the acousto-optic tuneable filter. This was done by laying out the phase modulator and the acousto-optic tuneable filter side by side. This showed that one of the pigtails from the acousto-optic tuneable filter required an extra 0.65 m of fibre to be inserted.

Appendix E

FBG 1: Centre wavelength 1551 nm, -3 dB bandwidth of 0.43 nm, UV laser wavelength 244 nm, scan velocity 0.014 mm/s, grating length 5 mm and laser power 90 mW. Produced 11/12/02.

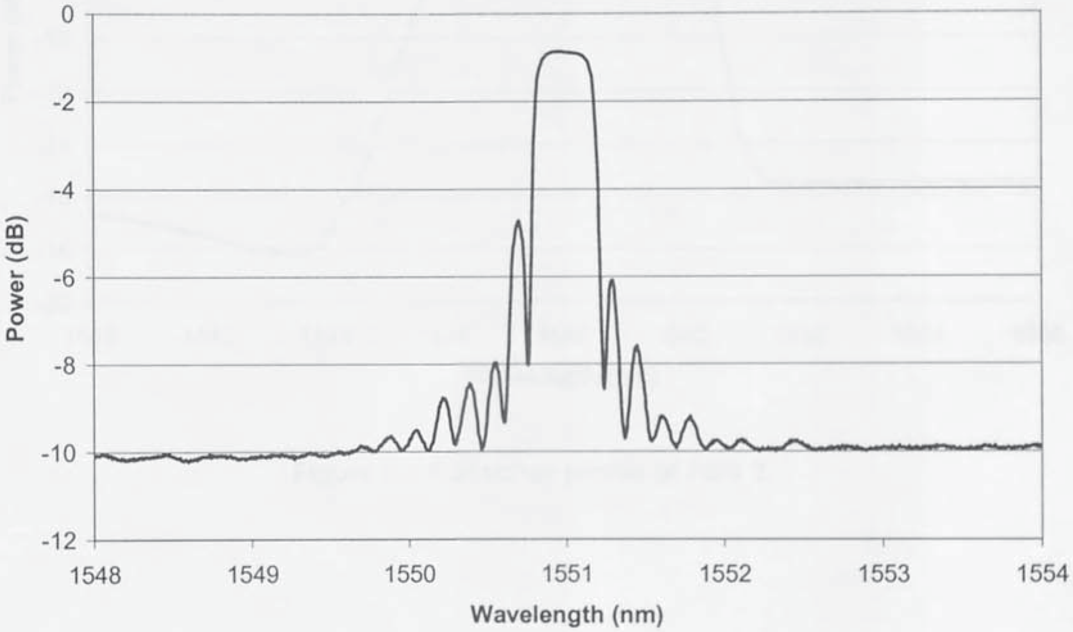

Figure E.1 Reflection profile of FBG 1.

FBG 2: Centre wavelength 1548.16 nm, -3 dB bandwidth of 5.4 nm, UV laser wavelength 244 nm, scan velocity 0.007 mm/s, grating length 4 mm and laser power 90 mW. Produced 11/09/03.

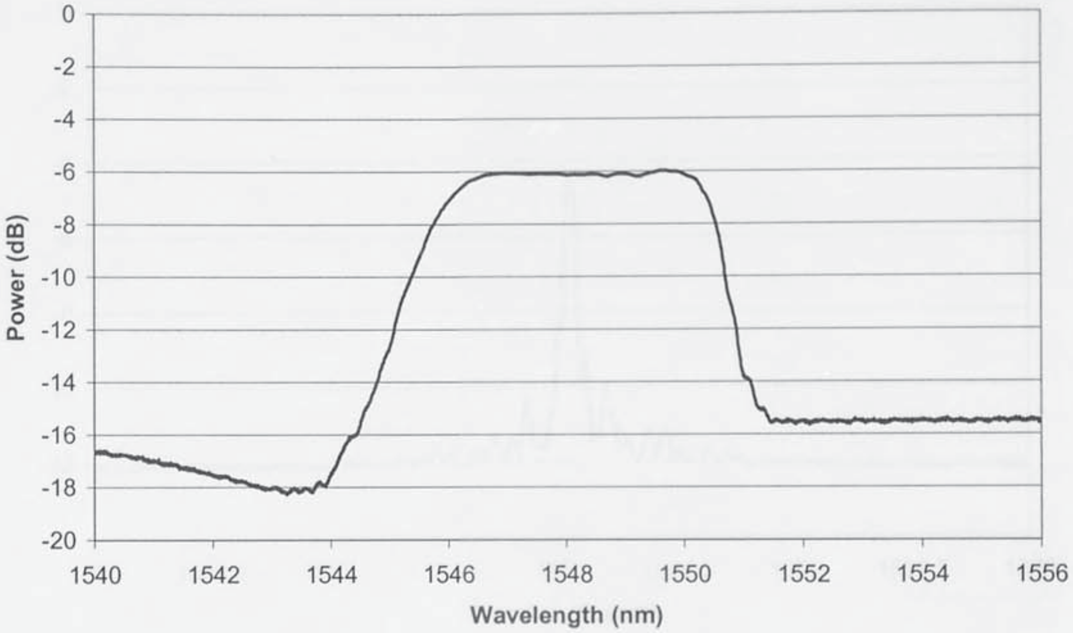

Figure E.2 Reflection profile of FBG 2.

FBG 3: Centre wavelength 1558.29 nm, -3 dB bandwidth of 0.125 nm, UV laser wavelength 244 nm, scan velocity 0.01 mm/s, grating length 4 mm and laser power 90 mW. Produced 11/12/02.

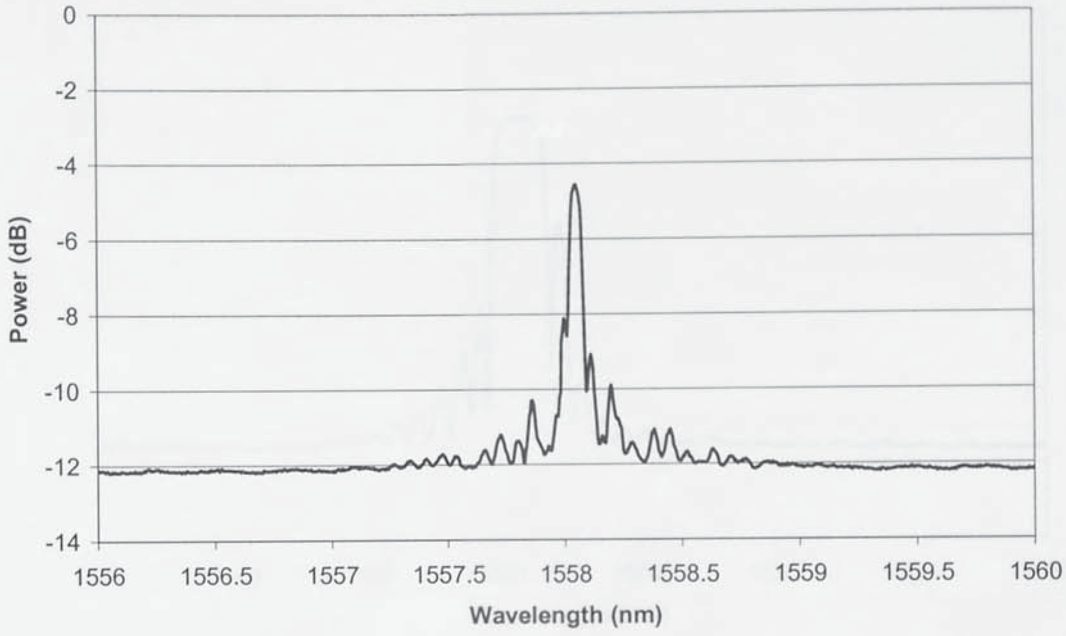

Figure E.3 Reflection profile of FBG 3.

FBG 4: Centre wavelength 1551.29 nm, -3 dB bandwidth of 0.46 nm, UV laser wavelength 244 nm, scan velocity 0.013 mm/s, grating length 5 mm and laser power 90 mW. Produced 11/12/02.

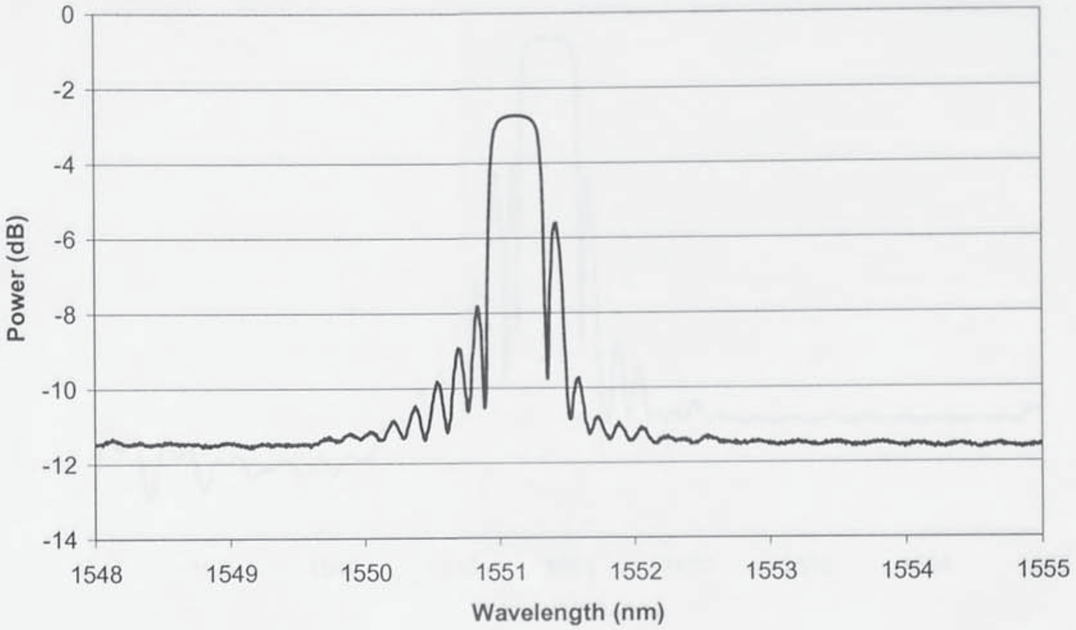

Figure E.4 Reflection profile of FBG 4.

FBG 5: Centre wavelength 1550.95 nm, -3 dB bandwidth of 0.46 nm, UV laser wavelength 244 nm, scan velocity 0.011 mm/s, grating length 5 mm and laser power 90 mW. Produced 11/12/02.

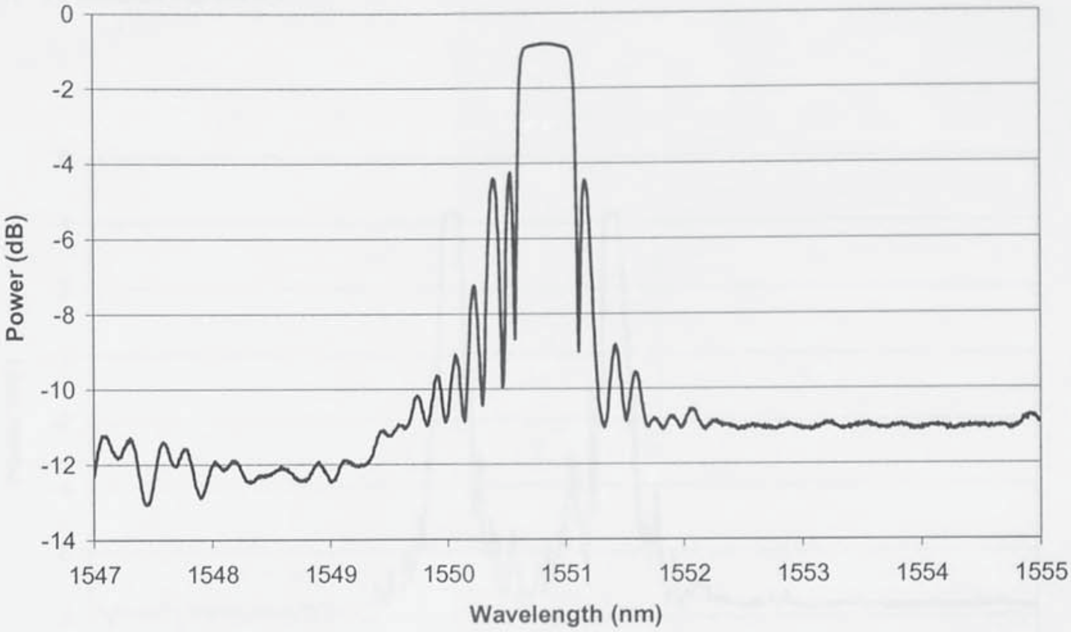

Figure E.5 Reflection profile of FBG 5.

FBG 6: Double peaked (superimposed) grating constructed using the stretch and write technique. First peak at wavelength 1549.73 nm with a -3 dB bandwidth of 0.22 nm and the second peak at wavelength 1550.91 with a -3 dB bandwidth of 0.22 nm, UV laser wavelength 244 nm, scan velocity 0.085 mm/s, grating length 25 mm and laser power 90 mW. Produced 02/06/03.

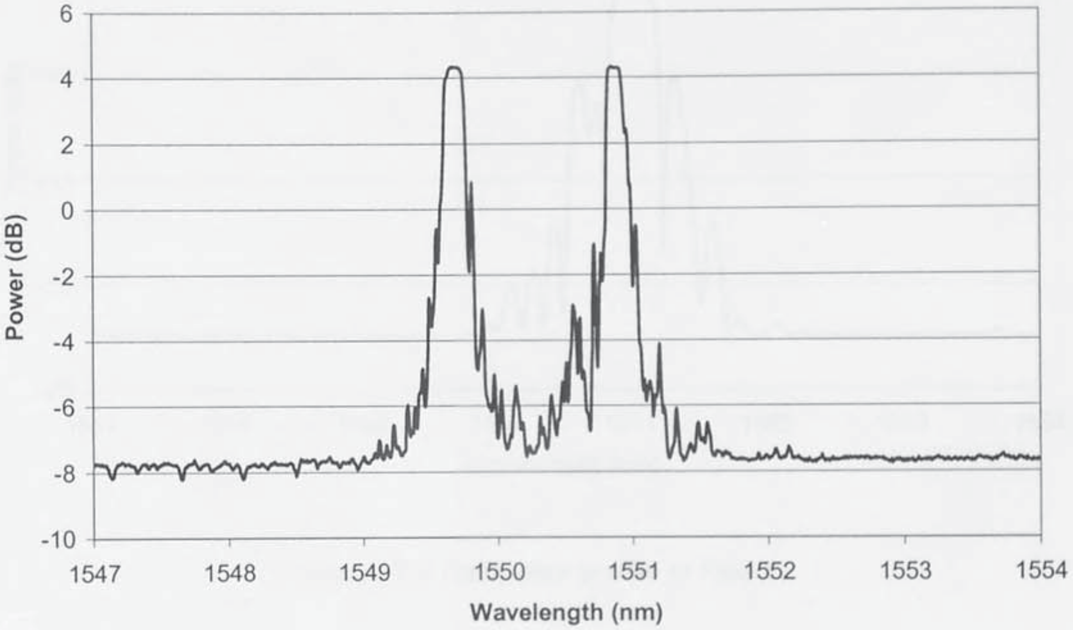

Figure E.6 Reflection profile of FBG 6.

FBG 7: Centre wavelength 1551.05 nm, -3 dB bandwidth of 0.81 nm, UV laser wavelength 244 nm, scan velocity 0.02 mm/s, grating length 25 mm and laser power 90 mW. Produced 04/06/03.

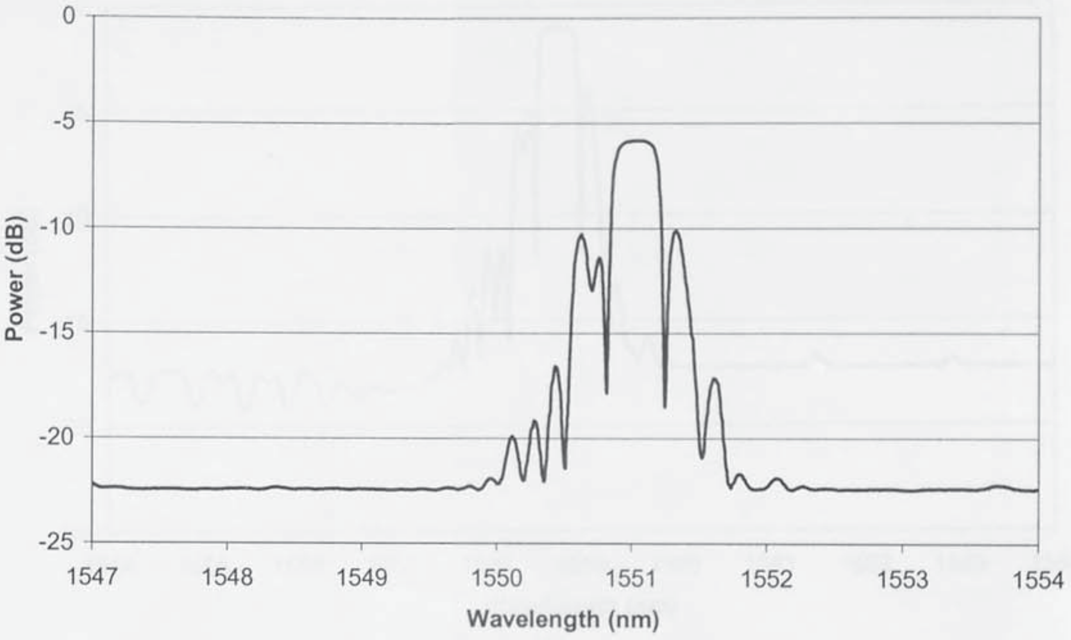

Figure E.7 Reflection profile of FBG 7.

FBG 8: Centre wavelength 1558.6 nm, -3 dB bandwidth of 0.8 nm, UV laser wavelength 244 nm, scan velocity 0.017 mm/s, grating length 5 mm and laser power 90 mW. Produced 15/12/03.

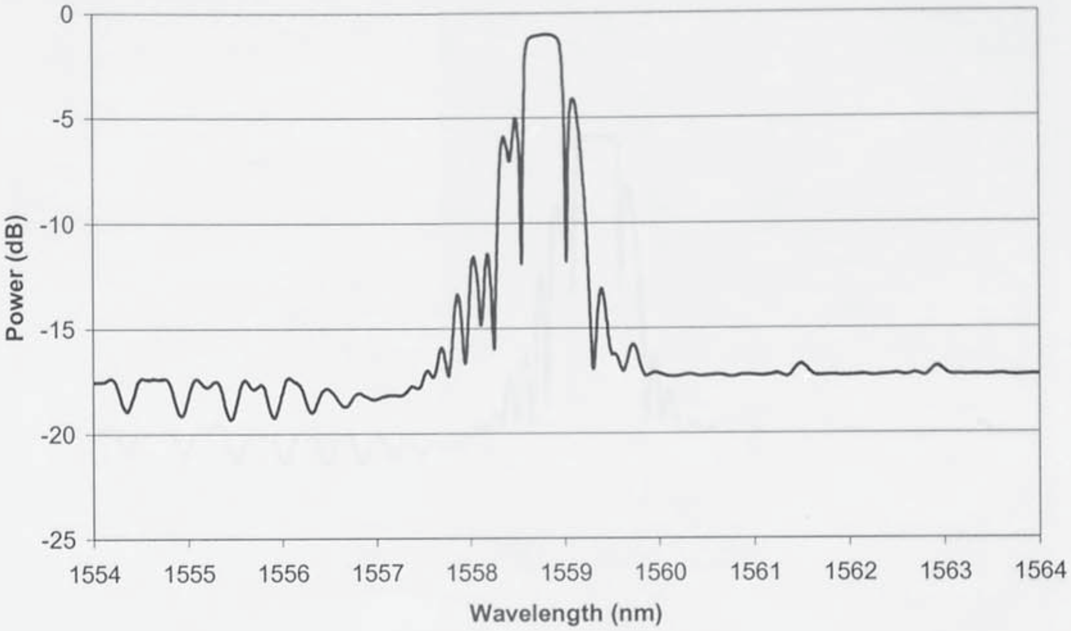

Figure E.8 Reflection profile of FBG 8.

FBG 9: Centre wavelength 1543.4 nm, -3 dB bandwidth of 0.8 nm, UV laser wavelength 244 nm, scan velocity 0.017 mm/s, grating length 5 mm and laser power 90 mW. Produced 15/12/03.

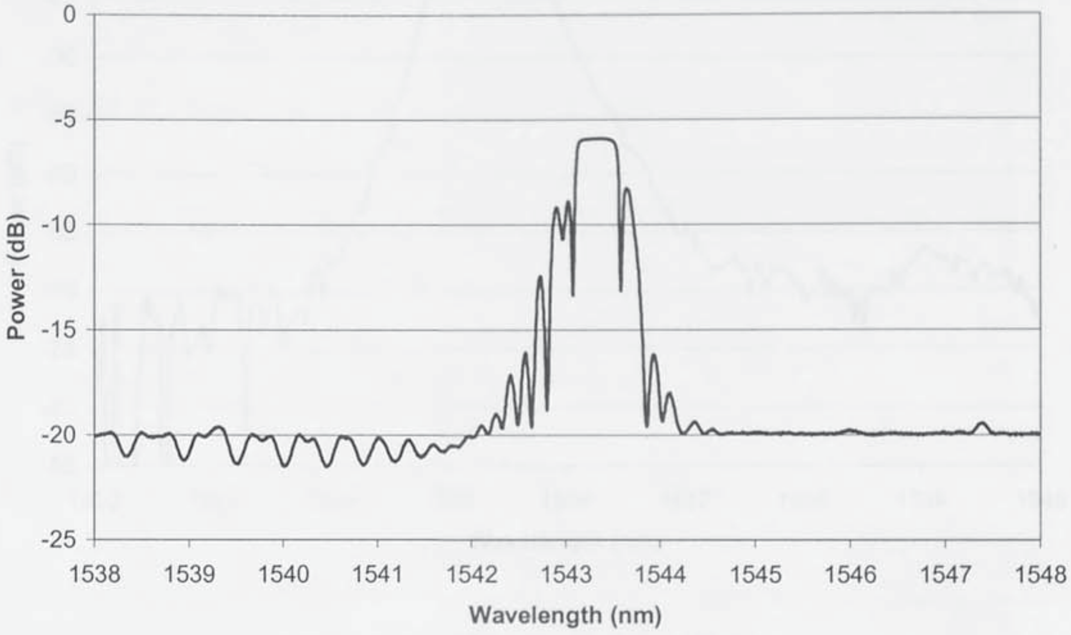

Figure E.9 Reflection profile of FBG 9.

FBG 10: Centre wavelength 1535.4 nm, -3 dB bandwidth of 0.85 nm. Unknown production data. Grating kindly donated by Barbara Cowie of Aston University.

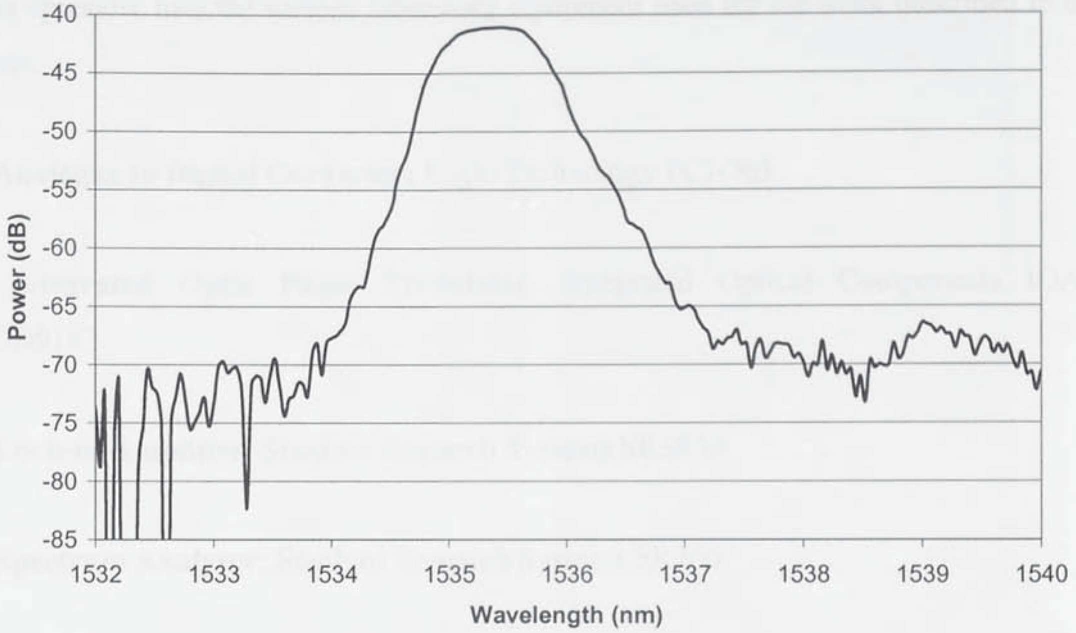

Figure E.10 Reflection profile of FBG 10.

Appendix F

This appendix lists the various laboratory equipment used for the work described in this thesis.

1. **Analogue to Digital Converter:** Eagle Technology PCI-703

2. **Integrated Optic Phase Modulator**: Integrated Optical Components IOAP-MOD9183

3. **Lock-in-Amplifier:** Stanford Research Systems SRS830

4. **Spectrum Analyser:** Stanford Research Systems SR760

5. **10 MHz Function Generator:** Thurlby Thandar Instruments TG1010A

6. **Oscilloscope:** Tektronix TDS3012

7. **Piezo Controller:** Physik Instrumente E710

8. **Piezo Translator:** Physik Instrumente P-840-30/40

9. **AOTF Driver:** Landwehr K101/K103/K104

10. **AOTF Electronics:** Frequency Mixer-Mini Circuits ZLW-6 and Voltage Controlled Oscillator-Mini Circuits POS-100

11. **Photodetector:** New Focus IR DC 125 MHz Low-Noise Photo-receiver

12. **Optical Spectrum Analyser:** ANDO AQ-1425

13. Adder, Amplifier and Bandpass Filter: The adder, amplifier and the bandpass filter construction is shown in figure F.1. The adder (summing amplifier with unity gain) because all the input resistors are equal including Ra then the output V_{out} of the adder circuit is given by [1]

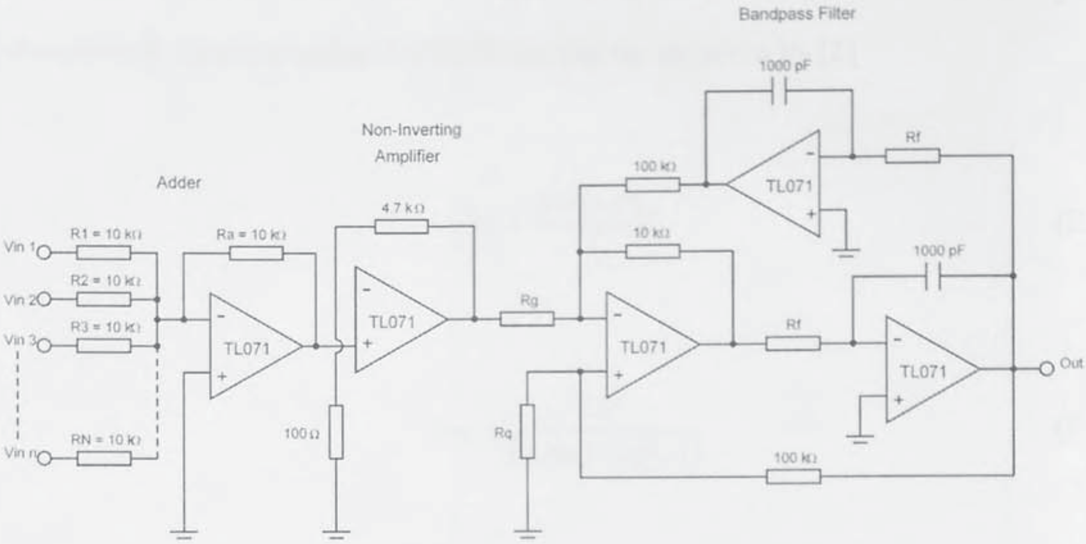

Figure F.1 The adder, amplifier and bandpass filter circuit.

$$V_{out} = -\left(\frac{V_{in1}}{R} + \frac{V_{in2}}{R} + \frac{V_{in3}}{R} + \dots\dots\dots \frac{V_{inN}}{R}\right)R = -\left(V_{in1} + V_{in2} + V_{in3} + \dots\dots\dots V_{inN}\right) \quad \text{(F.1)}$$

The non-inverting amplifier gain is given by [1]

$$G = 1 + \frac{R_f}{R_i} = 1 + \frac{4700}{100} = 48 \quad \text{(F.2)}$$

The bandpass filter is designed to be easily tuneable, the two resistors Rf set the centre frequency f_0, while Rq and Rg together determine gain G and the Q (which is a measure of sharpness of the passband at -3 dB). Rf, Rq and Rg are given by [2]

$$\mathrm{Rf} = \frac{5.03\times10_7}{f_0} \tag{F.3}$$

$$\mathrm{Rq} = \frac{10^5}{(3.48Q + G - 1)} \tag{F.4}$$

$$\mathrm{Rg} = \frac{3.16\times10^4 Q}{G} \tag{F.5}$$

References

[1] T. L. Floyd, "Electronics devices: electron flow version," *Prentice Hall*, ISBN: 0-13-649146-4, 1992

[2] P. Horowitz and W. Hill, "The art of electronics," *Cambridge University Press*, ISBN: 0-521-37095-7, 1992

Appendix G

Labview Program

The Labview program developed to interrogate chirped Bragg grating sensors selectively displayed the voltage level output of selected optical channel monitor (OCM) channels numerically and graphically. A screen capture of graphical user interface is shown in figure G.1. The user can select the appropriate OCM output channel as well as defining the start of sampling channel. The points on the graph show the voltage level in the

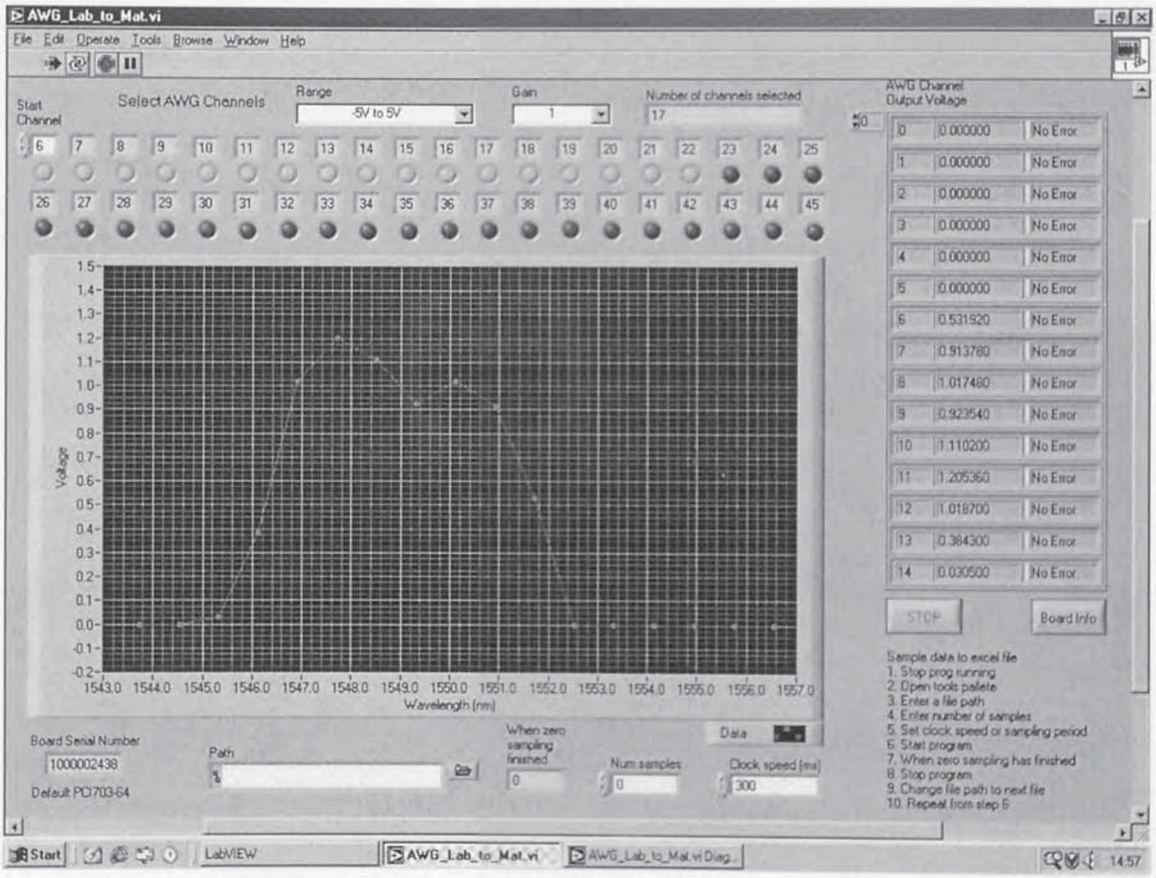

Start Channel: 6

Range: -5V to 5V

Gain: 1

Number of channels selected: 17

AWG Channel Output Voltage

0	0.000000	No Error
1	0.000000	No Error
2	0.000000	No Error
3	0.000000	No Error
4	0.000000	No Error
5	0.000000	No Error
6	0.531920	No Error
7	0.913780	No Error
8	1.017480	No Error
9	0.923540	No Error
10	1.110200	No Error
11	1.205360	No Error
12	1.018700	No Error
13	0.384300	No Error
14	0.030500	No Error

Board Serial Number: 1000002438

Default PCI703-64

Path: %

When zero sampling finished: 0

Num samples: 0

Clock speed (ms): 300

Sample data to excel file
1. Stop prog running
2. Open tools pallete
3. Enter a file path
4. Enter number of samples
5. Set clock speed or sampling period
6. Start program
7. When zero sampling has finished
8. Stop program
9. Change file path to next file
10. Repeat from step 6

Figure G.1 Screen capture of the Labview graphical user interface.

selected channels, the right most point being channel 6 which happens to be the selected start channel. Therefore, the points on the graph from right to left are displaying the voltage levels in channels 6 – 22. To the right of the GUI is the numerical voltage readout of each selected OCM channel which could be scrolled through using the button at the top left corner of the table. At the bottom right and middle of the GUI are the operating instructions and user settings.

Appendix H

Graphical Fitting Methods used in Section 6.6

To recover the position of the chirped grating a suitable fitting method was required. The adopted approach was to develop a Matlab program that read the data captured using the Labview program and use it to test various fitting methods. For each position of the chirped grating (as it was stretched through the corresponding OCM channels) the Labview program recorded 40 samples of the voltage present in each channel. The Matlab program took these 40 samples, calculated a mean [1] voltage in each OCM channel to produce a set of data (as a voltage level in each channel) representing the position of the chirped grating. This information could then be utilised in various ways

1. The first attempt was to fit a second order polynomial (using the Matlab function POLYFIT) to the data and track the peak position.
2. The second attempt was to fit a third order polynomial to the date and track the peak position.
3. Finally a the centroid of the data was calculated, using [2]

$$Centroid = \frac{\sum (i \times V_i)}{\sum V_i} \tag{H.1}$$

where i is the sampled OCM channel and V_i is the ith OCM channel voltage level output. The results of all three methods are shown in figure H.1 for convenience. As can be seen

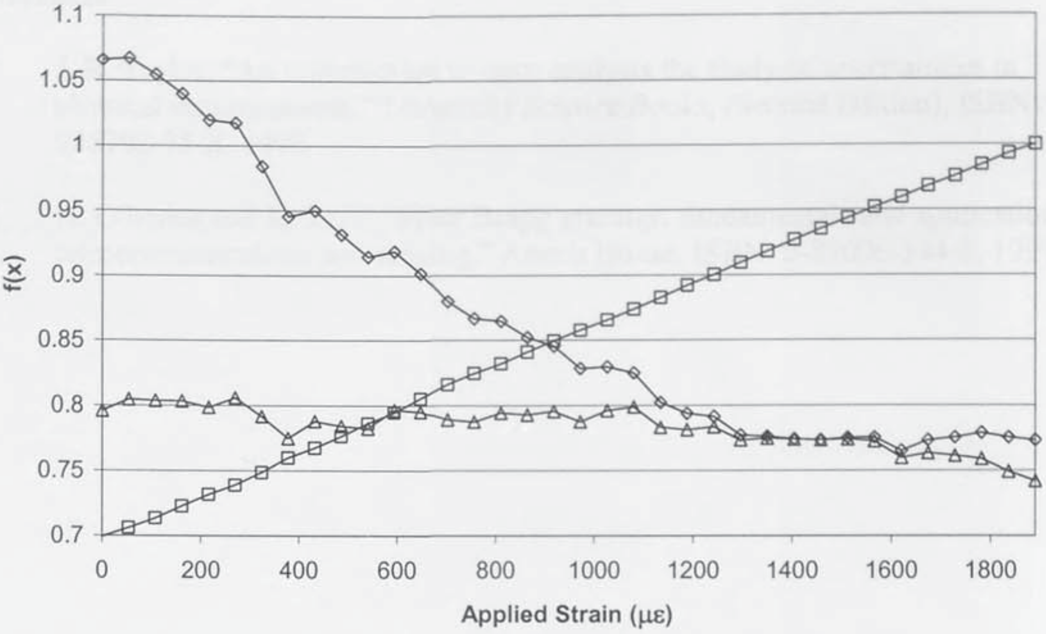

Figure H.1 Plot of the various fitting methods. Second order polynomial (triangles), third order polynomial (diamonds) and centroid (squares).

from figure H.1 the most linear response is a clearly a result of the centroid fit (squares). Therefore, this method was selected to recover the grating position in the experimental work described in section 6.6.

References

[1] J. R. Taylor, "An introduction to error analysis the study of uncertainties in physical measurements," *University Science Books*, (Second Edition), ISBN: 0-935702-75-X, 1997

[2] A. Othonos and K. Kalli, "Fiber Bragg gratings: fundamentals and applications in telecommunications and sensing," Artech House, ISBN: 0-89006-344-3, 1999

Appendix I

Difference between the Theoretical and Experimental Data for Active Interferometric Sensor Interrogation

Difference between the experimental and theoretical results verses the Mirror displacement for OCM channels $(13 \leftrightarrow 12)$ are shown in figure I.1.

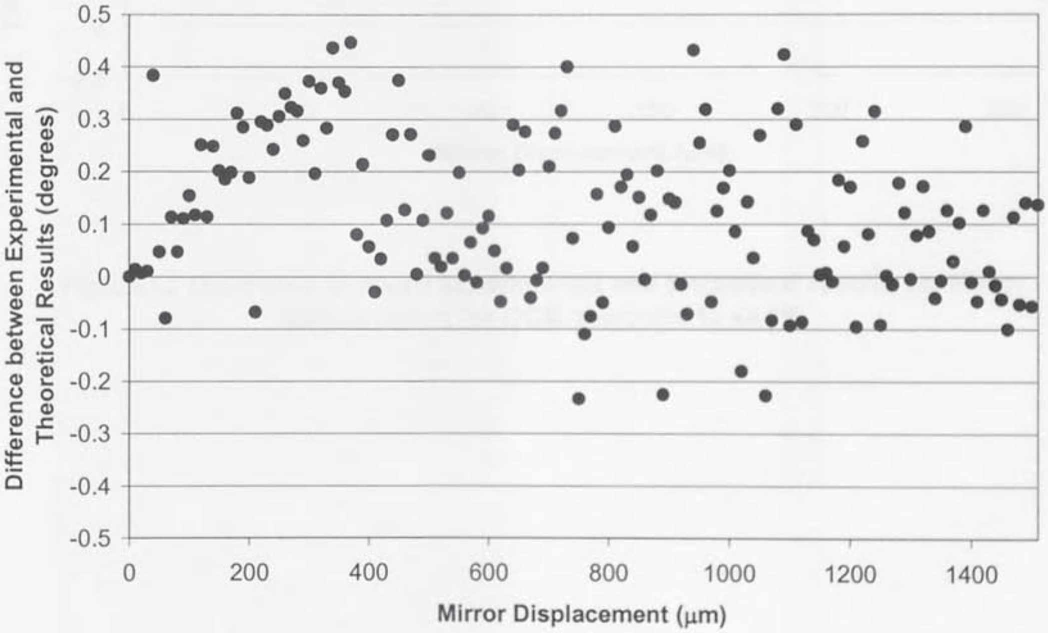

Figure I.1 Difference between experimental and theoretical results vs. Mirror displacement for OCM channels 13 ↔ 12.

Difference between the experimental and theoretical results verses the Mirror displacement for OCM channels $(13 \leftrightarrow 19)$ are shown in figure I.2.

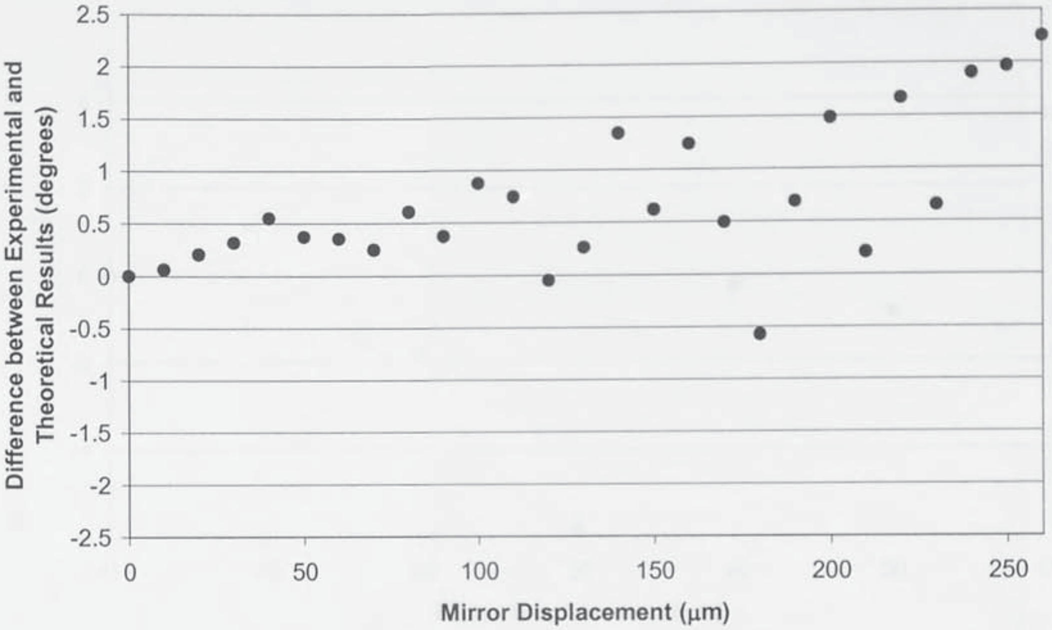

Figure I.2 Difference between experimental and theoretical results vs. Mirror displacement for OCM channels 13 ↔ 19.

Difference between the experimental and theoretical results verses the Mirror displacement for OCM channels $(13 \leftrightarrow 40)$ are shown in figure I.3.

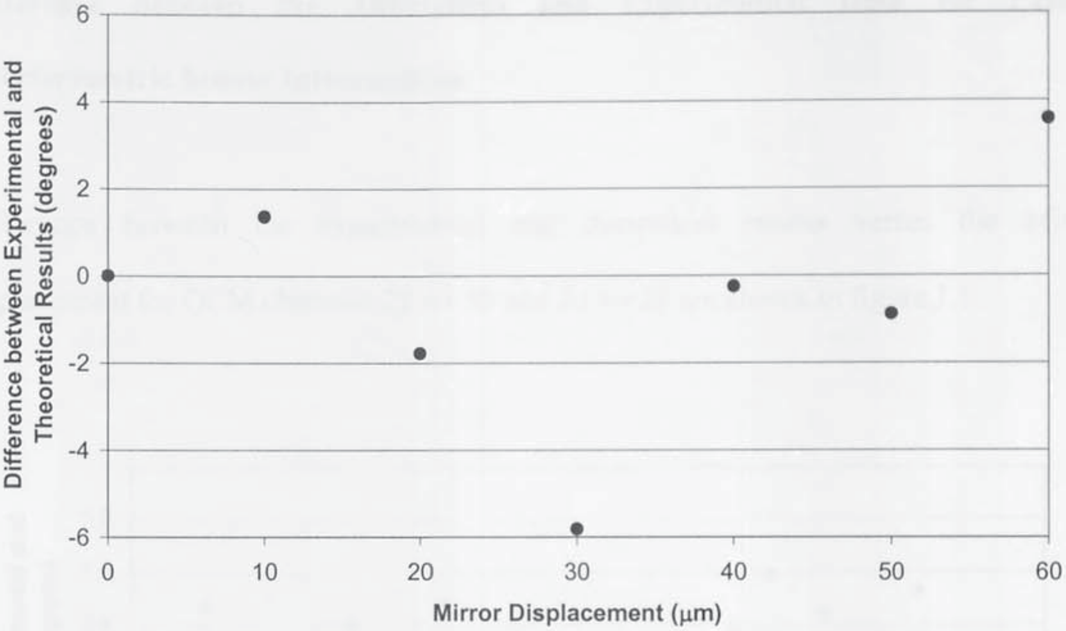

Figure I.3 Difference between experimental and theoretical results vs. Mirror displacement for OCM channels 13 ↔ 40.

Appendix J

Difference between the Theoretical and Experimental Data for Passive Interferometric Sensor Interrogation

Difference between the experimental and theoretical results verses the Mirror displacement for OCM channels 21 ↔ 30 and 20 ↔ 29 are shown in figure J.1.

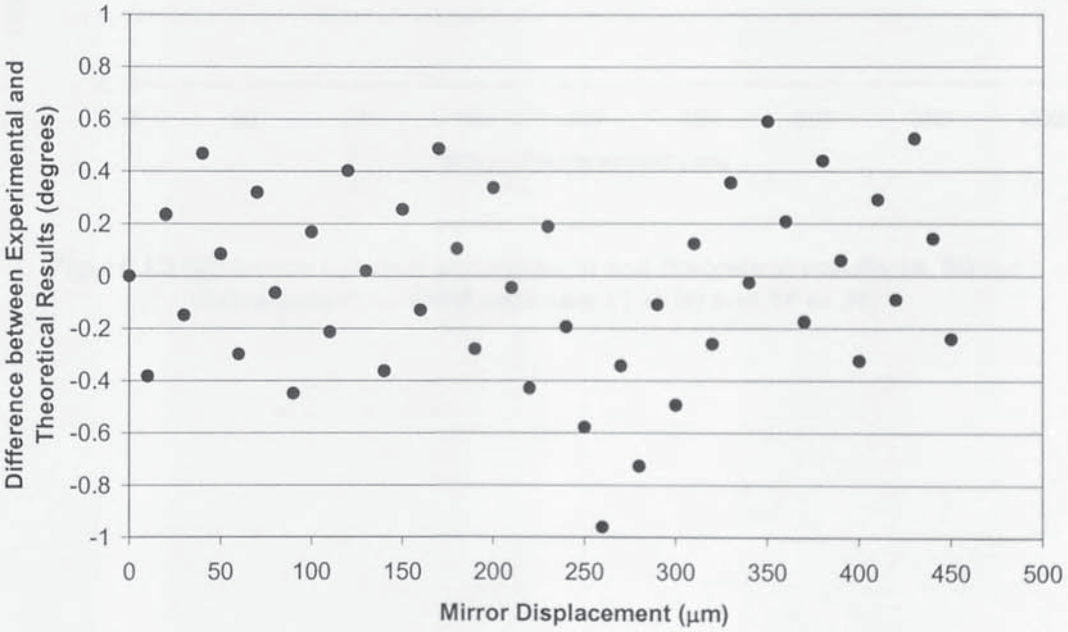

Figure J.1 Difference between experimental and theoretical results vs. Mirror displacement for OCM channels 21 ↔ 30 and 20 ↔ 29.

Difference between the experimental and theoretical results verses the Mirror displacement for OCM channels 21 ↔ 30 and 17 ↔ 26 are shown in figure J.2.

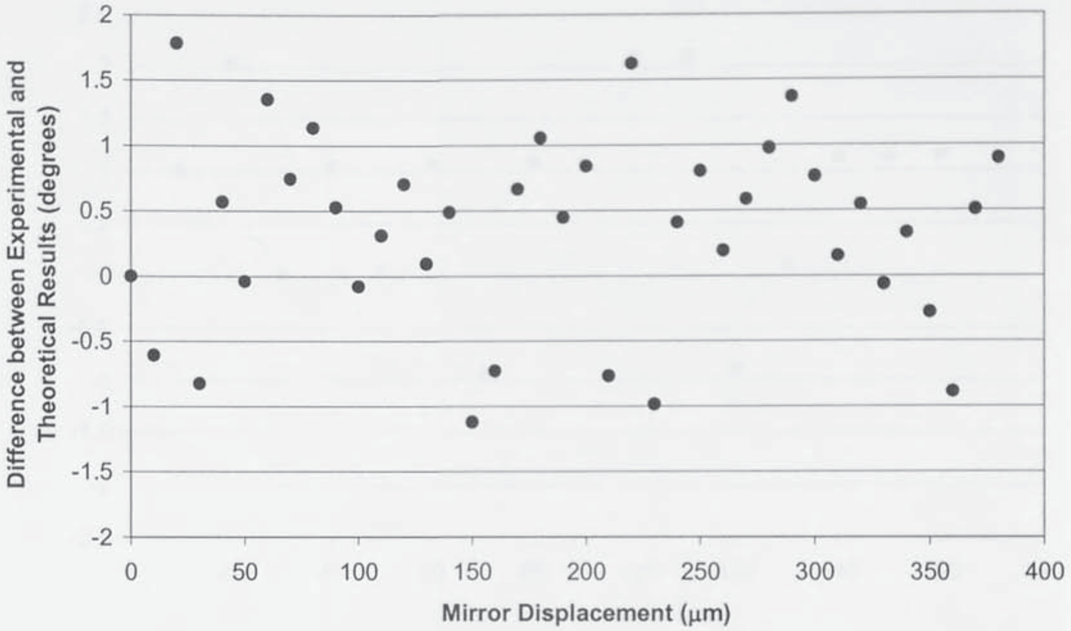

Figure J.2 Difference between experimental and theoretical results vs. Mirror displacement for OCM channels 21 ↔ 30 and 17 ↔ 26.

Difference between the experimental and theoretical results verses the Mirror displacement for OCM channels 21 ↔ 30 and 11 ↔ 20 are shown in figure J.3.

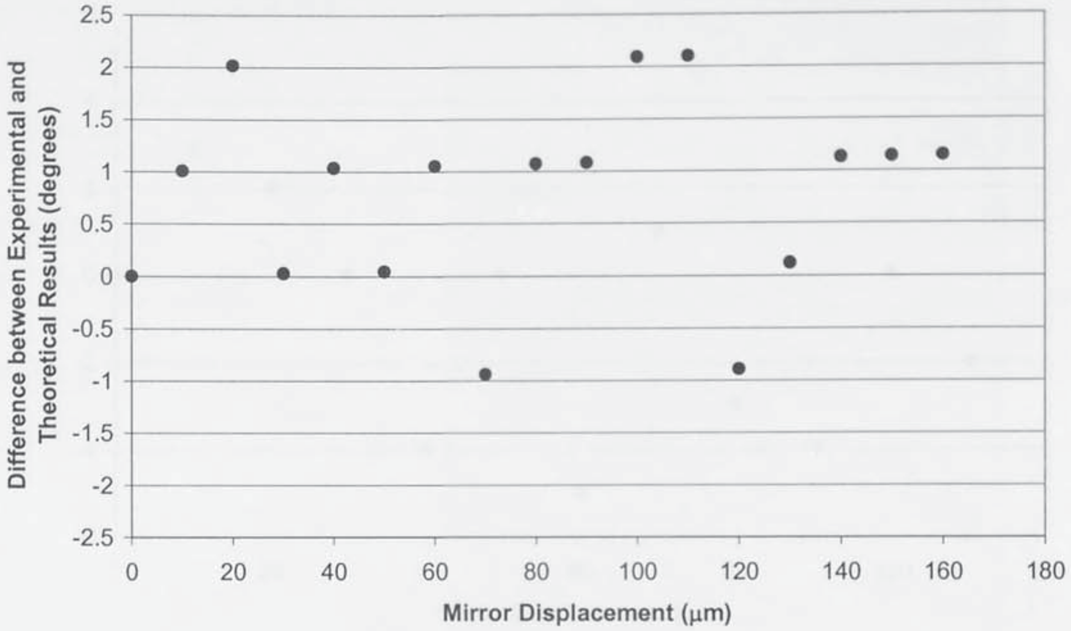

Figure J.3 Difference between experimental and theoretical results vs. Mirror displacement for OCM channels 21 ↔ 30 and 11 ↔ 20.

Difference between the experimental and theoretical results verses the Mirror displacement for OCM channels 21 ↔ 30 and 6 ↔ 15 are shown in figure J.4.

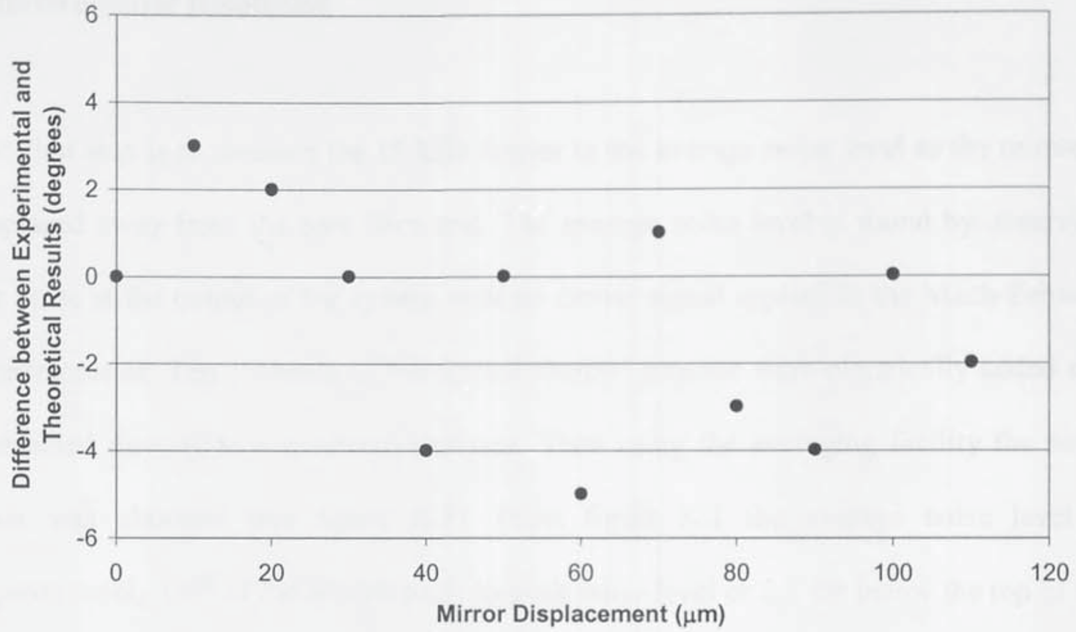

Figure J.4 Difference between experimental and theoretical results vs. Mirror displacement for OCM channels 21 ↔ 30 and 6 ↔ 15.

Appendix K

Interferometric Resolution

The first step is to measure the 10 kHz carrier to the average noise level as the mirror is displaced away from the bare fibre end. The average noise level is found by observing the noise at the output of the system with no carrier signal applied to the Mach-Zehnder interferometer. Ten channels of the optical channel monitor were electrically added and connected directly to a spectrum analyser. Then using the averaging facility the noise floor was obtained (see figure K.1). From figure K.1 the average noise level is approximately 1/6th of the overall peak-to-peak noise level or 2.5 dB below the top of the noise. The next step is to gather values of the carrier amplitude as the mirror is displaced

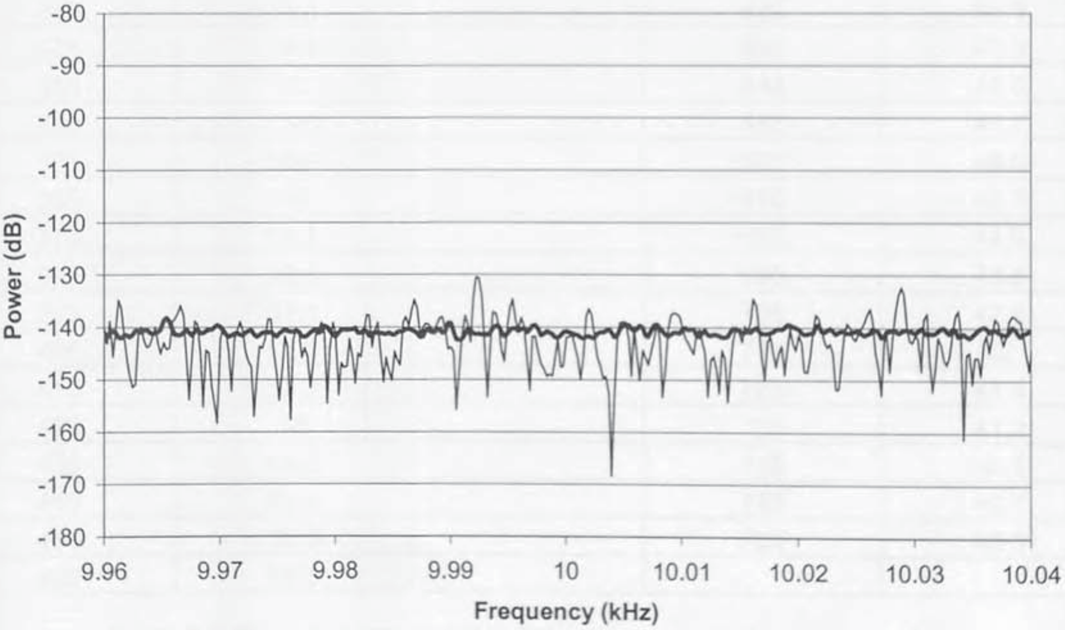

Figure K.1 Plot of the noise floor and the average noise level (heavy line).

from the fibre end. The mirror was positioned at 165 μm from the fibre end (equal to the effective source coherence length) and displaced away from the fibre to 765 μm (past the operational range of the interferometric sensor) in 10 μm steps and the carrier amplitude recorded (see table K.1).

Mirror Displacement (μm)	Carrier Amplitude (dB)		Mirror Displacement (μm)	Carrier Amplitude (dB)
165	50.5		475	58.5
175	50.9		485	58.3
185	51.2		495	57.9
195	51.4		505	57.4
205	51.7		515	57
215	52		525	56.5
225	52.1		535	56
235	52.4		545	55.3
245	52.7		555	54.7
255	53		565	54.3
265	53.3		575	53.5
275	53.6		585	52.7
285	53.8		595	52.1
295	54		605	51.4
305	54.2		615	51
315	54.5		625	50.3
325	54.8		635	49.5
335	55		645	48.6
345	55.6		655	47.7
355	55.8		665	46.6
365	56		675	45.7
375	56.2		685	44.9
385	56.6		695	43.8
395	57.1		705	42.8
405	57.6		715	42
415	57.8		725	41.6
425	58		735	41.2
435	58.2		745	40.8
445	58.4		755	40.7
455	58.6		765	40.6
465	58.6			

Table K.1 Experimental results of the signal to average noise ratio.

The average noise level determines the minimum detectable signal sideband level and hence the minimum amplitude of the mirror displacement. Therefore, the two sideband powers that would appear level with the noise floor would each have amplitudes of

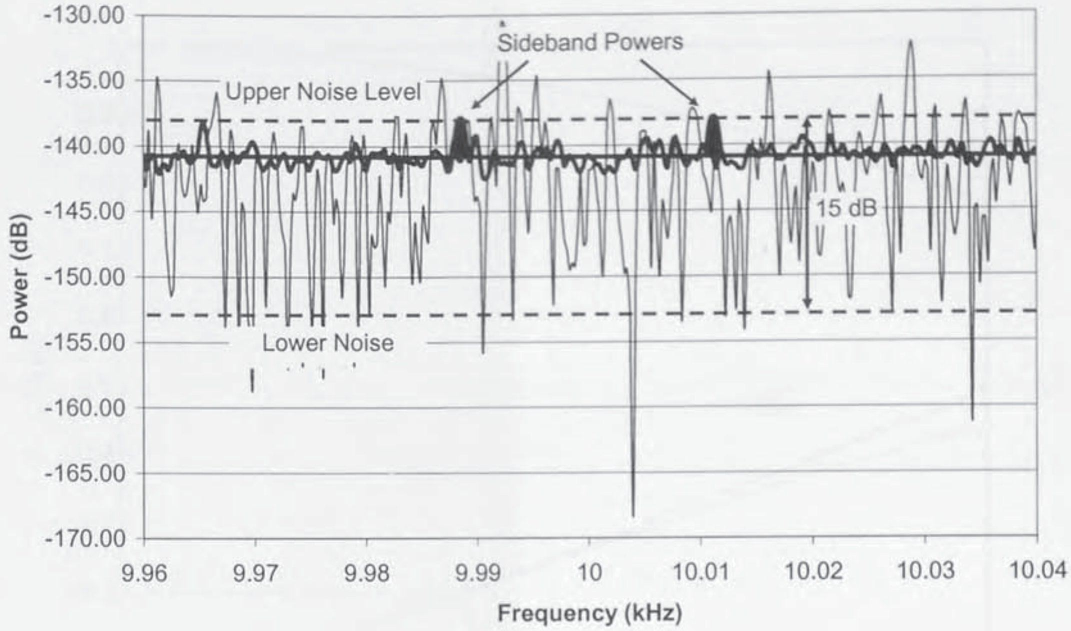

Figure K.2 Diagram depicting the sideband noise level from the average to the upper noise level.

around 2.5 dB. Hence, the recorded signal to noise level values listed in table L.1 are made worse by 2 × 2.5 dB. The values are then converted to a dimensionless ratio i.e. converted from decibels, scaled to 1 Hz bandwidth, made better again by 2 (for the two sidebands) and square rooted to produce the noise ratios N in $\sqrt{Hz}$ of each measured point. The interferometric resolution can then be found by using the Bessel functions $J_0(\Delta\phi)$ and $J_1(\Delta\phi)$. If the assumption is made that all of the minimum detectable sidebands are going to be small then J_0 can be assumed to be 1 and J_1 a straight line, as shown in figure K.3, then the inverse Bessel function can be used to find values for J_1, given by

$$J_1 = \frac{1}{N} \qquad \left[\frac{1}{\sqrt{Hz}}\right] \tag{K.1}$$

The values for $\Delta\phi$ can then be found by multiplying J_1 by 2. Once the values for $\Delta\phi$

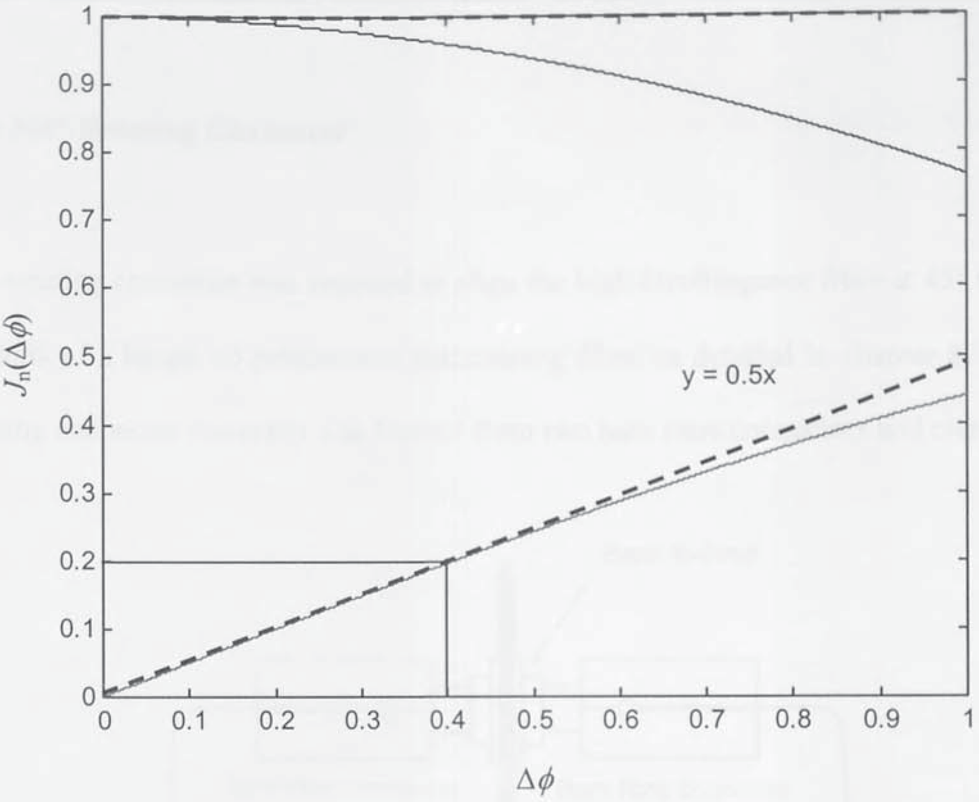

Figure K.3 Plot of J_0 and J_1 Bessel functions.

are known then the minimum detectable values for the cavity displacement ΔL can be obtained from

$$\Delta L = \frac{\Delta\phi\,\lambda}{4\pi n} \qquad \left[\frac{m}{\sqrt{Hz}}\right] \tag{K.2}$$

where λ is the central wavelength of the source and n is the refractive index of air (1.0003).

Appendix L

The 360° Rotating Connector

The rotating connector was required to align the high-birefringence fibre at 45° to that of the axis of a length of polarisation maintaining fibre, as detailed in chapter 8. A single rotating connector assembly was formed from two bare fibre connectors and one back-to-back. The back-to-back connector was de-assembled to remove the screw thread and fixed to a supporting frame. The two bare fibre connectors could then be inserted into either side of the modified back-to-back and freely rotated through 360° (see figure L.1). Although it was not what would be expected in an industrial solution the connector worked for the purpose of the laboratory experiment and at minimal cost.

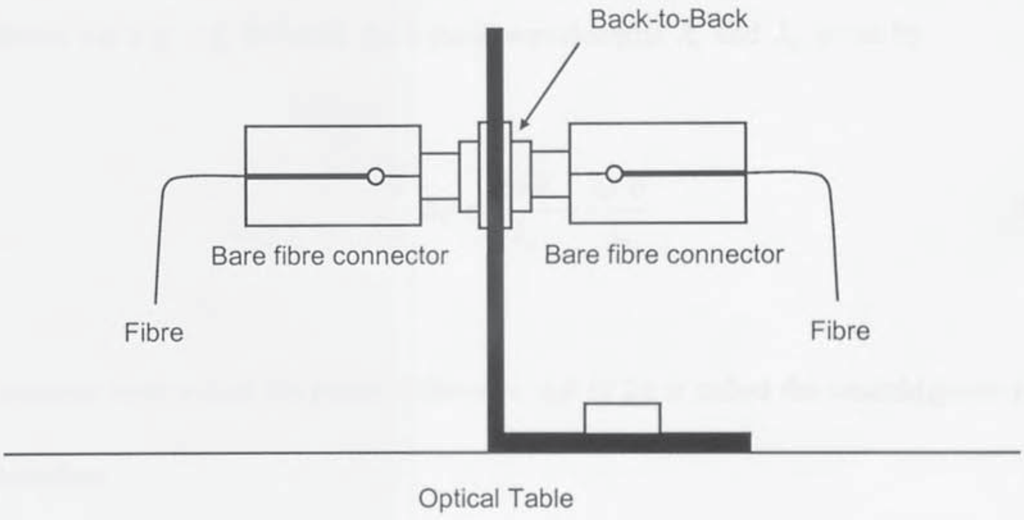

Figure L.1 Diagram of the 360° rotating connector.

Appendix M

This appendix derives the unambiguous range equations for the Mach-Zehender and Fizeau or low-finesse Fabry-Pérot interferometers.

Unambiguous Range Mach-Zehnder Interferometer

The unambiguous range for the Mach-Zehnder interferometer is derived from phase difference $\Delta\phi = \phi_1 - \phi_2$ between the light at wavelengths λ_1 and λ_2 given by

$$\Delta\phi = \frac{2\pi\,\delta}{\lambda_1} - \frac{2\pi\,\delta}{\lambda_2} \tag{M.1}$$

The distance over which the phase difference $\Delta\phi$ is 2π is called the unambiguous range δ_u, therefore

$$2\pi = \frac{2\pi\,\delta}{\lambda_1} - \frac{2\pi\,\delta}{\lambda_2} \tag{M.2}$$

simplifying and rearranging

$$1 = \frac{\delta}{\lambda_1} - \frac{\delta}{\lambda_2} \tag{M.3}$$

$$\lambda_1 \lambda_2 = \delta \lambda_2 - \delta \lambda_1 \tag{M.4}$$

$$\lambda_1 \lambda_2 = \delta (\lambda_2 - \lambda_1) \tag{M.5}$$

gives

$$\delta_u = \frac{\lambda_1 \lambda_2}{\lambda_2 - \lambda_1} \tag{M.6}$$

Unambiguous Range Extrinsic Fizeau Interferometer

The unambiguous range for the extrinsic Fizeau interferometer is the exactly the same derivation as above but the phase difference $\Delta\phi = \phi_1 - \phi_2$ between the light at wavelengths λ_1 and λ_2 is given by

$$\Delta\phi = \frac{4\pi\delta}{\lambda_1} - \frac{4\pi\delta}{\lambda_2} \tag{M.7}$$

giving

$$\delta_u = \frac{1}{2}\left(\frac{\lambda_1 \lambda_2}{\lambda_2 - \lambda_1}\right) \tag{M.6}$$

Appendix N

Difference between the Theoretical and Experimental Data for the Interferometric Sensing using an Acousto-Optic Tuneable Filter

Difference between the experimental and theoretical results verses the Mach-Zehnder optical path displacement for OCM channels 21 ↔ 30 and 6 ↔ 15 are shown in figure N.1.

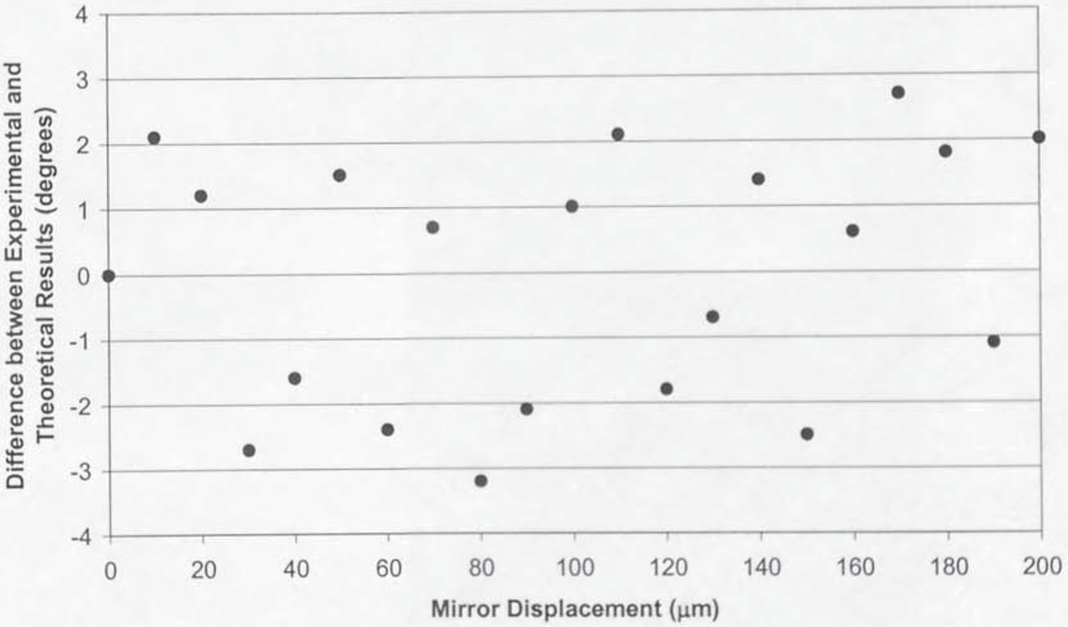

Figure N.1 Difference between experimental and theoretical results vs. Mach-Zehnder optical path displacement for OCM channels 21 ↔ 30 and 6 ↔ 15.